

Christoph Schmüdderich

Contributions to the stability assessment
of slopes subjected to seismic loading

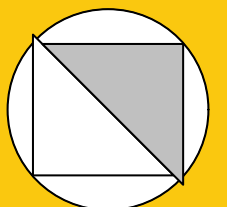
Bochum 2024

Heft 80

Schriftenreihe des Lehrstuhls für
Bodenmechanik, Grundbau und Umweltgeotechnik

Herausgeber: Torsten Wichtmann

ISSN 2699-1020



Ruhr-Universität Bochum

Schriftenreihe Bodenmechanik, Grundbau und Umweltgeotechnik

Heft 80

Herausgeber:

Prof. Dr.-Ing. habil. Torsten Wichtmann

Ruhr-Universität Bochum

Fakultät für Bau- und Umweltingenieurwissenschaften

Lehrstuhl für Bodenmechanik, Grundbau und Umweltgeotechnik

44801 Bochum

Telefon: 0234/ 3226135

Telefax: 0234/ 3214236

Internet: www.bgu.ruhr-uni-bochum.de

ISSN 2699-1020

© 2024 der Herausgeber

Contributions to the stability assessment of slopes subjected to seismic loading

Dissertation

as a requirement for the degree of
Doktor-Ingenieur (Dr.-Ing.)

at the Faculty of
Civil and Environmental Engineering
Ruhr-Universität Bochum

by
Christoph Schmüdderich

Reviewers

Prof. Dr.-Ing. habil. Torsten Wichtmann
Prof. Dipl.-Ing. Dr.techn. Franz Tschuchnigg
Prof. Dr.-Ing. Carlos Eduardo Grandas Tavera

Bochum, 2024

Preface of the editor

Lignite opencast mines are often recultivated as lakes. The embankments of these lakes are mainly composed of loose to medium dense artificial fills. If the lakes are located in a region with earthquake risk, the proof of slope stability for the embankments has to consider the seismic loading. During a seismic event shear waves propagate through the soil. Under almost undrained conditions the shear waves can lead to a build-up of excess pore water pressure, thus a reduction of effective stress. In the extreme case the effective stress vanishes completely and the soil is said to have “liquefied”. The reduction of effective stress means a reduction of the shear strength on potential failure surfaces. The reduced shear strength and the inertia forces resulting from the acceleration of the soil mass lead to a decreased slope stability compared to static conditions.

The methods for the proof of the seismic slope stability can be roughly divided into two groups: The pseudo-static approaches consider the accelerations by inertia forces and deliver a global factor of safety or degree of mobilization, respectively. However, accumulated excess pore water pressures and spatial fluctuations of the accelerations being particularly relevant for larger slope systems cannot be adequately taken into account by the existing approaches or commercial programs. The second category comprises methods which evaluate slope stability based on a deformation criterion. Deformations caused by the seismic event are predicted, for example using dynamic finite element simulations, and compared to tolerable values. However, the choice of these limit values is often rather subjective. Furthermore, previous studies were mainly restricted to rather simple constitutive models and neglected consolidation effects during and after the earthquake event. In his dissertation Christoph Schmüdderich has combined both approaches. He has developed advanced numerical methods that allow to analyze the temporal development of the stability of water-saturated slopes during seismic events, based on both the deformations and a factor of safety. The methods allow to consider spatially fluctuating fields of accumulated excess pore water pressures and accelerations. These fields are obtained from dynamic finite element simulations with advanced constitutive models and transferred to the stability analyses. For the analysis of seismic slope stability Christoph Schmüdderich has developed four different approaches, based on the „Limit equilibrium method“ (LEM), the „Finite element limit analysis“ (FELA), the „Strength reduction finite element analysis“ (SRFEA) and the „Strain-dependent slope stability“ (SDSS). He has implemented these approaches and successfully verified them by a comparison to commercial programs or well-documented benchmarks from the literature, including parametric studies on homogeneous slopes and also more complex boundary conditions. The potential of the four

approaches could be demonstrated based on an application to the synthetic example of an embankment of a lake in a recultivated lignite opencast mine. The subsequent application of the methods to two well-documented centrifuge model tests from the VELACS and the LEAP projects, considering a water-saturated dam or a shallow embankment, respectively, represents an important step towards the validation of the methods. Christoph Schmüdderich clearly works out the differences, advantages and deficits of the various approaches. Furthermore, he is able to demonstrate that the computational costs for the SDSS, which involves the simulation of numerous element tests, can be significantly reduced by applying Machine Learning algorithms, without losing much accuracy.

The dissertation of Christoph Schmüdderich represents an important step towards more comprehensive and realistic numerical investigations of the behavior and stability of water-saturated slopes under earthquake loading. The proposed approaches are of particular interest for the proof of the stability of embankments of lakes in abandoned opencast mines in seismic regions. In the framework of the dissertation a number of very powerful, well-documented and verified numerical tools have been developed which are applicable to such problems in future.

Torsten Wichtmann

Acknowledgment

This research was carried out at the Chair of Foundation Engineering, Soil and Rock Mechanics at Ruhr-Universität Bochum under the supervision of Prof. Dr.-Ing. habil. Tom Schanz and from 2019 at the Chair of Soil Mechanics, Foundation Engineering and Environmental Geotechnics at Ruhr-Universität Bochum under the supervision of Prof. Dr.-Ing. habil. Torsten Wichtmann.

At first, I want to thank my two supervisors, who guided and inspired me throughout my PhD studies. Prof. Schanz sparked my interest in research, in particular in soil mechanics and geotechnical engineering. His unwavering determination to explore complex problems and to seek explanations based on general principles of soil mechanics had a great influence on me and my understanding of scientific work. I am very grateful for the many discussions we had during my time as a student and doctoral candidate. Unfortunately, this time came to an abrupt end in October 2017 when he passed away suddenly and much too early. In April 2019, Prof. Wichtmann took over as the head of the Chair of Soil Mechanics, Foundation Engineering and Environmental Geotechnics at Ruhr-Universität Bochum. First and foremost, I would like to thank Prof. Wichtmann for accepting me as PhD student and allowing me to continue my PhD journey. In addition, I want to express my gratitude to Prof. Wichtmann for suggesting this very interesting research topic that I had the opportunity to work on for the past four years. With his continuous guidance and support Prof. Wichtmann encouraged me to work hard and to successfully complete my dissertation. His ideas and visions of the research topic made it possible for the concepts developed in the framework of this thesis to be further explored at the Chair and hopefully soon to be applied in geotechnical practice.

I want to thank my co-advisors Prof. Franz Tschuchnigg and Prof. Carlos Eduardo Grandas Tavera for the interest they have shown in my work and for the helpful comments they have provided to my thesis. I also want to thank Prof. Daniel Balzani, who chaired the doctoral committee and showed great interest in my research project. I owe special thanks to Prof. Tschuchnigg for his impact on my research, his continuous support and feedback. The collaboration we established since my research stay at TU Graz in 2018 had a significant impact on my work and my personal development, and helped me to focus on research, in particular during the difficult 1.5 years without a chair leading the geotechnical group in Bochum.

Special thanks to Dr. Jan Machaček, Prof. Patrick Staubach and Dr. Luis Felipe Prada-Sarmiento for their continuous support within the last four years, their feedback and the

endless discussions that we had. Jan Macháček and Patrick Staubach helped me getting familiar with finite element programs and gave me the opportunity to contribute to the finite element software package `numgeo`, while Felipe Prada was a tremendous help in getting familiar with the implementation of constitutive models as well as with numerous "Gedankenexperimenten". Being able to contribute to `numgeo` by implementation of elastoplastic constitutive models and the strength reduction method was a huge milestone for this research project that allowed to extend existing approaches for seismic slope stability assessment.

I would also like to thank all of my colleagues from the Chair of Foundation Engineering, Soil and Rock Mechanics / Chair of Soil Mechanics, Foundation Engineering and Environmental Geotechnics at Ruhr-Universität Bochum. Together we have been through some hard times, but we also enjoyed a lot of nice activities, such as excursions, trips, conferences, summer and Christmas parties, and lunch breaks. As we always managed to establish a pleasant and welcoming atmosphere, I really enjoyed working at the Chair. For the time we spent together and the numerous discussions we had I am very thankful.

Last, and most importantly, I want to thank my family, in particular my beloved wife Friederike and our lively daughter Luise, for their endless support during both pleasant and challenging periods of my PhD journey. For your patience, sacrifice and numerous encouragements I am deeply grateful.

Christoph Schmüdderich

Abstract

Stability analyses are used to evaluate the level of safety for natural or man-made slopes or other geotechnical structures in terms of a single scalar value – the factor of safety (FoS). Considering slopes subjected to seismic loading, many simplifications are required when adopting common stability approaches, whereby accurate incorporation of effective stresses, excess pore water pressures or accelerations is mostly not possible. The current thesis was motivated by the lack of sophisticated and holistic approaches for seismic slope stability assessment. While this topic was assessed in preceding works based on simplified stability approaches or with the focus on deformations and liquefaction susceptibility, the present work focused on the development of seismic slope stability approaches performed parallel or subsequent to dynamic finite element analyses (DFEA), which can provide accurate spatial and temporal distributions of stresses, excess pore water pressures (Δp^w) and accelerations during a seismic event.

Four approaches based on limit equilibrium method (LEM), finite element limit analysis (FELA), strain-dependent slope stability (SDSS) and strength reduction finite element analysis (SRFEA) were developed or extended to enable a more rigorous assessment of the seismic slope stability. In contrast to conventional approaches, the methods developed in this work allow to investigate the evolution of the FoS during the dynamic loading and account for the influence of excess pore water pressures that may accumulate during dynamic loading. As commercial LEM and FEM codes do not meet the requirements associated with the four previously mentioned approaches in a comprehensive manner, a substantial part of this work was devoted to the development of a new software package for limit equilibrium analyses (`geoSlice`), the implementation of three elastoplastic constitutive models and a strength reduction scheme in the finite element software package `numgeo`, as well as the exhaustive verification of the methods and models based on comparative analyses with commercial codes and the study of benchmark problems.

The applicability of the approaches was shown for boundary value problems in different scales, where DFEA and subsequent stability analyses were conducted for an opencast slope and two centrifuge model tests. The study of all three examples indicated that stability analyses considering inertial forces (LEM, FELA, SRFEA) show an influence of the seismic excitation on the evolution of the FoS at an earlier point in time compared to approaches not explicitly accounting for inertial forces (SDSS). Contrary to conventional approaches neglecting the influence of accumulated excess pore water pressures, it was observed that Δp^w has a decisive impact on the seismic slope stability. Interestingly,

analyses based on SRFEA showed that inertial forces may temporarily stabilize gentle slopes such that practically no additional shear resistance due to frictional or cohesive tangential forces is required, resulting in FoS exceeding the one corresponding to the static situation.

Zusammenfassung

Stand sicherheitsanalysen werden verwendet, um das Sicherheitsniveau natürlicher oder künstlicher Böschungen oder anderer geotechnischer Strukturen in Form eines einzigen skalaren Wertes zu bewerten - der Stand sicherheit (engl. factor of safety, FoS). Bei Böschungen, die einer seismischen Belastung ausgesetzt sind, sind viele Vereinfachungen erforderlich, wenn gängige Methoden zur Ermittlung der Stand sicherheit angewandt werden, wobei eine akkurate Berücksichtigung von effektiven Spannungen, Porenwasserüberdrücken oder Beschleunigungen meist nicht möglich ist. Die vorliegende Arbeit wurde durch den Mangel an fortschrittlichen und ganzheitlichen Ansätzen zur Beurteilung der Stand sicherheit von Böschungen unter seismischer Anregung motiviert. Während dieses Thema in vorangegangenen Arbeiten auf der Grundlage vereinfachter Stand sicherheitsansätze oder mit dem Fokus auf große Verformungen und der Überschreitung des Verflüssigungswiderstands bewertet wurde, konzentrierte sich die vorliegende Arbeit auf die Entwicklung von Ansätzen zur Bewertung der Stand sicherheit von Böschungen unter seismischer Anregung auf Basis der Ergebnisse von dynamischen Finite-Elemente-Analysen (DFEA). Letztere liefern akkurate Informationen über räumliche und zeitliche Verteilungen von Spannungen, Porenwasserüberdrücken (Δp^w) und Beschleunigungen während eines seismischen Ereignisses, die anschließend in den Stand sicherheitsanalysen berücksichtigt werden sollen.

Vier Ansätze, die auf der Grenzgleichgewichtsmethode (engl. limit equilibrium method, LEM), der Finite-Elemente Limit Analysis (FELA), dem Konzept der dehnungsabhängigen Stand sicherheit (engl. strain-dependent slope stability, SDSS) und der Festigkeitsreduktion in einer Finite-Elemente-Analyse (engl. strength reduction finite element analysis, SRFEA) basieren, wurden entwickelt bzw. erweitert, um eine genauere Bewertung der Stand sicherheit von Böschungen unter seismischer Anregung zu ermöglichen. Im Gegensatz zu konventionellen Ansätzen ermöglichen es die in dieser Arbeit entwickelten Methoden, die Entwicklung der Stand sicherheit während der seismischen Anregung zu untersuchen und den Einfluss von Porenwasserüberdrücken zu berücksichtigen, welche sich während der seismischen Anregung akkumulieren können. Da kommerzielle LEM- und FEM-Codes die mit den vier vorgenannten Ansätzen verbundenen Anforderungen nicht umfassend erfüllen, war ein wesentlicher Teil dieser Arbeit der Entwicklung eines neuen Softwarepakets für die LEM (`geoSlice`), der Implementierung von drei elastoplastischen Stoffmodellen und der Implementierung einer Festigkeitsreduktion in das Finite-Elemente-Softwarepaket `numgeo` gewidmet. Umfassende Verifizierungen der Methoden und Modelle wurden auf der Grundlage vergleichender Analysen mit kommerziellen LEM-, FEM-

und FELA-Programmen sowie der Untersuchung von bekannten Benchmark-Problemen durchgeführt.

Die Anwendbarkeit der Ansätze wurde für Randwertprobleme in verschiedenen Maßstäben gezeigt, wobei dynamische FE Simulationen und anschließende Standsicherheitsanalysen für eine synthetische Tagebauseeböschung und zwei Zentrifugenmodellversuche durchgeführt wurden. Die Untersuchung aller drei Beispiele zeigte, dass Standsicherheitsanalysen, welche Trägheitskräfte berücksichtigen (LEM, FELA, SRFEA), einen Einfluss der seismischen Anregung auf die Entwicklung der Standsicherheit zu einem früheren Zeitpunkt zeigen, verglichen mit Ansätzen, welche diese nicht explizit berücksichtigen (SDSS). Im Gegensatz zu konventionellen Ansätzen, die den Einfluss von akkumulierten Porenwasserüberdrücken vernachlässigen, wurde beobachtet, dass Δp^w einen entscheidenden Einfluss auf die Standsicherheit von Böschungen unter seismischer Anregung hat. Interessanterweise zeigten Analysen auf der Grundlage der SRFEA, dass Trägheitskräfte Böschungen geringer Neigung vorübergehend so stabilisieren können, dass praktisch kein zusätzlicher Scherwiderstand aufgrund von Reibungs- oder Kohäsionskräften erforderlich ist, wodurch Standsicherheitswerte über dem des statischen Falls erreicht werden können.

Contents

Table of contents	ix
1. Introduction	1
1.1. Background and motivation	1
1.2. Objectives	3
1.3. Layout of the thesis	4
2. State of the art	7
2.1. Slope stability analysis	7
2.1.1. Limit equilibrium method (LEM)	7
2.1.2. Limit analysis (LA)	13
2.1.3. Strength reduction finite element analysis (SRFEA)	15
2.1.4. Finite element limit analysis (FELA)	18
2.1.5. Stress-based analysis (SBA)	19
2.1.6. Strain-dependent slope stability (SDSS)	20
2.2. Slope stability analysis for seismic loading	22
2.2.1. Pseudo-static analysis (PSA)	23
2.2.2. Pseudo-dynamic analysis	24
2.2.3. Permanent-displacement analysis	26
2.2.4. Dynamic finite element analysis (DFEA)	27
2.3. Material models	29
2.3.1. Mohr-Coulomb (MC)	29
2.3.2. Matsuoka-Nakai (MN)	37
2.3.3. Constitutive models for dynamic finite element analyses	43
2.3.4. Hypoplasticity with Intergranular Strain (Hypo-IGS)	43
3. Implementation of limit equilibrium method	47
3.1. Motivation	47
3.2. General structure	48

3.3.	Keywords and features	53
3.4.	Verification	61
3.4.1.	Implemented methods	62
3.4.2.	Hydrostatic pore water pressures	68
3.4.3.	Pseudo-static analysis	71
3.4.4.	Benchmark problems	72
4.	Implementation of elastoplastic constitutive models	83
4.1.	Motivation	83
4.2.	Standard Elastoplasticity	84
4.3.	Return mapping algorithms	87
4.4.	Verification	91
4.4.1.	General concept	91
4.4.2.	Mohr-Coulomb model	92
4.4.3.	Matsuoka-Nakai model	99
5.	Implementation of strength reduction analysis	105
5.1.	Motivation	105
5.2.	General concept	105
5.3.	Preliminary investigations	109
5.4.	Verification	113
5.4.1.	Homogeneous slopes	113
5.4.2.	Benchmark problems	116
6.	Approaches for the assessment of seismic slope stability	119
6.1.	Motivation	119
6.2.	Spatial pseudo-static analysis using LEM	120
6.3.	Cluster-based pseudo-static analysis using FELA	122
6.3.1.	General idea	122
6.3.2.	Mapping of stresses	125
6.3.3.	Mapping of inertial forces	127
6.3.4.	Mapping of friction angle	128
6.3.5.	Consideration of a non-associated flow rule	130
6.4.	Strain-dependent slope stability for earthquake loading	132
6.4.1.	Motivation	132
6.4.2.	Shape of the slip surface	133
6.4.3.	Reference state for normalization	135

6.4.4. Constitutive model	137
6.5. Spatial pseudo-static analysis using SRFEA	138
6.6. Major differences of the proposed approaches	141
7. Saturated opencast slope subjected to seismic loading	145
7.1. Motivation	145
7.2. Dynamic finite element analysis	145
7.2.1. Finite element model	145
7.2.2. Results	149
7.3. Assessment of seismic slope stability	151
7.3.1. Spatial pseudo-static analysis using LEM	151
7.3.2. Cluster-based pseudo-static analysis using FELA	153
7.3.3. Strain-dependent slope stability for earthquake loading	159
7.3.4. Spatial pseudo-static analysis using SRFEA	164
7.3.5. Discussion	165
8. Centrifuge model tests	171
8.1. Overview	171
8.2. Verification of Liquefaction Analyses by Centrifuge Studies (VELACS)	172
8.2.1. Dynamic finite element analysis	172
8.2.2. Assessment of seismic slope stability	177
8.3. Liquefaction Experiments and Analysis Projects (LEAP)	188
8.3.1. Dynamic finite element analysis	188
8.3.2. Assessment of seismic slope stability	195
9. Enhanced strain-dependent slope stability using machine learning	205
9.1. Motivation	205
9.2. Sampling strategy	206
9.3. Replacement of simple shear tests	209
9.4. Assessment of seismic slope stability	212
9.5. Influence of optimization technique	215
9.6. Evaluation of failure mechanisms	217
10. Summary, Conclusions and Outlook	221
10.1. Summary	221
10.2. Conclusions	223
10.3. Recommendations for further investigations	226

Bibliography	229
A. geoSlice – Keyword manual	253
B. Verification of the General Classic plasticity model	263
C. Settings of machine learning algorithms	269

1. Introduction

1.1. Background and motivation

When opencast mines are decommissioned, the areas occupied by opencast mining will be recultivated, where the residual pits are frequently refilled with soil or water, resulting in so-called residual lakes. The enclosing slopes of such lakes are often made of uncompacted material obtained from the excavation pit, which is excavated on the exploitation side, transported via conveyor belts to the spreader side and dumped there with so-called spreaders. After the rise of the water level in the residual lakes, the pores of the uncompacted material are filled with water. If the opencast mining area and the residual lakes are located in seismically active areas, as in the case of the Rhenish lignite mining area (Dahmen et al., 2014), earthquake loading must be considered when assessing the stability of the slopes.

As uncompacted materials tend to compact under shear loading, saturated uncompacted materials are prone to liquefaction under (fast) cyclic shearing, for instance due to seismic loading. Due to the severity of the consequences in case of large liquefaction events, assessment of the seismic stability of slopes composed of saturated uncompacted materials is first and foremost focused on prevention of such liquefaction events. Note that for cases where excess pore water pressures due to cyclic shearing do not accumulate up to a magnitude that liquefaction is induced, they may still lead to a significant reduction of effective stresses and, correspondingly, to a reduction of shear resistance. As a direct consequence of reduced shear resistances along potential slip surfaces, slope stability is also decreased. For this reason, stability analyses must be conducted to evaluate the influence of the seismic loading on the slope stability.

For the Rhenish lignite mining area, stability of slopes subjected to earthquake loading is examined following the guidelines of RfS (2013) using either Bishop's method of slices (Bishop, 1955; Bishop and Morgenstern, 1960) or composite failure mechanisms composed of rigid elements sliding along straight slip lines. Seismic effects are considered using the

pseudo-static approach with inertial forces determined based on slice weights, peak ground accelerations (PGA) and pseudo-static coefficients χ . The latter factor can be estimated for shallow or deep slip surfaces in accordance with Triantafyllidis and Grandas-Tavera (2013). Note that this approach to evaluate slope stability does not account for spatial variation of inertial forces, as schematically depicted in Fig. 1.1. In fact, a constant peak ground acceleration is considered throughout the domain, where the PGA value is estimated based on the location and the probability of occurrence of an earthquake with a predefined magnitude (Grünthal et al., 2009). Following the suggestions by Goldscheider et al. (2010), excess pore water pressures can be estimated based on material type and horizontal/vertical accelerations. The excess pore water pressures approximated in this manner can then be used in stability analyses using Bishop's method of slices. Note that following this approach, peak values of accelerations and excess pore water pressures likely coincide due to their direct dependency. In the stability analyses, the evolution of the factor of safety (FoS) can not be investigated as neither inertial forces, nor excess pore water pressures are considered to vary during earthquake loading.

A computational more elaborate approach for the estimation of seismic effects on open-cast slopes is to perform dynamic finite element analyses (DFEA) utilizing sophisticated constitutive models capturing effects of density (pyknotropy) and confining pressure (barotropy), stress/strain history as well as accumulation of strains. Besides the spatial distribution of accelerations and accumulated excess pore water pressures as well as their temporal evolution, DFEA yields information about displacements that can be further evaluated to assess slope stability. Among others, investigations for opencast slopes of the Rhenish lignite mining area utilizing DFEA were conducted by Macháček (2020) focusing

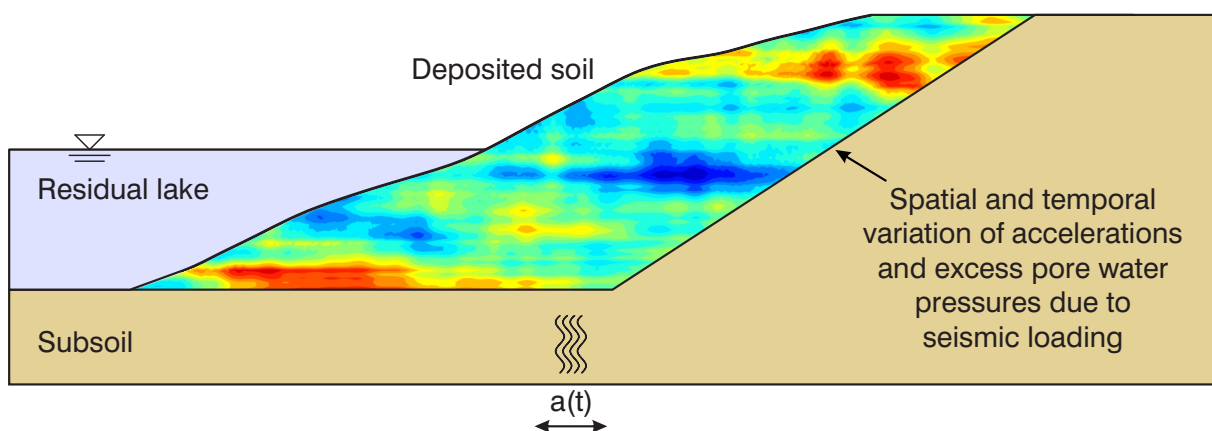


Figure 1.1: Schematic illustration of the spatial variation of accelerations and excess pore water pressures due to earthquake loading

on the accumulation of displacements and potential liquefaction events. Note that the aim of that work was not to quantify the level of safety of the slopes in terms of a single scalar value, for instance a FoS defined with regard to soil's shear strength. Though, a convenient option to quantify the level of safety could be the definition of FoS with regard to maximum displacements obtained from the DFEA and project-specific allowable displacements. However, as the definition of the latter requires substantial experience of practitioners, potentially resulting in different threshold values defined by different practitioners, this type of slope stability assessment must be regarded as rather subjective.

Contributing to the above discussion, the focus of this thesis is the development of approaches to assess the seismic slope stability. All approaches should enable assessment of seismic slope stability based on results obtained from DFEA, allowing for spatially accurate estimation of seismic effects. The definition of the FoS should not be related to project-specific allowable displacements but rather based on objective criteria, for instance soil's shear strength or mobilization of shear stresses. As different methods (e.g. limit equilibrium method, limit analysis or strength reduction method) and software packages can be applied to achieve this goal with different degrees of accuracy, four fundamentally different concepts are followed. Depending on the availability of tools (e.g. software packages) to assess slope stability, an appropriate approach can be selected.

1.2. Objectives

The main aim of this work is to extend existing and develop new approaches for the assessment of the seismic slope stability. Ultimately, depending on the availability of tools and software packages, the required level of accuracy and reliability as well as the tolerable amount of computational costs and time, suggestions should be given, which of these approaches should be applied to predict accurate stability estimates. Following the concept presented and applying the approaches developed in this thesis, it is believed that design approaches for slopes and dams subjected to seismic loading are improved with regard to accuracy, reliability and economic savings.

Although not strictly linked to, to some extent, the present work builds on the work of Machaček (2020), who investigated the seismic slope stability of an opencast slope and a centrifuge model test by use of dynamic finite element analyses (DFEA). DFEA was conducted using the finite element software package `numgeo`, which was initially developed by Machaček (2020) and, among others, further extended in Staubach (2022). Note that

major goals of the present work could only be achieved due to the possibility of contributing to `numgeo` by implementation of elastoplastic constitutive models and other features. The present work differs from the work by Machaček (2020) in the sense that stability assessment is not exclusively conducted based on the results of the DFEA, but also based on the results of stability analyses performed subsequently to the DFEA. Thereby, in addition to the evaluation of displacements, peak ground accelerations and potential liquefaction, the level of safety can be quantified in terms of FoS. Furthermore, the present work extends the concept of strain-dependent slope stability proposed by Nitzsche and Herle (2020) by adaption to earthquake loading and reduction of computational costs using machine learning approaches.

As the main aim of this thesis covers multiple aspects of different complexity, the following objectives are defined:

- Development of a new limit equilibrium (LE) software package serving as a basis for a modified pseudo-static approach taking into consideration temporal and spatial variations of accelerations and accumulated excess pore water pressures. Validation of the different stability evaluation methods and features implemented in this software package by comparative analyses with well-established LE software packages.
- Implementation of two elastoplastic constitutive models (Matsuoka-Nakai and Mohr-Coulomb) in the finite element software package `numgeo`. Validation of the implementations of the constitutive models based on simulations of representative element tests considering different materials.
- Implementation of a strength reduction method in `numgeo`. Validation of the strength reduction scheme based on comparative analyses with well-established finite element software packages via investigation of parametric studies and benchmark problems.
- Development and detailed description of different approaches for the assessment of the stability of slopes subjected to seismic loading. Demonstration of the applicability of these seismic stability approaches for boundary value problems of different scales. Discussion regarding similarities, differences, reliability and computational costs associated with the different approaches.

1.3. Layout of the thesis

After this introductory chapter, an overview over the most popular methods for the assessment of slope stability under static and seismic loading is provided. Considering that

early development of these methods started many decades ago, emphasis is put on those that are further developed in this thesis. In addition, Chapter 2 sheds light on popular elastoplastic and hypoplastic constitutive models for soils used in dynamic and/or stability analyses.

As a basis for the `Spatial pseudo-static analysis using LEM` presented in Chapter 6, a limit equilibrium software package named `geoSlice` has been developed based on the method of slices in this thesis. Details with regard to the general structure, features and keywords are provided in Chapter 3. Moreover, verification of the methods and most important features implemented is reported in this chapter. Within the scope of the verification, comparative analyses of `geoSlice` with two well-established LEM software packages are conducted evaluating FoS and shapes of critical slip surfaces for a multitude of different benchmark examples. A keyword manual for `geoSlice` can be found in Appendix A.

Within the scope of this thesis, three elastoplastic constitutive models – the Mohr-Coulomb model (Sloan and Booker, 1986; Abbo and Sloan, 1995; Abbo et al., 2011), the Matsuoka-Nakai model (Matsuoka and Nakai, 1974) and the General Classic Plasticity model (Lagioia and Panteghini, 2016; Lester and Sloan, 2018) have been implemented in `IncrementalDriver` (Niemunis, 2008) and `numgeo` (Machaček, 2020; Staubach, 2022). Chapter 4 covers the general concept of elastoplasticity, return mapping algorithms and verification of the former two models, while verification of the latter model is reported in Appendix B. For all models, verification includes comparative analyses of the implemented models with similar models incorporated in well-established finite element software packages in terms of results from different element tests (triaxial compression/extension and direct simple shear tests).

Chapter 5 focuses on the implementation of the strength reduction method into the finite element software package `numgeo`. After introducing the general concept as well as preliminary attempts to define failure within the scope of a strength reduction analysis, parametric studies and simulations of benchmark examples are conducted. For verification purposes, comparative analyses are performed using two well-established finite element software packages. Note that Chapters 4 and 5 serve as basis for the `Spatial pseudo-static analysis using SRFEA` discussed in Chapter 6.

Chapter 6 is devoted to the main objective of this thesis, which is the assessment of the stability of slopes subjected to seismic loading. Four approaches based on limit equilibrium method (LEM), finite element limit analysis (FELA), strain-dependent slope stability (SDSS) and strength reduction finite element analysis (SRFEA) are presented and detailed

explanations are provided. Similarities and differences of the approaches are emphasized to enhance the comprehensibility of the discussions related to different boundary value problems investigated in Chapters 7 and 8.

To emphasize the applicability of the four approaches discussed in Chapter 6, the stability of a saturated opencast mine slope subjected to seismic loading is assessed in Chapter 7. In a first step, seismic loading of the opencast slope is considered in a fully-coupled dynamic finite element analysis (DFEA) with the results of the DFEA presented in terms of the evolution of spatial distribution of accelerations and excess pore water pressures. Subsequently, the four seismic stability approaches (Chapter 6) are applied to assess the FoS time history of the opencast slope. Lastly, the approaches are evaluated with regard to similarities, differences, reliability and computational costs.

To evaluate the seismic slope stability for real case studies, two centrifuge model tests – Verification of Liquefaction Analyses by Centrifuge Studies (VELACS) and Liquefaction Experiments and Analysis Projects (LEAP) – are investigated in Chapter 8. DFEA and subsequent assessment of the seismic slope stability are conducted for a dam (VELACS) and a gentle slope (LEAP). Results of the DFEA are compared to the results obtained in the centrifuge model tests in terms of displacements, accelerations and excess pore water pressures. Stability assessment is performed with LEM, SDSS and SRFEA. FoS time histories are investigated and discussed with regard to the results of the experiments.

As the concept of the **Strain-dependent slope stability (SDSS) for earthquake loading** introduced in Chapter 6 is associated with large computational costs, Chapter 9 emphasizes how machine learning (ML) algorithms can be adapted to the concept of SDSS by replacing element test simulations. Sampling, training and testing of ML algorithms are discussed for the simulation of direct simple shear element tests, analyzing accuracy and reduction of computational costs with different ML algorithms. Besides evaluation of ML algorithms on the element test scale, SDSS with ML is compared to the SDSS without ML for the stability assessment of the opencast mine slope subjected to seismic loading discussed in Chapter 7.

In Chapter 10, conclusions of the present work are drawn and suggestions for potential extensions are provided.

2. State of the art

2.1. Slope stability analysis

If the resistance due to shear strength is not sufficient to withstand external driving forces, inclined soil or rock slopes may undergo large deformations, often referred to as slope instability or slope failure. To prevent large deformations, slopes are commonly designed such slope stability is not endangered by ensuring that shear strength is sufficient. Evaluation of slope stability is one of the fundamental tasks in geotechnical engineering. Within the last century, many different methods for the evaluation of slope stability have been developed, out of which the most popular methods are summarized in the following sections. To quantify the level of safety for a slope with regard to a scalar value, the factor of safety (FoS) is commonly used, where $\text{FoS} > 1.0$ and $\text{FoS} < 1.0$ denote stable and unstable states, respectively. Considering a specific method to perform slope stability analysis, the FoS allows an objective evaluation of slope stability, not affected by subjective judgments of individuals performing the analyses (e.g. practitioners). In general, slope stability analyses attempt to determine the critical failure surface that is associated with the minimum FoS.

2.1.1. Limit equilibrium method (LEM)

Limit equilibrium method (LEM) is a collective term that covers a wide range of different approaches, which are characterized by similar assumptions with respect to the shape of the slip surface, the strategy of locating the critical slip surface, the stress distribution and the definition of yield strength along the slip surface. All limit equilibrium methods have in common that the analysis of the slope stability is conducted for a predefined slip surface. Depending on the limit equilibrium method utilized, the failure body is approximated by a single or multiple (rigid) wedges, which allows for relative displacements with respect to neighboring elements. Although the shape of the slip surface has to be selected in advance, the geometrical type is not identical in all approaches. Popular geometrical types include

circles, logarithmic spirals, wedges, polygons or other shapes, while it is widely known that the shape of the slip surface of real case slope failures depends on many factors, such as soil type, drainage conditions, subsoil layering, etc. To identify the critical slip surface as the one which yields the least limit load (e.g. bearing capacity, earth pressure) or factor of safety (slope stability), limit equilibrium methods require many analyses for different positions of the slip surface, for instance many variations of the center point and the radius in case of a circular slip surface shape. To efficiently locate the critical slip surface without relying on a brute-force approach applying all combinations possible, advanced optimization techniques can be utilized. Further details regarding different optimization techniques are discussed in Chapter 3. As the stress distribution along the slip surface is unknown a priori, assumptions regarding this stress distribution are necessary, for instance by subdivision of the failure mass into smaller units. However, different assumptions are made in different LE approaches in order to overcome this drawback and approximate the stress distribution along the slip surface. Considering the shear resistance that can be mobilized along the slip surface, assumptions are to be made with respect to the degree of mobilization and the ultimate strength. Commonly it is assumed that the shear strength is fully mobilized along the slip surface and the maximum shear strength of the material is given by simple failure criteria, for instance Tresca or Mohr-Coulomb criterion, where the former is commonly utilized for cohesive soils and undrained conditions, whereas the latter is more applicable for frictional and frictional-cohesive soils and drained conditions. Furthermore, it should be noted that, in contrast to limit analysis, which is discussed in the subsequent section, the kinematic admissibility of the slip surface is not necessarily checked in LEM. Among others, popular methods within the group of limit equilibrium methods are the method of slices (Terzaghi, 1943; Janbu, 1954; Bishop, 1955; Bishop and Morgenstern, 1960; Morgenstern and Price, 1965; Spencer, 1967), the block sliding method or the Kinematic Element Method (KEM) (Gußmann, 1986, 2000; Schmüdderich et al., 2017a,b; Qarmout et al., 2019a,b), the former being further elaborated here as it is utilized intensively throughout this thesis. Note that, in contrast to the method of slices which does not account for kinematic admissibility of the slip surface, KEM accounts for kinematic admissibility of the failure mechanism by use of a hodograph linking the virtual displacements of elements with common element edges.

In advance to the discussion of different approaches and their (implicit) assumptions, the general methodology of the method of slices is introduced. To approximate the stress distribution along the slip surface, the sliding body is subdivided in a predefined number of slices. The orientation of the slices can be horizontal or vertical, where the latter represents the common choice. The number of the slices is usually of subordinate importance,

provided a sufficiently large number is chosen (usually 100 or more). As the method of slices requires to solve the equilibrium of forces and/or moments with respect to the global system representing the collection of slices as well as to individual slices, distinction between both cases is made here using the labels `global` and `local`, respectively. For each slice, the local forces acting on the slice are determined, assuming that the line of action of all forces intersects the local center of the slice, ensuring that the local equilibrium of moments is ensured. Among others, forces acting on a slice include self weight of the slice, concentrated or distributed external loads, hydrostatic pore water pressures, excess pore water pressures, inertial forces due to seismic actions, or reaction forces due to constructional elements such as anchors, piles, geogrids, nails or walls. The normal interslice forces acting on both vertical edges representing reaction forces from the neighboring slices are determined based on the local equilibrium of horizontal forces by consecutive evaluation of interslice forces in all slices starting at the first or last slice as only a single unknown interslice force needs to be evaluated due to zero outer edge height. The vertical interslice force is determined according to Eq. 2.1 where E is the lateral interslice force, $f(x)$ is a interslice force function and λ is a scaling parameter.

$$X = E \lambda f(x) \quad (2.1)$$

The shear resistance in the slip surface of each slice can be expressed with respect to a failure criterion (e.g. Mohr-Coulomb) employing the shear strength parameters of the material at the slice base, the effective normal force N' on the base of the slice and the FoS. In case of drained conditions, the effective cohesion c' and the effective friction angle φ' should be used whereas for undrained conditions and fine-grained soils, the undrained shear strength s_u should be applied. Inserting all relations in the local equilibrium of vertical forces yields the effective normal force N' on the base of the slice (Eq. 2.2)

$$N'_i = \frac{W_i + X_i - X_{i+1} - l_i \left(u_i \cos \alpha_i + \frac{c'_i}{\text{FoS}} \sin \alpha_i \right)}{\cos \alpha_i + \frac{\tan \varphi'_i \sin \alpha_i}{\text{FoS}}} \quad (2.2)$$

where the index $[]_i$ refers to the number of the slice, $l = b / \cos \alpha$ is the length of the slice base, b is the width of the slice, α is the angle between the slice base and the horizontal axis, W is the weight of the slice, X_i and X_{i+1} are the vertical interslice forces, u is the average pore water pressure at the base of the slice, and FoS is the factor of safety (see e.g. Fig 2.1). Following the Mohr-Coulomb failure criterion and focusing on the effects due to soil self weight, pore water pressure, friction and cohesion, the FoS based on the global equilibrium of moments and based on the global equilibrium of horizontal forces

are determined according to Eq. 2.3 and Eq. 2.4, respectively, with R_i denoting the radius for each slice.

$$\text{FoS}_M = \frac{\sum_i R_i \cdot (c'_i l_i + N'_i \tan \varphi'_i)}{\sum R_i \cdot W_i \sin \alpha_i} \quad (2.3)$$

$$\text{FoS}_F = \frac{\sum (c'_i l_i \cos \alpha_i + N'_i \tan \varphi'_i \cos \alpha_i)}{\sum (N'_i + u_i l_i) \sin \alpha_i} \quad (2.4)$$

The factor of safety is obtained in an iterative manner, where based on an initial guess of the FoS, the effective normal force N' (Eq. 2.2) and subsequently the updated FoS is determined in accordance with Eq. 2.3 or Eq. 2.4. The iteration process is finished when the iterative change of the factor of safety is less than a predefined tolerance. In DIN-4084 (2021), it is recommended to use a tolerance of 3% to exit the iteration loop, however, the default tolerance used in many commercial LEM codes is smaller. It should be noted that Eq. 2.3 and Eq. 2.4 in the form presented here do not account for external concentrated or distributed loads, inertial forces, excess pore water pressures, or reaction forces due to constructional elements. Moreover, it is assumed in Eq. 2.3 that the slip surface may be of a circular or non-circular (e.g. a logarithmic spiral) shape, thus, the radius is not necessarily constant for all slices. Considering a circular slip surface, Eq. 2.3 simplifies as the constant radius can be factored out of the summation terms in the nominator and the denominator.

Bishop (1955) proposed a rigorous and a simplified way to determine the factor of safety, referred to as **rigorous** and **simplified** Bishop method in this study, respectively. Both methods evaluate the factor of safety based on the global equilibrium of momentum given in Eq. 2.3 for a circular slip surface, as shown in Fig. 2.1. However, in contrast to the

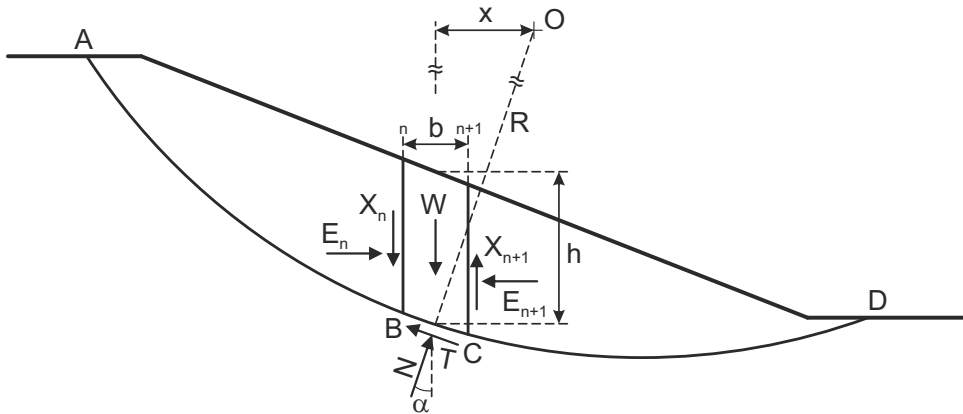


Figure 2.1: Slip circle and resulting forces acting in an arbitrary slice, modified after Bishop (1955)

rigorous method, where the resulting interslice force may be inclined with respect to the horizontal ($X \geq 0$), in the simplified method, it is assumed that the resulting interslice force is horizontal ($X = 0$ due to $\lambda = 0$ in Eq. 2.1), which has a direct impact on the normal reaction force on the base of the slice calculated according to Eq. 2.2. Bishop (1955) and Bishop and Morgenstern (1960) state that the difference in the factor of safety obtained using the rigorous and the simplified method should not be larger than 1% for circular slip surfaces. Krahn (2003) also reports that the difference between the rigorous and the simplified Bishop method is small for circular slip surfaces, but emphasizes that it is significantly larger for other shapes of the slip surface. In contrast to the Bishop method, Janbu (1954) used the global horizontal force equilibrium to determine the factor of safety (Eq. 2.4). Analyses with Janbu's method are commonly conducted for (almost) planar slip surfaces, for example sliding on a weak thin layer. Similar to Bishop's method, Janbu's method is often implemented in its simplified version, thus, neglecting vertical interslice forces. Krahn (2003) reported that the difference between the general and simplified Janbu method in terms of the factor of safety is small for slip surfaces of planar or wedge type, however, it is significantly larger for other shapes, for instance circular slip surfaces.

As neither Bishop's method nor Janbu's method considers both, the global moment equilibrium and the global horizontal force equilibrium, other methods have been proposed satisfying both equilibrium conditions, for instance by Morgenstern and Price (1965) and Spencer (1967). To satisfy both equilibrium conditions, the interslice force parameter λ , which describes the inclination of the resulting interslice force ($\lambda = \tan \theta$), is varied until both equilibrium conditions yield similar factors of safety (see e.g. Fig. 2.2). Note that the shape of the slip surface may change the influence of λ on the factor of safety based on both global equilibrium equations (Eq. 2.3 and Eq. 2.4). This effect has been demonstrated, among others, by Krahn (2003) considering several different shapes of the slip surface (Fig. 2.3). Due to the necessity of solving the equilibrium equations multiple times within the λ iteration loop, it should be clear that the computational effort to obtain an FoS according to Morgenstern and Price (1965) and Spencer (1967) is larger compared to the simplified Bishop or simplified Janbu method. The main difference between Spencer's method and the Morgenstern and Price (M&P) method is the definition of the interslice force function ($f(x)$ in Eq. 2.1), which is constant in the former method, whereas it changes with respect to the number of the current slice in the latter method. Therefore, in Spencer's method, all interslice forces (resulting from E and X) are inclined with the same angle to the horizontal axis. In contrast, an interslice force function, commonly a halfsine function, is utilized in the M&P method, resulting in (almost) horizontal

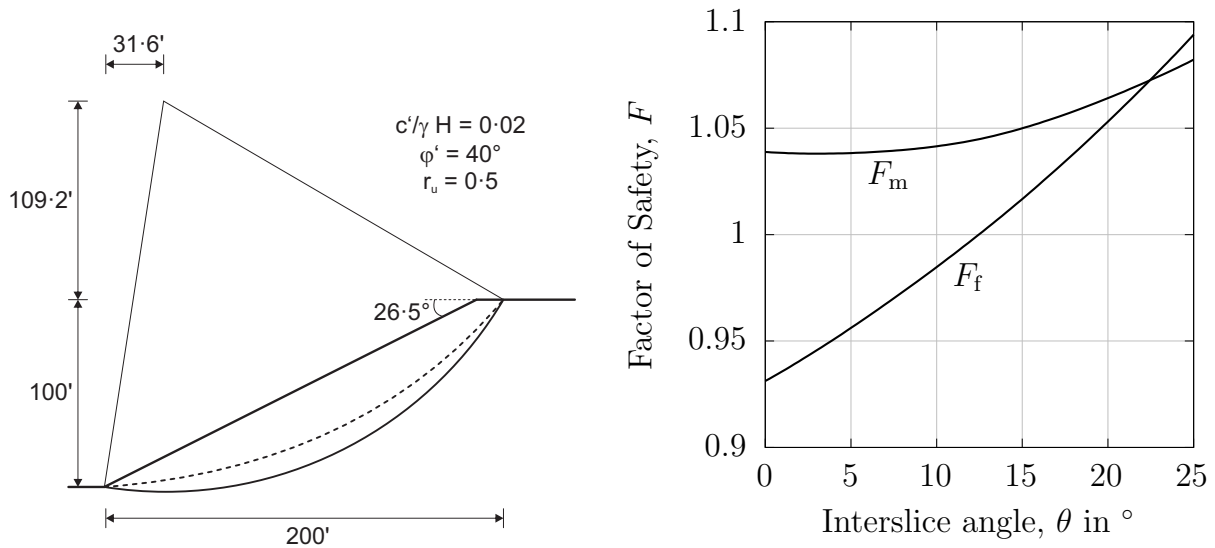


Figure 2.2: Influence of orientation of interslice forces on the factor of safety based on the global equilibrium of horizontal forces (F_f) or moments (F_m) for a slope of height H considering a pore pressure ratio r_u , modified after Spencer (1967)

interslice forces at the entry and exit slices and interslice forces with increasing inclination towards the central slice.

Besides the higher computational effort of the Spencer and the Morgenstern and Price method compared to the Bishop and Janbu method, additional difficulties may arise due to convergence issues related to the former two methods. As the objective function does not necessarily converge for every slip surface, the center of the critical slip surface may be very close to other center points which did not converge. This fact increases the difficulty to propose a proper and robust LEM implementation, which satisfies the global equilibrium of moments and horizontal forces. Several authors proposed strategies on how to implement the Spencer and the Morgenstern and Price method, for instance Morgenstern and Price (1967), Fredlund and Krahn (1977), Zhu et al. (2001, 2003, 2005) and Zolfaghari et al. (2005), however, there is no guarantee that these implementations yield reliable estimates of the FoS for every slope stability problem. Further details regarding the implementation of limit equilibrium methods are provided in Chapter 3.

As limit equilibrium methods are developed solely based on statics and do not account for physics in terms of strains, displacements and displacement compatibility, careful interpretation of the results is necessary. As discussed at the beginning of this section and reported for instance by Krahn (2003), the stress distribution along the slice bases assumed in LEM may significantly differ from the stress distribution obtained using a

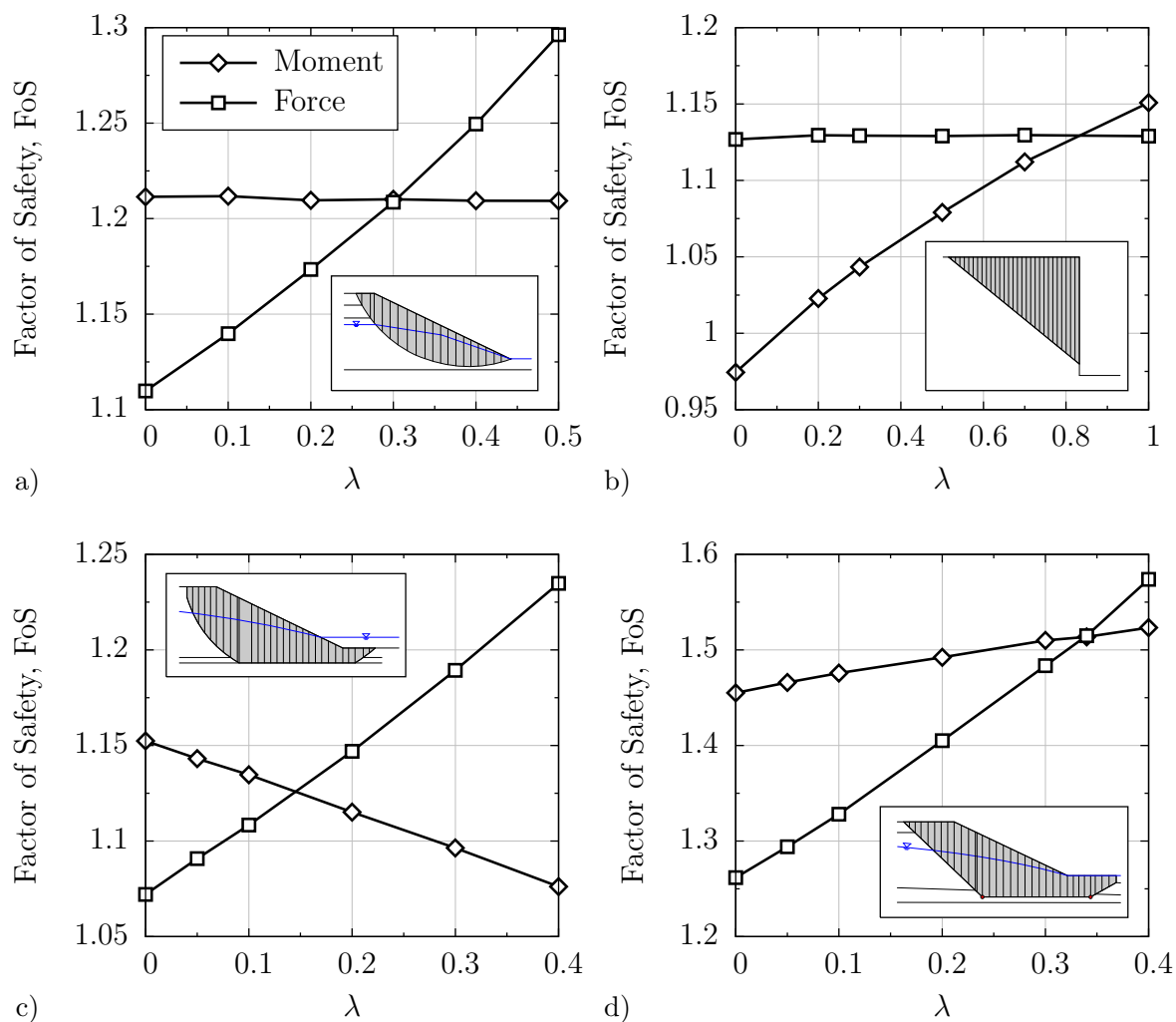


Figure 2.3: Influence of λ on FoS obtained from global equilibrium of momentum and horizontal forces for different shapes of the slip surface, modified after Krahn (2003)

finite-element simulation. Cases with large differences cover steep slopes and slopes with constructional elements, whose influence is accounted for in single slices (e.g. anchor forces). Moreover, it should be noted that the assumption made with regard to the orientation of the interslice forces also has a decisive impact on the factor of safety.

2.1.2. Limit analysis (LA)

Limit analysis is based on the limit theorems of plasticity discussed, among others, by Drucker et al. (1952). The limit theorems are defined based on a lower and upper bound theorem, which are presented here following the formulation of Chen (2013):

Theorem 1 (lower bound): If an equilibrium distribution of stress σ_{ij}^E covering the whole body can be found which balances the applied loads T_i on the stress boundary A_T and is everywhere below yield $f(\sigma_{ij}^E) < 0$, then the body at the loads T_i, F_i (body loads) will not collapse.

Theorem 2 (upper bound): If a compatible mechanism of plastic deformation $\dot{\varepsilon}_{ij}^{p*}, \dot{\varepsilon}_i^{p*}$ is assumed, which satisfies the condition $\dot{\varepsilon}_i^{p*} = 0$ on the displacement boundary A_u , then, the loads T_i, F_i determined by equating the rate at which the external forces do work to the rate of internal dissipation will be higher or equal to the actual limit load.

Note that the term *compatible* refers to the kinematic compatibility of the failure mechanism. Following the above definitions, a static admissible stress field should satisfy the equilibrium conditions and the stress boundary conditions and should nowhere violate the yield criterion. A kinematic admissible velocity field should satisfy the velocity boundary conditions and the strain and velocity compatibility. An associated flow rule is required as normality ensures that stress and velocity characteristics are parallel. In addition, a convex yield surface and an associated flow rule are required to guarantee that $\Delta\sigma_{ij} \cdot \dot{\varepsilon}_{ij}$ produces the maximum dissipation. Similar to the limit equilibrium method, a failure surface is assumed and the minimum failure load is sought. However, it should be noted that a limit equilibrium solution is not necessarily a limit analysis solution as kinematic admissibility is not checked. On the other hand, every limit analysis solution can also be considered a limit equilibrium solution. Considering identical shapes of the failure surface, for many practical applications, LEM and upper bound limit analysis yield similar/identical ultimate loads.

As limit analysis has been used to evaluate slope stability for more than 50 years in research, correspondingly, many studies have been conducted. However, since limit analysis in its original form is not applied in this thesis, only a few studies are mentioned here. Chen et al. (1969) conducted a parametric study for slopes of various inclinations ($15^\circ \leq \beta \leq 90^\circ$) and compared stability numbers of benchmark limit equilibrium solutions with the ones obtained using limit analysis and rotational failure mechanisms of log-spiral shape. They concluded that reasonable good agreement between limit equilibrium and upper bound limit analysis solutions is seen for a wide range of different slope geometries. Michalowski (1995) analyzed limit equilibrium and limit analysis solutions for slopes of different inclinations utilizing translational and rotational failure mechanisms with emphasis on the effect of interslice forces and pore water pressures. Michalowski (1995) showed that rotational LA yields better (lower) results compared to translational LA. Moreover, LEM and rotational LA approaches provide similar critical $\gamma H/c$ ratios for a

wide range of different friction angles. Almost all results are bounded by results of translational LA considering full interslice strength and zero interslice strength. Michalowski (2002) performed parametric studies and proposed slope stability design charts using the rotational LA with slip surfaces of log-spiral shape considering variations of the slope geometry in terms of the sloping angle β and height H , the friction angle φ , the cohesion c , the pore pressure ratio r_u and the seismic horizontal coefficient k_h .

2.1.3. Strength reduction finite element analysis (SRFEA)

In contrast to limit load problems (e.g. bearing capacity or earth pressure problem) in which a load is increased until collapse or failure is obtained, slope stability problems are analyzed by finding the critical strength of a material that causes failure. In strength reduction finite element analysis (SRFEA), the critical strength is found by division of the shear strength parameters (tangent of friction angle $\tan \varphi'$ and cohesion c') by a strength reduction factor (SRF) which is assumed to be equivalent to the factor of safety (FoS). The FoS can be expressed as the ratio of the shear strength at current and failure state, expressed in terms of the shear strength parameters as depicted in Eq. 2.5

$$\text{FoS} = \frac{\tan \varphi}{\tan \varphi_{\text{red}}} = \frac{c}{c_{\text{red}}} \quad (2.5)$$

where φ_{red} and c_{red} refer to the reduced friction angle and the reduced cohesion at failure state, respectively. Considering simple elastoplastic constitutive models, a yield surface needs to be defined to distinguish between elastic and elastoplastic stress states. The yield surface is expressed in terms of a yield function, which considers the current stress state, the material shear strength parameters and potentially additional state variables (e.g. plastic strains). Among others, well-known yield functions are Tresca, von Mises, Drucker-Prager, Mohr-Coulomb or Matsuoka-Nakai, where the latter two are further elaborated in Sections 2.3.1 and 2.3.2, respectively. However, it should be noted that the corresponding simple elastic-perfectly plastic constitutive models using these respective yield functions can not accurately approximate the soil's behavior under complex boundary conditions.

To conduct a strength reduction in a finite element framework, in general, two different concepts can be followed, as for instance described in Potts and Zdravković (2012) and Chen et al. (2019). The first concept (SR1) is related to a continuous reduction of shear strength parameters within a single simulation. Starting with the original shear strength parameters, the FoS is continuously changed and equilibrium of the system is sought. If equilibrium can be found, the factor of safety is increased in the following increment

leading to reduced shear strength parameters. This increment loop is continued until failure is obtained. In contrast, the second concept (SR2) is related to a series of restart analyses with different sets of reduced shear strength parameters. To be more specific, considering a reference state defined by an initial stress field, multiple restart analyses are conducted each starting from the same benchmark state but applying a different factor of safety. Within the restart, the shear strength parameters used are the reduced parameters, thus, a sudden reduction is considered. Given a predefined factor of safety, a restart analysis is considered to have converged if equilibrium is obtained within a user defined number of iterations. The latter concept can be conducted either by monotonically increasing the FoS in increments until failure is obtained or utilizing a bracketing solution approach, where first a stable and an unstable solution is sought and the gap between both brackets is reduced subsequently.

Potts and Zdravković (2012) discussed advantages and drawbacks of both approaches. Advantages of SR1 include that only a single analysis is required to obtain the FoS and that the SR1 approach presented by Potts and Zdravković (2012) can be adapted to any (advanced) constitutive model. However, this requires modifications of the finite element implementation, which is only possible in case of full access to the FE code. Considering SR2, no modification of the implementation is required, however, only simple elastoplastic constitutive models can be used. Considering well-known commercial geotechnical finite element and finite difference codes, both concepts are utilized. Among other codes, strength reduction via a continuous analysis is performed in *Plaxis* (Brinkgreve and Bakker, 1991; Brinkgreve et al., 2017), *Geo5* (GEO5 Slope Stability, 2020), *ICFEP* (Potts and Zdravković, 1999, 2012) and *OpenGeoSys* (Kolditz et al., 2012), whereas restart analyses are conducted in *FLAC* (Dawson et al., 1999; Itasca Consulting Group, 2020), *DIANA* (DIANA FEA BV, 2020), *ZSoil* (Zace Services Ltd, Software engineering, 2020) and *Slope64* (Griffiths and Lane, 1999; Smith et al., 2013).

At least as essential as the decision of the strategy followed to conduct the strength reduction analysis is the definition of failure for which the factor of safety is sought. Common criteria to define failure include (1) bulging of the slope expressed in terms of large nodal displacements or shear strains (Donald et al., 1988; Wei et al., 2009), (2) a continuous plastic zone extending from the top to the bottom of the slope (Matsui and San, 1992; Zheng et al., 2005) and (3) non-convergence of the solution indicated by large unbalanced forces (Griffiths and Lane, 1999; Dawson et al., 1999). However, it should be noted that the former two criteria are based on a rather subjective judgments, as has also been discussed by Chen et al. (2019). Moreover, as convergence in finite element simulations

is „decided” based on prescribed convergence criteria, numerous different approaches to this exist and to date none of these approaches have proven to be „universally valid”. Comparing different widely used finite element programs, one observes that these criteria span from rather simple and „loose” (**Plaxis**, **Tochnog**) to comparably sophisticated and „strict” (**Abaqus**, **Ansys**). Therefore, it is important to note that an assessment of stability based on convergence or non-convergence might be highly dependent on the choice of the convergence criterion (Zheng et al., 2005; Chen et al., 2019). In addition, the influence of the convergence criterion on the FoS increases for more complex boundary value problems. As an alternative, energy based criteria have been used recently by Tu et al. (2016), Chen et al. (2019) and Huang et al. (2020) to identify slope failure with SRFEA.

To avoid termination of strength reduction analyses based on non-convergence or other criteria mentioned above, **Plaxis** and **Geo5** follow a continuation strategy by taking advantage of the arc-length method, which was initially proposed by Riks (1979), further developed, among others, by Crisfield (1981) and adopted to strength reduction finite element analysis by Brinkgreve and Bakker (1991). In the arc-length method, an additional load multiplier is used to scale the contributions of the external forces. However, as this load multiplier is unknown, an additional scalar equation is added to the system of equations.

Considering finite element strength reduction analysis conducted using advanced constitutive models, care should be taken in case of elastoplastic models with material strain softening, which may result in numerical instabilities and mesh dependency (Galavi and Schweiger, 2010). These problems can be overcome by taking advantage of mesh refinement or regularization approaches such as gradient theories (Zervos et al., 2001; Papanicolopoulos and Zervos, 2010), nonlocal approaches (Eringen, 1981; Bažant and Jirásek, 2003; Galavi and Schweiger, 2010; Summersgill et al., 2017; Staubach et al., 2022b) or others. In case constitutive models from different model families are utilized in SRFEA, difficulties may arise due to the definition of failure since shear strength is usually not constant but dependent on other state variables such as the current void ratio. Still, stability analyses taking into consideration advanced constitutive models have been conducted via SRFEA, for instance using clay hypoplasticity (Kadlíček and Mašín, 2020) or barodesy (Schneider-Muntau et al., 2018; Tschuchnigg et al., 2019).

2.1.4. Finite element limit analysis (FELA)

The finite element limit analysis (FELA) is based on the lower and upper bound theorems of plasticity introduced by Drucker et al. (1952). Application of lower and upper bound finite element analysis to geotechnical problems considering plane-strain conditions has been conducted as early as Lysmer (1970) and Bottero et al. (1980). Based on these works many contributions enabled continuous improvement of both methods (Sloan, 2013). Following the lower and upper bound theorems of plasticity, the restrictions of both theorems are also essential for finite element limit analysis. Therefore, a rigorous lower or upper bound solution can only be determined if it is based on a statically admissible stress field or a kinematically admissible velocity field, respectively (Sloan, 2013). In addition, it has to be assured that the material utilized is rigid-perfectly plastic and follows an associated flow rule. Moreover, calculations are only valid for small deformations. To obtain rigorous lower and upper bound solutions, which bracket the exact solution from below and above, respectively, simulations with FELA have to be performed using the correct element types, see remarks below (Sloan, 2013). The methods permit discontinuities in the stress and velocity fields (Merifield et al., 1999). Compared with traditional incremental finite element method, the procedures are very fast and straightforward to use (Sloan, 2005), giving the limit load directly, without the need to perform a complete incremental analysis. This is a major advantage in large-scale three-dimensional applications, where stability analysis using the conventional finite element method is both difficult and time consuming (Sloan, 2013).

Adaption of FELA to perform strength reduction analyses has been discussed by Sloan (2013) and Krabbenhoft and Lyamin (2015), where the latter approach is also used in *OptumG2* (OptumG2, 2019), which is also applied in this thesis. Similar to limit load problems investigated with FELA, a lower and an upper bound solution are investigated in the stability analyses. Note that the smaller the gap between both solutions, the more accurate is the prediction of the exact solution. Application of FELA for slope stability problems has been conducted, for instance in Tschuchnigg et al. (2015b) and Mahmoudi et al. (2020).

To quantify the gap between both solutions, the concept of the worst case error discussed in Krabbenhoft (2018) can be applied. The worst case error is defined as $\varepsilon_{wc} = (UB - LB) / (UB + LB)$ (Krabbenhoft, 2018; Schmüdderich et al., 2020d) with LB and UB denoting lower and upper bound results, respectively.

2.1.5. Stress-based analysis (SBA)

To overcome drawbacks of limit equilibrium methods mentioned above and discussed, among others, by (Krahn, 2003), stress-based approaches can be utilized to evaluate slope stability in terms of a factor of safety. Stability analysis is conducted based on a stress field obtained using a numerical analysis, for instance finite element analysis or finite difference analysis. The stress field represents the current situation, thus, no reduction of the shear strength parameters or other constitutive parameters is conducted. Slope stability is analyzed on a predefined slip surface, discretized by a user defined number of points where stresses from the stress field are interpolated for each node along the slip surface. Similar to limit equilibrium approaches, the general idea of stress-based approaches is to compare the shear forces and shear resistance, the latter governed by the shear strength of the material and the normal effective stresses, based on the equilibrium of forces or moments. A general description to evaluate the FoS following a stress-based approach is given in Eq. 2.6 with τ_{f_i} and τ_i denoting the shear strength and shear stresses acting along a section ΔL_i of the slip surface.

$$\text{FoS} = \frac{\int_A^B \tau_{f_i} dL}{\int_A^B \tau_i dL} \approx \frac{\sum_{i=1}^{N_s} \tau_{f_i} \Delta L_i}{\sum_{i=1}^{N_s} \tau_i \Delta L_i} \quad (2.6)$$

To evaluate the maximum shear resistance, assumptions with respect to the failure criterion (e.g. Mohr-Coulomb failure criterion) are required. Usually, nodes along the slip surface are treated individually, thus, no information is shared between the different nodes along the slip surface during the stability analysis. Therefore, it is not possible to analyze progressive failure as this would require information exchange, for instance to allow for redistribution of stresses during the stability analysis. In general, transfer of state variables (e.g. void ratio, plastic strains, etc.) from the finite element simulation to the slope stability analysis is not considered, thus, effects such as stress history (e.g. excavation process) can not be considered realistically. Only the current stress state has an influence on the factor of safety determined based on a stress-based approach.

Development of stress-based approaches and investigation of slope stability problems using stress-based approaches has been conducted for instance by Zou et al. (1995), Farias and Naylor (1998), Krahn (2003), Guo et al. (2011), and Liu et al. (2020). Further details and discussions with regard to advantages and drawbacks of stress-based approaches are provided in the following section.

2.1.6. Strain-dependent slope stability (SDSS)

To evaluate the stability of slopes considering the current stress state, the stress history, the soil density as well as a realistic stress-strain behavior, Nitzsche and Herle (2020) proposed a concept referred to as „strain-dependent slope stability”. In a manner similar to other stress-based approaches (Zou et al., 1995; Farias and Naylor, 1998; Guo et al., 2011; Liu et al., 2020), the factor of safety is calculated for an arbitrarily chosen slip surface of predefined shape discretized using a user-defined number of points. Using a pre-calculated stress field, such as the one obtained using the finite element method, stresses are interpolated for each point and rotated in the direction of the slip surface to analyze the normal and shear stress components. In contrast to other approaches that define the factor of safety with respect to resisting and driving forces evaluated in terms of integrals of shear strength and shear stresses, respectively, Nitzsche and Herle (2020) define the factor of safety based on the mobilization of shear stresses while taking the soil’s stress-strain behavior into account. To accomplish this, it is suggested to conduct element tests (simple shear tests) for each point along the potential slip surface considering its current stress state to subsequently evaluate the mobilization of shear stresses with increasing shear strains. For each slip surface with length L , Nitzsche and Herle (2020) evaluate the global mobilized shear resistance ratio $T(\gamma)$ according to Eq. 2.7 as the mobilized shear stresses τ_{mob} with respect to the shear strain γ integrated for the segments i with individual length L_i , divided by the initial shear stresses τ_0 integrated over the same segments. Note that L_i may be omitted in case all segments are of the same length.

$$T(\gamma) = \frac{\sum_i \tau_{\text{mob},i}(\gamma) L_i}{\sum_i \tau_{0,i} L_i} \quad (2.7)$$

Upon shearing and depending on the soil density, the $T(\gamma)$ curve depicted in Fig. 2.4(a) and (b) may be characterized by monotonically increasing shear stresses or by a peak state followed by a reduction of shear stresses, respectively. The former, pure contractive behavior, is typical of loose sandy soils or normally consolidated clays, whereas the latter, contractive behavior followed by dilatant response, is typical of dense sandy soils and overconsolidated clays. However, the latter type of behavior (peak state followed by shear stress reduction) can only be numerically simulated in a simple shear test if the constitutive model used in the simulation is either capable of capturing strain softening (in the case of elastoplastic models) or takes into account the effect of pyknotropy (in case of hypoplastic models). Moreover, advanced constitutive features, for instance small strain stiffness (Benz, 2007; Benz et al., 2009; Niemunis et al., 2011), intergranular strain

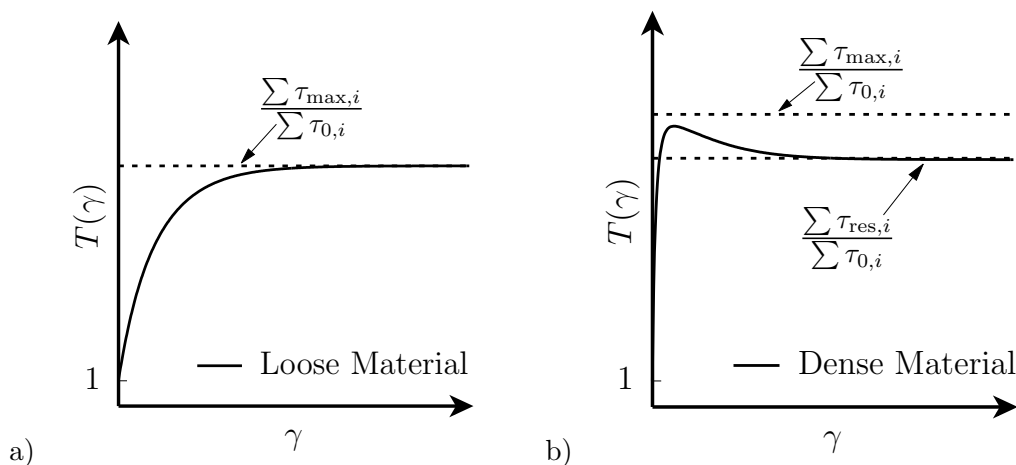


Figure 2.4: Global mobilized shear resistance ratio $T(\gamma)$ for (a) a loose and (b) a dense material

(Niemunis and Herle, 1997) or destructuration (Taiebat et al., 2010), may also result in similar curve trends.

Based on the global mobilized shear resistance ratio $T(\gamma)$, the maximum and residual values (T_{\max} , T_{res}) as well as the corresponding shear strains (γ_{\max} , γ_{res}) are identified, wherein the residual value corresponds to a shear strain beyond which T remains constant. As indicated in Fig. 2.5, Nitzsche and Herle (2020) suggest to evaluate the strain-dependent slope stability for a particular slip surface as $\text{FoS}(\gamma) = T_{\max}$ for $\gamma \leq \gamma_{\max}$ and $\text{FoS}(\gamma) = T(\gamma)$ for $\gamma > \gamma_{\max}$. It should be noted that γ_{\max} and γ_{res} coincide for strain hardening materials. Furthermore, for softening materials, T_{\max} is usually smaller than the ratio of the sum of the individual maximum shear stresses divided by the sum of the initial shear stresses as also depicted in Fig. 2.4(b). The reason for this particularity is that the local maxima of the shear stresses are usually not mobilized at the same shear strain in each point. Therefore, at a certain shear strain, the peak state may be reached at one point whereas softening is already seen for other points. The critical slip surface is identified as the slip surface that yields the minimum factor of safety when the objective function is defined with respect to the factor of safety at a given shear strain.

Compared to other approaches which can be used for the analysis of slope stability problems, a major advantage of the concept presented by Nitzsche and Herle (2020) summarized above is the possibility for evaluation of the FoS considering sophisticated constitutive models. This includes the simulation of the element tests as well as the finite element simulation conducted to obtain the initial stress field for stability analysis. Thus, it is not only the stress state that can be transferred from the initial slope model to the element

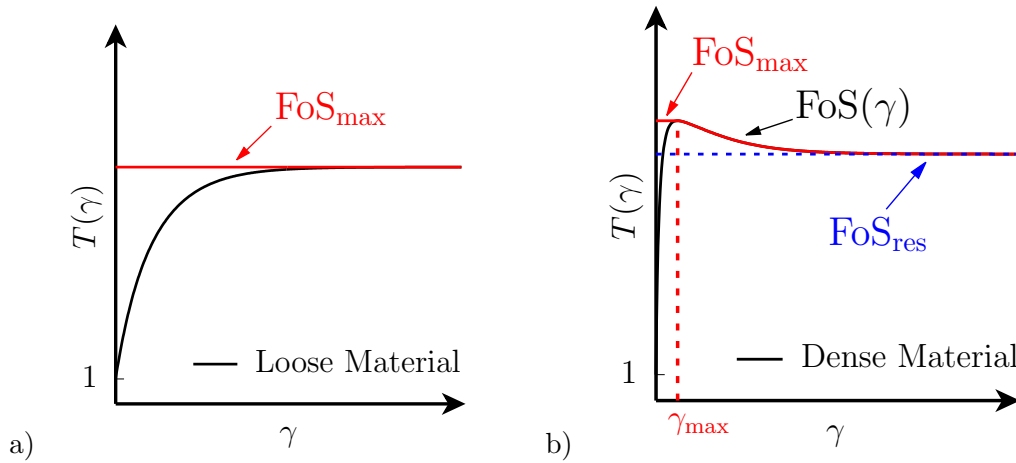


Figure 2.5: Strain-dependent slope stability $FoS(\gamma)$ for (a) a loose and (b) a dense material

test model, but all internal and additional state variables of the constitutive model which enable to approximate stress history, density changes, evolution of small strain stiffness etc. on the small scale test level. In fact, this allows for a significantly better approximation of shearing resistance on the slip surface than traditional stress-based analyses using initial stress fields obtained from linear elastic or elastoplastic analyses.

Still, it should be noted that the concept of strain-dependent slope stability proposed by Nitzsche and Herle (2020) cannot be used to detect progressive failure in a slope arising from softening behavior. Considering a finite-element simulation with a constitutive model capturing material softening, it should be clear that as soon as one material point softens, the decrease of the deviatoric stress causes stress redistributions around it inducing, in many cases, softening in neighboring points. However, as the points along the slip surface are treated individually in the strain-dependent slope stability (and other stress-based approaches), stress redistribution is not possible, thus, progressive failure cannot be captured.

2.2. Slope stability analysis for seismic loading

The classical methods for accounting for the seismic impact on the stability of slopes are the pseudo-static analysis (PSA), the permanent-displacement analysis and the stress-deformation analysis (Newmark, 1965; Kramer, 1996; Jibson, 2011), where the latter is also referred to as dynamic finite element analysis in this thesis.

2.2.1. Pseudo-static analysis (PSA)

The evaluation of the factor of safety of slopes subjected to earthquake loading is often conducted based on two subsequent steps where the effects of the earthquake loading are estimated first and the stability analysis is performed subsequently. One approach to perform the latter is by utilizing slope stability methods as discussed in Section 2.1 combined with a pseudo-static analysis (PSA). In PSA, seismic effects are approximated via a static force, usually expressed in terms of a seismic coefficient, acting in a potential sliding mass. This force $F_{h/v}$ is determined based on the seismic coefficient acting in horizontal (k_h) or vertical (k_v) direction and the total weight W in accordance with Eq. 2.8 and Eq. 2.9, respectively.

$$F_h = \frac{a_h \cdot W}{g} = k_h \cdot W \quad (2.8)$$

$$F_v = \frac{a_v \cdot W}{g} = k_v \cdot W \quad (2.9)$$

In its original form, PSA is applied in combination with limit equilibrium methods (LEM) for the analysis of planar or circular slip surfaces discretized as single rigid bodies or multiple slices. As depicted in Fig. 2.6, the pseudo-static force is considered as an additional force with a component in horizontal and vertical direction to be included in the equilibrium of forces and/or moments. Note that in contrast to horizontal seismic coefficients that yield smaller FoS when directed towards the slope toe, for vertical seismic coefficients, both directions/signs need to be checked to identify the one that yields the minimum FoS. Besides LEM (Leshchinsky and San, 1994; Baker et al., 2006; Goldscheider et al., 2010; Hleibieh and Herle, 2019a), evaluation of the factor of safety for slopes and earth dams subjected to earthquake loading has also been conducted by combining PSA with other methods, for instance limit analysis (Ausilio et al., 2000; Loukidis et al., 2003), strength reduction finite element analysis (Baker et al., 2006) or finite element limit analysis (Loukidis et al., 2003; Li et al., 2021).

The seismic coefficient is commonly assumed to be constant with respect to the location and the dynamic loading time as the time step corresponding to the most critical acceleration is analyzed. Note that for many projects, assumptions are required to approximate the effects of the dynamic loading in terms of acceleration time histories or peak ground accelerations (PGA). In most studies, the seismic coefficient is approximated with respect to the earthquake signal at the bedrock, the soil properties and layering or with the peak ground acceleration rather than being directly evaluated from dynamic analyses. Depending on the severity of the earthquake, Terzaghi (1950) suggested typical values of k_h

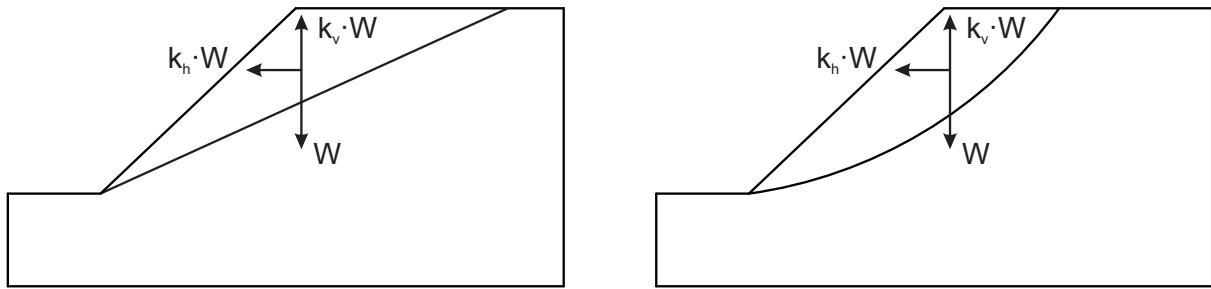


Figure 2.6: Consideration of pseudo-static forces for planar and circular slip surfaces

ranging between 0.1 and 0.5, whereas Seed (1979) proposed smaller values of k_h ranging between 0.12 and 0.14. Alternatively, k_h is either linked to PGA or to allowable displacements. To avoid over-conservative estimates in cases where the seismic coefficients are determined based on PGA in combination with Eq. 2.8 and Eq. 2.9, multiplication with a factor $0 \leq \chi \leq 1.0$ is usually considered, for instance $\chi = 0.5$ as discussed in Kramer and Smith (1997) and Goldscheider et al. (2010). To determine ranges for χ in accordance with shallow and deep slip surfaces, investigations were performed by Triantafyllidis and Grandas-Tavera (2013) using two-dimensional numerical simulations with the hypoplastic model. Alternatively, the seismic coefficients can be back-calculated from permanent-displacement analysis, which is introduced in the next section, by defining project-specific allowable displacements (Bray and Travasarou, 2009; Macedo and Candia, 2020).

Note that, in contrast to the permanent-displacement analysis and the stress-deformation analysis which provide information on potential slope deformations, PSA only represents one instant in time and predicts either a factor of safety for a given acceleration or a yield acceleration for a slope at limit state, where the latter is the favorable option (Abramson et al., 2001; Jibson, 2011).

2.2.2. Pseudo-dynamic analysis

In contrast to the pseudo-static approach, in which horizontal and vertical seismic coefficients are applied constant with respect to time and space, the pseudo-dynamic approach enables to account for spatial and temporal variation of the seismic coefficients. This is accomplished by consideration of primary compression and shear waves propagating from a reference level (e.g. slope toe) vertically upwards through a soil body. As discussed, among other authors, by Steedman and Zeng (1990), Choudhury and Nimbalkar (2005) and Hazari et al. (2020), the variation of the horizontal and vertical accelerations a_h and a_v with regard to time t and vertical position z (Fig. 2.7) can be approximated by a

other authors, seismic slope stability analyses using the pseudo-dynamic approach or extensions thereof have been conducted by Hazari et al. (2020) using the limit equilibrium method, by Qin and Chian (2018) and Zhang and Yang (2021) using the upper bound limit analysis and by Zhou and Qin (2020) using the finite element upper bound analysis.

Note that pseudo-dynamic approaches are based on a rough estimate of the acceleration time history by a (harmonic) function as described above and cannot accurately predict the effects of an earthquake loading. Shortcomings with regard to this approach are related to missing physics, for instance as reflections at the ground surface or reflection, refraction and absorption of waves at layer boundaries are not considered accurately. To predict better the time history of accelerations, accumulations of strains, and build-up of excess pore water pressures, dynamic finite element analysis (DFEA) - previously referred to as stress-deformation analysis - need to be conducted using sophisticated constitutive models.

2.2.3. Permanent-displacement analysis

The permanent-displacement analysis is based on the sliding block method proposed by Newmark (1965). In its original form, Newmark's method treats the potential slip masses of a landslide as a rigid-plastic body as depicted in Fig. 2.8. The sliding mass does not deform internally, but starts moving along a discrete shear surface when a critical acceleration is exceeded. This acceleration – also referred to as the yield acceleration – is determined from a pseudo-static analysis (PSA) by iterative adjustment until $FoS = 1.0$ is obtained. Newmark's method calculates the cumulative permanent displacement of the block as it is subjected to the action of an earthquake acceleration-time history by double integration of those accelerations exceeding the yield acceleration. Thereby, no permanent displacements at accelerations below the critical or yield level are considered. Both methods (PSA and original Newmark method) ignore the reduction in shear strength that may take place during an earthquake, the influence of relatively small but long-standing oscillations on slope stability, and treat independently the determination of the factor of safety and the estimation of slope displacements.

Within the last 50 years, continuous improvement of Newmark's method enabled to overcome the major drawbacks mentioned beforehand, for instance by consideration of soil deformability, damping, degradation of yield accelerations, spatial distribution of yield accelerations or excess pore-water pressure build-up. Among other authors, extensions of the Newmark method have been proposed by researchers based on decoupled and

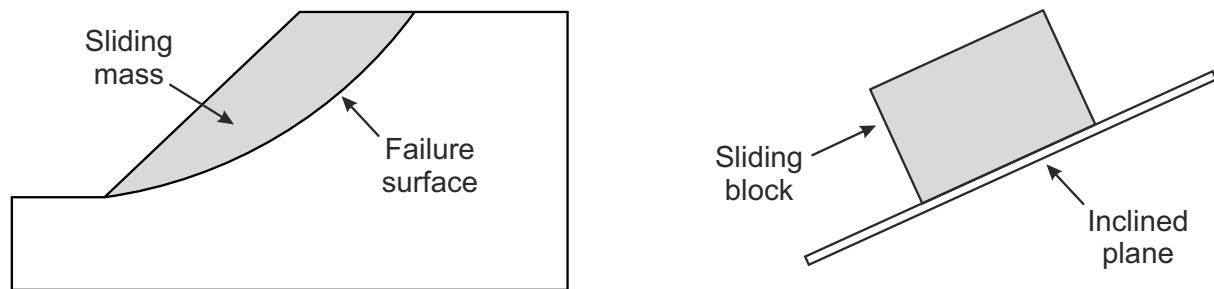


Figure 2.8: General concept of Newmark's sliding block method

coupled analyses (Seed and Martin, 1966; Makdisi and Seed, 1978; Lin and Whitman, 1983; Kramer and Smith, 1997; Bray and Rathje, 1998; Rathje and Bray, 2000; Bray and Travararou, 2009; Rathje and Antonakos, 2011; Tropeano et al., 2017; Jafarian and Lashgari, 2017; Leshchinsky et al., 2018; Mathews et al., 2019; Ji et al., 2021). Decoupled analyses consider an independent evaluation of the dynamic response and the permanent displacement, whereas in coupled analyses the ground motion is determined with regard to the plastic sliding displacement. Note that to quantify the seismic slope stability in terms of a FoS based on the permanent-displacement analyses following Newmark's method or extensions thereof, project-specific allowable displacements or velocities need to be defined.

2.2.4. Dynamic finite element analysis (DFEA)

In case inertial and damping effects or temporal variations should be considered in a finite element analysis, the time dependent behavior of the system needs to be simulated in terms of a dynamic analysis. For this, the system of equations solved by the finite elements needs to be extended (compared to the static case) by including inertial and damping terms. Assuming a linear relationship between \mathbf{K} and \mathbf{u} , the linearized system of equations can be expressed as (Bathe, 2006)

$$\mathbf{M}\ddot{\mathbf{u}} + \mathbf{C}\dot{\mathbf{u}} + \mathbf{K}\mathbf{u} = \mathbf{R} \quad (2.15)$$

where \mathbf{M} is the mass matrix, \mathbf{C} is the damping matrix, \mathbf{K} is the stiffness matrix, \mathbf{R} is the vector of external nodal forces, gathering contributions of body forces and surface tractions, and \mathbf{u} , $\dot{\mathbf{u}}$ and $\ddot{\mathbf{u}}$ denote the nodal displacements, velocities and accelerations, respectively. Note that the type of solution variables, in this case \mathbf{u} , depends on the element type formulation. To account for elements with different types of solution variables, for instance u-p elements discretizing the displacements of the solid phase \mathbf{u} and the pore

water pressure p^w , a more general definition can be used with \mathbf{d} , $\dot{\mathbf{d}}$ and $\ddot{\mathbf{d}}$ denoting the solution variables, their first and second time derivatives, respectively. The general system of equations can be expressed as

$$\mathbf{r}(\mathbf{d}, \dot{\mathbf{d}}, \ddot{\mathbf{d}}) = s_D \mathbf{M} \ddot{\mathbf{d}} - \mathbf{f}(\mathbf{d}, \dot{\mathbf{d}}) \quad (2.16)$$

where \mathbf{r} and \mathbf{f} denote the residuum and the assembled contributions of internal and external forces, while s_D is used to switch between static ($s_D = 0$) and dynamic ($s_D = 1$) simulations. Note that time dependency of the solution is obtained by considering that the solution variables and their derivatives are functions of time. To account for this, different time integration schemes can be adopted, for instance Newmark's method (Newmark, 1959) or the Hilber-Hughes-Taylor time integration scheme (Hilber et al., 1977) that is an extension of the former time integration method. Further information and details about time integration schemes can also be found in Machaček (2020) and Staubach (2022).

In general, dynamic finite element analysis (DFEA) allows to determine the spatial and temporal evolution of accelerations, accumulated strains and the build-up of excess pore water pressure during the seismic loading, provided that sophisticated constitutive models and coupled elements (u-p) are used. However, similar to the permanent displacement method, quantitative evaluation of slope stability needs to be conducted based on project-specific criteria such as allowable displacements or velocities. In case Federal Institutes or official authorities request an additional evaluation of the slope stability under earthquake loading in terms of a factor of safety, as discussed for instance by Goldscheider et al. (2010), Dahmen et al. (2014), Mittmann et al. (2015) and Eyll-Vetter (2015), results of DFEA should be further processed in slope stability analyses.

Combining SRFEA and DFEA in a way that repeated DFEA are conducted with different sets of reduced soil shear strength (Karray et al., 2018, 2019) and stiffness parameters (Ma et al., 2021), the FoS can be determined based on more general criteria, such as a rapid increase of displacements or numerical non-convergence. Note that significant repetitions of DFEA are associated with substantial computational costs. Alternatively, a more rational two-step approach can be followed, where LEM, LA, SRFEA, FELA or stress-based analyses are conducted based on the results of the DFEA at different time steps of the seismic loading. However, despite Hleibieh and Herle (2019a) and Schmüdderich et al. (2022a), not many attempts were made to transfer information (e.g. stresses, pore water pressures and other state variables) between DFEA and consecutive stability analyses.

2.3. Material models

In this section, three material models are explained in detail due to their importance for this work. The Mohr-Coulomb (MC) model and the Matsuoka-Nakai (MN) model are implemented in `numgeo` and verified using element test simulations in Chapter 4. Ultimately, both models (MC and MN) are used in combination with the strength reduction method implemented in Chapter 5. The hypoplastic model is introduced due to its application for the estimation of seismic effects using dynamic finite element analyses and the estimation of the factor of safety based on the concept of strain-dependent slope stability.

2.3.1. Mohr-Coulomb (MC)

As noted in Section 2.1.1, considering normal and shear stresses acting on a plane, the basic Mohr-Coulomb criterion limits the maximum shear strength of a material with respect to its shear strength parameters φ and c and the normal effective stress ($\sigma'_n = \sigma_n - u$) acting on that plane (Coulomb, 1776) according to Eq. 2.17.

$$\tau_{\max} = (\sigma_n - u) \tan \varphi + c \quad (2.17)$$

Extending the Mohr-Coulomb criterion to three-dimensional space expressed in terms of principal stresses σ_1 , σ_2 and σ_3 , the shape of the Mohr-Coulomb criterion is represented by a hexagonal pyramid with the tip of the pyramid (apex) located on the hydrostatic axis at a distance of $c \cdot \cot \varphi$ from the origin. As depicted in Fig. 2.9, the hexagonal pyramid is defined by the yield surface which is composed of six faces. The yield functions and

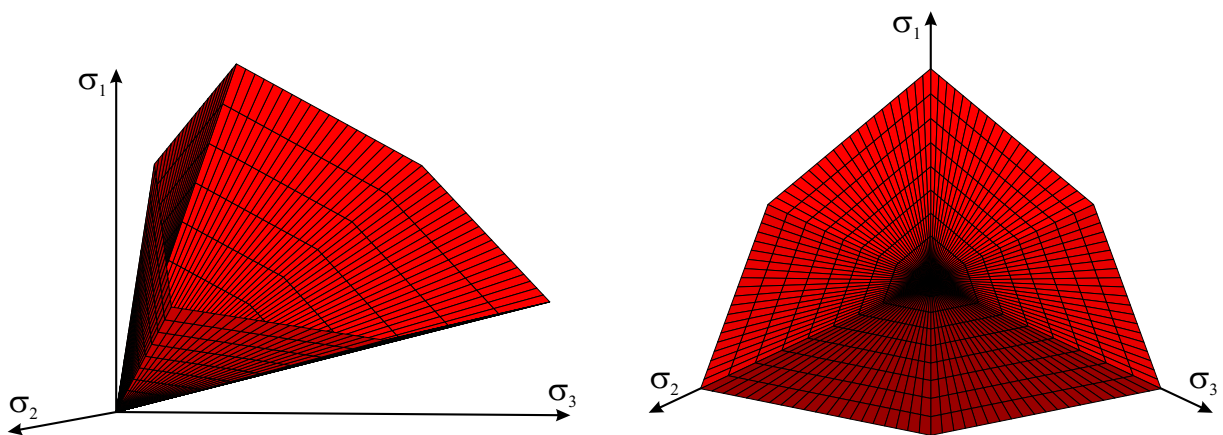


Figure 2.9: Mohr-Coulomb yield surface composed of six faces plotted in principal stress space

derivatives are well defined on the surfaces. However, the derivatives can not be found easily for the intersections between two faces (i.e. edges/corners in the deviatoric plane) as those represent singularities. In literature, different strategies have been proposed to handle these singularities, as will be further elaborated in the subsequent paragraphs.

Considering principal stresses ordered numerically, only one sector of the yield function of the Mohr-Coulomb model needs to be analyzed. Considering the Mohr-Coulomb model in the deviatoric plane normalized by the mean stress $p = (\sigma_1 + \sigma_2 + \sigma_3)/3$, this sector is shown in Fig. 2.10, where potential stress states range between triaxial compression and triaxial extension states with Lode angles of $\theta = 30^\circ$ and $\theta = -30^\circ$, respectively. It should be noted that stress states could only be assigned to the other sectors if the order of principle stresses is neglected.

Considering mechanical sign convention with tensile stresses positive and principle stresses ordered such that $\sigma_1 \leq \sigma_2 \leq \sigma_3$, the yield function can be expressed according to Eq. 2.18. From this equation it can be seen that the intermediate stress σ_2 is not considered in the yield function, thus, changes of σ_2 that do not lead to a change in the order of the principle stresses have no effect on the response obtained with the Mohr-Coulomb model.

$$F_{MC} = -(\sigma_1 - \sigma_3) + (\sigma_1 + \sigma_3) \sin \varphi - 2c \cos \varphi \quad \text{for} \quad \sigma_1 \leq \sigma_2 \leq \sigma_3 \quad (2.18)$$

As the implementation of the Mohr-Coulomb model is difficult due to the singularities at the corners and the apex of the yield surface, researchers (Griffiths, 1986, 1990; Schweiger,

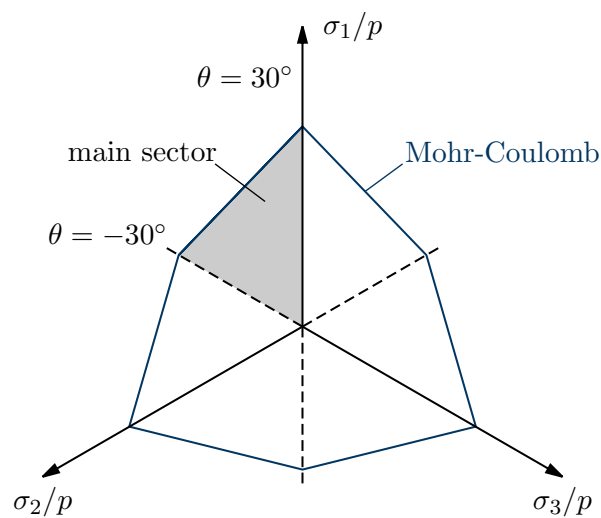


Figure 2.10: Shape of the Mohr-Coulomb yield surface in the deviatoric plane with emphasis on the main sector for potential stress states

1994; Clausen et al., 2010) investigated to what extent the Drucker-Prager model was an appropriate alternative for simulating geotechnical boundary value problems. In general, the Drucker-Prager model is described by a yield surface with the shape of a cone, which is differentiable everywhere except for the tip of the cone. Considering the shape of the yield surface in the deviatoric plane, the isotropic Drucker-Prager model is described by a circle with the center located at the hydrostatic axis. The distance between the hydrostatic axis and the yield surface on the deviatoric plane is dependent on the first stress invariant I_1 and the second deviatoric stress invariant J_2 but independent of the Lode angle θ (i.e. identical in every direction) and can be expressed as

$$F_{\text{DP}} = \sqrt{3} J_2 + \alpha I_1 - \beta \quad (2.19)$$

where α and β are material parameters, which are related to the soil friction and cohesion, respectively. However, as the Mohr-Coulomb model is not described by a yield surface with the shape of a circle in the deviatoric plane, different fits of the Drucker-Prager model to the Mohr-Coulomb model are possible. The common fits depicted in Fig. 2.11 are (1) an external cone fitted to the compression corner of the MC model, (2) a cone fitted to the extension corner of the MC model and (3) an internal/inscribed cone that touches the MC yield surface without intersecting it. Determination of α and β for the cones (1) - (3) can be conducted based on the shear strength parameters φ and c , as discussed for instance by Clausen et al. (2010).

Considering the external and internal cones, Griffiths (1990) evaluates the equivalent Mohr-Coulomb friction angle φ_{MC} for different Lode angles θ , which represent the friction

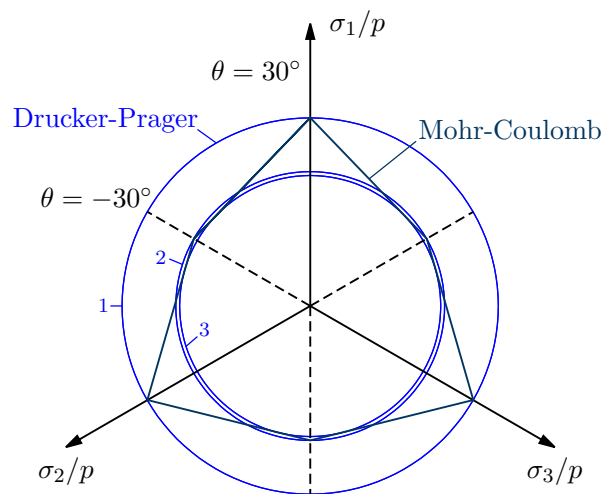


Figure 2.11: Mohr-Coulomb and Drucker-Prager criteria on the deviatoric plane considering (1) external, (2) extension and (3) internal fit

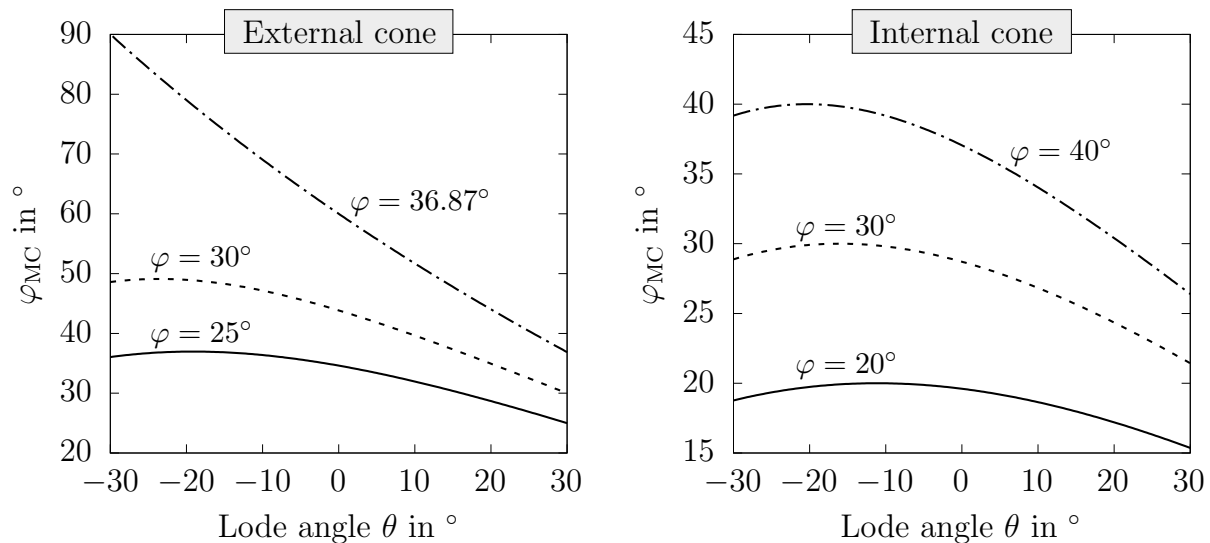


Figure 2.12: Equivalent friction angle variation for different external and internal cones, modified after Griffiths (1990)

angle that needs to be used in combination with the Mohr-Coulomb model to obtain the same size of the yield surface in the deviatoric plane at a given Lode angle. As can be seen from Fig. 2.12 the equivalent friction angle significantly changes with varying Lode angle, which makes it very difficult to define proper values for α and β to avoid large over- or underestimation of the size of the Drucker-Prager yield surface in case of varying Lode angles. In fact, it is seen in this figure for the external cone and a friction angle of $\varphi = 36.87^\circ$ that the equivalent friction angle approaches $\varphi_{MC} \rightarrow 90^\circ$ for Lode angles approaching the triaxial extension corner with $\theta \rightarrow -30^\circ$. This massive over-estimation was also reported by Bishop (1966). In case of element test simulations with a limited range of different Lode angles, a convenient fit of the Drucker-Prager yield surface might be found, still, it should be noted that these fits do not perform well for geotechnical boundary value problems covering large ranges of Lode angles.

Clausen et al. (2010) studied the differences between the Mohr-Coulomb and the Drucker-Prager model based on two- and three-dimensional bearing capacity analyses considering different sizes of the cones based on the concepts described above. Although for plane strain conditions, the inscribed fit of the Drucker-Prager model resulted in approximately similar results as the Mohr-Coulomb model in terms of the bearing capacity, the stiffness was not well approximated, yielding completely different settlements when reaching the ultimate limit load. Moreover, for three-dimensional conditions, none of the fits was capable to provide appropriate predictions, neither for the bearing capacity nor for the stiffness. As the differences in terms of bearing capacity and stiffness obtained using the

Mohr-Coulomb model and different fits of the Drucker-Prager model were found to be very large, Clausen et al. (2010) concluded that the Drucker-Prager model should only be considered an educational model in soil mechanics, rather than a model to be actually used for simulations of real case geotechnical applications. Similar observations and concluding statements were also made earlier by Schweiger (1994) based on simulations of the earth pressure problem.

As the Drucker-Prager model can not be considered an alternative to the Mohr-Coulomb model for geotechnical applications, other alternatives were sought. To circumvent the difficulties of the Mohr-Coulomb model associated with the singularities at the edges between two yield surfaces as well as at the tip/apex, where the derivatives of the yield surfaces are not defined, two strategies are commonly followed: (1) definition of the yield function using multiple surfaces in combination with the Koiter (1953) rule, as for instance discussed in Ristinmaa and Tryding (1993), Clausen et al. (2006) or Huang and Griffiths (2008), or (2) definition of a smooth (rounded) approximation of the original Mohr-Coulomb yield function, where the derivatives are well-defined for all Lode angles. With regard to the latter concept, different approximations with rounded compression and extension corners in the deviatoric plane have been proposed, for instance by utilizing the Von Mises criterion to round off the MC corners (Owen and Hinton, 1980). However, considering a MC model with rounded corners, the question arises whether continuity between the regular surfaces and the rounded ones can be guaranteed with respect to the yield function as well as its derivatives.

A few years after the study of Owen and Hinton (1980), Sloan and Booker (1986) proposed an alternative approximation of the Mohr-Coulomb model with rounded corners in the deviatoric plane (Fig. 2.13). In contrast to the definition of the Mohr-Coulomb yield function with respect to principle stresses (Eq. 2.18), a definition based on the works of Nayak and Zienkiewicz (1972) was proposed by Sloan and Booker (1986) according to Eq. 2.20, where the stress state is considered in terms of the stress invariants σ_m , $\bar{\sigma}$ and θ , representing the mean stress, the deviatoric stress and the Lode angle, respectively.

$$F_{\text{MC}} = \begin{cases} \sigma_m \sin \varphi + \bar{\sigma}(\cos \theta - \frac{1}{\sqrt{3}} \sin \varphi \sin \theta) - c \cos \varphi = 0 & \text{for } |\theta| \leq \theta_t \\ \sigma_m \sin \varphi + \bar{\sigma}(A - B \sin 3\theta) - c \cos \varphi = 0 & \text{for } |\theta| > \theta_t \end{cases} \quad (2.20)$$

Moreover, the yield function serves as a switch between the original formulation and the approximated (rounded) formulation of the Mohr-Coulomb yield function based on a comparison of the current Lode angle θ and the transition Lode angle θ_t , the latter representing an additional parameter of the proposed material model. Considering Lode

angles $\theta \leq \theta_t$, the original Mohr-Coulomb yield function is used, whereas for $\theta > \theta_t$, the approximation function is applied. Forcing continuity of the yield function and the first derivative (C1 continuity) at $\theta = \theta_t$, the parameters A and B were determined. The analytical solutions for A and B with respect to the Lode angle θ , the transition Lode angle θ_t and the friction angle φ are not discussed here, but can be found in Sloan and Booker (1986).

Comparing the yield function proposed by Sloan and Booker (1986) to the original model, it is apparent from Fig. 2.13 that the approximation of the yield function is an inside round-off of the Mohr-Coulomb corners when plotted in the deviatoric plane, thus, the elastic zone of the proposed model is smaller compared to the original model for $\theta > \theta_t$. Moreover, the difference between both models is more pronounced for triaxial compression conditions with Lode angles of $\theta = 30^\circ$ compared to triaxial extension conditions with Lode angles of $\theta = -30^\circ$. Considering a triaxial compression test simulated with the original and the approximated Mohr-Coulomb model, it should be clear that the ultimate deviatoric stress is smaller using the latter model. Sloan and Booker (1986) reported for the case of a triaxial compression test ($\theta = 30^\circ$) with a friction angle of $\varphi = 30^\circ$ and a transition Lode angle of $\theta_t = 25^\circ$ that the difference in the maximum deviatoric stress between the exact and the rounded MC model was smaller than 4.3%. Considering the selection of θ_t , it is apparent from this figure that larger values of θ_t lead to a closer fit, whereas smaller values of θ_t lead to a larger deviation from the original model as the smooth approximation starts at smaller (absolute) Lode angles. For practical use, Sloan and Booker (1986) recommend using a transition angle in the range of $\theta_t = 25^\circ$ to 29° as it allows for an accurate approximation of the Mohr-Coulomb model, whereas larger

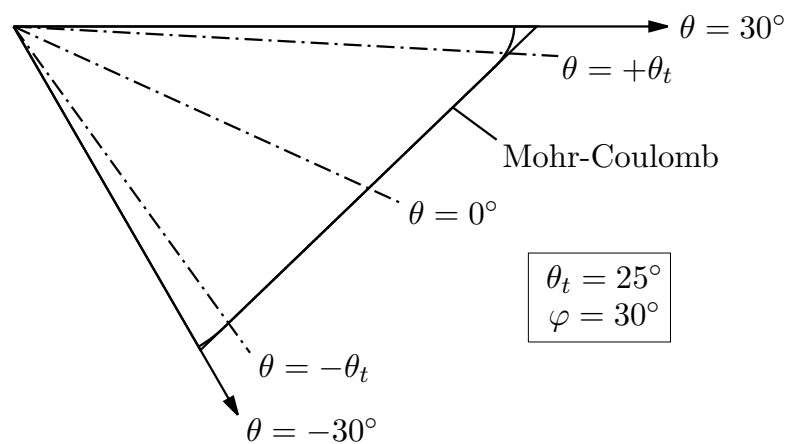


Figure 2.13: Mohr-Coulomb yield surface in the deviatoric plane with rounded vertices, modified after Sloan and Booker (1986)

values of θ_t close to 30° should not be selected in order to avoid issues with regard to the determination of the fitting parameters A and B .

Abbo and Sloan (1995) proposed a more convenient form of the yield surface proposed by Sloan and Booker (1986) by introducing $K(\theta)$ serving as the split function between the original and the approximated Mohr-Coulomb model with respect to θ and θ_t . Moreover, they extended the approximation of the Mohr-Coulomb model proposed by Sloan and Booker (1986) by addition of a hyperbolic surface, which eliminates the singularity at the tip of the pyramid of the Mohr-Coulomb model. The updated equation of the yield function and the function $K(\theta)$ are given in Eq. 2.21 and Eq. 2.22, respectively, where a is a new parameter of the material model controlling the shape of the hyperbolic surface as depicted in Fig. 2.14.

$$F_{MC} = \sigma_m \sin \varphi + \sqrt{\bar{\sigma}^2 K^2(\theta) + a^2 \sin^2 \varphi} - c \cos \varphi = 0 \quad (2.21)$$

$$K(\theta) = \begin{cases} \cos \theta - \frac{1}{\sqrt{3}} \sin \varphi \sin \theta & \text{for } |\theta| \leq \theta_t \\ A - B \sin 3\theta & \text{for } |\theta| > \theta_t \end{cases} \quad (2.22)$$

As the distance between the tip of the MC model and the origin can be determined from $d = c \cdot \cot \varphi$ (unless $\varphi = 0^\circ$), the parameter a can be expressed as $a = \alpha \cdot d$ with $0 \leq \alpha \leq 1$. As shown in Fig. 2.15(a), for $\alpha \rightarrow 0$, the hyperbolic approximation approaches the original Mohr-Coulomb yield function, whereas $\alpha = 1$ results in a yield function that does not allow for tensile stresses. However, it is obvious from Fig. 2.15(b) that the hyperbolic approximation also impacts the size of the yield surface in the deviatoric (π) plane, where larger values of α lead to a smaller elastic zone. For practical purposes, Abbo

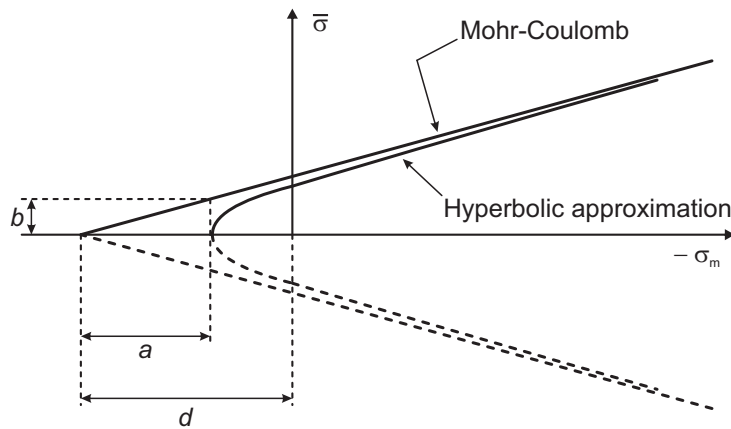


Figure 2.14: Hyperbolic approximation to Mohr-Coulomb yield function, modified after Abbo and Sloan (1995)

and Sloan (1995) recommend using $\alpha = 0.05$, as results obtained with this approximation are almost identical to the ones obtained with the original model.

Abbo et al. (2011) further extended the works of Sloan and Booker (1986) and Abbo and Sloan (1995) by replacing the C1 continuous approximation of the Mohr-Coulomb yield surface by a C2 continuous approximation, which ensures continuity of the yield function as well as its first and second derivative. Therefore, Abbo et al. (2011) extended the function $K(\theta)$ by addition of a third term, which includes an additional fitting parameter C as shown in Eq. 2.23.

$$K(\theta) = \begin{cases} A + B \sin 3\theta + C \sin^2 3\theta & \text{for } |\theta| > \theta_t \\ \cos \theta - \frac{1}{\sqrt{3}} \sin \varphi \sin \theta & \text{for } |\theta| \leq \theta_t \end{cases} \quad (2.23)$$

Compared to the original formulations presented in Sloan and Booker (1986) and Abbo and Sloan (1995), it should be noted that also the sign of the second term (related to parameter B) has been reversed. To obtain C2 continuity, it needs to be ensured that the two functions yield identical results if the Lode angle is identical to the transition Lode angle. Therefore, the system of equations composed of $K(\theta)$, $dK/d\theta$ and $d^2K/d^2\theta$ was solved for the parameters A , B and C at $\theta = \theta_t$. Again, the analytical solution for A , B and C is not presented here, but can be found in Abbo et al. (2011). Analyzing the shape of the yield surface presented in Fig. 2.16, it is apparent that the C2 approximation of the Mohr-Coulomb yield function is slightly outside of the C1 approximation and, thus, resembles a better fit to the original yield function.

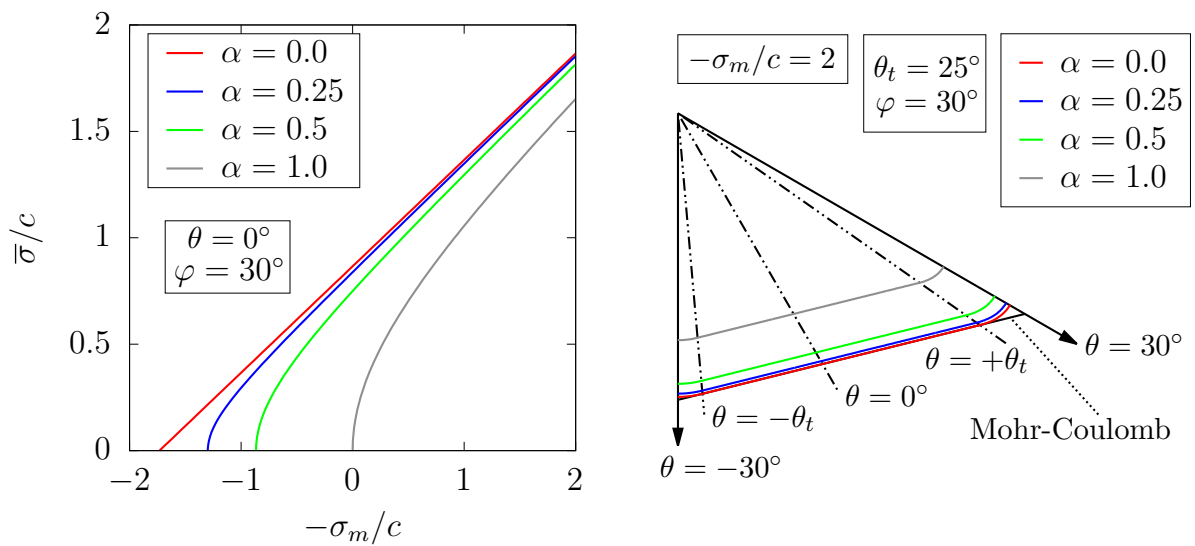


Figure 2.15: Hyperbolic approximation to Mohr-Coulomb meridional section and rounded hyperbolic yield surface in the deviatoric plane, modified after Abbo and Sloan (1995)

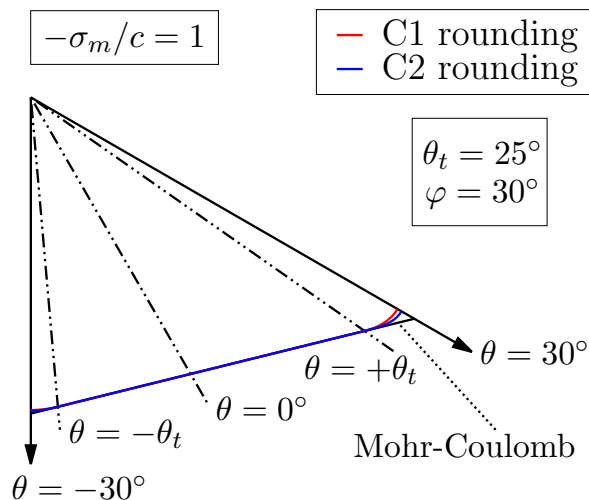


Figure 2.16: Rounding of Mohr–Coulomb failure criterion in deviatoric plane, modified after Abbo et al. (2011)

More importantly, it should be noted that the main advantage of the approximation of the Mohr-Coulomb model proposed by Abbo et al. (2011) is the continuity with respect to the second derivative of the yield and potential surface which enables usage of proper return mapping schemes and determination of the consistent tangent stiffness to obtain better numerical convergence of the model. For practical use, Abbo et al. (2011) suggest a lower limit of $\theta_t \geq 25^\circ$ and an upper limit of $\theta_t \leq 29.5^\circ$, which for instance result in 5.3% and 0.56% reduction of the maximum strength, respectively, in case of $\varphi = 45^\circ$. However, it should be clear that this reduction is only observed for triaxial conditions with Lode angles $|\theta| \approx 30^\circ$, whereas for plane strain conditions such as 2D slope stability or bearing capacity analyses no reduction is observed due to $|\theta| < \theta_t$.

2.3.2. Matsuoka-Nakai (MN)

The Matsuoka-Nakai failure criterion proposed by Matsuoka and Nakai (1974) has initially been formulated for granular materials based on the concept of the spatial mobilized plane (SMP) as an extension of the concept of mobilized planes, discussed among others by Matsuoka (1974). Following these concepts, a mobilized plane describes the maximum ratio of shear to normal stresses, $(\tau/\sigma_n)_{\max}$, on a two-dimensional plane. Considering principle stresses σ_1 , σ_2 and σ_3 , there are three mobilized planes, which are defined on the two-dimensional planes spanned by each two unit vectors (i.e. σ_1 - σ_2 , σ_1 - σ_3 and σ_2 - σ_3) while it is assumed that the third principle stress component (i.e. the intermediate stress) has no effect on the mobilized planes. However, taking into account that the shear

strength of soils does depend on the intermediate principle stress, as for instance shown by Sutherland and Mesdary (1969) and Ramamurthy and Rawat (1973) presenting results from true triaxial tests on sand, Matsuoka and Nakai (1974) defined the concept of the SMP considering all principle stresses, where the SMP results from the combination of the mobilized planes. A schematic illustration of the mobilized planes and the SMP in the three-dimensional principle stress space is depicted in Fig. 2.17. The failure criterion based on the SMP according to Matsuoka and Nakai (1974) is given in Eq. 2.24, where I_1 , I_2 and I_3 denote the first, second and third stress invariant, respectively, and φ_{ij} denotes the mobilized friction angle in the principle plane i, j .

$$\begin{aligned} \frac{\tau}{\sigma_N} &= \sqrt{\frac{I_1 I_2 - 9 I_3}{9 I_3}} \\ &= \frac{2}{3} \sqrt{\frac{(\sigma_1 - \sigma_2)^2}{4\sigma_1\sigma_2} + \frac{(\sigma_2 - \sigma_3)^2}{4\sigma_2\sigma_3} + \frac{(\sigma_3 - \sigma_1)^2}{4\sigma_3\sigma_1}} \\ &= \frac{2}{3} \sqrt{\tan^2 \varphi_{12} + \tan^2 \varphi_{23} + \tan^2 \varphi_{31}} \end{aligned} \quad (2.24)$$

Considering that the Matsuoka-Nakai failure criterion should coincide with the Mohr-Coulomb failure criterion for triaxial compression and triaxial extension ($\theta = \pm 30^\circ$) with two identical principle stresses, one summand under the root vanishes while the other two are identical, thus, Eq. 2.24 simplifies to

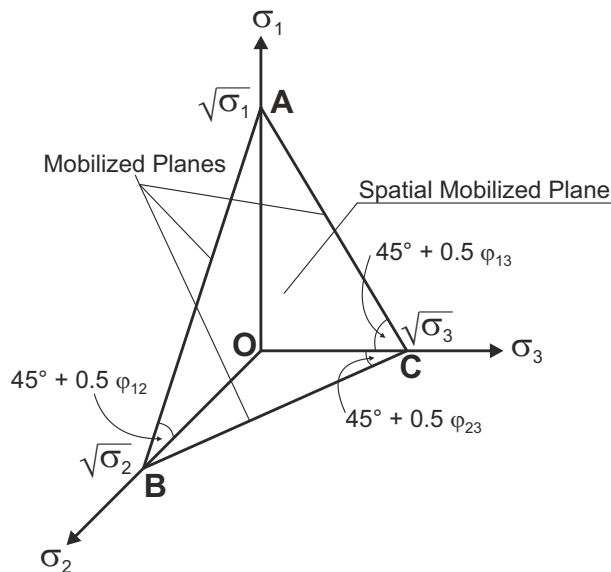


Figure 2.17: Mobilized planes and spatial mobilized plane, modified after Matsuoka and Nakai (1974)

$$\begin{aligned}
\sqrt{\frac{I_1 I_2 - 9 I_3}{9 I_3}} &= \frac{2}{3} \sqrt{2 \tan^2 \varphi} \\
\frac{I_1 I_2 - 9 I_3}{9 I_3} &= \frac{8}{9} \tan^2 \varphi \\
\frac{I_1 I_2}{I_3} - 9 &= 8 \tan^2 \varphi \\
\frac{I_1 I_2}{I_3} &= 8 \tan^2 \varphi + 9 = \frac{9 - \sin^2 \varphi}{1 - \sin^2 \varphi} = K_{\text{MN}}
\end{aligned} \tag{2.25}$$

Therefore, the yield function of the Matsuoka-Nakai model can be formulated according to Eq. 2.26 in terms of the stress invariants I_1 , I_2 and I_3 and the shape parameter K_{MN} , which is controlled by the internal friction angle (Eq. 2.27).

$$F_{\text{MN}} = \frac{I_1 I_2}{I_3} - K_{\text{MN}} \leq 0 \tag{2.26}$$

$$K_{\text{MN}} = 8 \tan^2 \varphi + 9 = \frac{9 - \sin^2 \varphi}{1 - \sin^2 \varphi} \tag{2.27}$$

As the original concept of the spatial mobilized plane (SMP) proposed by Matsuoka and Nakai (1974) was solely developed for granular materials, cohesive soils could not be considered. Therefore, Matsuoka and Sun (1995) proposed a modified concept called 'Extended Spatially Mobilized Plane (Extended SMP)' to consider frictional and cohesive materials. The general idea of the Extended SMP is that the yield function is not evaluated for the current stress σ_{ij} , but for a translated stress $\hat{\sigma}_{ij}$. This is achieved by a translation of the current stress tensor along the hydrostatic axis according to

$$\hat{\sigma}_{ij} = \sigma_{ij} + \sigma_0 \delta_{ij} \tag{2.28}$$

where $\sigma_0 = c \cdot \cot \varphi$ and δ_{ij} denote the bonding stress and the Kronecker delta, respectively. The yield function for the extended Matsuoka-Nakai criterion $F_{\text{E-MN}}$ takes into consideration the translated stress in terms of updated stress invariants \hat{I}_1 , \hat{I}_2 and \hat{I}_3 , which are determined with respect to the translated stress $\hat{\sigma}_{ij}$. The update yield function then reads

$$F_{\text{E-MN}} = \frac{\hat{I}_1 \hat{I}_2}{\hat{I}_3} - K_{\text{MN}} \leq 0 \tag{2.29}$$

where the definition of K_{MN} remains unchanged. In contrast to the Mohr-Coulomb model and its approximations discussed above, the Matsuoka-Nakai yield surface is described by a single continuous surface in the three-dimensional principle stress space, as shown in

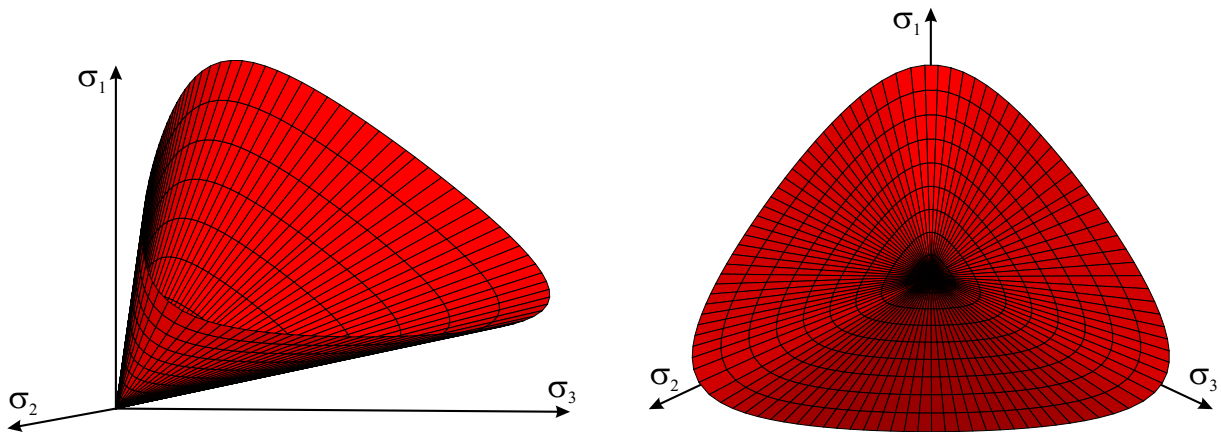


Figure 2.18: Shape of the Matsuoka-Nakai yield surface in principal stress space

Fig. 2.18. Except for the tip of the surface, the MN yield surface is fully differentiable, whereby it is not necessary to find approximations to that surface to avoid singularities.

Comparing the Matsuoka-Nakai yield surface to the Mohr-Coulomb surface on the deviatoric plane, it is apparent from Fig. 2.19 that while both surfaces coincide for triaxial compression and triaxial extension with Lode angles $\theta = \pm 30^\circ$, the MN surface has a larger distance to the hydrostatic axis and allows for larger deviatoric stresses for Lode angles $-30^\circ < \theta < 30^\circ$, for instance for plane strain conditions. The difference between both surfaces can be expressed in terms of the equivalent Mohr-Coulomb friction angle, as discussed among others by Griffiths (1990) for the original Matsuoka-Nakai model and by

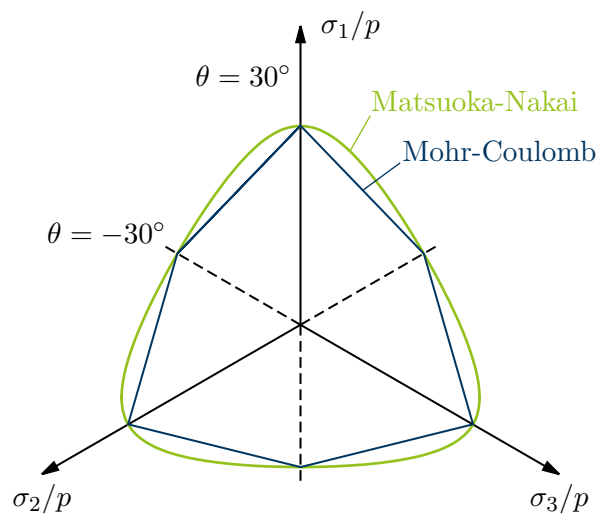


Figure 2.19: Shape of the Matsuoka-Nakai and the Mohr-Coulomb yield surface in the deviatoric plane

Griffiths and Huang (2009) and Jiang and Wang (2011) for the extended Matsuoka-Nakai model. Exemplary trends emphasizing the difference between both models in terms of the equivalent Mohr-Coulomb friction angle are shown in Fig. 2.20(a) for a granular soil and (b) for a cohesive-frictional soil with increasing normalized cohesion c/σ_3 .

Major limitations of the original and the extended Matsuoka-Nakai model with the formulations presented above have been discussed, among others, by Panteghini and Lagioia (2014a). In their study, the authors emphasize that, following the exact formulations, the MN criterion is actually satisfied along three different surfaces (Fig. 2.21), where only the one in the positive octant is required. However, due to the presence of the other two surfaces, the overall function is not convex as the value of the yield function does not monotonically increase for a stress point whose distance towards the yield surface is incrementally increased. Note that the distance between surfaces reduces with increasing friction angle, whereas intersections of the surfaces are observed for the extended MN criterion with cohesion values larger than zero. For this reason, Panteghini and Lagioia (2014a) proposed a reformulation of the MN criterion in accordance with Eq. 2.30 that neglects the second and third surface and guarantees convexity of the yield function.

$$f = g(\theta)\sqrt{J_2} - \eta I_1 = 0 \quad (2.30)$$

$$g(\theta) = 2\sqrt{3} \cos\left(\frac{1}{3} \arccos[\xi \sin(3\theta)]\right) \quad (2.31)$$

$$\eta = \sqrt{\frac{m-9}{m-3}} \quad , \quad \xi = m \sqrt{\frac{m-9}{(m-3)^3}} \quad , \quad m = K_{MN} \quad (2.32)$$

Lagioia and Panteghini (2016) made an effort to develop a unique general formulation of a yield function that allows to switch between several popular yield surfaces, for instance von Mises, Drucker-Prager, Tresca, Mohr-Coulomb, Matsuoka-Nakai, Lade-Duncan as well as rounded versions of Tresca and Mohr-Coulomb. The general formulation of the yield function is given in Eq. 2.33. In this equation, the term $\Gamma(\theta)$ is dependent on three shape parameters (α , β and γ) that can be adjusted in a way that the yield surface of the general model coincides with the aforementioned popular yield surfaces. Lagioia and Panteghini (2016) provide a table with the shape parameter values to fit the different yield surfaces. For example, by setting $\alpha = 1$, $\beta = 0$ and $\gamma = 1$, the Drucker-Prager or von Mises model is obtained. Lester and Sloan (2018) further extended this research and provided details on the implementation of the general classic plasticity model. Note that

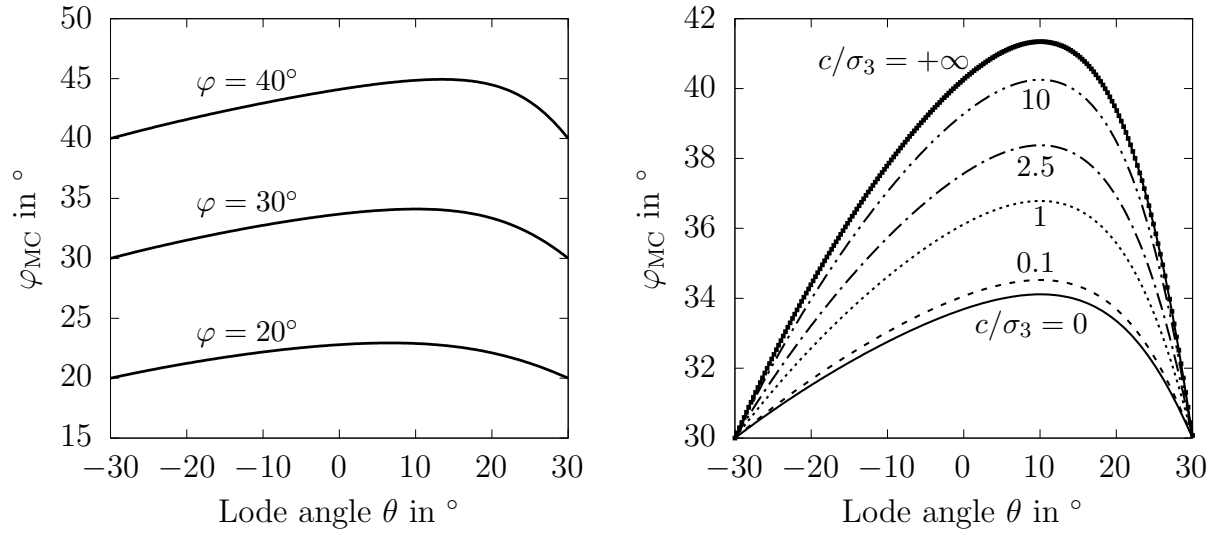


Figure 2.20: Equivalent Mohr-Coulomb friction angle for (a) the Matsuoka-Nakai model considering variations of the internal friction angle and (b) the extended Matsuoka-Nakai model considering variations of the normalized cohesion, modified after Griffiths (1990) and Griffiths and Huang (2009)

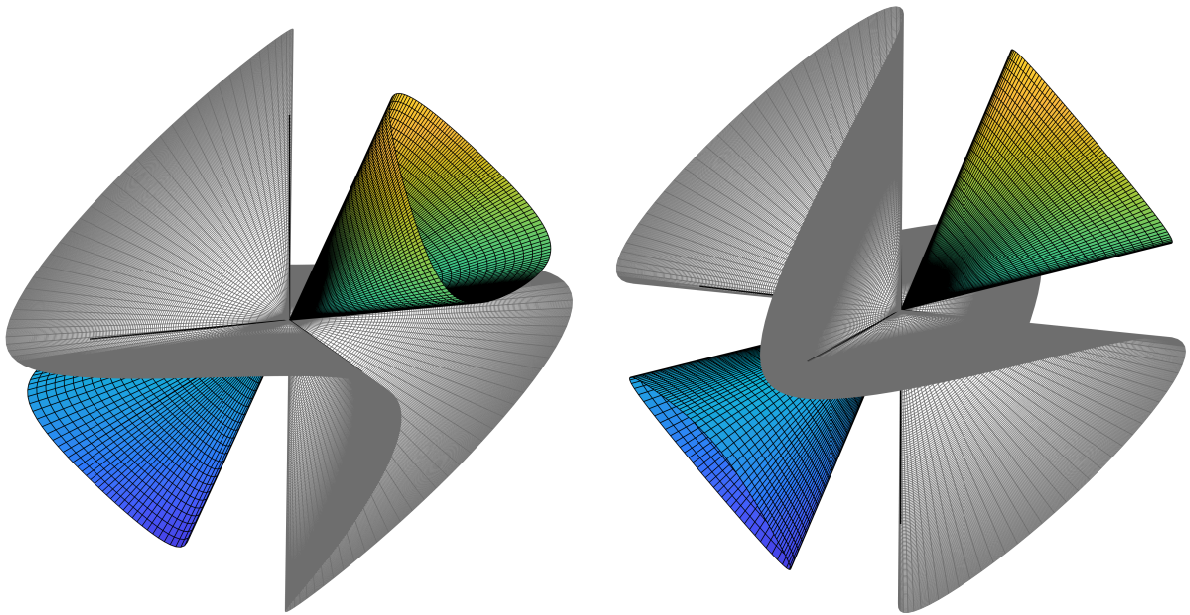


Figure 2.21: Plot of the original Matsuoka-Nakai failure surface in principle stress space, modified after Panteghini and Lagioia (2014b)

the general model ensures convexity for all yield surfaces as well as C2 continuity.

$$f = -(K + M \cdot p) + \Gamma(\theta)\sqrt{J_2} \quad (2.33)$$

$$M = \frac{6 \cdot \sin \varphi}{\sqrt{3}(3 - \sin \varphi)}, \quad K = c \cdot M \cdot \cot \varphi \quad (2.34)$$

$$\Gamma(\theta) = \alpha \cos \left(\frac{1}{3} \arccos [\beta \sin(3\theta)] - \gamma \frac{\pi}{6} \right) \quad (2.35)$$

2.3.3. Constitutive models for dynamic finite element analyses

In recent years, different sophisticated constitutive models have been used in dynamic finite element analysis (DFEA) to analyze the liquefaction and deformation behavior of earth dams and artificial slopes under earthquake loading. Among others, the generalized plasticity (Pastor et al., 1990), the hypoplastic model with intergranular strain (von Wolfersdorff, 1996; Niemunis and Herle, 1997), the MSS model (Kavvasdas and Amorosi, 2000), the PDMY02 model (Yang et al., 2003; Mazzoni et al., 2006), the PMY model (Mazzoni et al., 2006), the endochronic model (López-Querol and Blázquez, 2006), the SANISAND family of models (Dafalias and Manzari, 2004; Taiebat and Dafalias, 2008; Barrero et al., 2020), the UBCSand model (Beaty and Byrne, 2011), the ISA Sand model (Fuentes, 2014; Fuentes and Triantafyllidis, 2015), the ISA Clay model (Fuentes et al., 2018), the PM4Sand model (Boulanger and Ziotopoulou, 2015) and the PM4Silt model (Boulanger and Ziotopoulou, 2018, 2019) were used for the different analyses. These analyses included the back calculation of centrifuge tests related to the VELACS project (Verification of Liquefaction Analyses by Centrifuge Studies) (Muraleetharan et al., 2004; Machaček et al., 2018; Machaček, 2020), the LEAP-UCD-2017 project (Liquefaction Experiments and Analysis Projects) (Kutter et al., 2020; Chen et al., 2020; Montgomery and Ziotopoulou, 2020; Tsiaousi et al., 2020; Yang et al., 2020; Reyes et al., 2021) and the LEAP-Asia-2019 project (Chen et al., 2021; Reyes et al., 2021) as well as the investigation of the earthquake resistance of earth dams (Fernandez-Merodo et al., 2004; López-Querol and Moreta, 2008; Elia et al., 2011; Pelecanos et al., 2015; Han et al., 2016; Boulanger, 2019; Wu et al., 2021) and open pit mine slopes (Machaček et al., 2018; Machaček, 2020). As DFEA is performed using the hypoplastic model with intergranular strain to assess the seismic slope stability in this thesis, only this constitutive model is further elaborated in this section.

2.3.4. Hypoplasticity with Intergranular Strain (Hypo-IGS)

Hypoplasticity is a family of incrementally non-linear constitutive models that, unlike the classical elastoplasticity framework, do not split strain increments into elastic and plastic portions. Therefore, hypoplasticity does not require the explicit formulation of any surface like the plastic potential or the yield surface. It belongs to the group of path-dependent and rate-independent constitutive models, i.e., the sequence of deformation increments influences accumulated stresses, but the duration of the deformation processes or individual increments is insignificant (Niemunis, 2003). The hypoplastic formulation accounts

for density (pyknosity) and confining pressure (barotropy) effects and incorporates the critical state line in the form of a potential compression law (Bauer, 1996). The model requires the calibration of 8 material parameters: the critical friction angle φ_c , the void ratios (at zero mean stress) at densest state e_{d0} , at critical state e_{c0} and the maximum void ratio in a suspension e_{i0} , the granular hardness h_s , and the exponents n , α and β .

The main constitutive equation of the hypoplastic constitutive model in the version of von Wolffersdorff (1996) presents the objective stress rate $\dot{\hat{\sigma}}$ in non-linear dependency of the strain rate $\dot{\hat{\epsilon}}$ as follows:

$$\dot{\hat{\sigma}} = \left(\mathbf{L} + f_d \mathbf{N} \frac{\dot{\hat{\epsilon}}}{\|\dot{\hat{\epsilon}}\|} \right) : \dot{\hat{\epsilon}} \quad (2.36)$$

Thereby, \mathbf{L} is a fourth order tensor linear in $\dot{\hat{\epsilon}}$, whereas \mathbf{N} is a second order tensor non-linear in $\dot{\hat{\epsilon}}$. Both tensors are functions of effective stress and void ratio as depicted in the following equations

$$\mathbf{L} = f_b f_e \frac{1}{\hat{\sigma} : \hat{\sigma}} (F^2 \mathbf{l} + a^2 \hat{\sigma} \hat{\sigma}) \quad (2.37)$$

$$\mathbf{N} = f_d f_b f_e \frac{F a}{\hat{\sigma} : \hat{\sigma}} (\hat{\sigma} + \hat{\sigma}^*) \quad (2.38)$$

where

$$\hat{\sigma} = \boldsymbol{\sigma} / \text{tr} \boldsymbol{\sigma}, \quad \hat{\sigma}^* = \hat{\sigma} - \frac{1}{3} \mathbf{1} \quad (2.39)$$

$$a = \frac{\sqrt{3}(3 - \sin \varphi_c)}{2\sqrt{2} \sin \varphi_c} \quad (2.40)$$

In the above equations, \mathbf{l} is the fourth order identity tensor and $\hat{\sigma} \hat{\sigma}$ is a dyadic product. F is a stress-dependent factor taking into consideration the Matsuoka-Nakai criterion and the Lode angle θ .

$$F = \sqrt{\frac{1}{8} \tan^2 \psi + \frac{2 - \tan^2 \psi}{2 + \sqrt{2} \tan \psi \cos 3\theta}} - \frac{1}{2\sqrt{2}} \tan \psi \quad (2.41)$$

$$\tan \psi = \sqrt{3} \|\hat{\sigma}^*\|, \quad \cos 3\theta = -\sqrt{6} \frac{\text{tr}(\hat{\sigma}^* \cdot \hat{\sigma}^* \cdot \hat{\sigma}^*)}{[\hat{\sigma}^* : \hat{\sigma}^*]^{3/2}} \quad (2.42)$$

The scalar factors f_d , f_e and f_b taking into account the mean stress p and the void ratio e are determined according to

$$f_d = \left(\frac{e - e_d}{e_c - e_d} \right)^\alpha \quad (2.43)$$

$$f_e = \left(\frac{e_c}{e} \right)^\beta \quad (2.44)$$

$$f_b = \frac{h_s}{n} \left(\frac{e_{i0}}{e_{c0}} \right)^\beta \frac{1 + e_i}{e_i} \left(\frac{3p}{h_s} \right)^{1-n} \left[3 + a^2 - a\sqrt{3} \left(\frac{e_{i0} - e_{d0}}{e_{c0} - e_{d0}} \right)^\alpha \right]^{-1} \quad (2.45)$$

As mentioned above, a compression law (Bauer, 1996) is utilized in the hypoplastic model to account for the fact that the void ratios decrease with increasing mean stress.

$$\frac{e_i}{e_{i0}} = \frac{e_c}{e_{c0}} = \frac{e_d}{e_{d0}} = \exp \left[- \left(\frac{3p}{h_s} \right)^n \right] \quad (2.46)$$

Note that the hypoplastic model does not predict accurate responses upon load reversals. The reason for this is that changes in the strain path do not result in an increased hypoplastic stiffness, although this phenomenon has been observed in laboratory experiments. As a consequence – especially for cyclic loading – large strains are accumulated within each cycle, resulting in an unrealistic soft response (Wichtmann, 2005), which is often referred to as ratcheting. To overcome this issue, the concept of intergranular strain (IGS) was introduced by Niemunis and Herle (1997). Memorizing the latest strain history, IGS is a strain tensor that is considered an additional state variable. IGS modifies the hypoplastic model to obtain a larger stiffness upon unloading and strain direction changes. In addition, IGS yields a quasi-elastic response of the model in case of small strain levels. To consider IGS in the hypoplastic model, the definition of the tensor \mathbf{M} (Eq. 2.36) is modified in accordance with

$$\mathbf{M} = [\rho^\chi m_T + (1 - \rho^\chi) m_R] \mathbf{L} + \begin{cases} \rho^\chi (1 - m_T) \mathbf{L} : \overset{\rightarrow}{\mathbf{h}} \overset{\rightarrow}{\mathbf{h}} + \rho^\chi \mathbf{N} \overset{\rightarrow}{\mathbf{h}} & \text{for } \overset{\rightarrow}{\mathbf{h}} : \overset{\rightarrow}{\dot{\boldsymbol{\varepsilon}}} > 0 \\ \rho^\chi (m_R - m_T) \mathbf{L} : \overset{\rightarrow}{\mathbf{h}} \overset{\rightarrow}{\mathbf{h}} & \text{for } \overset{\rightarrow}{\mathbf{h}} : \overset{\rightarrow}{\dot{\boldsymbol{\varepsilon}}} \leq 0 \end{cases} \quad (2.47)$$

where $\overset{\rightarrow}{\mathbf{h}}$ and $\overset{\rightarrow}{\mathbf{h}}$ are the IGS tensor and its direction, respectively, $\rho = \|\overset{\rightarrow}{\mathbf{h}}\|/R$ is the degree of mobilization of intergranular strain with R representing the maximum value of IGS and χ is a constant. In addition, m_T and m_R control the increase in stiffness due to changes in the direction of loading, referring to the case of rotations by $\alpha = 90^\circ$ and $\alpha = 180^\circ$, respectively, with α denoting the angle between the most recent and current strain direction according to

$$\alpha = \arccos \left(\overset{\rightarrow}{\mathbf{h}} : \overset{\rightarrow}{\dot{\boldsymbol{\varepsilon}}} \right) \quad (2.48)$$

The evolution in IGS is defined with respect to $\overset{\rightarrow}{\dot{\boldsymbol{\varepsilon}}}$, $\overset{\rightarrow}{\mathbf{h}}$, R and the exponent β_R via

$$\overset{\rightarrow}{\mathbf{h}} = \begin{cases} \left[1 - \overset{\rightarrow}{\mathbf{h}} \overset{\rightarrow}{\mathbf{h}} \left(\frac{\|\overset{\rightarrow}{\mathbf{h}}\|}{R} \right)^{\beta_R} \right] : \overset{\rightarrow}{\dot{\boldsymbol{\varepsilon}}} & \text{for } \overset{\rightarrow}{\mathbf{h}} : \overset{\rightarrow}{\dot{\boldsymbol{\varepsilon}}} > 0 \\ \overset{\rightarrow}{\dot{\boldsymbol{\varepsilon}}} & \text{for } \overset{\rightarrow}{\mathbf{h}} : \overset{\rightarrow}{\dot{\boldsymbol{\varepsilon}}} \leq 0 \end{cases} \quad (2.49)$$

Note that the initialization of IGS (e.g. $\mathbf{h}_0 = \pm R \mathbf{1}$ or $\mathbf{h}_0 = \mathbf{0}$) may have a significant impact on the response of the hypoplastic model (Buehler, 2006). This impact on the

integration point level can also propagate to the entire boundary value problem, resulting in different predictions (e.g. bearing capacity or slope stability) with regard to the choice of \mathbf{h}_0 . Therefore, the history of the soil (e.g. deposition, compaction, excavation, etc.) should be considered carefully.

Estimation of equivalent elastic properties

To enable shear waves traveling through a transition from a linear elastic to a hypoplastic material without notable changes in the velocities, it is important to minimize differences in the shear stiffness between the elastic layer and the hypoplastic layer. Wegener and Herle (2012) proposed a concept to determine the shear modulus of the hypoplastic model with intergranular strain. The shear modulus at small strains G_0 (so within the range of the IGS extension) of the Hypo+IGS model can be approximated based on Eq. 2.50, where p is the mean effective stress, and m_R , h_s , n , e_{c0} and β are parameters of the hypoplastic model and the factors f_a and f_K are calculated according to Eq. 2.51 and Eq. 2.52, respectively.

$$G_0 = m_R \frac{h_s}{n} \left(\frac{3p}{h_s} \right)^{1-n} \left(\frac{e_{c0}}{e} \right)^\beta \cdot f_a \cdot f_K \quad (2.50)$$

$$f_a = \left(\frac{e_{i0}}{e_{c0}} \right)^\beta \frac{1 + e_{i0}}{e_{i0}} \left[3 + a^2 - a\sqrt{3} \left(\frac{e_{i0} - e_{d0}}{e_{c0} - e_{d0}} \right)^\alpha \right]^{-1} \quad (2.51)$$

$$f_K = \frac{1}{2} \frac{(1 + 2K)^2 + a^2(1 - K)}{1 + 2K^2} \quad \text{with} \quad K = \frac{\sigma_2}{\sigma_1} \quad \text{and} \quad a = \frac{\sqrt{3}(3 - \sin \varphi_c)}{2\sqrt{2} \sin \varphi_c} \quad (2.52)$$

Note that above equations only hold if $p \ll h_s$ since then $e_d \approx e_{d0}$, $e_c \approx e_{c0}$ and $e_i \approx e_{i0}$. Otherwise, the dependency of the void ratio $e_c(p)$ on the mean effective stress must be taken into account. For a given soil state, the shear modulus can be calculated with and without consideration of the influence of the mean effective stress on the void ratios according to Bauer (1996). Furthermore, it should be noted that by setting $m_R = 1$, the calculated G_0 corresponds to the shear modulus of the (purely) hypoplastic model.

3. Implementation of limit equilibrium method

3.1. Motivation

A widely used method to evaluate the stability of slopes subjected to earthquake loading in terms of a factor of safety is the pseudo-static analysis (PSA), which has been introduced in Section 2.2.1. As reported, drawbacks of the PSA include that temporal and spatial variations due to the earthquake loading can not be considered directly, but indirectly in terms of pseudo-static coefficients and inertial forces, which can only be estimated in an approximate manner. Considering measurements of peak ground accelerations and applying concepts for reduction of the acceleration magnitudes with increasing depth, as proposed for instance by Seed and Idriss (1971), Liao and Whitman (1986), Youd and Idriss (2001) or Kishida et al. (2009), a rough approximation of a potential spatial distribution of accelerations can be made. Utilizing further approaches, for example by Biondi et al. (2002), estimation of earthquake induced excess pore water pressures can also be included. Those are of high importance as the effective stresses may change during earthquake loading, which can cause significant loss of shear strength and slope failure. In this thesis, an approach is developed where prior to the limit equilibrium analyses, a dynamic finite element simulation is conducted to accurately approximate the effect of the earthquake loading. Subsequently, the spatial distributions of pseudo-static coefficients obtained from accelerations and the excess pore water pressures should be transferred to the limit equilibrium analyses to evaluate the slope stability in terms of the factor of safety.

Despite the availability of many well-established commercial LEM softwares (e.g. GGU-Stability (2021), GeoStudio (2020), Slide2 (2022) and GEO5 Slope Stability (2020)) for slope stability analyses, it is rather difficult to find an LEM code which satisfies the requirements described above, allows for users-implemented features and enables automation of simulations using external scripts (e.g. Matlab, Python, etc.). Therefore, a new

limit equilibrium program called `geoSlice` is developed in this thesis. `geoSlice` is based on the method of slices and implemented in Python.

Among others, popular features and methods implemented in `geoSlice` cover different limit equilibrium methods (e.g. Bishop, Janbu, etc.), advanced optimization techniques, different types of external loads, precise separation of slices at intersections of the slip surface with soil layers and phreatic levels, import of spatial distributions of pseudo-static coefficients and user excess pore water pressures and impenetrable layers. A schematic illustration of a slope subjected to seismic loading and corresponding forces acting in a representative slice are depicted in Fig. 3.1. It is apparent from this figure that pseudo-static forces and excess pore water pressures are applied to account for the seismic loading, however, to also consider long water waves at the free water surface, additional forces ΔW are considered (Goldscheider et al., 2010). Further details about the general structure of `geoSlice and the implemented features are provided in Section 3.2 and Section 3.3, respectively, whereas a comprehensive verification of different implemented features based on comparative analyses with commercial LEM codes and benchmark examples is provided in Section 3.4.`

3.2. General structure

The main structure of the program covers tasks, which will be further explained in the subsequent paragraphs: (1) data input, (2) initialization, (3) generation of circular slip surface, (4) determination of slice forces, (5) evaluation of factor of safety, (6) optimization of circular slip surface, (7) generation and optimization of non-circular slip surface and (8) post-processing. It should be noted that the tasks (3 - 5) are executed within the

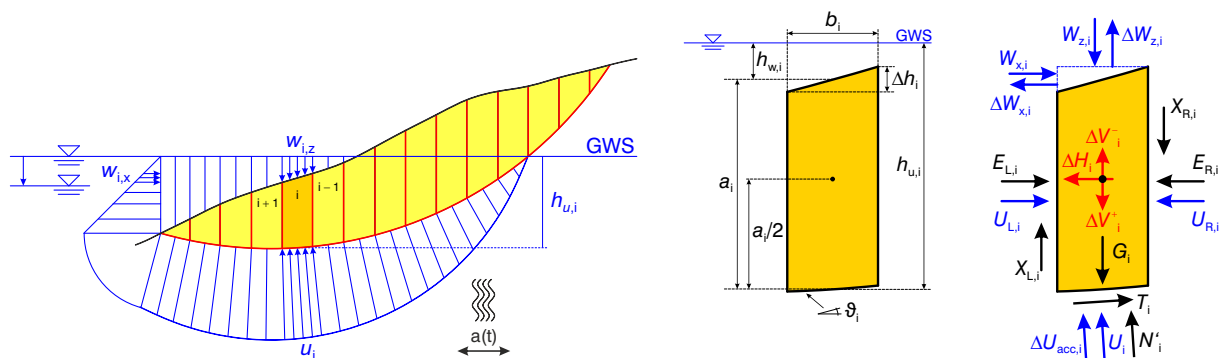


Figure 3.1: Schematic illustration of a slope subjected to seismic loading and corresponding forces acting in a representative slice

optimization process (6), while the optimization process for a non-circular slip surface is characterized by some modifications.

Data input: The program starts by reading an input file, which should contain all information about problem geometry, soil layers, material properties, phreatic levels, etc. These blocks of data need to be defined in terms of keywords followed by the respective information. The input file needs to be written in **YAML** format considering the general rules for formatting **YAML** files, where the latter can be verified using open access online tools (e.g. [Onlineyamltools \(2022\)](#)). Editing of input files can be done using basic text editors such as Notepad++ or SublimeText. The keywords are used to define the main features (e.g. geometry, soil layers, phreatic level), the shape and location of the slip surface, the method of analysis, the optimization technique and additional features. Further information about the keywords and the respective features are discussed in the subsequent paragraphs and in Appendix A. Input files of examples analyzed with **geoSlice** with regard to the verification process are provided in the next section. Once all information is read by the input routine and checks of a correct definition of input statements have been finished, databases are created for all active features to be considered in the slope stability analysis.

Initialization: After the input fields have been read and the data class has been created, initialization of the core element (main class) is conducted, which covers all information with regard to the individual slices such as geometry variables and forces related to different influencing parameters (e.g. unit weight, pore water pressure, external loads, inertial effects). Moreover, entry and exit point boundaries are defined with regard to the actual slope geometry. Lastly, initialization of advanced features is executed for those features which are activated in the current analysis. However, this only applies to features, which are independent of the location of the slip surface and the subdivision into slices. In case of the features dealing with spatial distributions of pseudo-static coefficients and excess pore water pressures, interpolation functions are trained at this stage to allow for a fast evaluation of the spatially distributed data during the stability analysis. In case the geogrid feature is used, the location and strength of the individual geotextiles is defined. Moreover, the stone column feature can be considered within the initialization following the averaging approach for shear strength parameters proposed by [Priebe \(1995\)](#).

Generation of circular slip surface: For the generation of slip surfaces, the entry-exit method (see e.g. [GeoStudio \(2020\)](#)) is used in **geoSlice**. In its current implementation, three values are required to create the slip circle – the entry point, the exit point and

the ratio of the sagitta to the distance between entry and exit point, where the latter is related to the radius of the circle and, thereby, the curvature of the slip circle. From these three input values and using basic math manipulation, the center point coordinates and the radius of the circle are obtained. Here, it may be questioned, why the latter variables (i.e. circle center coordinates and radius) have not been used for the definition of the slip circle, however, the entry-exit method was chosen as it allows for a more precise definition of the slip surfaces investigated. Considering the number of slices defined in the input file, assuming equivalent widths of the slices (at this point) and rearranging the circle equation, the coordinates of the slice bases are determined. Although the generation of the slip surface could be finished after these steps, two features may, if activated, interfere with the surface, leading to modifications of the slip surface shape. The first feature to mention here is the bedrock or impenetrable layer feature, which generates a composite slip surface defined by a regular slip circle, which is cut at the intersection with the bedrock layer (see e.g. the schematic illustration in Fig. 2.3(c)). Using this feature, composite slip surfaces can be investigated for instance to analyze the slope stability with a slip surface following a thin weak interlayer. The second feature – referred to as *EnhancedSlices* – does not change the shape of the slip surface but rather the number of slices as additional slices are introduced at every intersection of the slip surface with layer changes, the phreatic level and (if active) the bedrock/impenetrable layer. By activation of this feature, a clear definition of shear strength parameters in the vicinity of layer changes and a precise determination of water pressures is ensured for each slice. After consideration of all features influencing the shape of the slip surface and the number of slices, shear parameters are determined at the slice bases. Furthermore, it should be noted that taking into consideration further control features, for instance related to the minimum size or height of the slip surface, classification of slip surfaces as *invalid* may dismiss further analyses of the respective surfaces.

Determination of slice forces: For each type of force to be considered in the analysis, a separate array with the size of the number of slices is initialized, where the components related to the individual slices are determined simultaneously taking advantage of NumPy array operations. These operations are utilized as computational costs are significantly smaller compared to consecutive evaluation of slice forces using loop structures. Forces to be evaluated for the slope stability analysis include forces due to soil unit weights, hydrostatic water pressure, free surface water, concentrated and distributed external loads, inertial effects, excess pore water pressure, geogrids and cohesion, while forces due to friction are evaluated separately due to their dependency on the normal effective stress. With regard to the forces listed above, some details are emphasized

here as they may differ from common procedures. In contrast to many commercial LEM codes, `geoSlice` allows for a distinction between unsaturated and saturated unit weights, which enables a more accurate determination of slice weights. Moreover, resulting forces from hydrostatic water pressures are accounted for with regard to two different inputs: a phreatic level (e.g. groundwater table) defined via a poly-line and a pore-pressure ratio relating the hydrostatic water pressure to the total stress at the slice base. Similar to other LEM schemes, inertial forces are calculated using the total soil weight and pseudo-static coefficients. However, in this implementation of the method of slices it is possible to either consider a constant pseudo-static coefficient for the whole domain or spatially distributed pseudo-static coefficients defined via user inputs. The latter procedure is also utilized to account for forces resulting from spatially distributed excess pore water pressures. Thereby, it is possible to conduct slope stability analysis taking into consideration spatially distributed pseudo-static coefficients and excess pore water pressures obtained from a dynamic finite element analysis.

Evaluation of factor of safety (FoS): Depending on the stability method chosen, the factor of safety is evaluated with respect to the global equilibrium of momentum and/or the global equilibrium of horizontal forces defined in their basic forms in Eq. 2.3 and Eq. 2.4, respectively. Currently, the following methods are implemented in `geoSlice`: Simplified and General Bishop method, Simplified Janbu method, Spencer method and Morgenstern & Price method (Bishop, 1955; Janbu, 1954; Spencer, 1967; Morgenstern and Price, 1965). Further methods to be implemented soon include the General Janbu method as well as the Sarma method (Sarma, 1973). To obtain the factor of safety (FoS) with respect to either the global equilibrium of momentum or horizontal forces, a single loop structure is used, during which the FoS is continuously updated until the difference of the FoS at the beginning and end of an iteration is smaller than a tolerance value. Considering methods that satisfy both types of equilibrium (e.g. Spencer method and Morgenstern & Price method) a second loop is used to vary the interslice force parameter λ until the intersection of the equilibrium of momentum and horizontal forces is found.

Optimization: Considering a set of input parameters $x_1, x_2, \dots, x_i, \dots, x_n$ with given ranges and a scalar (objective) function of these parameters $\mathcal{F}(x_1, x_2, \dots, x_i, \dots, x_n)$ to be optimized, the idea is to find the best combination of input parameters that yields the optimal result for \mathcal{F} (e.g. the lowest/highest value). In this case, the objective function is defined with regard to the FoS and the optimal solution is characterized as the set of input parameters that relates to the slip surface with the lowest FoS. The input parameters to be varied within the optimization process are the geometrical parameters (entry-, exit-points

and the sagitta ratio) that define the shape of the slip surface. The objective function takes the information provided by the main and data classes, generates a slip surface for a given set of input parameters, determines the forces in the slices, evaluates the FoS and returns it thereafter. However, as the optimal combination of input parameters can hardly be found by manual manipulation, automated optimization techniques should be used. In general, an optimization algorithm selects a set of input parameters considering lower and upper bounds for each parameter, evaluates the objective function for this set and saves the output returned by the objective function, before repeating the process with the next set of input parameters. In its simplest form (e.g. a brute grid search), a predefined number of sets is evaluated and the optimal result is obtained by comparison of all individual results, not considering any type of learning within the optimization process. In contrast to this simple concept, advanced optimization algorithms consider different types of learning techniques within the optimization process to enhance the quality of the optimization result. In `geoSlice`, locating the critical slip surface can be conducted via different optimization schemes taking advantage of open-source implementations provided within the `scipy` and `pyswarm` libraries. Among others, a brute grid search, Differential Evolution (DE) (Storn and Price, 1997) and Particle Swarm Optimization (PSO) (Clerc, 2013) can be used in the stability analysis. Based on the experience gained from the analysis of many examples testing different optimization schemes to find the most reliable methods, it is recommended to apply either brute grid search or DE rather than PSO, as the latter showed larger scatter for repeated optimization runs.

Generation and optimization of non-circular slip surfaces: As real case slip surfaces do not necessarily follow circular shapes, results of LEM analyses based on slip circles may overestimate the FoS. For this reason a topological optimization can be conducted subsequently to the slip circle optimization to identify the most critical non-circular slip surface. Further details about the topological optimization are provided in the next section as well as in the discussions of the benchmark examples in Section 3.4.4.

Post-processing: After the optimization, the set of optimal input parameters is returned to the main routine and a single stability run with this optimal set is conducted to obtain detailed information (e.g. geometry and forces) with respect to each slice associated with the critical slip surface. For a thorough analysis of the results, detailed information (e.g. coordinates, radii, weights, external and inertial forces, forces due to water pressures, effective normal forces, interslice forces) for each slice are saved to a file. Moreover, a graphical output is generated emphasizing the problem investigated and the optimal solution defined in terms of the coordinates and the radius of the critical slip

circle and the graphical representation of it. To enhance comprehensibility, handling and work flow of `geoSlice`, it is intended to soon incorporate the pre- and post-processing into the main routine by creating a graphical user interface, which should also enable to create proper input files.

3.3. Keywords and features

In this section, a more thorough description of the keywords and associated features is provided. To do so, an input file of a slope studied within the verification section (Fig. 3.8) is explained in detail. The slope geometry and soil materials have been chosen as $\beta = 26.67^\circ$, $H = 10$ m, $h = 5$ m, $\gamma = \gamma_{\text{sat}} = 20$ kN/m³, $\varphi = 25^\circ$ and $c = 4$ kPa, where β , H and h denote the slope inclination, the slope height and the height of the groundwater table above the slope toe, respectively. The distances from the slope toe to the left and bottom boundaries are both equal to 10 m and the distance from the slope crest to the right boundary is 20 m. The origin of the coordinate system is identical to the toe of the slope.

For more clarity, distinction is made here between the format used for the keywords and corresponding entries in the input file and the general explanations by emphasis of the former with gray background color. Moreover, it should be noted that the `#` symbol in the input file is used for comments in the YAML format, where lines starting with this symbol are only included to enhance comprehensibility of the input file. In addition, the reader should be aware that all counters used to define dependencies (e.g. layer nodes, layer materials) start with the index zero, thus, for instance referring to the third material is conducted using a counter with a value of two.

Nodes, **GwtNodes**: Several geometrical features (e.g. layers, phreatic level, bedrock feature) require the specification of poly-lines, which are defined via sets of nodes. These poly-lines should extend from the left to the right outside boundaries to ensure that the geometrical features work properly. For the definition of nodes, x- and y-coordinates need to be provided for each node along the ground surface and any layer boundary. The nodes related to the bottom of the model do not need to be defined as a separate keyword (*Depth*) is used to define the distance towards the bottom boundary. Moreover, the group of nodes does not necessarily need to be sorted as long as the respective features (e.g. the layer definition) refer to the correct order of nodes. As indicated by the keyword names, distinction is made between **Nodes** and **GwtNodes**, where the former is used to

define layers and bedrocks and the latter is used to define the ground water table. For the example slope, the groups of nodes and ground water nodes are defined as:

<pre># Nodes: [x, y] Nodes: - [-10, 0] # Node No. 0 - [0, 0] # Node No. 1 - [20, 10] # Node No. 2 - [40, 10] # Node No. 3</pre>	<pre># Ground Water Nodes: [x, y] GwtNodes: - [-10, 0] # GwtNode No. 0 - [0, 0] # GwtNode No. 1 - [20, 5] # GwtNode No. 2 - [40, 5] # GwtNode No. 3</pre>
--	--

Materials, Layers, Depth: For each material set, the unit weight of the unsaturated and saturated soil γ and γ_{sat} , the friction angle φ , the cohesion c and the name need to be selected. Multiple material datasets are defined in separate lines following the same format as depicted in the gray box below. With known nodes and materials, layers can be created by definition of the upper layer boundary, which also corresponds to the ground surface in case of the first layer. Using the *Layer* keyword, two subsequent lines need to be defined for each layer: the first line denotes the material type of the layer and the second line refers to the nodes. As the layer material type and the layer nodes must be defined in subsequent lines, multiple layers are specified as 'layer packages'. In case material datasets are not referred to in any layer (e.g. unused material datasets), these material datasets are skipped in the analysis and will not appear in the graphical output. To finalize the definition of the layers, the height of the lowest layer is specified using the *Depth* feature, which denotes the distance between the model base and the lowest layer node used.

<pre># Materials: # [γ, γ_{sat}, φ, c, name] Materials: - [20, 20, 25, 4, Soil] # Material No. 0</pre>	<pre># Layers: # 1st line: MaterialType of layer i # 2nd line: [Node numbers of layer i] Layers: - - 0 # MaterialType of layer No. 0 - [0, 1, 2, 3] # Nodes of layer No. 0</pre>
<pre># Depth below the lowest layer Depth: 10</pre>	

Groundwater, PWPratio: Hydrostatic water pressures can be defined with regard to two different features. The *Groundwater* feature representing the phreatic level inside and outside of the slope is specified via selection of GwtNodes. Using this feature, the hydrostatic pressures are calculated based on the hydrostatic water height, neglecting tensile (suction) stresses above the water head. Regarding the selection of the GwtNodes, a proper order of the nodes (continuously increasing/decreasing x-values) needs to be ensured. In contrast to the determination of the hydrostatic water pressures with regard

to a water level, the pore water pressure ratio (*PWPratio*) allows to determine pore water pressures with regard to the total vertical stress via $u = r_u \cdot \gamma \cdot H$ (Bishop, 1955; Bishop and Morgenstern, 1960), assuming that the pore water pressure ratio is constant throughout the domain. Considering analyses with `geoSlice`, it should be noted that only one feature for pore water pressure determination can be active. In case both features are defined and $r_u = 0.0$, *Groundwater* feature will be active, whereas if $r_u > 0.0$, the *PWPratio* feature will be active and the *Groundwater* feature is neglected. For the current example, the features are selected as depicted in the gray boxes below.

```
# Ground water table: [GwtNode numbers]
```

```
Groundwater: [0, 1, 2, 3]
```

```
# Pore pressure ratio ( $r_u$ )
```

```
PWPratio: 0.0
```

`EntryExit`, `NumSlices`, etc.: To control the area, in which the most critical slip surface is searched for, the input parameter ranges for the optimization process need to be defined. As mentioned in the previous section, the slip surface is created using the Entry-Exit method utilizing three input parameters: the entry point, the exit point and the sagitta ratio, where the latter is defined as the ratio of the sagitta s to the distance between the entry- and exit point (see Fig. 3.2). The ranges for the former two input parameters are specified using the *EntryExit* keyword, where four values (i.e. x -coordinates) are inserted, describing the spans of both input parameters in x -direction. For the example studied within this section, ranges of $[-5, 0]$ and $[15, 30]$ are defined, as shown in the gray box below. Moreover, to control the curvature of the slip circles investigated, the *hRatio* keyword is used, where values in the range $(0.0 : 0.5]$ can be specified, noting that values of 0.0 and 0.5 represent circles with radii $R \Rightarrow \infty$ and $R = s$, respectively. To further control the size of the slip surface, for instance to avoid analysis of too shallow slip surfaces, two additional keywords can be used, which limit the minimum width and height of the slip surface. The *MinWidth* feature ensures a minimum horizontal distance between the entry and exit points, whereas the *MinHeight* feature provides a lower limit for the absolute value of the sagitta of the slip surface. It should be noted that the latter

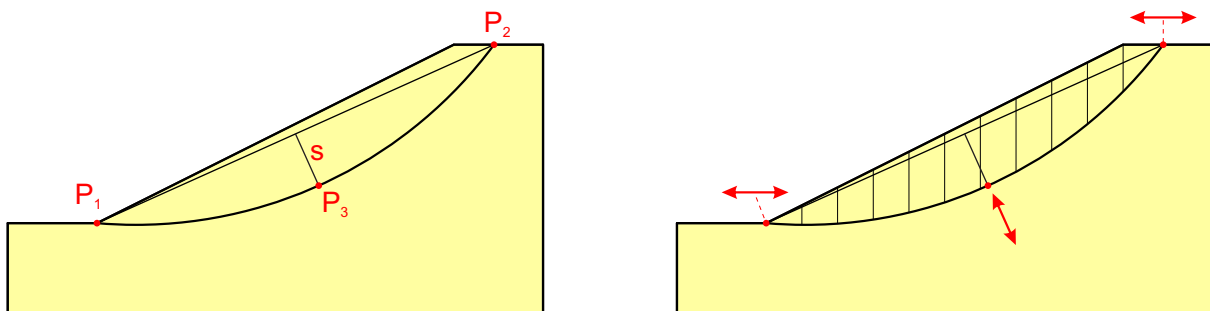


Figure 3.2: Generation of a slip surface via Entry-Exit method

feature could also be implemented in a way that the height of the largest slice must not be smaller than the *MinHeight*. However, this requires many additional computations before an invalid slip surface is neglected. For the example studied here, the values of *MinWidth* and *MinHeight* have been selected close to zero as these additional control features were not actively used. To divide the slip surface into vertical slices, the number of slices needs to be defined. Moreover, the *EnhancedSlices* feature enables consideration of additional slices at intersections with layer boundaries, ground water levels or bedrock layers. The idea of this feature is that each slice is sub-divided to more accurately locate these intersections. For each intersection found, an additional slice is added to the group of slices. Although in this example only a single layer is investigated, the *EnhancedSlices* feature is used to better locate the intersection of the slip surface and the ground water table.

```
# Entry-exit spans in x-direction
```

```
# Input: [4 x-values]
```

```
EntryExit: [-5, 0, 15, 30]
```

```
# Minimum width of slip surface
```

```
MinWidth: 0.001
```

```
# Minimum height of slip surface
```

```
MinHeight: 0.001
```

```
# Curvature of slip surface
```

```
hRatio: [0.01, 0.5]
```

```
# Number of Slices
```

```
NumSlices: 100
```

```
# Determination of slices
```

```
# (0: Normal, 1: Enhanced)
```

```
EnhancedSlices: 1
```

Method, LambdaSlice, Tolerance: As the evaluation of the factor of safety depends on the method used within the slope stability analysis, the *Method* keyword is used to select between four different methods: Bishop, Janbu, Spencer and Morgenstern & Price. In case the Bishop or Janbu method is selected, further specification is possible using the *LambdaSlice* keyword, which enables specifying the rotation of the interslice forces according to the parameter λ , where $\lambda = 0.0$ yields the simplified Bishop method and simplified Janbu method. Lastly, the *Tolerance* feature can be specified, which denotes the tolerance value within the FoS iteration loop. Although DIN-4084 (2021) recommends a tolerance of 3% for the determination of the utilization factor (i.e. $\mu = 1/\text{FoS}$), default tolerance values used in commercial LEM codes are usually much smaller, e.g. 0.1% as indicated below.

```
# Method of analysis
```

```
# (0: Bishop, 1: Janbu)
```

```
# (2: Spencer)
```

```
# (3: Morgenstern & Price)
```

```
Method: 0
```

```
# Interslice force rotation
```

```
# (e.g. for rigorous Bishop method)
```

```
LambdaSlice: 0.0
```

```
# Tolerance for determination of FoS
```

```
Tolerance: 0.001
```

Optimization: As the objective and general structure of the optimization within slope stability analyses has already been explained in the previous section, only a few details are added in this paragraph. The keyword *Optimization* is used in combination with an abbreviation referring to one of the different optimization algorithms presented above (e.g. Brute, DE, PSO). The settings of the different optimization algorithms can – up to this point – only be changed in the Python code and not via the input. However, it is planned to also enable more flexibility with regard to the optimization settings of all algorithms as soon as the preprocessing is coupled with a graphical user interface. As can be seen from the gray box below, in this example Differential Evolution optimization algorithm is utilized.

```
# Optimization algorithm
# (Brute: Brute Grid Search)
# (DE: Differential Evolution)
# (PSO: Particle Swarm Optimization)
Optimization: DE
```

Additional features: Although not used in this example, further keywords and corresponding features are explained in the following paragraphs. To clarify the required format of the inputs related to these features, artificial values have been inserted.

Bedrock, DeltaHw: To insert an impenetrable layer, the *Bedrock* keyword is used, where the consecutive input is a list of node numbers. For this, it is to be ensured that the nodes are defined using the respective keyword. In contrast to the definition of layers, the bedrock feature does not require to start and extend up to outer horizontal boundaries as it is extended horizontally to the outer boundaries. To consider rapid changes of the free water level associated with long water waves generated by seismic loading, while the pore water pressures inside the soil domain remain unchanged (Goldscheider et al., 2010), the *DeltaHw* keyword is used, which requires the definition of the change in the water level height of the free water surface.

```
# Bedrock layer [node numbers]
Bedrock: [13, 14]
```

```
# Free water level change  $\Delta h_w$ 
DeltaHw: 0.0
```

Cload, Dload: External loads (concentrated or distributed) acting in vertical ('V'), horizontal ('H') direction or perpendicular ('P') to the ground surface can be considered. The former two are related to the global coordinate system (i.e. positive to the right and top), whereas the latter ('P') considers compressive forces positive. Inclined loads can be obtained by a combination of vertical and horizontal loads. All loads are assumed to act permanently, thus, there is yet no possibility to automatically check if transient loads

should be considered or not as they might act in a favorable direction. Assuming that all loads are applied to the ground surface, the general format to specify concentrated and distributed loads requires the definition of the horizontal positions x_i and corresponding loads q_i .

```
# Concentrated loads:
```

```
# [x, Q, 'V/H/P']
```

```
Cload:
```

```
- [30, -25, 'V']
```

```
# Distributed loads:
```

```
# [x_start, x_end, q_start, q_end, 'V/H/P']
```

```
Dload:
```

```
- [22, 26, -10, -12, 'V']
```

PseudoStatic, **ExcessPWP**: As emphasized in the beginning of this chapter, one of the main reasons for the implementation of an extended limit equilibrium method is the capability to perform slope stability analyses taking into account spatial distributions of pseudo-static coefficients k_h and k_v and excess pore water pressures obtained from dynamic finite element simulations. For this, a structure had to be implemented, which would allow to import user data. Moreover, an interpolation strategy had to be defined, which ensures a transformation of the scattered data to a spatial distribution, where evaluation of pseudo-static coefficients or excess pore water pressure is enabled anywhere within the limits of the scattered data. In **geoSlice**, interpolation of k_h , k_v and Δp^w is performed using the **LinearNDInterpolator** from **scipy**. The user-data itself should be provided as a text file containing column-sorted table data with the first two columns representing x- and y-coordinates and the subsequent column(s) denoting pseudo-static coefficients or the excess pore water pressure. The format to be used for the import of user data is identical for *PseudoStatic* and *ExcessPWP* and is depicted in the gray box denoting the excess pore water pressure feature.

```
# Pseudo-static coefficients:
```

```
# format 1: Constant, [ $k_h$ ,  $k_v$ ]
```

```
# format 2: User, Path to file
```

```
PseudoStatic:
```

```
- Constant
```

```
- [0.1, 0]
```

```
# Excess pore water pressure:
```

```
# format 1: User, Path to file
```

```
ExcessPWP:
```

```
- User
```

```
- user_excess_pwp.txt
```

Beside considering the spatial distribution of these variables, a second option is available with regard to pseudo-static coefficients, as for other applications it may also be of interest to prescribe constant pseudo-static coefficients throughout the domain. A format is provided to analyze the stability of a slope based on constant k_h and k_v values. In general, it should be noted that horizontal pseudo-static coefficients are always considered pointing towards the slope toe, while for each slip surface investigated vertical pseudo-static

coefficients are varied in their direction (upwards, downwards) to find the less favorable scenario. Therefore, no manual checks with regard to the direction of the vertical pseudo-static coefficients and the corresponding factors of safety need to be conducted.

StoneColumn: To include subsoil improvement using granular columns installed via vibro replacement in stability analyses, a common approach is the consideration of an improved area with modified soil properties (shear strength parameters) according to Priebe (1995). For the implementation of this approach in `geoSlice`, an analytical solution has been derived using `Mathematica`, which – in contrast to the equations given in (Priebe, 1995) – enables variable inputs of the Poisson’s ratio of the soil ν_{soil} . Information to be specified in the input file with regard to this approach include the number of the soil material, which is improved by the column installation, and its Poisson’s ratio, the shear strength (φ_{col}) and relative stiffness of the column material $E_{\text{col}}/E_{\text{soil}}$ and the geometrical setup in terms of the area ratio A_{col}/A . For practical use, it should be noted that no additional material is created when using the *StoneColumn* feature, but an existing material set is updated. Thus, in case multiple layers refer to one material but only a single one is improved, the original material set needs to be inserted twice.

```
# Stone Columns (Priebe approach) [Mat-No,  $\nu_{\text{soil}}$ ,  $\varphi_{\text{col}}$ ,  $E_{\text{col}}/E_{\text{soil}}$ ,  $A_{\text{col}}/A$ ]
StoneColumn:
- [2, 0.3, 40, 20, 0.115]
```

Geogrid: To account for geosynthetics in slope stability analyses, the *Geogrid* feature can be used, which has been implemented in `geoSlice` in a slightly simplified way. The simplifications refer to the orientation of the geogrid and the determination of the vertical stresses acting on the geogrid, where the former is restricted to a perfectly horizontal orientation and the latter is calculated with regard to an average soil unit weight γ defined in the input file. To specify the position and length of the geogrid, the coordinates of the left and right end need to be specified (x_1 , x_2 , y). The tensile force of the geogrid is determined based on the pull-out resistance of the geogrid, which is calculated from the relevant anchorage length, the overburden pressure and the frictional resistance defined by $\mu \cdot \tan \varphi$. To limit the tensile force, the pull-out resistance can not be larger than the allowable material resistance $R_{\text{b,k}}$.

```
# Geogrids: [ $x_1$ ,  $x_2$ ,  $y$ ,  $\gamma$ ,  $\varphi$ ,  $\mu$ ,  $R_{\text{b,k}}$ ]
Geogrid:
- [2, 17, 5.5, 19, 32.5, 0.9, 50]
```

```
# TensionCrack:  $z_0$ 
TensionCrack: 0.63
```

Considering the global momentum of horizontal forces, the sum of the tensile forces of all geogrids is considered as additional resisting force. In case of the global equilibrium of

momentum, the sum of the products of the individual tensile forces and respective lever arms is added to the resisting moments.

TensionCrack: In case tensile stresses exceed the tensile strength of a material, a crack opens up and, depending on the position of this crack, its presence may have a large impact on the stability of a slope. This can be explained with regard to the fact that shear stresses can not be transferred across tension cracks, which reduces the overall shear resistance along a potential slip surface. The maximum length of tension cracks z_0 can be estimated based on Eq. 3.1 according to (Spencer, 1968, 1973; Baker, 1981; DIN-4084, 2021). An alternative strategy to account for tension cracks does not explicitly define the maximum length, but rather sets a limit to the slice base angle (see e.g. GeoStudio (2020)) and neglects slices inclined at higher angles than the slope of the active earth pressure wedge ($45^\circ + \varphi/2$).

$$z_0 = \frac{2c}{\gamma} \tan\left(45^\circ + \frac{\varphi}{2}\right) \quad (3.1)$$

In `geoSlice`, tension cracks can be accounted for using the respective feature, which allows for a more precise determination of the factor of safety for steep cohesive slopes. For this, the maximum length of the tension crack needs to be specified, for instance based on Eq. 3.1. Furthermore, as it is not ensured that the largest tension crack is associated with the lowest FoS, the length of the actual tension crack z_{tc} is considered as an additional input parameter in the optimization process with limits of $0 \leq z_{tc} \leq z_0$. Although not considered in the example discussed above, using the input parameters and Eq. 3.1, a maximum tension crack length of $z_0 = 0.63$ m is obtained. Note that water pressures in tension cracks as a result of tension cracks filled with water are considered in accordance with the global water level.

TopologicalOptimization: To investigate whether the critical slip surface might be of a non-circular shape, a topological optimization can be conducted subsequently to the optimization of the analyses based on circular slip surfaces. To do so, the keyword should be used in the input file together with the required inputs. Motivated by the strategy conducted in GeoStudio (2020), the slip surface is defined by a predefined number of nodes (n_0), which are optimized consecutively, considering hulls limiting possible locations of the nodes and an angle of concavity (α_{concave}), which can be set to zero to ensure analysis of convex slip surfaces only. The possible locations of the interior nodes (n^i) are sampled using Latin-Hypercube sampling (LHS), which ensures a proper distribution of the samples in the input parameter space. Surface nodes at the entry and the exit areas of the slip surface are only varied along the ground surface (n^s). For each combination

of nodes, the slip surface is defined as follows: connecting the points via straight lines or cubic splines (χ_{interp}) and knowing the number of slices to be used in the stability analysis, the actual subdivision into slices is conducted via interpolation. As soon as no further changes of the critical slip surface are observed (ε_{tol} related to FoS) for a constant number of nodes (n_0) used for the interpolation of the slices on consecutive optimizations of the complete slip surface, the number of nodes is increased by adding nodes at the positions with largest distances to the other nodes until the final number of nodes is reached (n_{final}). Thereby, the shape of the non-circular slip surface is refined in steps, creating a well defined poly-line. Additional inputs of the topological optimization are ϑ_a and ϑ_p , which specify the maximum (absolute) inclinations of the slices at the active and passive wedges. These angles can for instance be calculated based on Rankine's theory by $45^\circ \pm \varphi/2$. However, it should be noted that slices of critical slip surfaces may also be inclined steeper than these angles, for example in case of slopes with weak layers as discussed in Section 3.4.4.

```
# Topological Optimization: [n0, nfinal, ns, ni, χinterp, αconcave, ϑa, ϑp, εtol]  
TopologicalOptimization: [8, 20, 30, 80, 0, 0, 60, 30, 0.001]
```

Although not used in the example described above, the inputs of the topological optimization depicted in the gray box result in the following settings: the discretization of the slip surface is started with 8 nodes (2 surface and 6 interior nodes), which are increased up to 20 nodes during the optimization process as soon as the critical FoS after two consecutive optimization runs does not change by more than $\varepsilon_{\text{tol}} = 0.001$. In each iteration 30 variations of each surface node and 80 variations of each interior node are investigated. The nodes are connected via straight lines ($\chi_{\text{interp}} = 0$) and only fully convex slip surfaces are accepted ($\alpha_{\text{concave}} = 0^\circ$).

3.4. Verification

Verification of the methods and features implemented in `geoSlice` is performed in terms of comparative analyses for different examples. As a first step, homogeneous dry slopes with varying geometries and soil shear strength parameters are investigated using different methods of slices in Section 3.4.1. Subsequently, verification of the determination of pore water pressures and pseudo-static coefficients is conducted in Sections 3.4.2 and 3.4.3, respectively. Results of analyses are presented in terms of design charts, including results obtained using well-established commercial LEM codes, `GGU-Stability` (GGU-Stability, 2021) and `SLOPE/W (GeoStudio)` (GeoStudio, 2020) for comparison. Lastly, in

Section 3.4.4, results of benchmark examples covering layered soil strata, weak layers and pore water pressure ratios investigated with `geoSlice` are compared to results reported in different studies.

3.4.1. Implemented methods

As a first step of the verification process, a comprehensive parametric study is conducted for shallow to steep slopes ($10^\circ \leq \beta \leq 80^\circ$) under dry conditions considering circular slip surfaces, variations of the shear parameters (φ, c) and different methods of slices (i.e. simplified Bishop method, simplified Janbu method, Morgenstern & Price method). The objective of this step is to verify if the core structure of the program `geoSlice` has been implemented correctly. This includes the generation of circular slip surfaces, the determination of forces due to unit weight and shear resistance, the evaluation of the factor of safety with regard to the global equilibrium of momentum or/and horizontal forces and the optimization routines. For a condensed representation, results of the parametric study with regard to each method are evaluated independently in terms of normalized stability charts as used for instance by Hoek and Bray (1981), Gußmann (1990) and Steward et al. (2011).

For the parametric analyses conducted in this section, ranges of normalized shear parameters are selected as $0 \leq c/(\gamma H \text{ FoS}) \leq 0.25$ and $0 \leq \tan \varphi/\text{FoS} \leq 2.0$, where γ , H and FoS are the soil unit weight, the slope height and the factor of safety. Assuming an input factor of safety (e.g. $\text{FoS} = 1.0$) and constant values of β and $c/(\gamma H \text{ FoS})$, a single result point of this chart is obtained by variation of the friction angle until the input and output factors of safety are identical. To obtain the design curves, which are plotted without any smoothing or fitting, analyses have been performed for step sizes of $\Delta c/(\gamma H \text{ FoS}) = 0.0025$ and $\Delta c/(\gamma H \text{ FoS}) = 0.005$ for $0 \leq c/(\gamma H \text{ FoS}) \leq 0.05$ and $0.05 \leq c/(\gamma H \text{ FoS}) \leq 0.25$, respectively. In addition to the analyses conducted with `geoSlice`, further analyses are performed with `GGU-Stability` and `GeoStudio` for comparison and verification. To ensure comparability of the results, no tension crack feature is used for the analyses with `geoSlice` and `GeoStudio`.

Starting with the slope stability analysis using the simplified Bishop method, the results of the parametric study obtained using the three LEM codes are summarized in terms of a design chart in Fig. 3.3. Note that close agreement between the results of `geoSlice` and the two commercial LEM codes could only be obtained in case tensile normal effective stresses not violating the Mohr-Coulomb failure criterion were accepted. In case no tensile

normal effective stresses were accepted, for instance due to consideration of a tension cut-off criterion, the design curves would be (slightly) translated towards larger φ - c combinations, indicating that a higher shear strength is required to obtain an equilibrium for an initially selected FoS. As depicted in Fig. 3.3, good agreement between the results of `geoSlice` (solid lines) and `GeoStudio` (square symbols) is obtained for a wide range of combinations for β , c and φ . Although slight deviations are observed for $\beta = 80^\circ$ and $c/(\gamma H \text{ FoS}) > 0.1$, which may also be attributed to the quality of the optimization process, systematic differences cannot be seen when comparing `geoSlice` and `GeoStudio`. Comparing results obtained with `geoSlice` and `GGU-Stability` (triangular symbols), good agreement is observed for $\beta \leq 60^\circ$. However, systematically increasing deviations between `geoSlice` and `GGU-Stability` can be concluded for increasing slope angles and

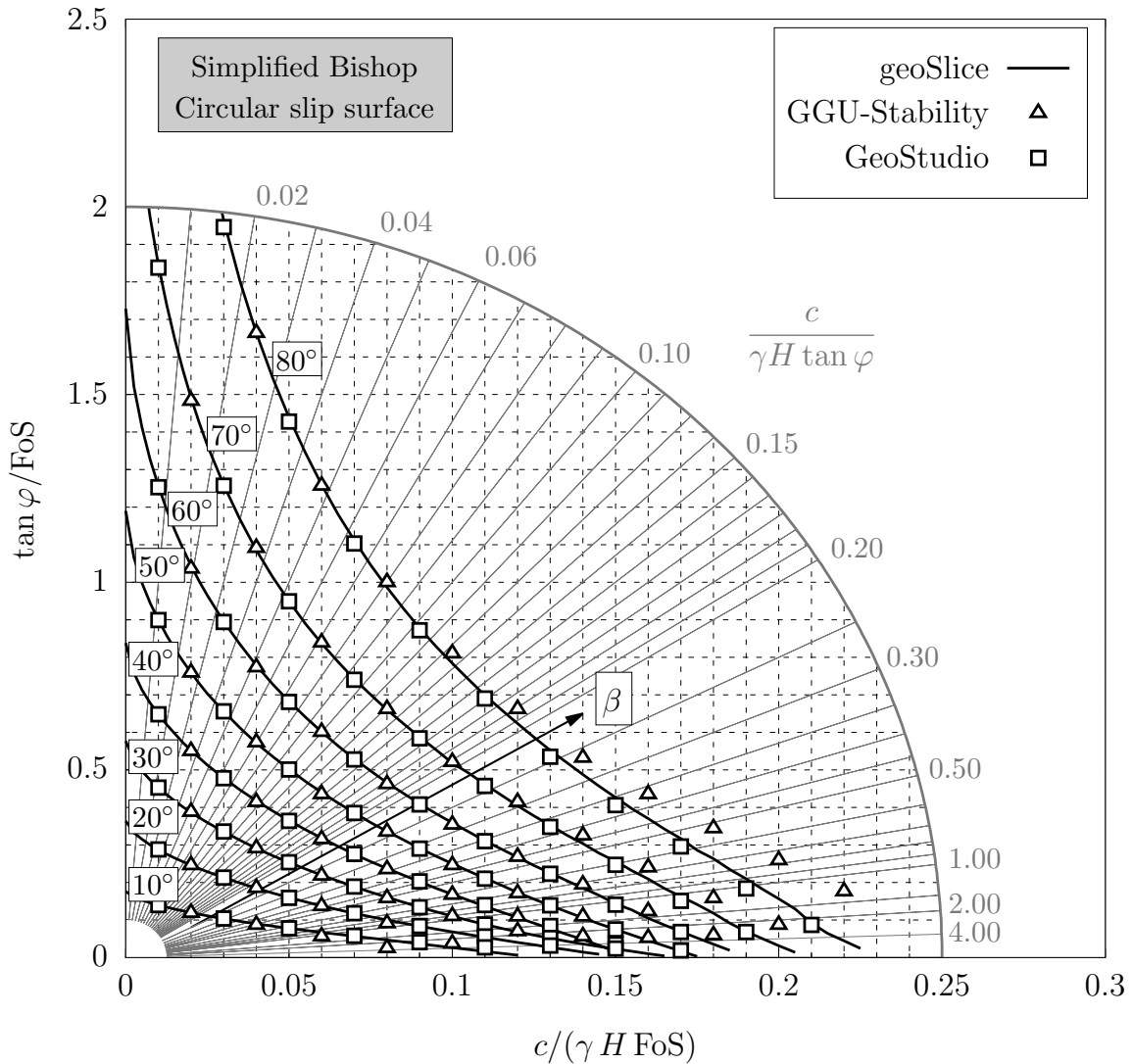


Figure 3.3: Simplified Bishop stability chart for dry slopes and circular slip surfaces

increasing values of normalized cohesion. A potential explanation for these deviations obtained for steep slopes composed of cohesion-dominated soils can be given with regard to the critical failure mechanisms, which show clear differences in the shapes obtained with `geoSlice` and `GeoStudio` compared to the ones obtained with `GGU-Stability`.

These differences in the shapes of the critical slip surfaces obtained using the simplified Bishop method implemented in different LEM codes are investigated with regard to stability analyses for an example slope with $\beta = 80^\circ$, $H = 10$ m, $\gamma = 20$ kN/m³ and $c = 40$ kPa considering friction angles in the range of $10^\circ \leq \varphi \leq 40^\circ$. The results obtained using `geoSlice`, `GeoStudio` and `GGU-Stability` are presented in terms of the critical slip surfaces and associated factors of safety in Fig. 3.4 and Tab. 3.1, respectively. It is apparent from this figure that the shapes of critical slip surfaces are slightly different comparing `geoSlice` and `GeoStudio`. Considering that the factors of safety (Tab. 3.1) are similar, the differences may be related to a more advanced optimization algorithm (DE instead of grid search) used in combination with the former LEM code. Analyzing the shape of the critical slip surfaces determined using `GGU-Stability` it is observed that it is composed of a circular and a linear (almost vertical) part, where the latter – although not clearly explained in the respective manual – might represent a tensile crack, where no shear resistance is generated over the length of the tensile crack. Additional analyses utilizing a tension crack feature in `geoSlice` and `GeoStudio` should be supplemented to continue this discussion.

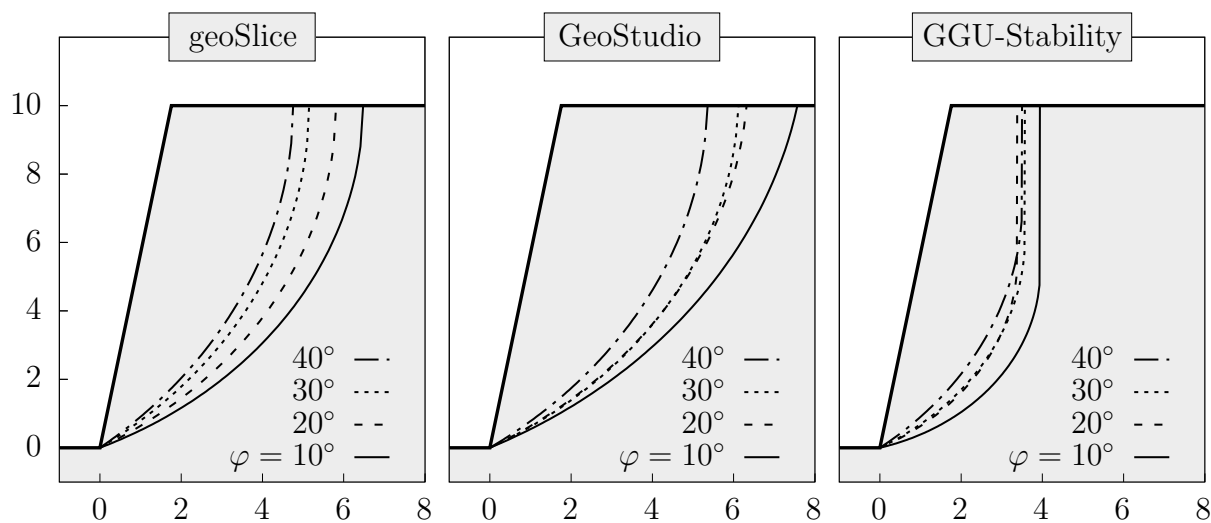


Figure 3.4: Critical slip surfaces obtained via `geoSlice`, `GeoStudio` and `GGU-Stability` for a steep cohesive slope ($\beta = 80^\circ$, $c = 40$ kPa, $\gamma = 20$ kN/m³) with $10^\circ \leq \varphi \leq 40^\circ$

Table 3.1: FoS obtained via different LEM codes for a steep cohesive slope

LEM code	$\varphi = 10^\circ$	$\varphi = 20^\circ$	$\varphi = 30^\circ$	$\varphi = 40^\circ$
geoSlice	1.015	1.169	1.337	1.529
GeoStudio	1.038	1.188	1.370	1.550
GGU-Stability	0.926	1.103	1.281	1.482

Recapturing the objective of this first parametric study, it can be concluded from the comparison of `geoSlice` and the commercial LEM codes that the implementation of the basic features covering the handling of unit weights, shear parameters and the determination of the factor of safety with regard to the global equilibrium of momentum using the simplified Bishop method was successful. To additionally verify the determination of the factor of safety with regard to the global equilibrium of horizontal forces, a second parametric study is performed using the simplified Janbu method. Besides the simplified Bishop method, the simplified Janbu method is implemented in many LEM codes, for instance in `GeoStudio` and `GGU-Stability`. However, in contrast to the former LEM code, which allows to evaluate the slope stability using the simplified Janbu method considering circular slip surfaces, the latter code only offers the possibility to evaluate the FoS with the simplified Janbu method using block slip surfaces, as depicted for instance in Fig. 2.3(d). As currently, not considering the bedrock feature, only circular slip surfaces can be used for slope stability analyses in `geoSlice`. The verification is performed by comparison with results obtained using `GeoStudio`.

Similar to the first parametric study utilizing the simplified Bishop method, the ranges of the geometry and soil parameters are selected as $10^\circ \leq \beta \leq 80^\circ$, $0 \leq c/(\gamma H \text{ FoS}) \leq 0.25$ and $0 \leq \tan \varphi / \text{FoS} \leq 2.0$ for the second parametric study. The results of this study obtained using the simplified Janbu method and only considering circular slip surfaces are presented in terms of a stability chart in Fig. 3.5. As can be seen from this plot, very good agreement between the results obtained using `geoSlice` and `GeoStudio` is obtained for a wide range of different soil shear strength parameters and geometries of the slope. Small deviations may be attributed to slightly different success during the optimization process, however, no systematic deviations are observed. Therefore, it can be noted that also the simplified Janbu method has been implemented correctly in `geoSlice`.

As the simplified Bishop method and the simplified Janbu method can not be considered rigorous since neither of them ensures that the global equilibrium of momentum and

horizontal forces is satisfied simultaneously, a third parametric study is required using a method that satisfies the requirements, such as the Spencer method or the Morgenstern and Price method. As the former can be considered a special case of the latter method in case the interslice force function is equal to unity, the Morgenstern and Price method is selected here. For the simulations conducted in this parametric study, only circular slip surfaces are investigated and a half-sine interslice forces function is chosen. Verification is conducted with respect to results obtained with *GeoStudio* solely as the Morgenstern and Price method is not implemented in *GGU-Stability*. As for the first two parametric studies, similar parameter ranges are utilized.

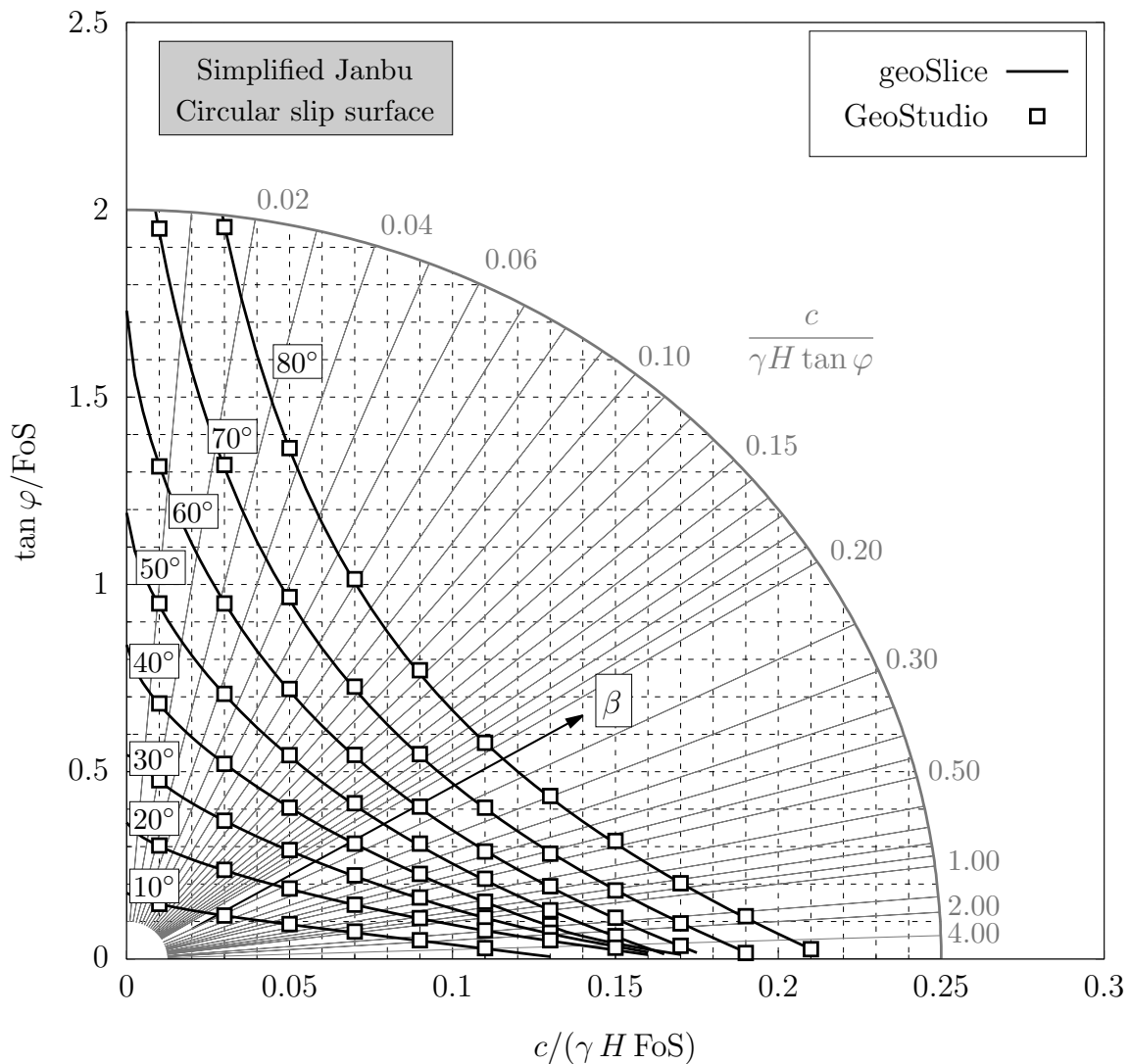


Figure 3.5: Simplified Janbu stability chart for dry slopes and circular slip surfaces

The results of the parametric study using the Morgenstern and Price method are presented in Fig. 3.6. Overall, good agreement between the results obtained with `geoSlice` and `GeoStudio` is achieved, although minor deviations are observed for slope angles $\beta \geq 70^\circ$. Potential reasons for these deviations may be manifold, for instance accuracy of the optimization process, differences in the implementation of the interslice forces or convergence issues due to the non-linearity of the objective function. In fact, it was observed that due to the latter reason, it is rather difficult to implement this method in a robust and stable way. Similar observations have also been reported, among others, by Morgenstern and Price (1967), Ching and Fredlund (1983) and Zhu et al. (2005). Moreover, it should be noted that the range of the interslice parameter λ should be

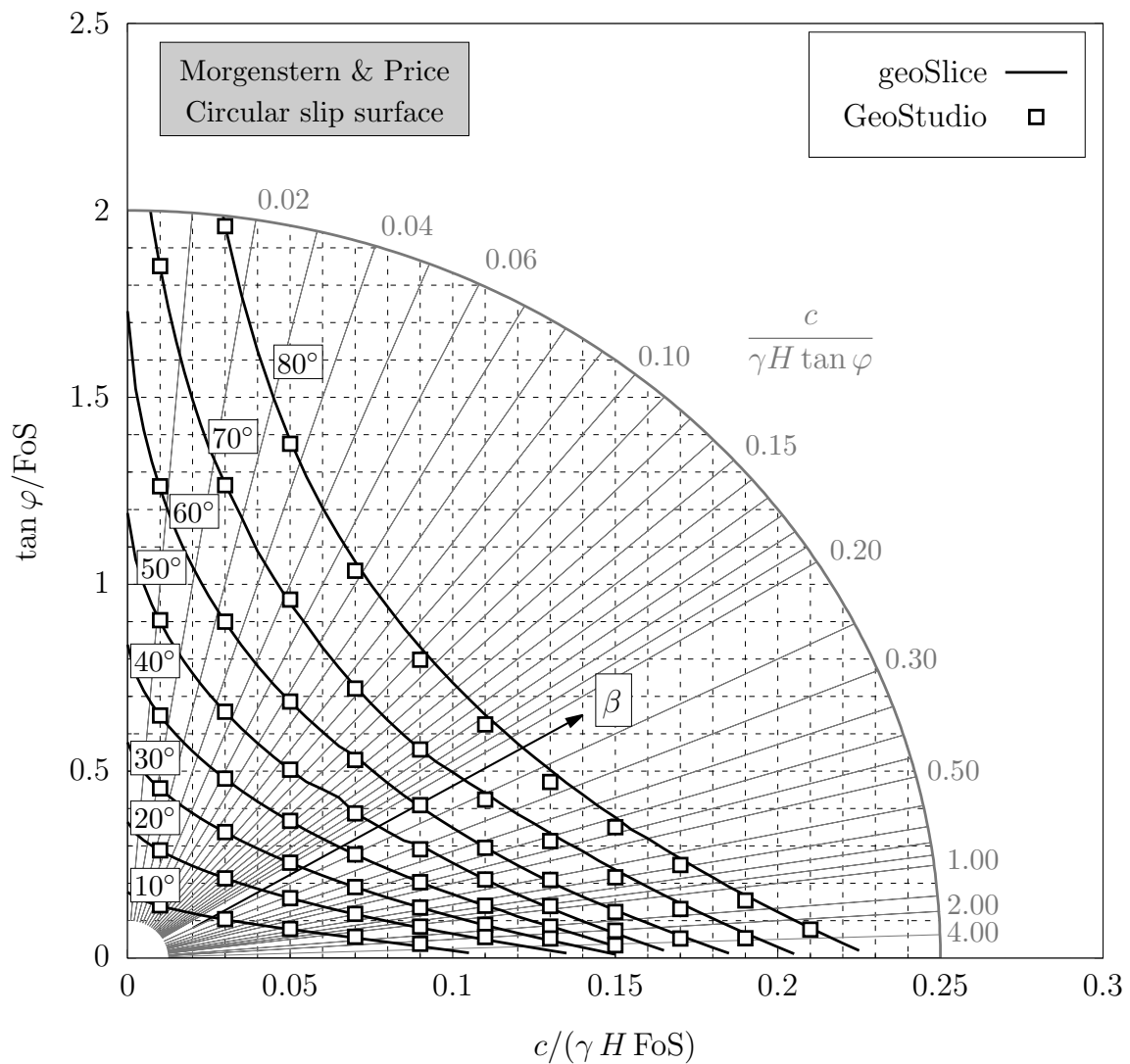


Figure 3.6: Morgenstern & Price stability chart for dry slopes and circular slip surfaces

selected carefully. In contrast to the ranges schematically depicted in Fig. 2.3, the upper limit of λ to be investigated for the detection of the intersection between the equilibrium of momentum and horizontal forces curves should be $\lambda_{\max} > \tan \varphi$.

In general, it can be concluded from the parametric studies conducted on dry slopes in this section that – despite slight deviations in the last parametric study – good overall agreement of the implemented methods was achieved for a wide range of geometries (e.g. shallow to steep slopes) and shear strength parameters. In the subsequent sections, features covering pore water pressures and pseudo-static analyses are verified.

General remark: It should be noted that the stability charts presented in Figs. 3.3, 3.5 and 3.6 were not only prepared for verification purposes but may also serve as comprehensive design charts for practical use. For this, the gray solid lines denote constant ratios of known properties H , γ , c , and φ . Considering a homogeneous slope with known geometry (β , H) and soil properties (γ , c , φ), the intersection of the corresponding gray line with the respective β curve directly yields the values for $c/(\gamma H \text{ FoS})$ and $\tan \varphi/\text{FoS}$, where either of both can be used to back-calculate the FoS.

3.4.2. Hydrostatic pore water pressures

As shown in Fig. 3.1, pore water pressures U , W , ΔW and ΔU_{acc} result from phreatic levels inside the soil domain, outside/above the soil domain (e.g. lakes), water level changes due to long waves and accumulated excess pore water pressures due to cyclic shearing, respectively. Focusing on static conditions ($\Delta W = 0$, $\Delta U_{\text{acc}} = 0$) and neglecting the effect of interslice shear forces (i.e. $X_{L/R} = 0$, no effect of $U_{L/R}$ on N') by using the simplified Bishop method, determination of hydrostatic pore water pressures U and external water pressures W can be verified. This is achieved by investigation of two example slopes depicted in Fig. 3.7(a) and (b) considering variations of the phreatic level inside the soil body and a global phreatic level, respectively. Since $W = 0$ holds in the first example, verification of the determination of U is ensured. Afterwards, knowing that the determination of U is correct, the second example allows to verify W .

To investigate the first effect, the influence of a rising phreatic level inside the soil domain on the factor of safety is studied for an example slope with $\beta = 26.67^\circ$ and $\varphi = 25^\circ$ considering variations of the normalized cohesion ratio with $c/(\gamma H) = 0.02$, 0.04 and 0.06 . No differentiation is made here between the soil unit weight below and above the phreatic level (i.e. $\gamma = \gamma_{\text{sat}}$) as the other LEM codes used for verification do not account for two independent soil material parameters to define the soil unit weight. Though not conducted

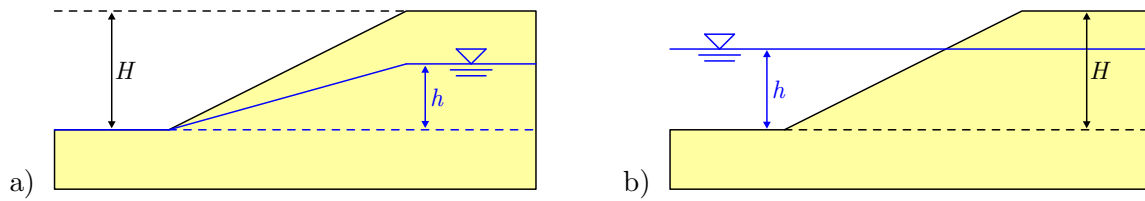


Figure 3.7: Verification of hydrostatic pore water pressures by variations of (a) the phreatic level inside the soil body and (b) the global phreatic level

here, workaround solutions could be used by choosing different materials below and above the phreatic level. The results of this study obtained with `geoSlice`, `GGU-Stability` and `GeoStudio` are compared in Fig. 3.8. This figure shows an almost perfect agreement between the results of all three LEM codes, indicating a proper implementation of the pore water pressures inside the soil domain U . As seen from this figure, the factor of safety significantly decreases with increasing phreatic level inside the soil domain in case the outside phreatic level remains unchanged at the level of the slope toe. Considering

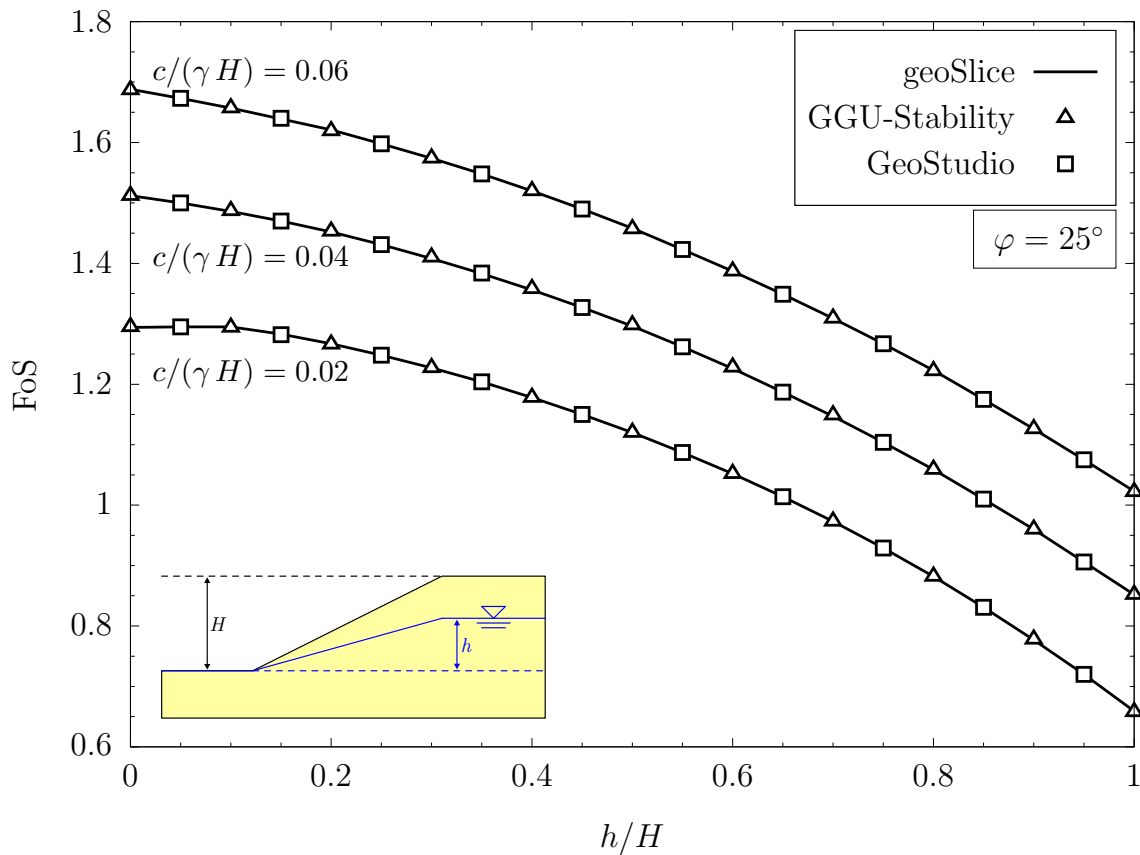


Figure 3.8: Influence of rising phreatic level inside the soil body on the factor of safety for a homogeneous slope with $\beta = 26.67^\circ$

the influence of the normalized cohesion on the FoS, it is observed that the FoS increases with increasing cohesion, while the general trend with regard to the effect of the phreatic level increase on the FoS remains almost unchanged.

To verify the determination of external water pressures W , the example slope schematically depicted in Fig. 3.7(b) is investigated for $\beta = 40^\circ$ and $\varphi = 25^\circ$ considering variations of the normalized cohesion ratio with $c/(\gamma H) = 0.02, 0.04$ and 0.06 . As mentioned before, it is assumed that soil unit weights below and above the phreatic level are identical. The results of this study obtained with `geoSlice`, `GGU-Stability` and `GeoStudio` are compared in Fig. 3.9. As can be seen from this figure, good agreement between all three LEM codes is obtained for almost all analyses, while only slight deviations for a few `GGU-Stability` simulations is observed. Investigating the general trend of the curves, it is apparent that the cohesion has a decisive impact on the FoS versus h/H curves, especially for larger h/H ratios, where the FoS significantly increases with increasing cohesion. Although not depicted in this plot, trial analyses confirmed that $\text{FoS}(h/H = 0.0)$

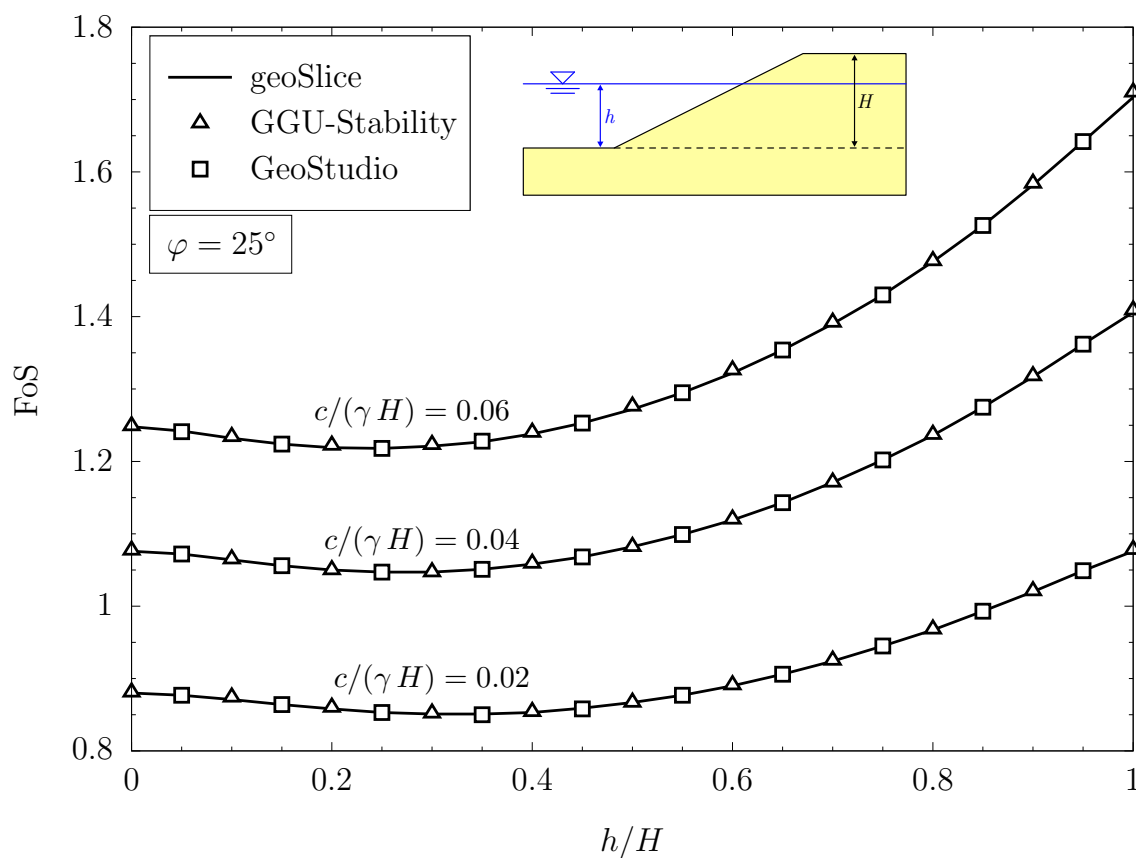


Figure 3.9: Influence of rising global phreatic level on the factor of safety for a homogeneous slope with $\beta = 40^\circ$

and $\text{FoS}(h/H = 1.0)$ are identical in case of $c = 0\text{ kPa}$ and $\gamma = \gamma_{\text{sat}}$. Thus, it should be clear that the critical phreatic level associated with the lowest FoS is obtained for intermediate heights. Considering the design of residual lake slopes, this fact should be kept in mind, especially if the increase of the water level is slow and the hazard posed by seismic loading is large.

In general, it has been shown with the parametric studies discussed in this section that the implementation of the hydrostatic pore water pressures U and W in `geoSlice` yields accurate results when compared to the well-established commercial LEM codes `GGU-Stability` and `GeoStudio`. Further analyses for the purpose of verification are conducted with regard to inertial forces defined via pseudo-static coefficients in the following section.

3.4.3. Pseudo-static analysis

To investigate the seismic slope stability with limit equilibrium methods, a pseudo-static analysis is commonly performed. In this section, comparative analyses are conducted to verify the LEM implementation with regard to horizontal and vertical pseudo-static coefficients (k_h, k_v) for the determination of inertial forces due to seismic actions, for instance earthquake loading. As many basic features of the LEM implementation have been verified in the previous sections, comparative analysis with `geoSlice` and `GGU-Stability` are conducted for variations of $k_h, k_v, c/(\gamma H \text{ FoS})$ and $\tan \varphi/\text{FoS}$, while the slope geometry is assumed constant with $\beta = 30^\circ$. Two scenarios are investigated with regard to the choice of the pseudo-static coefficients: (1) $k_h \geq 0.0, k_v = 0.0$ and (2) $k_h = 0.5, k_v \geq 0.0$. The results of the parametric study are presented in Fig. 3.10 with solid and dashed lines corresponding to the two scenarios, respectively. As mentioned in Section 3.3, the direction of the vertical pseudo-static coefficients is automatically checked, thus, identical results are obtained by prescribing positive and negative values.

As can be seen from this figure, good agreement between the results determined with `geoSlice` and `GGU-Stability` is obtained for a wide range of different pseudo-static coefficients and normalized shear strength parameters. As the consideration of pseudo-static coefficients in the implementation of an LEM code only requires a limited number of changes, and the agreement of the results studied here is very satisfying, there is – to the author’s opinion – no necessity to study and compare the effect of pseudo-static coefficients for slopes with other geometries. Still, the verification process is proceeded by the analysis of benchmark problems in the next section.

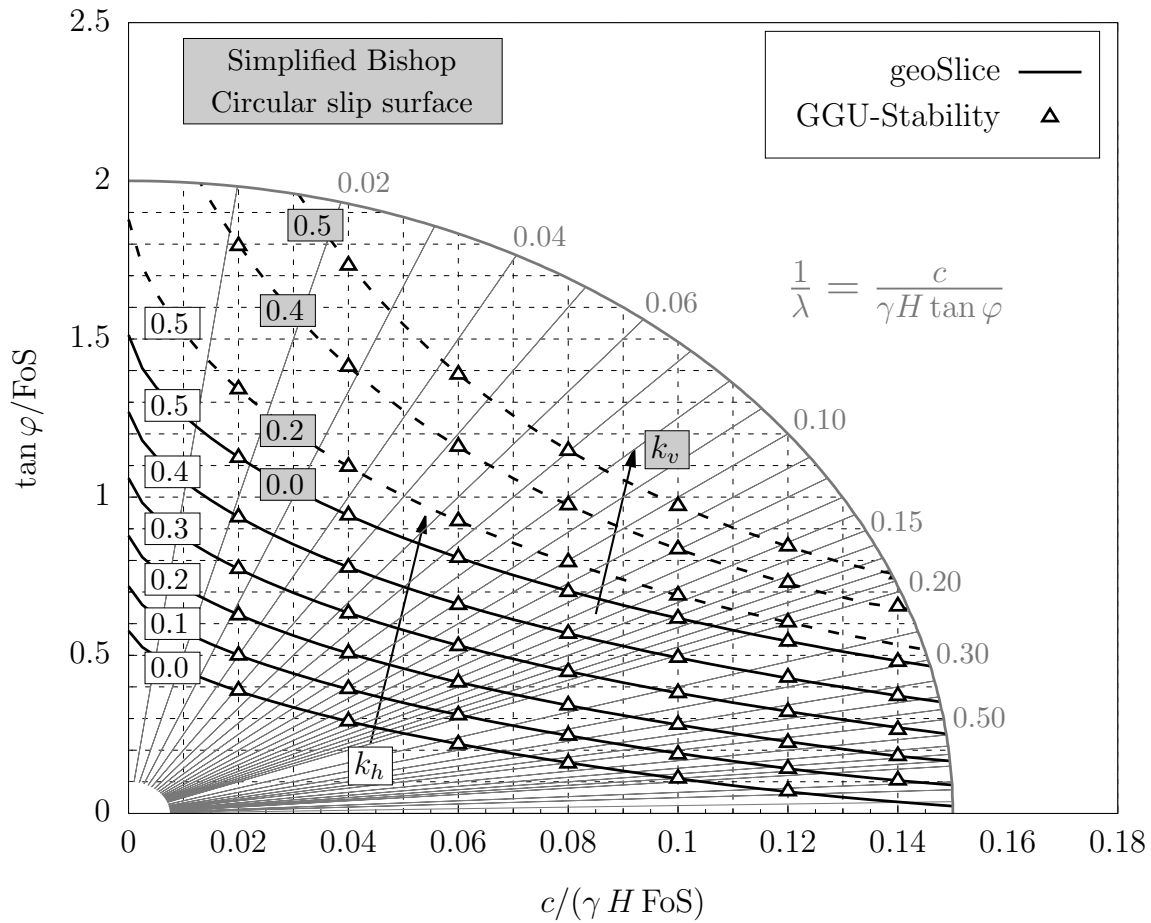


Figure 3.10: Influence of horizontal and vertical pseudo-static coefficients k_h and k_v on the factor of safety for a homogeneous slope with $\beta = 30^\circ$

3.4.4. Benchmark problems

In addition to the analysis of homogeneous slopes under different boundary conditions, benchmark examples are investigated to further verify the accuracy of the implemented LEM code. These benchmark examples have been selected as they have been investigated intensively by many authors applying different methods. The main features to be verified in this section cover handling of layered soils, thin weak layers, pore water pressure ratios, impenetrable layers and topological optimization.

The first benchmark example selected has been published by von Wolffersdorff (2019) and covers a large collaborative comparative analysis of the stability of a gravity wall considering three different soil layer setups. Comparison is conducted in terms of the factor of safety and the shape of the failure surface applying different FEM, FDM, FELA and LEM codes. A schematic illustration of the geometry and soil layer setups in-

investigated is depicted in Fig. 3.11. The sand and silt soil layers are characterized by $\gamma_{\text{Sand}} = 20 \text{ kN/m}^3$, $\varphi_{\text{Sand}} = 35^\circ$, $c_{\text{Sand}} = 0.1 \text{ kPa}$ and $\gamma_{\text{Silt}} = 20 \text{ kN/m}^3$, $\varphi_{\text{Silt}} = 20^\circ$, $c_{\text{Silt}} = 10 \text{ kPa}$, respectively, while the gravity wall is modeled as concrete with a unit weight of $\gamma_{\text{Concrete}} = 25 \text{ kN/m}^3$ and infinite shear strength. Note that a small cohesion value of 0.1 for the sand material has been chosen in von Wolfersdorff (2019) to avoid numerical instabilities. The distributed trapezoidal load is applied as design load with a maximum value of $q_{d,\text{max}} = 1.3 \cdot 20 = 26 \text{ kPa}$.

Although many different methods and codes have been utilized in (von Wolfersdorff, 2019) to evaluate the stability of the gravity wall, only selected results are used for the verification. The reason for this is that, in general, good agreement between FoS derived using different FE codes was obtained. The results obtained with *Plaxis2D* and *GGU-Stability* (von Wolfersdorff, 2019) are summarized in Tab. 3.2 together with results obtained using *geoSlice*, which have been determined considering the simplified Bishop method in combination with circular slip surfaces and the Morgenstern & Price method in combination with non-circular slip surfaces. Comparing the second and third row of this table, it is apparent that good agreement between the results obtained with *GGU-Stability* and *geoSlice* is obtained for all three cases. Minor deviations in the range of $\Delta\text{FoS} \approx 0.01$ are observed, which might result from small deviations in the location of the critical slip surface due to different optimization algorithms applied, where

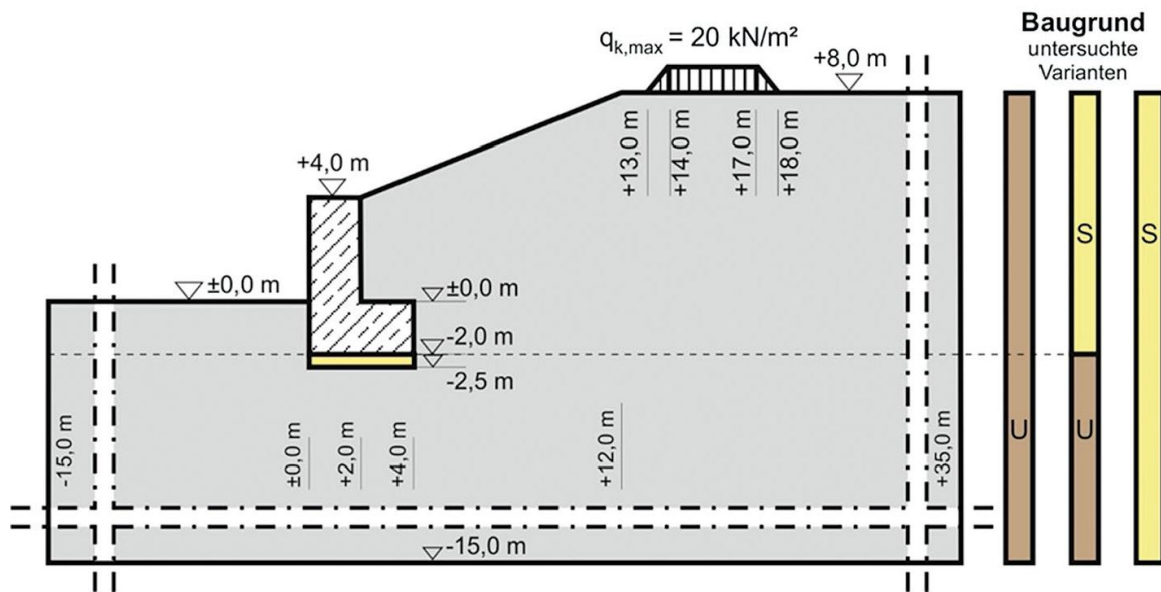


Figure 3.11: Stability of a gravity wall considering different soil layer setups (von Wolfersdorff, 2019)

Table 3.2: Comparison of FoS with benchmark data published in von Wolffersdorff (2019)

Reference	Software	Method	Soil layer setup		
			U/U	S/U	S/S
von Wolffersdorff (2019)	Plaxis2D	SRFEA	1.36	1.56	1.78
von Wolffersdorff (2019)	GGU-Stability	LEM ^{*,a}	1.58	1.89	2.19
Present study	geoSlice	LEM ^{*,a}	1.57	1.90	2.18
Present study	geoSlice	LEM ^{†,c}	1.38	1.57	1.80

*Bishop (simplified), †Morgenstern & Price method

^acircular slip surface, ^cnon-circular slip surface

grid search was used in the former and differential evolution in the latter LEM code. However, taking into consideration the results obtained using `Plaxis2D`, it is apparent that significantly smaller FoS are determined with strength reduction finite element analysis (SRFEA) compared to LEM schemes. An explanation for the differences of the FoS can be given with respect to the shape of the critical slip surfaces. In contrast to SRFEA, where the shape of the slip surface develops without restrictions, in LEM (second and third row) only circular slip surfaces are considered. Thereby, for cases where the critical slip surface is not well approximated by a circle, overestimation of the FoS is expected due to a lack of properly locating the critical slip surface. As shown in Tab. 3.2, the latter methods may significantly overestimate the FoS in case circular slip surfaces are considered. In contrast, it can be seen from the results presented in the last row of this table that applying the Morgenstern & Price method and utilizing non-circular slip surfaces via topological optimization (see Section 3.3) yields significantly improved predictions of the FoS with maximum deviations towards the SRFEA results of $\Delta\text{FoS} \approx 0.02$. This indicates the importance of the topological optimization implemented in `geoSlice` to enable the slope stability investigation with non-circular slip surfaces (Fig. 3.12).

The second benchmark example has been investigated, among others, by Krahn and Fredlund (1977), Fredlund and Krahn (1977), Baker (1980) and Leshchinsky and Ambauen (2015) and consists of six variations (labeled a - f) of a slope with a height of $H = 12.25$ m and an inclination of $l/H = 1/2$, where l is the width of the slope. The variations include a thin weak horizontal layer below the slope toe (b, d, f), a pore water pressure ratio of $r_u = 0.25$ (c, d) and an inclined phreatic level (e, f). The soil parameters of the core material are $\gamma_1 = 19 \text{ kN/m}^3$, $\varphi_1 = 20^\circ$ and $c_1 = 28 \text{ kPa}$, while the soil parameters of the

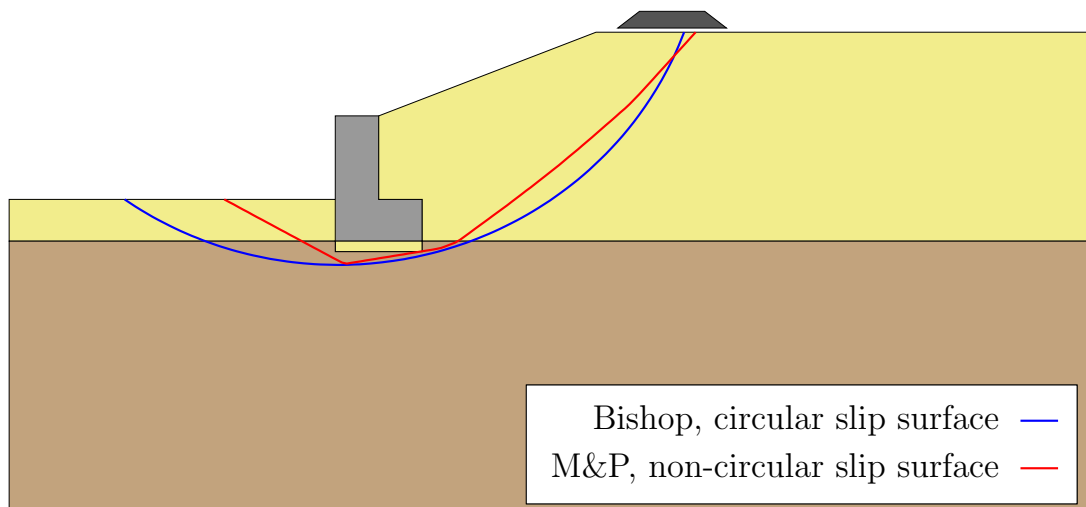


Figure 3.12: Circular and non-circular critical slip surfaces obtained with `geoSlice` for the benchmark example of a slope stabilized with a gravity wall (von Wolffersdorff, 2019)

thin weak layer are $\gamma_2 = 19 \text{ kN/m}^3$, $\varphi_2 = 10^\circ$ and $c_2 = 0 \text{ kPa}$. A schematic illustration of the six variations including critical slip surfaces obtained in different studies is depicted in Fig. 3.13. From this figure it is apparent that the shape of the critical slip surface is significantly affected by the presence of the thin weak layer, where the shape of the slip surface is almost circular for cases without this layer (a, c, e), while it strongly orientates along this layer in case it is present (b, d, f). The strong impact of the weak layer can also be seen by direct comparison of the FoS for two cases within the same row of this figure (e.g. a vs. b, c vs. d or e vs. f), which clearly emphasize the importance of the consideration of slip surfaces with shapes different from the circular type. Overall, this example has been selected as it allows to verify different features implemented in `geoSlice` such as handling of layered soils with thin weak layers, pore water pressure ratios, impenetrable layers and topological optimization.

The stability of all six variations of the slope has been investigated using `geoSlice` considering different assumptions with regard to the shape of the slip surface. The different shapes included circular, composite and non-circular slip surfaces, where the second is defined as a composite surface of a slip circle and an impenetrable layer located within the thin weak layer and the latter is the result of a topological optimization conducted based on the location of the critical slip circle. Moreover, SRFEA and FELA (lower and upper bound) simulations have been performed with `Plaxis2D` and `OptumG2`, respectively, for three cases (a, b, e), which serve as additional benchmark data. FoS determined for all variations of this benchmark example are summarized in Tab. 3.3 considering results

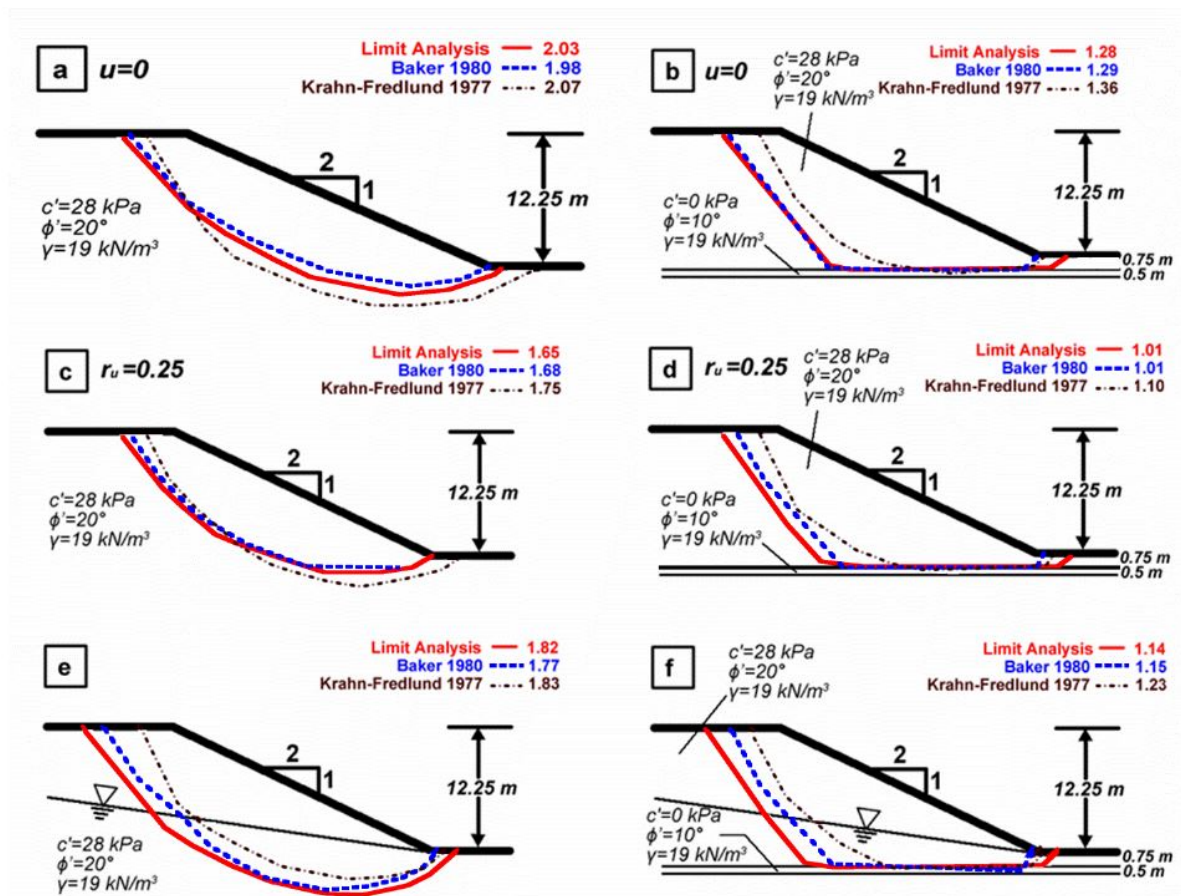


Figure 3.13: Stability of a homogeneous slope considering the effect of (b,d,f) a weak layer, (c,d) a pore water pressure ratio r_u and (e,f) an inclined phreatic surface (Leshchinsky and Ambauen, 2015)

presented in Krahn and Fredlund (1977), Baker (1980) and Leshchinsky and Ambauen (2015) as well as results obtained in the present study utilizing Plaxis2D, OptumG2 and geoSlice.

Comparing the results obtained in the previous studies, it is seen that the predicted FoS by Krahn and Fredlund (1977) are the largest for all six models, while the results of Baker (1980) and Leshchinsky and Ambauen (2015) yield the smallest predictions for cases without and with weak layer, respectively. Overall, comparing the results of those studies, differences of up to 7.3% are observed in the predicted FoS. Potential reasons for the differences seen may be attributed to different methods applied (LEM, LA) as well as different optimization schemes used. It should be noted that all analyses performed in Krahn and Fredlund (1977) were based on circular and composite slip surfaces with identical radii and circle centers, thus, no individual optimization was used for each of the

six models. Complementing these results by FoS values obtained using FE schemes such as SRFEA and FELA, it is observed that the predicted FoS obtained using `Plaxis2D` and `OptumG2` are slightly smaller compared to the previous studies. Still, the minimum FoS values of the previous studies show good agreement with the numerical results. Considering the results obtained using `geoSlice` it is apparent that the shape of the slip surface has a major impact on the predicted FoS (see Fig. 3.14). Good agreement of the simulations with circular slip surface is only obtained for models without weak layer, while significant overestimation is seen for the other cases. Evaluating the results obtained using the impenetrable layer feature creating composite slip surfaces and the topological optimization enabling determination of the FoS for non-circular slip surfaces, it is observed that both features enable accurate predictions of the FoS. However, it should be noted that both features do not necessarily give identical results and have their own advantages and drawbacks.

Comparing both features (impenetrable layer and topological optimization), it is to be noted that the computational costs associated with the impenetrable layer feature are significantly smaller compared to the topological optimization as no additional optimization is required. However, this feature can only be used if it is ensured that the failure surface

Table 3.3: Factor of safety obtained from different methods for six benchmark slopes

Reference	Method	Model					
		a	b	c	d	e	f
Krahn and Fredlund (1977)	LEM [†]	2.07 ^a	1.36 ^b	1.75 ^a	1.10 ^b	1.83 ^a	1.23 ^b
Baker (1980)	LEM ^{‡,c}	1.98	1.29	1.68	1.01	1.77	1.15
Leshchinsky and Ambauen (2015)	LA ^c	2.03	1.28	1.65	1.01	1.82	1.14
Present study (Plaxis2D)	SRFEA	1.94	1.22	–	–	1.74	–
Present study (OptumG2)	FELA	1.95	1.25	–	–	1.75	–
Present study (geoSlice)	LEM ^{†,a}	1.97	1.49	1.68	1.23	1.78	1.39
Present study (geoSlice)	LEM ^{†,b}	–	1.28	–	1.01	–	1.15
Present study (geoSlice)	LEM ^{†,c}	–	1.24	–	1.00	–	1.12

^acircular slip surface, ^bcomposite slip surface, ^cnon-circular slip surface

[‡]Spencer method, [†]Morgenstern & Price method

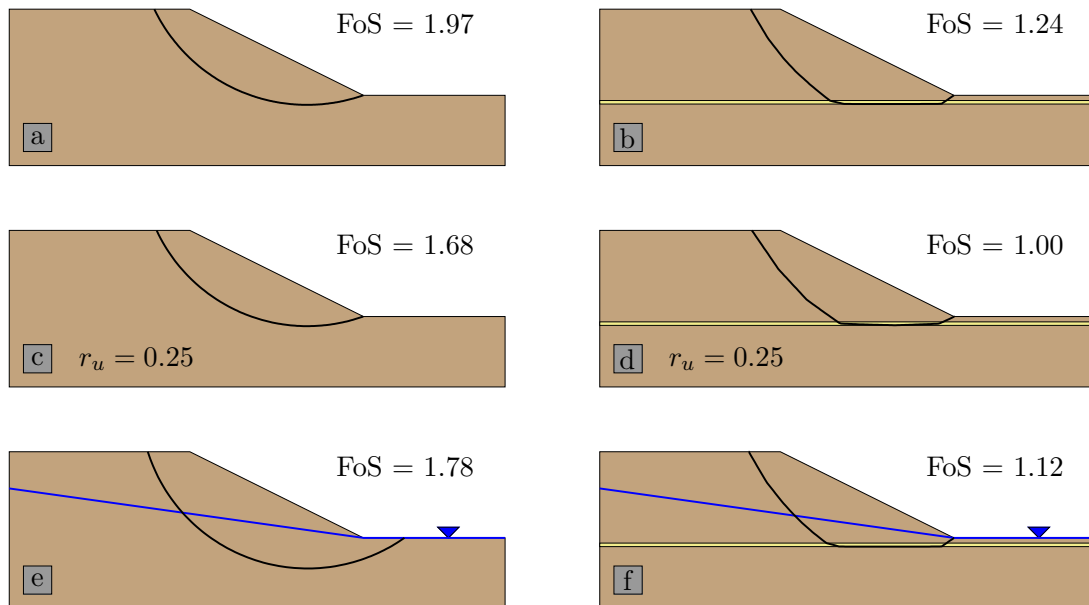


Figure 3.14: Critical slip surfaces and FoS obtained with `geoSlice` for the six slopes of the second benchmark example (Krahn and Fredlund, 1977) considering (a, c, e) circular and (b, d, f) non-circular slip surfaces

would pass through a narrow weak layer. In case it is not clear where the critical slip surface is located, as it was the case for instance for the first benchmark example studied in this section (Fig. 3.11), the impenetrable layer feature is not very helpful. The topological optimization is more versatile as less strict constraints are prescribed for the location and shape of the failure surface. Although the non-circular slip surfaces have been restricted to convex shapes for the examples studied within this thesis, in general, allowing for concave sections within the slip surface, topological optimization might also be applicable to more complex geotechnical boundary value problems, for instance the stability of slopes composed of block-in-matrix soils or rocks (bimsoils/bimrocks) (Montoya-Araque et al., 2020; Napoli et al., 2021). Nevertheless, it should be noted that the impenetrable layer feature could also be combined with the topological optimization to enable a precise approximation of the slip surface within the weak layer by the impenetrable layer feature and to allow for non-circular shapes within the remaining part due to the topological optimization.

The third benchmark example has been investigated by Zolfaghari et al. (2005), Cheng et al. (2007), Jurado-Piña and Jimenez (2015) and Liu et al. (2015, 2020). The slope is composed of four layers with inclined layer boundaries, where the third layer is a weak layer that dictates the shape of the critical slip surface. A schematic illustration of this

benchmark example including coordinates of the model and layer boundaries is provided in Fig. 3.15. With identical unit weights in all layers ($\gamma_{1-4} = 18.62 \text{ kN/m}^3$), the shear strength parameters associated with the four layers are defined as: $\varphi_1 = 20^\circ$, $c_1 = 15 \text{ kPa}$, $\varphi_2 = 21^\circ$, $c_2 = 17 \text{ kPa}$, $\varphi_3 = 10^\circ$, $c_3 = 5 \text{ kPa}$, $\varphi_4 = 28^\circ$, and $c_4 = 35 \text{ kPa}$. As for the second benchmark example, the effect of composite and non-circular slip surfaces on the FoS is evaluated. Therefore, analyses with `geoSlice` are conducted using circular, composite and non-circular slip surfaces. In addition, SRFEA is performed using `Plaxis2D`, which serves as additional benchmark data. The results of the previous analyses and those obtained in this thesis are summarized in Tab. 3.4 in terms of the FoS for the benchmark problem at hand.

It can be seen from the results presented in Tab. 3.4 that a wide range of different factors of safety have been obtained in previous studies with $1.095 \leq \text{FoS} \leq 1.50$. Though, the results obtained by Cheng et al. (2007), Jurado-Piña and Jimenez (2015), Liu et al. (2015) and Liu et al. (2020) indicate that $\text{FoS} \approx 1.1$ can be considered a reasonable estimate. This is also supported by the evaluation of the slope stability via SRFEA, which yields $\text{FoS} = 1.057$. Considering the results obtained with `geoSlice`, it is apparent that larger discrepancies in the FoS are obtained when utilizing circular slip surfaces. A similar observation is seen for the results reported by Zolfaghari et al. (2005) for analyses with circular slip surfaces. In contrast, it is observed for the `geoSlice` analyses based on composite and non-circular slip surfaces that the predicted FoS are in good agreement with the expected FoS based on the previous studies.

To investigate the critical slip surfaces associated with analyses with `geoSlice` based on circular, composite and non-circular slip surfaces, respective slip surfaces are depicted in

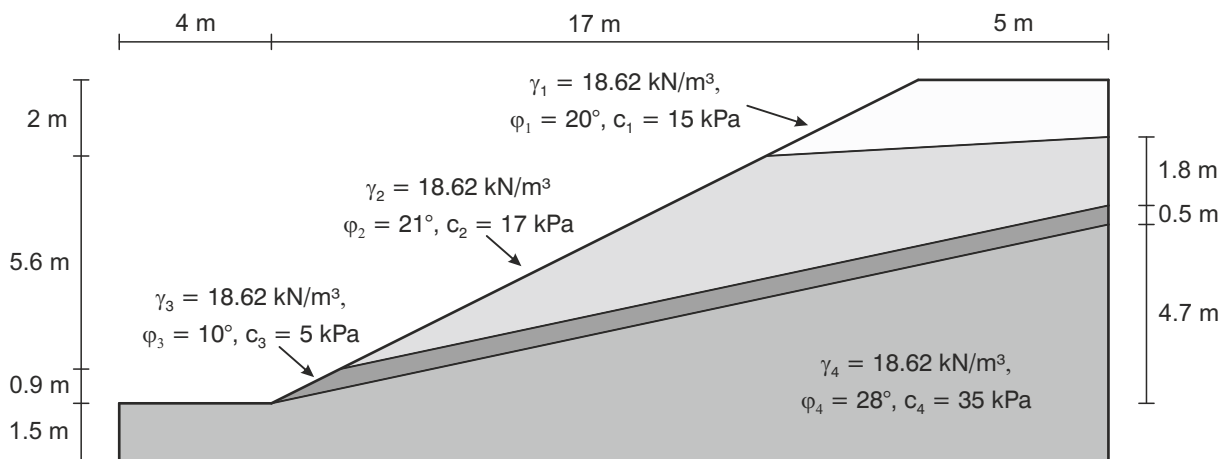


Figure 3.15: Geometry and soil parameter sets for the benchmark slope No. 3

Table 3.4: Comparison of FoS for the benchmark slope No. 3

Reference	Method	FoS
Zolfaghari et al. (2005)	LEM ^{†,a}	1.50
Zolfaghari et al. (2005)	LEM ^{†,c}	1.24
Cheng et al. (2007)	LEM ^{‡,c}	1.101
Jurado-Piña and Jimenez (2015)	LEM ^{‡,c}	1.105
Liu et al. (2015)	FELEM(EP)	1.095
Liu et al. (2020)	FELEM(E)	1.111
Present study (Plaxis2D)	SRFEA	1.057
Present study (geoSlice)	LEM ^{†,a}	1.444
Present study (geoSlice)	LEM ^{†,b}	1.132
Present study (geoSlice)	LEM ^{†,c}	1.105

^acircular slip surface, ^bcomposite slip surface, ^cnon-circular slip surface

[‡]Spencer method, [†]Morgenstern & Price method

Fig. 3.16. From this figure, it is apparent that the location and the shape of the critical slip surface – and thereby the FoS – is dependent on the initial restrictions/assumptions regarding the slip surface shape. For this benchmark example No. 3, the importance of features was emphasized that enable the analysis of slip surfaces with shapes different from the regular circular shape. From Fig. 3.16 it is observed that, in contrast to circular

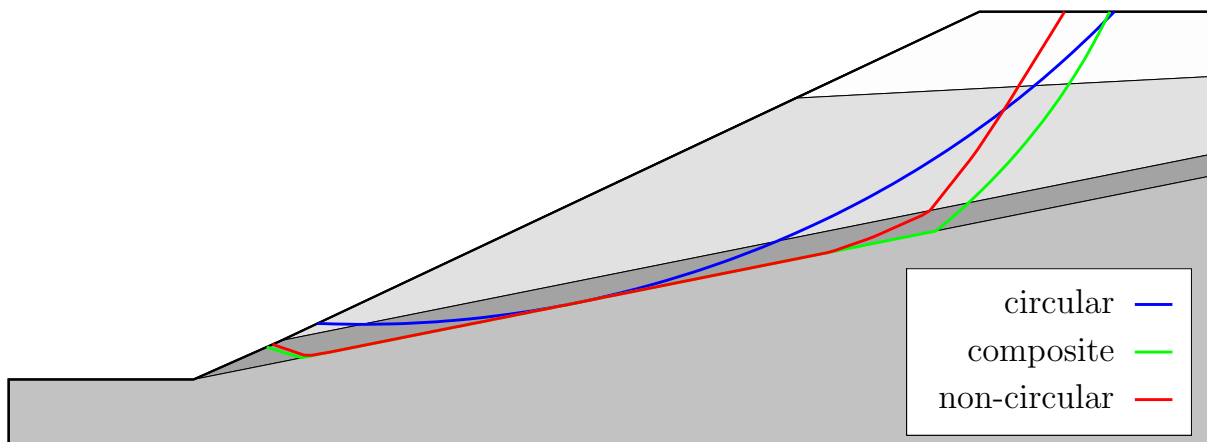


Figure 3.16: Circular, composite and non-circular critical slip surfaces obtained with `geoSlice` for the benchmark example of a slope composed of multiple inclined layers

shapes, analyses with composite and non-circular shapes predict critical slip surfaces that fall within the weak layer over long stretches, since shear strength is smaller in the weak layer, resulting in smaller FoS values. Note that composite slip surface shapes using the **Bedrock** feature can only be applied for cases where the location of the critical layer boundary (e.g. a weak soil layer) is known, otherwise – as shown in the first benchmark example – non-circular slip surfaces using **TopologicalOptimization** must be applied.

Based on the analyses of different benchmark examples in this section and the comparison with benchmark results presented in various studies, it can be concluded that the limit equilibrium method in terms of the method of slices including different advanced features has been implemented accurately in **geoSlice**. Minor differences between the results obtained in this thesis and previous studies may be attributed to different iteration or optimization schemes. However, no example showing large differences between predicted and expected factor of safety was found.

4. Implementation of elastoplastic constitutive models

4.1. Motivation

As the overall objective of this thesis is to perform stability analyses for a slope subjected to earthquake loading, one concept followed in this work is to conduct a decoupled dynamic strength reduction finite element analysis (DSRFEA) further elaborated in Chapters 5 and 6. Among others, this approach requires a FE software package allowing for dynamic finite element analyses (DFEA), sophisticated constitutive models capturing cyclic and dynamic material behavior, a strength reduction scheme, simple elastoplastic constitutive models for SRFEA, the capability to change constitutive models between consecutive loading steps and the possibility to implement additional features. As the number of requirements for the selection of an appropriate FE software package is large, it was decided to conduct this approach using the software `numgeo` (Machaček & Staubach, see e.g. Machaček (2020); Machaček et al. (2021); Staubach et al. (2022a,b) and www.numgeo.de). `numgeo` is a powerful FE software package capable to conduct DFEA. Sophisticated constitutive models needed for DFEA were implemented in `numgeo` prior to this work by the developers. Though, neither a strength reduction method nor simple elastoplastic models, which are commonly used in combination with SRFEA, were available in `numgeo`. Therefore, this chapter focuses on the implementation and verification of two elastoplastic constitutive models for `numgeo`, namely the Mohr-Coulomb model and the Matsuoka-Nakai model, which have been introduced in Section 2.3.1 and 2.3.2, respectively.

The choice of implementing the Mohr-Coulomb model and the Matsuoka-Nakai model¹ was made for the following reasons: to conduct a strength reduction analysis at different

¹Note that also the General Classic plasticity (GC) model discussed in the last paragraph of Section 2.3.2 was implemented in `numgeo`, allowing to perform simulations with the Drucker-Prager model, the Matsuoka-Nakai model and the Lade-Duncan model. The verification of the GC model with Matsuoka-Nakai yield function is provided in Appendix B.

times during a dynamic analysis, it needs to be ensured that the converged stress state of the current dynamic calculation step does not violate the yield surface of the elastoplastic model utilized in the SRFEA for the initial state of the subsequent static simulation. To enable a model change from an advanced constitutive model to a basic elastoplastic model, a combination of models is sought which uses similar definitions of yield, limit state or bounding surfaces. In this case, the most convenient combination was found to be the hypoplastic model and the Matsuoka-Nakai model for the dynamic analysis and the strength reduction analysis, respectively, as both models incorporate the Matsuoka-Nakai surface. However, to verify the strength reduction analysis it is more convenient to perform comparative analyses using an implementation of the Mohr-Coulomb model as there are only very few results of SRFEA conducted with Matsuoka-Nakai published so far, see for instance Tschuchnigg et al. (2019).

The structure of this chapter is as follows: first, the general concept of elastoplasticity is explained based on continuum mechanics conventions. Following, the implicit integration scheme is introduced including discussions with respect to different return mapping algorithms and a formulation to determine the consistent elastoplastic stiffness tensor. Lastly, verification of both elastoplastic models is conducted with respect to element test simulations by comparing results obtained using `numgeo` with those obtained using the implementations of the same constitutive models in other well-established FE codes. The element tests used for the verification cover triaxial compression and extension tests as well as simple shear tests starting from isotropic and anisotropic initial stress states.

4.2. Standard Elastoplasticity

In this section, the general concept of elastoplasticity is explained for the three-dimensional case using tensor notation with second and fourth order tensors highlighted in bold (e.g. stress tensor $\boldsymbol{\sigma}$) and sans serif script (e.g. fourth order identity tensor \mathbb{I}), respectively, while scalar values are denoted with non-bold italic script (e.g. scalar value of the yield function F). As this section only covers the general methodology of elastoplasticity from a continuum mechanics point, the interested reader may find further detailed information in well-established textbooks, for instance in Simo and Hughes (2006), de Souza Neto et al. (2011) and Borja (2013).

The basic assumption in elastoplasticity is that strains and strain rates can be split into elastic and plastic portions in accordance with the additive decomposition of strains.

Focusing on the strain rates, the total strain rate $\dot{\boldsymbol{\varepsilon}}$ represents the sum of the elastic strain rate $\dot{\boldsymbol{\varepsilon}}^e$ and the plastic strain rate $\dot{\boldsymbol{\varepsilon}}^p$, as given in Eq. 4.1.

$$\dot{\boldsymbol{\varepsilon}} = \dot{\boldsymbol{\varepsilon}}^e + \dot{\boldsymbol{\varepsilon}}^p \quad (4.1)$$

Considering isotropic Cauchy elasticity in the form of Hooke's law, the stress rate $\dot{\boldsymbol{\sigma}}$ is determined from the product of the elastic strain rate $\dot{\boldsymbol{\varepsilon}}^e$ and the fourth order isotropic elasticity tensor \mathbf{C}^e , where the latter is defined according to $\mathbf{C}^e = \lambda \mathbf{1} \otimes \mathbf{1} + 2\mu \mathbf{I}$ with the Lamé constants λ and μ . Including the concept of additive decomposition of strains according to Eq. 4.1 into the incremental stress-strain relation according to Hooke's law, one obtains

$$\dot{\boldsymbol{\sigma}} = \mathbf{C}^e : \dot{\boldsymbol{\varepsilon}}^e = \mathbf{C}^e : (\dot{\boldsymbol{\varepsilon}} - \dot{\boldsymbol{\varepsilon}}^p) \quad (4.2)$$

To control the evolution of the plastic strain rate $\dot{\boldsymbol{\varepsilon}}^p$ and the evolution of the internal variables \dot{q}_* the definitions given in Eq. 4.3 and in Eq. 4.4 are used, respectively

$$\dot{\boldsymbol{\varepsilon}}^p = \dot{\lambda} \frac{\partial G}{\partial \boldsymbol{\sigma}} \quad (4.3)$$

$$\dot{q}_* = -\dot{\lambda} \frac{\partial G}{\partial q_*} \quad (4.4)$$

where $\dot{\lambda} \geq 0$ is the plastic multiplier, $(\cdot)_*$ denotes a scalar or a vector with the dimension of the internal variables, G is the plastic potential function, $\partial G / \partial \boldsymbol{\sigma}$ is the direction of plastic flow (flow rule) and $\partial G / \partial q_*$ is the hardening rule. Inserting the definition of the plastic strain rate defined in Eq. 4.3 into Eq. 4.2, it follows that the stress rate can be calculated according to

$$\dot{\boldsymbol{\sigma}} = \mathbf{C}^e : \left(\dot{\boldsymbol{\varepsilon}} - \dot{\lambda} \frac{\partial G}{\partial \boldsymbol{\sigma}} \right) \quad (4.5)$$

Considering the plastic multiplier $\dot{\lambda}$, it needs to be ensured that the Kuhn–Tucker complementarity condition (Eq. 4.6) is satisfied for any loading condition, thus, the following set of equations is always satisfied

$$\dot{\lambda} \geq 0 \quad , \quad F(\boldsymbol{\sigma}, q_*) \leq 0 \quad , \quad \text{and} \quad \dot{\lambda} F(\boldsymbol{\sigma}, q_*) = 0 \quad (4.6)$$

where F is a scalar referred to as yield function, which enables to distinguish elastic ($F < 0$) and plastic states ($F = 0$), with the restriction that values larger than zero are not admissible. The yield function takes into account the current stress state $\boldsymbol{\sigma}$ and potentially additional internal variables q_* controlling the hardening and softening

behavior of the material, where in case of perfect plasticity, the latter variable is skipped. Considering the definition of the yield and plastic potential functions, it is possible to utilize identical functions ($G = F$, associated plasticity) or to use different functions ($G \neq F$, non-associated plasticity) to better capture the plastic soil behavior. To ensure consistency of the solution with respect to different loading scenarios, the consistency condition defined in Eq. 4.7 needs to be satisfied at any loading step.

$$\frac{\partial F}{\partial \boldsymbol{\sigma}} : \dot{\boldsymbol{\sigma}} + \frac{\partial F}{\partial q_*} \cdot \dot{q}_* = 0 \quad (4.7)$$

Inserting the stress rate defined in Eq. 4.5 into the consistency condition (Eq. 4.7), and expressing the derivatives $\partial F/\partial \boldsymbol{\sigma}$, $\partial G/\partial \boldsymbol{\sigma}$, $\partial F/\partial q_*$ and $\partial G/\partial q_*$ via \mathbf{n} , \mathbf{m} , ξ_* and h_* , respectively, the plastic multiplier is determined according to

$$\mathbf{n} : \mathbf{C}^e : \left(\dot{\boldsymbol{\varepsilon}} - \dot{\lambda} \mathbf{m} \right) - \dot{\lambda} \xi_* \cdot h_* = 0 \quad \Leftrightarrow \quad \dot{\lambda} = \frac{\mathbf{n} : \mathbf{C}^e : \dot{\boldsymbol{\varepsilon}}}{\mathbf{n} : \mathbf{C}^e : \mathbf{m} + \xi_* \cdot h_*} \quad (4.8)$$

Replacing $\dot{\lambda}$ in Eq. 4.5 by Eq. 4.8, it follows that the stress rate reads

$$\dot{\boldsymbol{\sigma}} = \mathbf{C}^e : \dot{\boldsymbol{\varepsilon}} - \frac{(\mathbf{n} : \mathbf{C}^e : \dot{\boldsymbol{\varepsilon}}) \mathbf{C}^e : \mathbf{m}}{\mathbf{n} : \mathbf{C}^e : \mathbf{m} + \xi_* \cdot h_*} \quad (4.9)$$

Rearrangement of terms and replacement of the denominator by $\chi = \mathbf{n} : \mathbf{C}^e : \mathbf{m} + \xi_* \cdot h_*$ yields a more convenient form of the stress rate

$$\begin{aligned} \dot{\boldsymbol{\sigma}} &= \mathbf{C}^e : \dot{\boldsymbol{\varepsilon}} - \frac{1}{\chi} (\mathbf{n} : \mathbf{C}^e : \dot{\boldsymbol{\varepsilon}}) \mathbf{C}^e : \mathbf{m} \\ &= \mathbf{C}^e : \dot{\boldsymbol{\varepsilon}} - \frac{1}{\chi} (\mathbf{C}^e : [\mathbf{m} \otimes \mathbf{n}] : \mathbf{C}^e) : \dot{\boldsymbol{\varepsilon}} \\ &= \underbrace{\left(\mathbf{C}^e - \frac{1}{\chi} \mathbf{C}^e : [\mathbf{m} \otimes \mathbf{n}] : \mathbf{C}^e \right)}_{\mathbf{C}^{ep}} : \dot{\boldsymbol{\varepsilon}} \end{aligned} \quad (4.10)$$

where $\mathbf{m} \otimes \mathbf{n}$ denotes the dyadic product of \mathbf{m} and \mathbf{n} , returning a fourth order tensor, and the term in brackets represents the fourth order elastoplastic tangent modulus \mathbf{C}^{ep}

$$\mathbf{C}^{ep} = \mathbf{C}^e - \frac{1}{\chi} \mathbf{C}^e : (\mathbf{m} \otimes \mathbf{n}) : \mathbf{C}^e \quad (4.11)$$

Rewriting the latter equation in index notation, the continuum elastoplastic tangent modulus is defined as

$$C_{ijkl}^{ep} = C_{ijkl}^e - \frac{C_{ijmn}^e m_{mn} n_{rt} C_{rtkl}^e}{n_{ij} C_{ijkl}^e m_{kl} + \xi_{*i} h_{*i}} \quad (4.12)$$

It should be noted that an exact elastoplastic step – as assumed in the derivation of the continuum solution presented here – is not necessarily successful in a finite-element framework. Therefore, return mapping schemes are commonly adopted which are based on the idea of an elastic predictor or trial stress and a plastic corrector stress. The former is determined as the sum of the current stress and the product of the total strain increment and the elastic stiffness tensor, which might bring the stress to a position outside of the yield surface, whereas the latter projects the stress back to the yield surface.

4.3. Return mapping algorithms

In this work, the primarily selected return mapping algorithm implemented in both elastoplastic constitutive models is the implicit *Closest Point Projection Method* (CPPM) initially proposed by Simo and Taylor (1985) in the version presented by Benz (2007), which is very similar to the *Backward Euler Return Scheme* and the *Closest Point Projection Method* discussed by Abbo (1997) and Huang and Griffiths (2009), respectively. In case the CPPM does not properly converge (e.g. for integration points within slope stability analyses with rather small stresses), a second return mapping scheme is implemented, namely the *Cutting Plane Algorithm* (CPA) discussed by Huang and Griffiths (2009). Moreover, instead of the continuum elastoplastic modulus derived in the previous section, a consistent elastoplastic modulus (Simo and Taylor, 1985; Benz, 2007; Huang and Griffiths, 2009) is determined, which allows for quadratic convergence when combined with CPPM. A schematic illustration of the CPPM and CPA is provided in Fig. 4.1. Details about the implementation of the return mapping algorithms (CPPM and CPA) and the consistent elastoplastic modulus are given in the following paragraphs.

Closest Point Projection Method (CPPM)

Considering non-associated perfect plasticity, a simplified version of the closest point projection method utilized in Benz (2007) is described in this section, in which internal variables controlling the material hardening and softening behavior are not included. The CPPM is implemented within a sub-stepping framework, which ensures that the applied strain increment $\Delta\varepsilon$ is divided in smaller sub-increments $\delta\varepsilon$ based on a predefined threshold strain increment. The previous converged step within the sub-stepping loop, the current step, for which equilibrium is sought, and the current iteration within the return mapping scheme are denoted as n , $n + 1$ and k , respectively. Moreover, the rate equation form used in the previous section is replaced by an incremental formulation,

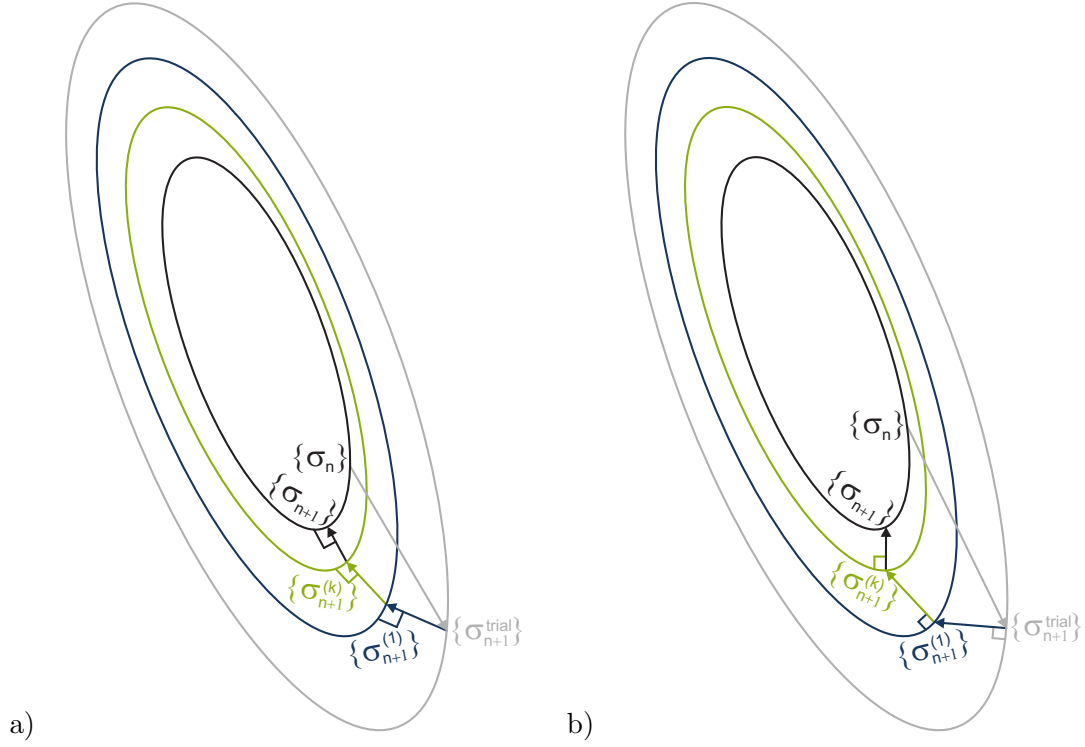


Figure 4.1: Schematic illustration of the (a) Closest Point Projection Method (CPPM) and the (b) Cutting Plane Algorithm (CPA), modified after Huang and Griffiths (2009)

where ${}^{n+1}\Delta\sigma_{ij}^{(k)}$ refers to the increment of stresses at the current iteration of the current step.

The general procedure of the CPPM is as follows:

1. For the current step ($n + 1$), initialize the iteration counter $k = 0$ and the initial plastic multiplier $\Delta\lambda = 0$
2. Calculate the trial (elastic) stress and the yield function for the trial stress

$${}^{Trial}\sigma_{ij} = {}^n\sigma_{ij} + C_{ijkl}^e {}^{n+1}\delta\varepsilon_{kl}$$

$${}^{Trial}F^{(0)} = F({}^{Trial}\sigma_{ij})$$

3. IF ${}^{Trial}F^{(0)} \leq 0$, update the stress (${}^{n+1}\sigma_{ij} = {}^{Trial}\sigma_{ij}$) and EXIT the algorithm
4. Determine the first derivatives of the yield and potential functions for the trial stress (${}^{Trial}n_{mn}, {}^{Trial}m_{pq}$) and calculate starting values for the return mapping algorithm

$$\Delta\lambda^{(k)} = \frac{{}^{Trial}F^{(0)}}{{}^{Trial}n_{nm} C_{nmpq}^e {}^{Trial}m_{pq}}$$

$${}^{n+1}\sigma_{ij}^{(k)} = {}^{Trial}\sigma_{ij} - \Delta\lambda^{(k)} C_{ijkl}^e {}^{Trial}m_{kl}$$

5. IF ${}^{n+1}F^{(k)} = F^{(n+1)}\sigma_{ij}^{(k)} \leq 0$, EXIT the algorithm

6. Calculate the derivatives ${}^{n+1}n_{mn}^{(k)}$, ${}^{n+1}m_{kl}^{(k)}$ and $\left. \frac{\partial m_{kl}}{\partial \sigma_{mn}} \right|_{n+1}^{(k)}$

7. Calculate the residual stress

$$r_{ij}^{(k)} = {}^{n+1}\sigma_{ij}^{(k)} - \left(Trial\sigma_{ij} - \Delta\lambda^{(k)} C_{ijkl}^e {}^{n+1}m_{kl}^{(k)} \right)$$

8. Update the plastic multiplier

$$\Xi_{ijmn}^{(k)} = \left(I_{ijmn} + \Delta\lambda^{(k)} C_{ijkl}^e \left. \frac{\partial m_{kl}}{\partial \sigma_{mn}} \right|_{n+1}^{(k)} \right)^{-1}$$

$$\delta\lambda^{(k)} = \frac{{}^{n+1}F^{(k)} - r_{ij}^{(k)} \Xi_{ijmn}^{(k)} {}^{n+1}n_{mn}^{(k)}}{C_{ijkl}^e {}^{n+1}m_{kl}^{(k)} \Xi_{ijmn}^{(k)} {}^{n+1}n_{mn}^{(k)}}$$

$$\Delta\lambda^{(k+1)} = \Delta\lambda^{(k)} + \delta\lambda^{(k)}$$

9. Update the stress tensor

$${}^{n+1}\sigma_{ij}^{(k+1)} = Trial\sigma_{ij} - \Delta\lambda^{(k+1)} C_{ijkl}^e {}^{n+1}m_{kl}^{(k)}$$

10. Update the iteration counter and return to Step 5

$$k = k + 1$$

It should be noted from the description of the CPPM presented above that the determination of the second derivative of the potential function (step 6) and the inverse of a fourth order tensor (step 8) lead to high computational costs of the CPPM when compared to other return mapping schemes (e.g. CPA). Still, in case the CPPM is coupled with a consistent elastoplastic modulus, quadratic convergence in the Newton-Raphson method can be achieved (Huang and Griffiths, 2009).

Consistent elastoplastic modulus

Utilizing the derivatives ${}^{n+1}n_{mn}$ and ${}^{n+1}m_{kl}$ and the fourth order tensor ${}^{n+1}\Xi_{ijmn}$ updated within the CPPM iterations as well as the fourth order isotropic elastic stiffness tensor C_{ijkl}^e , the consistent elastoplastic modulus C_{ijkl}^{ep} is calculated at the end of every step of the sub-stepping routine in accordance with Benz (2007) and Huang and Griffiths (2009) via

$$C_{ijkl}^{ep} = R_{ijkl} - \frac{R_{ijmn} {}^{n+1}m_{mn} {}^{n+1}n_{rs} R_{rskl}}{{}^{n+1}n_{ij} R_{ijkl} {}^{n+1}m_{kl}} \quad (4.13)$$

with

$$R_{ijkl} = {}^{n+1}\Xi_{ijmn} C_{mnkl}^e \quad (4.14)$$

Considering the sub-stepping approach in the material routine, the average stiffness determined by averaging over the elastic steps (n_e) and the elastoplastic steps (n_p) according to Eq. 4.15 is returned to the element routine and assembled to the global system of equations.

$$C_{mnpq} = \frac{\sum_i^{n_e} C_{mnpq,i}^e + \sum_j^{n_p} C_{mnpq,j}^{ep}}{n_e + n_p} \quad (4.15)$$

Cutting Plane Algorithm (CPA)

The cutting plane algorithm is a simple return mapping scheme that allows for returning to the yield surface without determination of second derivatives. However, although the computational effort of CPA is less compared to CPPM, it can only be combined with a consistent elastoplastic modulus if the fourth order tensor Ξ_{ijmn} is determined additionally, which again includes determination of the second derivative of the potential function and the inverse of a fourth order tensor. Huang and Griffiths (2009) noted that the CPA might also be combined with the continuum elastoplastic modulus according to Eq. 4.12, to avoid the determination of second derivatives.

The general procedure of the CPA is as follows:

1. For the current step ($n + 1$), initialize the iteration counter $k = 0$ and the initial plastic multiplier $\Delta\lambda = 0$
2. Calculate the trial (elastic) stress

$${}^{n+1}\sigma_{ij}^{(k)} = {}^n\sigma_{ij} + C_{ijkl}^e {}^{n+1}\Delta\varepsilon_{kl}$$

3. IF ${}^{n+1}F^{(k)} = F({}^{n+1}\sigma_{ij}^{(k)}) \leq 0$, EXIT the algorithm
4. Calculate the derivatives ${}^{n+1}n_{mn}^{(k)}$ and ${}^{n+1}m_{pq}^{(k)}$
5. Update the plastic multiplier

$$\Delta\lambda^{(k)} = \frac{{}^{n+1}F^{(k)}}{{}^{n+1}n_{nm}^{(k)} C_{nmpq}^e {}^{n+1}m_{pq}^{(k)}}$$

6. Update the stress tensor

$${}^{n+1}\sigma_{ij}^{(k+1)} = {}^{n+1}\sigma_{ij}^{(k)} - \Delta\lambda^{(k)} C_{ijkl}^e {}^{n+1}m_{kl}^{(k)}$$

7. Update the iteration counter and return to Step 3

$$k = k + 1$$

4.4. Verification

4.4.1. General concept

In this work, the Mohr-Coulomb model and the Matsuoka-Nakai model have been implemented in `Incremental Driver` and `numgeo` following the description of the models in Sections 2.3.1 and 2.3.2, respectively, and the implicit integration schemes described in Section 4.3. For verification, results of element test simulations performed with both models are compared to benchmark simulations using implementations of the same models in well-established FE codes. As depicted in Fig. 4.2, the element tests conducted include triaxial compression tests (TXC), triaxial extension tests (TXE) and direct simple shear tests (DSS). Considering the initial stress states, TXC, TXE and DSS_{iso} are performed starting from an initial isotropic mean effective stress of $p' = 100$ kPa, whereas DSS_{K0} is performed starting from an anisotropic state with an initial vertical effective stress of $\sigma'_v = 100$ kPa and a lateral stress of $\sigma'_h = K_0 \cdot \sigma'_v$, where the lateral earth pressure coefficient has been selected in accordance with $K_0 = 1 - \sin \varphi$ (Jaky, 1944). All tests have been performed under drained conditions.

Simulations of the element tests have been conducted for two different materials, a purely frictional material (Material 1) with a friction angle of $\varphi = 30^\circ$ and a cohesion of $c = 0$ kPa and a cohesive-frictional material (Material 2) with a friction angle of $\varphi = 20^\circ$ and a cohesion of $c = 20$ kPa. Further variation of material parameters considered in the verification process is related to the dilation angle ψ , which is varied in the range of $0.0 \leq \psi/\varphi \leq 1.0$. With regard to proper terminology, it should be noted that $\psi/\varphi = 1.0$ and $\psi/\varphi < 1.0$ are referred to as associated and non-associated flow rule, respectively. The elastic behavior in the MC and MN model is described with respect to the elastic material parameters: Young's modulus E and Poisson's ratio ν . Both elastic material parameters are kept constant throughout the verification and – if not further specified – take the values $E = 30.0$ MPa and $\nu = 0.333$. Increments of stresses and strains are given

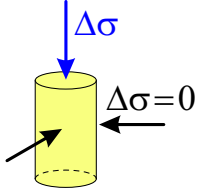
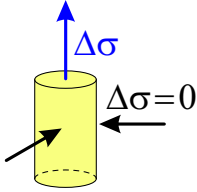
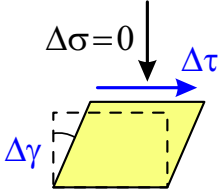
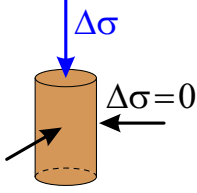
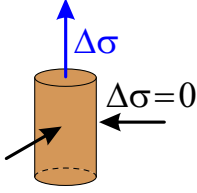
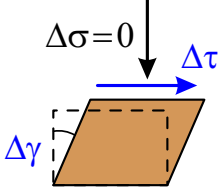
Material	TXC	TXE	DSS _{iso} / DSS _{K0}
Frictional $\varphi = 30^\circ$ $c = 0 \text{ kPa}$			
Cohesive-frictional $\varphi = 20^\circ$ $c = 20 \text{ kPa}$			

Figure 4.2: Overview of materials and tests used for verification of the elastoplastic models implemented within the framework of this study

here, thus, it should be clear that a test condition $\Delta\sigma = 0$ refers to a stress component that remains constant during the test.

4.4.2. Mohr-Coulomb model

In this work, the Mohr-Coulomb model in the version proposed by Abbo et al. (2011) has been implemented in `Incremental Driver` and `numgeo`. As discussed in Section 2.3.1, this model slightly deviates from the original Mohr-Coulomb model in terms of the shape of the yield surface due to a hyperbolic approximation in the meridional plane (i.e. deviatoric versus mean stress space) and rounded corners in the deviatoric plane, the former and latter controlled by material parameters describing the distance towards the apex $a = \alpha \cot \varphi$ and the transition Lode angle θ_t , respectively. Following the recommendations of Abbo and Sloan (1995) and Abbo et al. (2011) for practical use of the model, $\alpha \approx 0.05$ and $25^\circ \leq \theta_t \leq 29.5^\circ$ enable good approximations of the original model while ensuring numerical stability at the transition between the original surface and the approximation of the rounded corners. In this section, $\alpha = 0.05$ and $\theta_t = 29.5^\circ$ were selected. Additional simulations emphasizing the influence of the transition angle θ_t on the results of triaxial tests are presented subsequently to the verification at the end of this section.

The verification is conducted using benchmark simulations performed with the Mohr-Coulomb model available in `Plaxis2D` considering four element test setups (TXC, TXE,

DSS_{iso} and DSS_{K0}), two materials (frictional material and cohesive-frictional material) and four dilation ratios ($\psi/\varphi = 0.0$, $\psi/\varphi = 0.33$, $\psi/\varphi = 0.67$ and $\psi/\varphi = 1.0$). Further simulations performed for verification purposes also included variations of ν . Although similar good agreement between the benchmark and the current results were seen in those simulations, the results are not shown in order not to lose focus on the essential aspects.

The results of the triaxial compression (TXC) and extension (TXE) tests conducted with the purely frictional material (Material 1) are presented in terms of deviatoric stress q versus axial strain ε_1 and volumetric strain ε_{vol} versus axial strain ε_1 in Fig. 4.3. As can be seen from this figure, the results obtained with numgeo (solid lines) and Plaxis2D

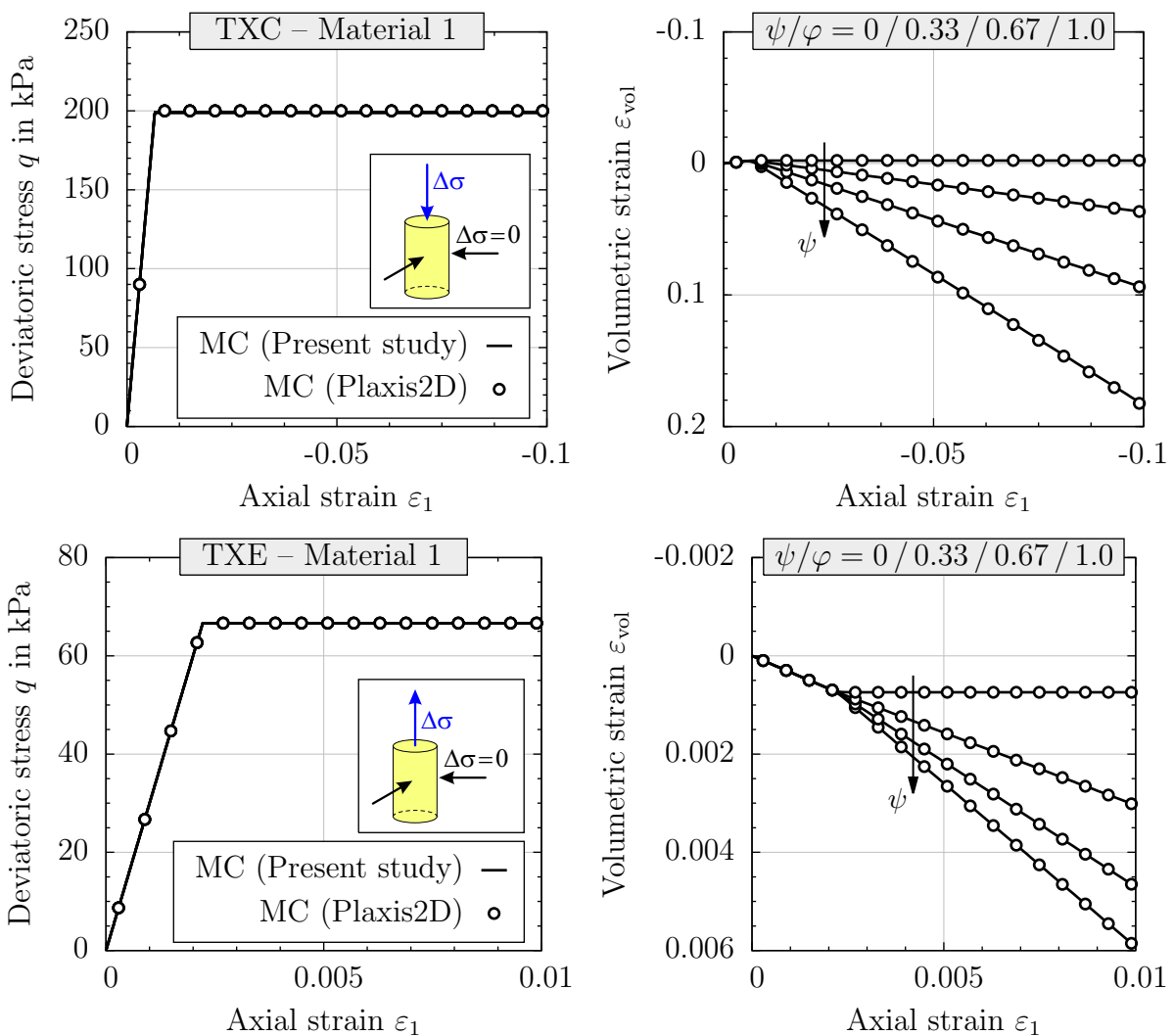


Figure 4.3: Deviatoric stresses and volumetric strains during triaxial compression and extension tests on a frictional material ($\varphi = 30^\circ$) simulated using the original Mohr-Coulomb model (Plaxis2D) and the approximation ($\theta_t = 29.5^\circ$, $\alpha = 0.05$, present study)

(symbols) are in good agreement. Only very small deviations are observed for the final deviatoric stress for all ψ/φ as well as for the volumetric strains for $\psi/\varphi \geq 0.67$. The differences between the models for triaxial compression ($\theta = 30^\circ$) and extension tests ($\theta = -30^\circ$) can be explained with regard to the shape of the yield surface. Since the surface (Abbo et al., 2011) is described by rounded corners in the deviatoric plane for $|\theta| > \theta_t = 29.5^\circ$, the distance between the hydrostatic axis and the yield surface at TXC and TXE is smaller, resulting in a reduced ultimate strength. Comparing the results of `numgeo` and `Plaxis2D` for the triaxial compression and extension tests, it is apparent that the differences with respect to deviatoric stresses and volumetric strains are smaller for the TXE test, since the shapes of the yield surfaces are in better agreement for $\theta = -30^\circ$ (Fig. 2.16). Moreover, Fig. 4.3 shows that a good agreement between the results of `numgeo` and `Plaxis2D` is obtained for different dilation angles, which mainly control the volumetric behavior in triaxial compression and extension tests.

To analyze the performance of the MC implementation under plane strain conditions, direct simple shear tests were conducted with `numgeo` and `Plaxis2D`. The results of the direct simple shear tests starting from an isotropic (DSS_{iso}) and from a K_0 (DSS_{K_0}) state conducted with the purely frictional material (Material 1) are presented in terms of shear stress τ versus shear strain γ and volumetric strain ε_{vol} versus shear strain γ in Fig. 4.4. It is obvious from this figure that – independent of the initial stress state and the dilation angle – the results of both models perfectly coincide for the DSS tests. As the Lode angles associated with the loading and the initial states in the direct simple shear tests are smaller than the transition Lode angle ($|\theta| \leq \theta_t$), both models are described by identical yield surfaces and by identical potential surfaces. Therefore, it should be clear that the same responses were expected. Considering all element tests conducted with Material 1, it can be concluded that the implementation of the approximated Mohr-Coulomb model performs well for purely frictional materials under different stress paths.

To ensure that the implementation also predicts the correct material responses for $c > 0$ kPa, the same four tests (TXC, TXE, DSS_{iso} and DSS_{K_0}) are repeated considering a cohesive-frictional material (Material 2). Considering a cohesive-frictional material with $c > 0$ kPa, it should be noted that the yield surface – with respect to the shape of the original MC model – is not only modified due to the rounded corners in the deviatoric plane, but also due to hyperbolic approximation in the meridional plane. In case of the purely frictional material, the hyperbolic approximation had no effect on the shape of the yield surface as the shape parameter $a = \alpha \cdot c \cdot \cot \varphi$ was zero due to $c = 0$ kPa. The results of the triaxial compression (TXC) and extension (TXE) tests conducted with the

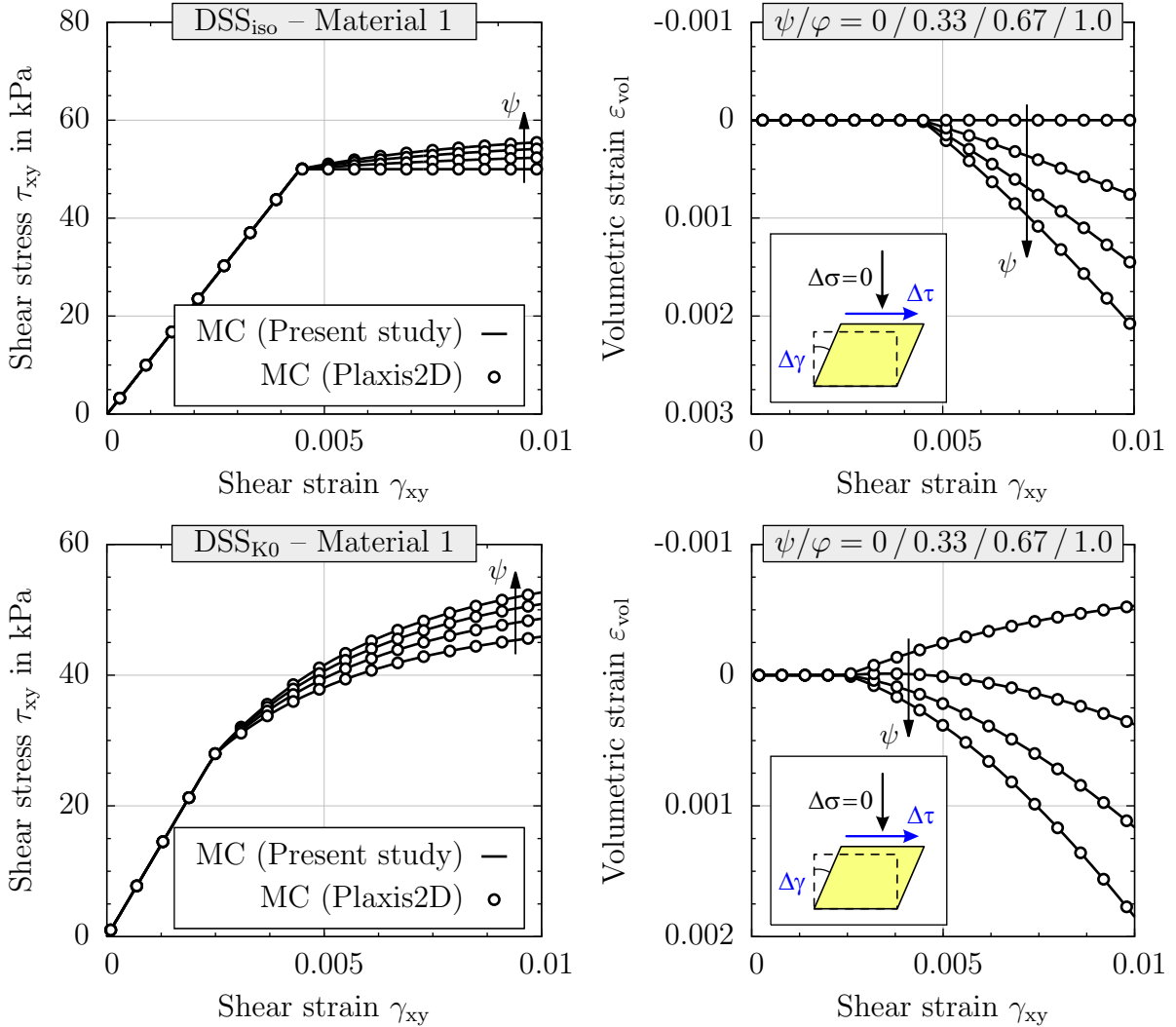


Figure 4.4: Shear stresses and volumetric strains during direct simple shear tests starting from an isotropic and K_0 stress state with a frictional material ($\varphi = 30^\circ$) simulated using the original Mohr-Coulomb model (Plaxis2D) and the approximation ($\theta_t = 29.5^\circ$, $\alpha = 0.05$, present study)

cohesive-frictional material (Material 2) are presented in terms of deviatoric stress q versus axial strain ε_1 and volumetric strain ε_{vol} versus axial strain ε_1 in Fig. 4.5. It is apparent from this figure that the deviatoric stresses as well as the volumetric strains compare well for the benchmark model and the model implemented in the present study. Although small deviations are observed, it can be stated that the influence of the approximation – with rounded corners in the deviatoric and a hyperbolic function in the meridional plane – on the results of both types of triaxial tests is small. A potential reason for this observation may be attributed to the fact that the shapes of the original and the modified

yield surface are very similar for compressive stresses, whereas differences may be more pronounced for stress paths directing towards the tip/apex of the yield surface.

Considering plane strain conditions, direct simple shear tests (DSS_{iso} and DSS_{K0}) were conducted with `numgeo` and `Plaxis2D` for Material 2. As can be seen from the results presented in the τ versus γ and ε_{vol} versus γ plots in Fig. 4.6, very good agreement is achieved for all simulations, including variations of the dilation angle ψ . Therefore, it can be concluded that the implementation of the Mohr-Coulomb model in the version

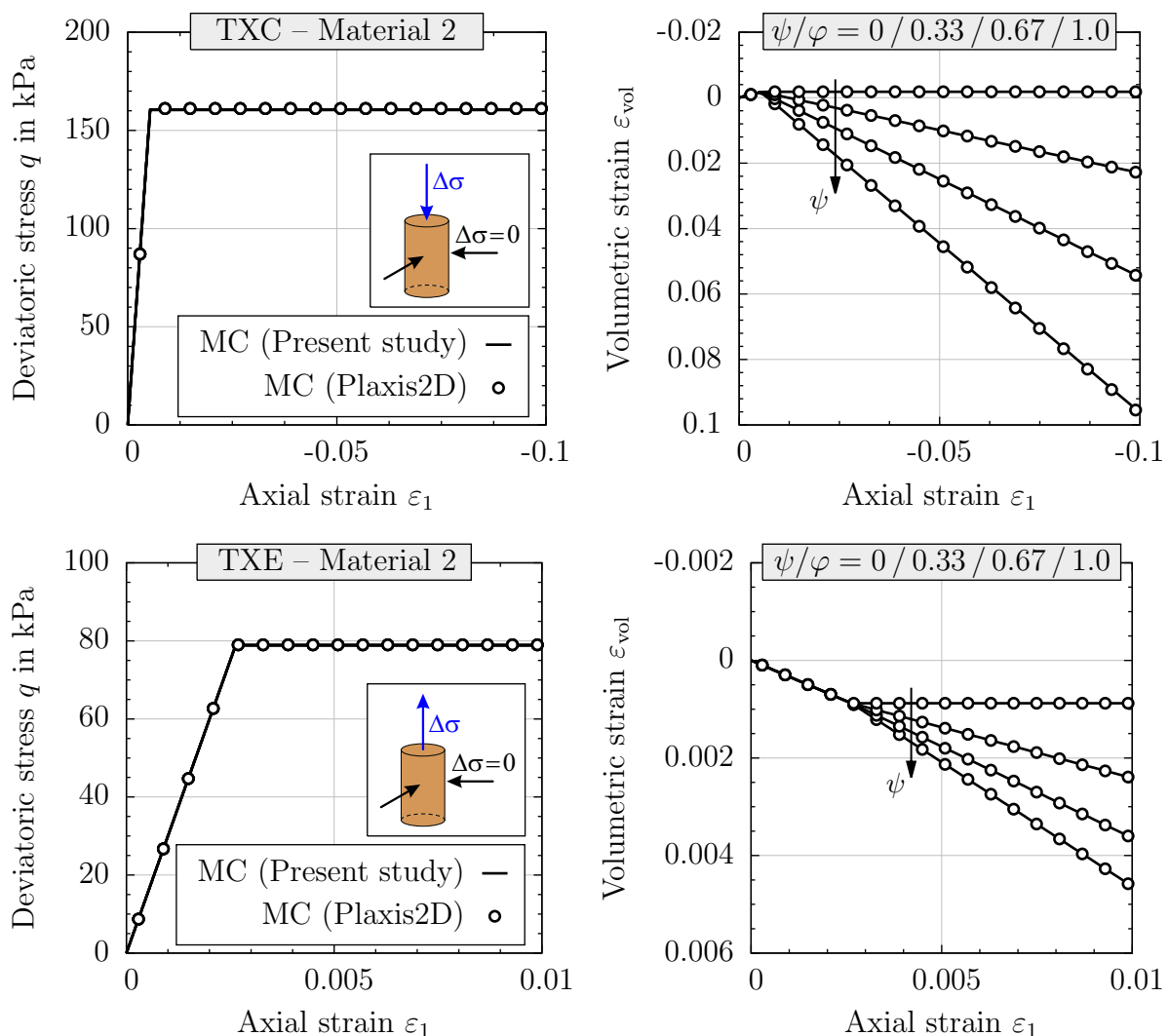


Figure 4.5: Deviatoric stresses and volumetric strains during triaxial compression and extension tests on a cohesive-frictional material ($\varphi = 20^\circ$, $c = 20$ kPa) simulated using the original Mohr-Coulomb model (Plaxis2D) and the approximation ($\theta_t = 29.5^\circ$, $\alpha = 0.05$, present study)

of Abbo et al. (2011) was successful for frictional and cohesive-frictional materials as well as for associated and non-associated flow rules. However, as the results obtained with numgeo and Plaxis2D do not perfectly match for triaxial compression and extension states due to the different shapes of the yield surface, discussion with respect to the effect of the material parameter θ_t is provided in the subsequent paragraphs to enhance the comprehensibility of the implemented model.

To emphasize the influence of the transition angle θ_t on the ultimate strength defined with regard to the deviatoric stress q under triaxial compression and extension conditions,

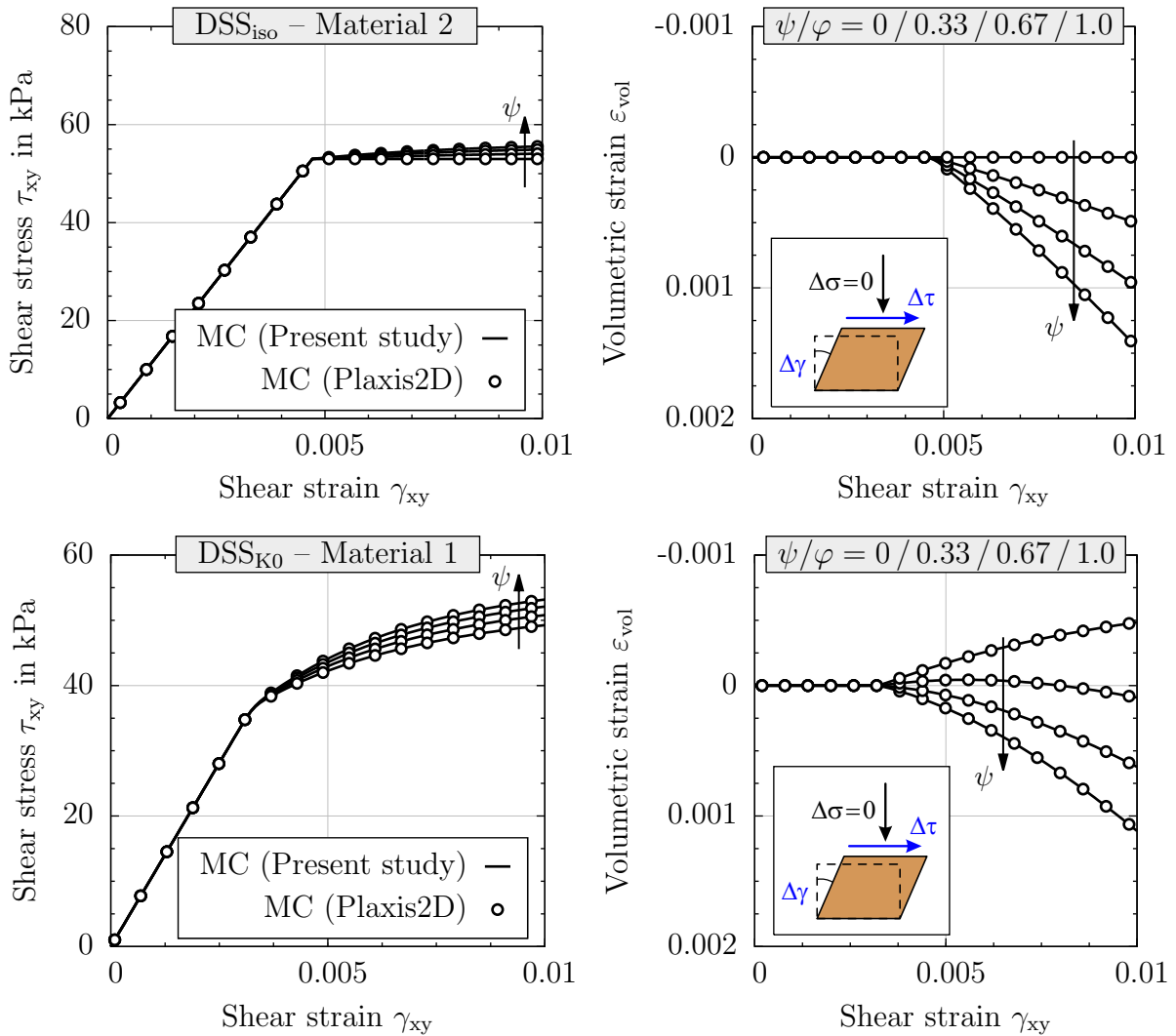


Figure 4.6: Shear stresses and volumetric strains during direct simple shear tests starting from an isotropic and K_0 stress state with a cohesive-frictional material ($\varphi = 20^\circ$, $c = 20$ kPa) simulated using the original Mohr-Coulomb model (Plaxis2D) and the approximation ($\theta_t = 29.5^\circ$, $\alpha = 0.05$, present study)

additional simulations (TXC and TXE) are performed using both materials and transition angles in the range of $25^\circ \leq \theta_t \leq 29.5^\circ$. The ultimate strength obtained in these simulations is normalized with respect to the ultimate strength of the original Mohr-Coulomb criterion, q_{MC} . The latter can either be taken from the respective *Plaxis2D* simulations or analytically determined using the definition of the Mohr-Coulomb criterion (Eq. 2.18) considering mechanical sign convention with principal stresses ordered according to $\sigma_1 \leq \sigma_2 \leq \sigma_3$. Rearranging terms with respect to Eq. 2.18, for a triaxial compression test with $\sigma_3 = \text{const}$ representing the lateral stress, the ultimate stress σ_1 acting in vertical direction is determined according to Eq. 4.16. In case of a triaxial extension test, where the lateral stress corresponds to σ_1 and the stress σ_3 in vertical direction is sought, Eq. 4.17 can be applied.

$$\sigma_{1,MC,ult} = \sigma_3 \cdot \frac{1 + \sin \varphi}{1 - \sin \varphi} - \frac{2 \cdot c \cdot \cos \varphi}{1 - \sin \varphi} \quad \text{for} \quad \sigma_1 \leq \sigma_2 \leq \sigma_3 \quad (4.16)$$

$$\sigma_{3,MC,ult} = \sigma_1 \cdot \frac{1 - \sin \varphi}{1 + \sin \varphi} + \frac{2 \cdot c \cdot \cos \varphi}{1 + \sin \varphi} \quad \text{for} \quad \sigma_1 \leq \sigma_2 \leq \sigma_3 \quad (4.17)$$

The results of this parametric study are presented in Fig. 4.7 in terms of q/q_{MC} versus θ_t plots for Material 1 and 2. As can be seen from this figure, the normalized ultimate strength increases with increasing transition angle, thus, the difference between the original and the approximated Mohr-Coulomb model decreases. Independent of the type of test (TXC, TXE) or the material, it is observed that the maximum deviation between both

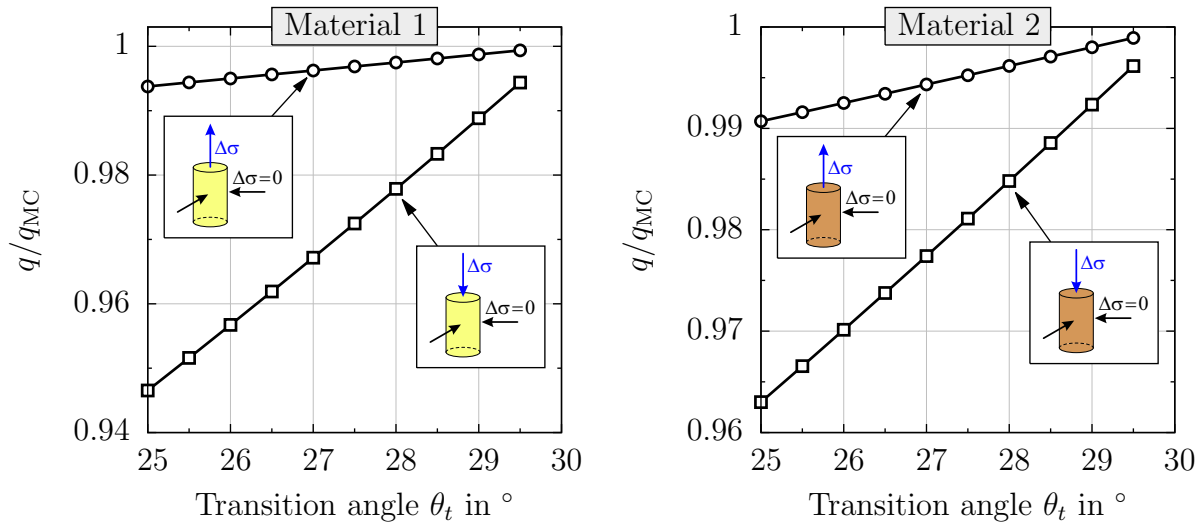


Figure 4.7: Influence of transition angle θ_t on normalized ultimate strength q/q_{MC} considering triaxial compression and extension tests for a purely frictional material ($\varphi = 30^\circ$) (left) and a cohesive-frictional material ($\varphi = 20^\circ$, $c = 20$ kPa) (right)

models is obtained for $\theta_t = 25^\circ$. Comparing q/q_{MC} for triaxial compression and extension tests, it is apparent that the normalized ultimate strength is significantly smaller for the former test with minimum values of 0.946 and 0.963 for the frictional and the cohesive-frictional material, respectively. In contrast, for the triaxial extension test, $q/q_{MC} > 0.99$ holds for both material parameter sets investigated here. As stated above and depicted in Fig. 2.16, these larger q/q_{MC} values for TXE can be explained with respect to a closer fit of the yield surfaces of the original and the approximated models in the deviatoric plane for triaxial extension conditions with $\theta = -30^\circ$ compared to triaxial compression conditions with $\theta = 30^\circ$.

Analyzing the difference between the models with respect to changing material parameters, it should be noted that for triaxial compression conditions (TXC) the normalized ultimate strength – as a measure of similarity between both models – decreases with increasing friction angle and increasing distance between the tip of the original and the approximated MC model (material parameter α). Moreover, a minor decrease of q/q_{MC} is observed for increasing cohesion values. In contrast, for triaxial extension conditions (TXE), it is observed that q/q_{MC} increases with increasing friction angle, while the other trends remain unchanged.

4.4.3. Matsuoka-Nakai model

Although many sophisticated constitutive models make use of the Matsuoka-Nakai criterion, for instance for the definition of the yield surface in the Hardening Soil Small model (Benz, 2007), the limit state surface in Hypoplasticity (von Wolfersdorff, 1996) or the bounding surface in Sanisand (Dafalias and Manzari, 2004; Taiebat and Dafalias, 2008), the original linear-elastic, perfectly-plastic Matsuoka-Nakai (MN) model is rarely implemented in geotechnical finite-element codes. Therefore, it is difficult to find MN implementations for verification purposes. Potential reasons for the lack of MN model implementations in these codes may be manifold and are not further discussed here. However, as finite-element codes such as **Abaqus** or **Plaxis** enable the import of user-defined material routines, verification of the MN model implemented in **Incremental Driver** and **numgeo** was conducted with such a routine. To be more specific, Prof. Franz Tschuchnigg and Mr. Stephan Rauter from TU Graz kindly provided results of benchmark simulations that have been performed using a MN implementation called 'Matsuoka-Nakai no hardening (MNnh)' developed by Prof. Thomas Benz, which was imported as a user-defined material into the finite-element code **Plaxis2D**.

Verification of the current implementation is conducted for the MN model with Drucker-Prager potential surface considering a cone fitted to the compression corners of the MC/MN model (i.e. cone '1' in Fig. 2.11). Similar to the verification procedure applied for the MC model, triaxial compression (TXC) and extension (TXE) tests as well as direct simple shear tests starting from an isotropic state (DSS_{iso}) and from a K_0 state (DSS_{K_0}) are simulated for two different materials, a purely frictional material and a cohesive-frictional material, considering the initial stress conditions reported in Section 4.4.1. Note that in contrast to the element test simulations with the MC model, the Poisson's ratio is calculated from $\nu = K_0/(1 + K_0)$ with $K_0 = 1 - \sin \varphi$. Regarding the variation of the dilation angle, three ratios of ψ/φ covering values between zero and one are investigated for verification purposes.

It should be noted here that – in contrast to the verification of the Mohr-Coulomb model performed in Section 4.4.2 – for the verification of the Matsuoka-Nakai model, no differences between the results of the MNnh and the MN model should be accepted since both models have been implemented with the same yield function (Eq. 2.26) and potential function (Eq. 2.19). Therefore, any deviations observed in the results of the element tests would indicate errors in the implementations. Moreover, as the Matsuoka-Nakai and the Mohr-Coulomb criterion should yield identical ultimate shear strength for triaxial compression and extension conditions due to the same size of the yield surface for $\theta = \pm 30^\circ$, results of the latter criterion can also be used for verification purposes.

The results of the triaxial compression (TXC) and extension (TXE) tests conducted with the purely frictional material (Material 1) are presented in deviatoric stress q versus axial strain ε_1 and volumetric strain ε_{vol} versus axial strain ε_1 plots in Fig. 4.8. It can be seen from this figure that the MNnh model imported as a user-defined material into `Plaxis2D` (symbols) and the MN model implemented in `numgeo` (solid lines) yield identical results in terms of ultimate shear strength as well as volumetric behavior. This observation also holds for variations of the dilation angle in the range of $0 \leq \psi/\varphi \leq 1.0$. Comparing the results of the triaxial tests conducted with the MN model on Material 1 depicted in Fig. 4.8 with the results of the original Mohr-Coulomb model shown in Fig. 4.3 very good agreement of the ultimate strength is observed, which can be seen as an additional indicator for a correct implementation of the Matsuoka-Nakai model.

Investigating the behavior under plane strain conditions in terms of direct simple shear tests starting from either isotropic or anisotropic stress states on a purely frictional material, it can be seen from Fig. 4.9 that the shear stress versus shear strain curves as well as the volumetric strain versus shear strain curves are identical for the MNnh benchmark sim-

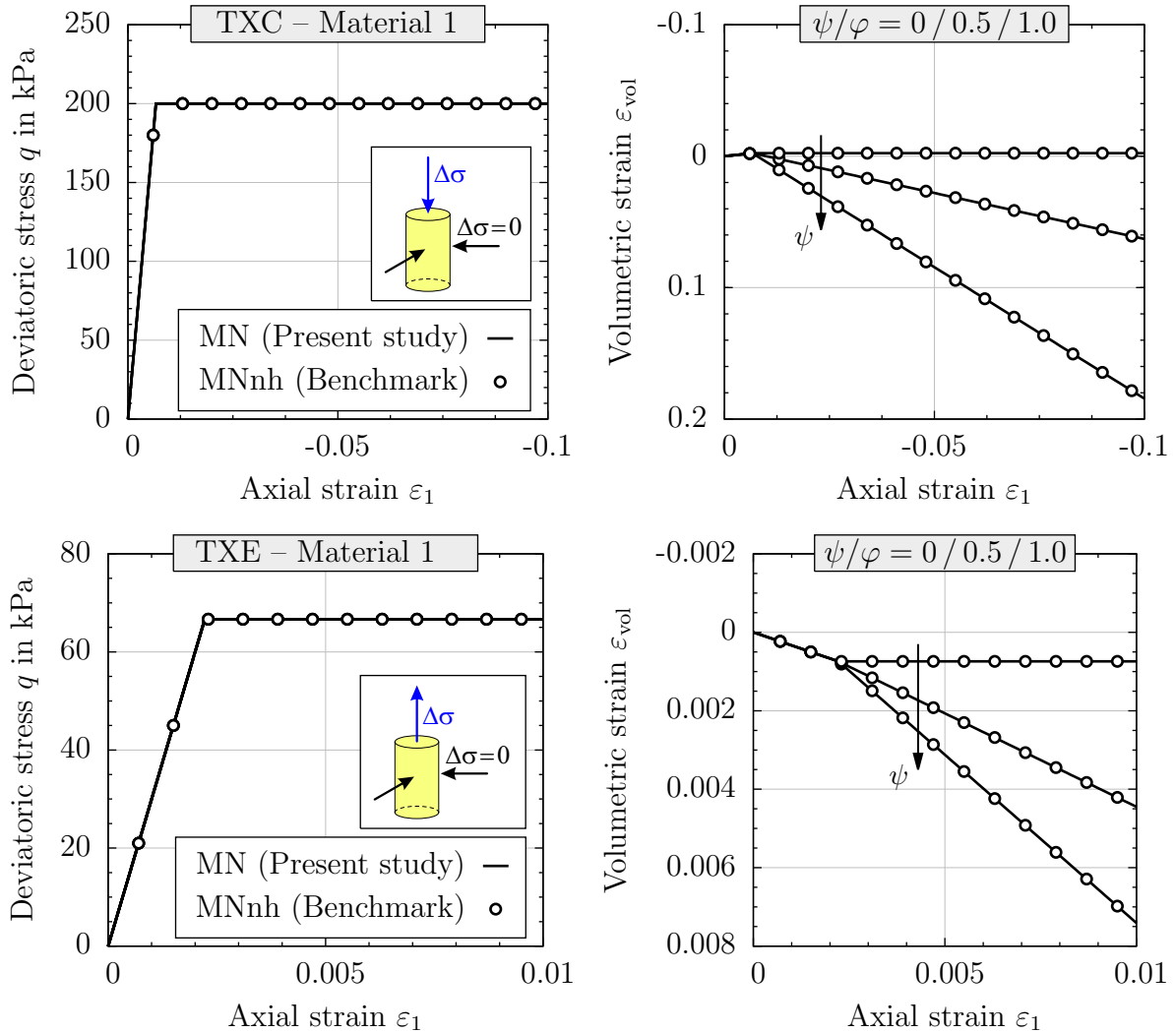


Figure 4.8: Deviatoric stresses and volumetric strains during triaxial compression and extension tests on a frictional material ($\varphi = 30^\circ$) simulated using two implementations of the Matsuoka-Nakai (MN) model

ulations and the MN model implemented in `numgeo`. This applies for the non-associated cases with $\psi/\varphi = 0.0$ and $\psi/\varphi = 0.5$ as well as for the case of an associated flow rule considering $\psi/\varphi = 1.0$. Furthermore, analysis of the volumetric strains obtained for the DSS_{K0} test reveals that the contractive and the dilative volumetric behavior is captured precisely. Therefore, it can be concluded that the Matsuoka-Nakai model, which has originally been formulated for purely frictional soils, has been implemented accurately. Further simulations are conducted to also verify the implementation of the extended Matsuoka-Nakai model (Matsuoka and Sun, 1995; Griffiths and Huang, 2009), which enables the additional consideration of the cohesion.

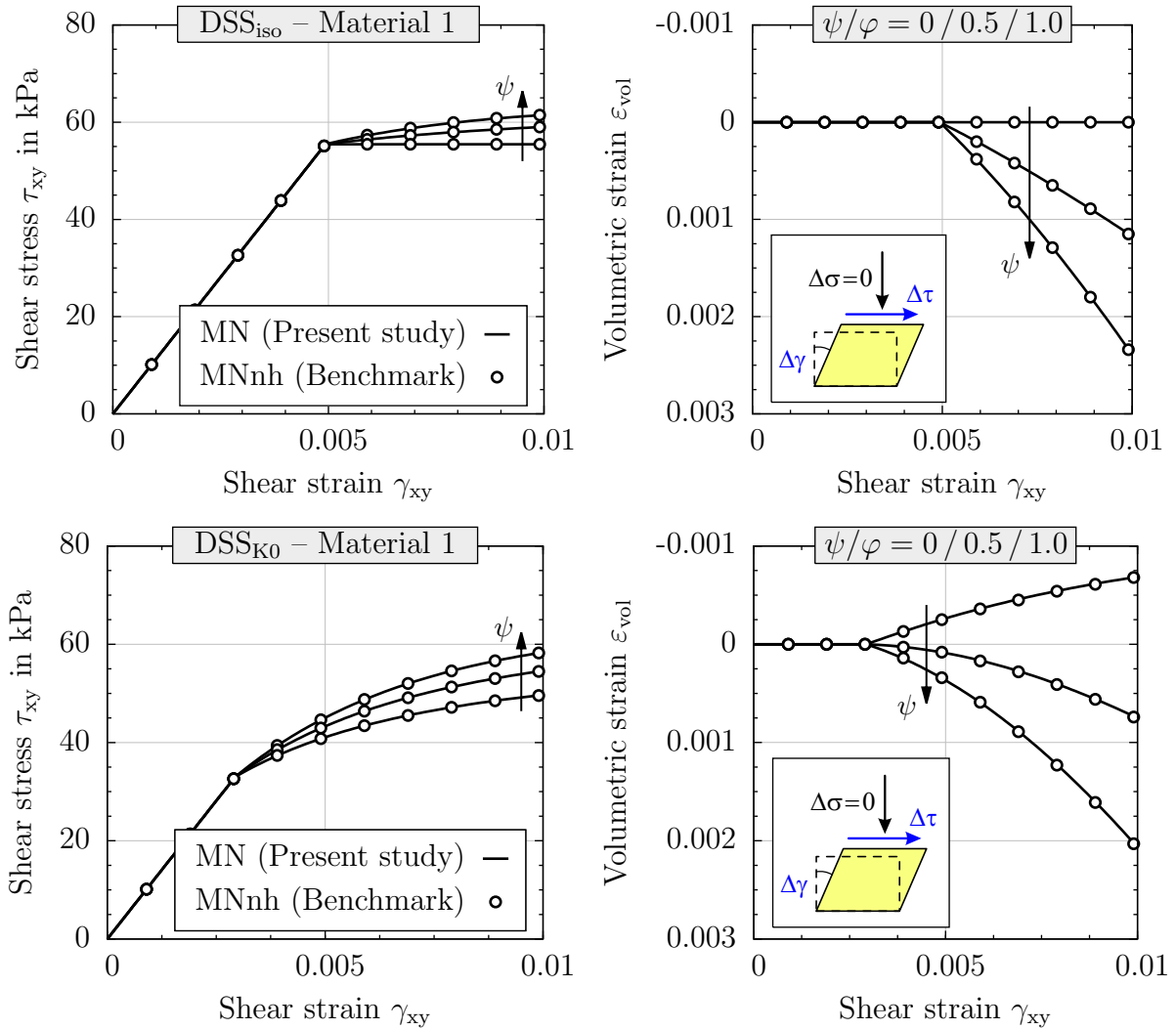


Figure 4.9: Shear stresses and volumetric strains during direct simple shear tests starting from an isotropic and K_0 stress state with a frictional material ($\varphi = 30^\circ$) simulated using two implementations of the Matsuoka-Nakai (MN) model

For verification of the extended Matsuoka-Nakai model, triaxial compression (TXC) and extension (TXE) tests and simple shear tests (DSS_{iso} and DSS_{K_0}) are conducted using a cohesive-frictional material with the shear parameters provided in Fig. 4.2 and a Poisson's ratio of $\nu = K_0/(1 + K_0) = 0.397$. In Fig. 4.10, the evolution of deviatoric stresses and volumetric strains are presented for TXC and TXE tests. Considering that the MNnh implementation also incorporates the definitions of the extended Matsuoka-Nakai model, it is clear from this figure that good agreement between the results of the benchmark model and the current implementation is obtained for triaxial conditions. This also holds

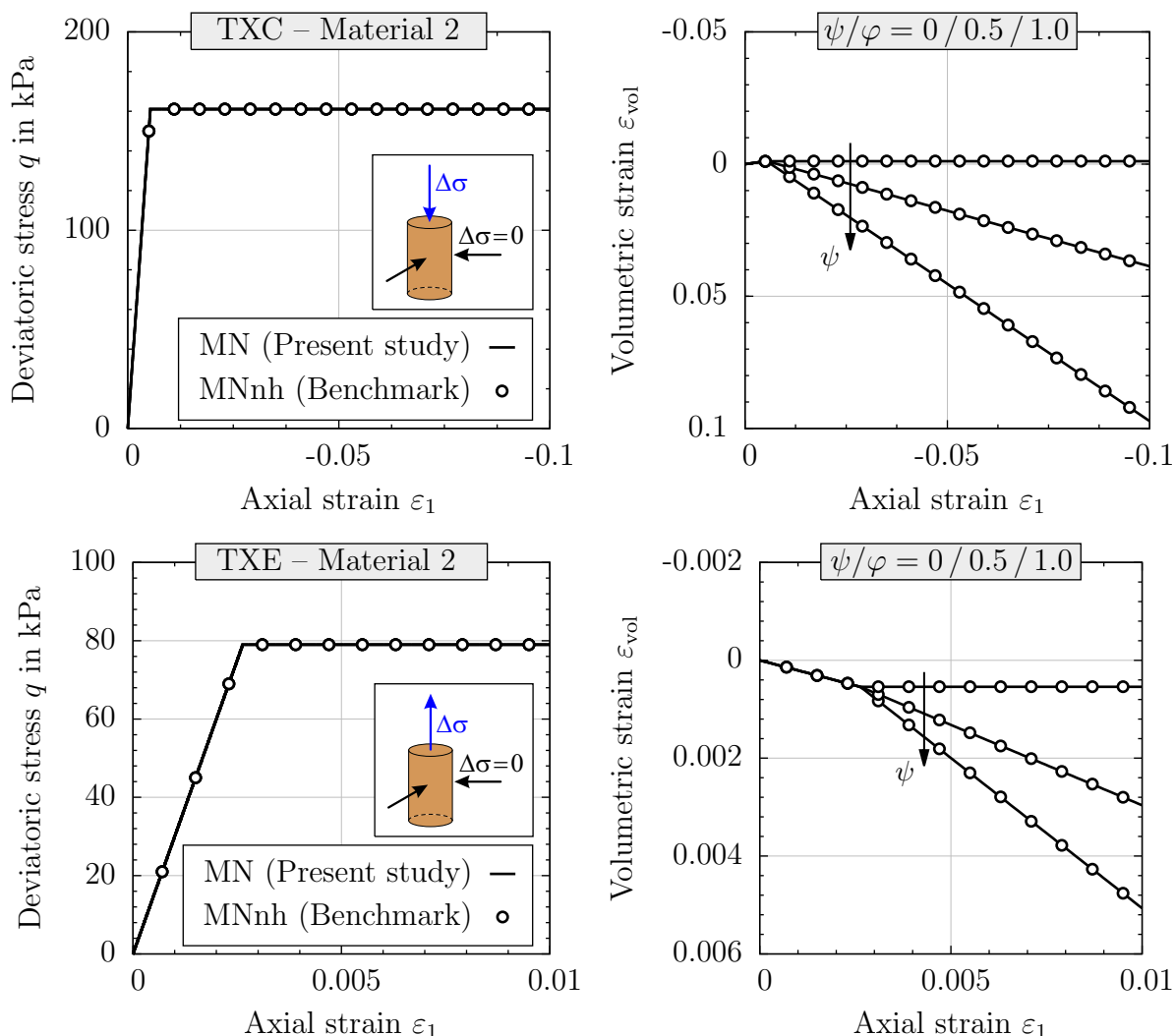


Figure 4.10: Deviatoric stresses and volumetric strains during triaxial compression and extension tests on a cohesive-frictional material ($\varphi = 20^\circ$, $c = 20$ kPa) simulated using two implementations of the Matsuoka-Nakai (MN) model

for plane strain conditions analyzed in terms of simple shear tests starting from isotropic and anisotropic stress states with results depicted in Fig. 4.11.

In this section, it has been shown with the help of a series of element test simulations and comparisons to benchmark simulations that both models, the approximated Mohr-Coulomb model proposed by Abbo et al. (2011) as well as the extended Matsuoka-Nakai model (Matsuoka and Sun, 1995; Griffiths and Huang, 2009), have been implemented accurately into `numgeo`. The implementations of the models into the latter finite element code will be further elaborated with regard to strength reduction analyses discussed in the subsequent chapter.

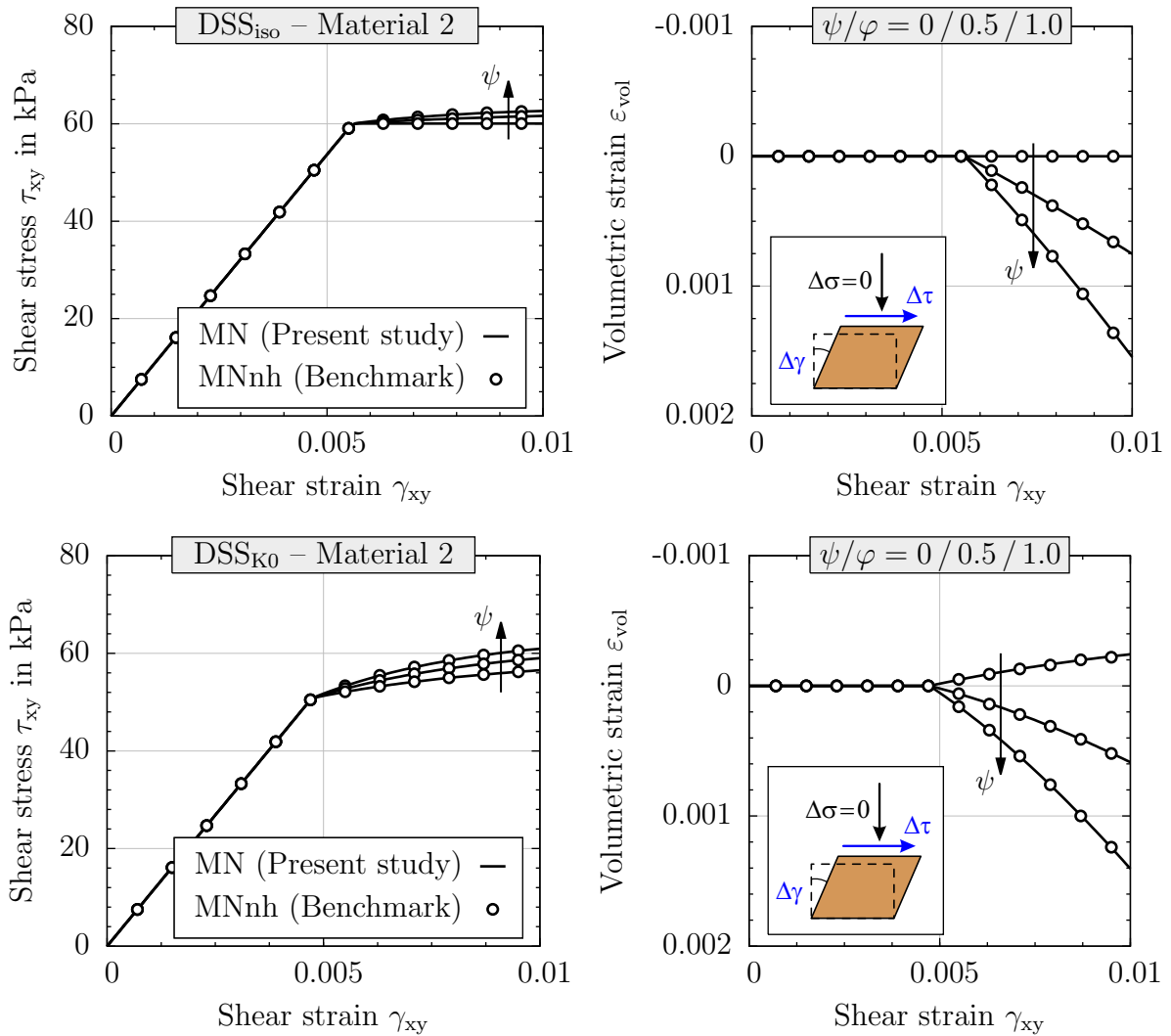


Figure 4.11: Shear stresses and volumetric strains during direct simple shear tests starting from an isotropic and K_0 stress state with a cohesive-frictional material ($\varphi = 20^\circ$, $c = 20$ kPa) simulated using two implementations of the Matsuoka-Nakai (MN) model

5. Implementation of strength reduction analysis

5.1. Motivation

As mentioned in Chapters 1 and 4, the overall objective of the implementation of the strength reduction method in `numgeo` is to perform seismic slope stability assessment in `numgeo`. To accurately approximate the seismic effects and their spatial and temporal variations, a dynamic finite element analysis (DFEA) is required that utilizes sophisticated constitutive models capturing effects such as stress/strain history, accumulation of strains and excess pore water pressures. Utilizing the results of the DFEA, stability assessment should be conducted based on objective criteria rather than project-specific limiting/allowable displacements. For this, a subsequent strength reduction finite element analysis (SRFEA) using a simple elastoplastic model should be performed. Two elastoplastic constitutive models, Mohr-Coulomb (MC) and Matsuoka-Nakai (MN), have been implemented and verified, as already presented in Chapter 4. Accordingly, the implementation of a SRFEA is presented in this chapter, since this analysis type was not available in `numgeo`, so far. Besides a detailed description of the implementation and discussions with regard to appropriate convergence criteria, verification of the strength reduction method is conducted for both elastoplastic models (MC, MN), while also considering the influence of associated and non-associated plasticity. Note that only static conditions are presumed in this chapter, while discussions with regard to considerations necessary to allow for a preceding DFEA are included in Section 6.5.

5.2. General concept

The strength reduction method implemented in `numgeo` can be used in combination with the Mohr-Coulomb and Matsuoka-Nakai model, so far. Still, the overall concept allows for

further elastoplastic models to be considered in a strength reduction analysis with minor changes. As described in detail in Section 2.1.3, in SRFEA, the shear strength parameters of the soil are incrementally reduced in accordance with a strength reduction factor (SRF) until failure is obtained. The SRF is applied to the tangent of the friction angle and the cohesion to ensure equal proportion of shear resistances by frictional and cohesive terms throughout the strength reduction. Assuming that the factor of safety (FoS) is identical to the SRF, Eq. 2.5 can be rearranged for the determination of the reduced shear strength parameters c_{red} , φ_{red} and ψ_{red} as follows

$$c_{\text{red}} = \frac{c}{\text{FoS}} \quad , \quad \tan \varphi_{\text{red}} = \frac{\tan \varphi}{\text{FoS}} \quad \text{and} \quad \tan \psi_{\text{red}} = \frac{\tan \psi}{\text{FoS}} \quad (5.1)$$

To control the incremental reduction of the shear strength parameters, an initial value of the factor of safety (FoS_0) and a step size (ΔFoS) need to be prescribed in the calculation type definition, where the latter remains constant throughout the simulation. During a strength reduction analysis, FoS is incrementally increased, which results in an incremental reduction of the shear strength parameters. Note that concepts for adaptive step-size adjustment (Van Langen and Vermeer, 1990; Van Langen, 1991) could be used here, however, preliminary studies showed less good predictions of the critical FoS obtained within this framework. To enable strength reduction in specific clusters of the model, an additional keyword (***Reducible strength**) is introduced in `numgeo` for the material definition. Thereby, computational costs associated with a shear strength reduction can be reduced for cases where the area of interest is known a priori. Furthermore, failure needs to be defined to allow for an automatic evaluation of stable and unstable states.

As described in Section 2.1.3, failure can be detected based on different approaches in SRFEA, for instance a continuous band of plastic points, large displacements, non-convergence or other energy-based concepts. To detect non-convergence, convergence criteria have to be checked, where failure is obtained for cases when, depending on the definition, one single or multiple convergence criteria could not be met within a pre-defined number of iterations. In `numgeo`, force-based, energy-based or solution-based (i.e. displacement-based) criteria can be applied, either for the average of all types of degrees of freedom (DoF, e.g. displacement and pore water pressure) or for each DoF individually.

The global convergence criteria for unbalanced energy, unbalanced forces and maximum change in solution used in `numgeo` are given in Eq. 5.2, Eq. 5.3 and Eq. 5.4, respectively, where $\|\sqcup\|_2$ is the Euclidian norm and $\sqcup^{(i)}$ refers to the current iteration of the current

increment.

$$|(\mathbf{r}^{(i)})^T \mathbf{c}^{(i)}| \leq \epsilon^e |(\mathbf{r}^{(i=0)})^T \Delta \mathbf{d}^{(i)}| \quad (5.2)$$

$$\|\mathbf{r}^{(i)}\|_2 \leq \epsilon^r \max \left(\|\mathbf{f}_{\text{ext}}\|_2, \|\mathbf{f}_{\text{int}}\|_2, \|\mathbf{M} \ddot{\mathbf{d}}\|_2 \right) \quad (5.3)$$

$$\|\mathbf{c}^{(i)}\|_2 \leq \epsilon^d \|\Delta \mathbf{d}^{(i)}\|_2 \quad (5.4)$$

Here, $\mathbf{r} = \mathbf{f}_{\text{int}} - \mathbf{f}_{\text{ext}}$, \mathbf{c} , $\Delta \mathbf{d}$ denote the residuum of the right-hand side, the correction and the solution increment, \mathbf{f}_{ext} , \mathbf{f}_{int} and $\mathbf{M} \ddot{\mathbf{d}}$ refer to the external, internal and inertial load vectors and ϵ^e , ϵ^r and ϵ^d are the allowable errors for the energy-based, the forced-based and the solution-based convergence criteria, respectively. To decide which convergence criterion may serve as the critical one to detect non-convergence in a strength reduction analysis in `numgeo`, the suitability of all criteria described above is checked with regard to reliability and robustness considering different effects. Those effects include dependencies on the overall model size, the area of interest, the mesh discretization, the allowable number of iterations to find equilibrium and material effects such as associativity, where the former two are discussed in this and the following section, while the latter one is addressed in Section 5.4. Note that analyses with regard to the mesh discretization and the allowable number of iterations have been studied, but are not explicitly reported here. A suitable criterion is found in case that for a fixed allowable error, accurate FoS values are predicted independently of those effects.

Preliminary studies showed that none of the convergence criteria defined above is capable to accurately predict the FoS for all scenarios investigated. To be more specific, the force-based criterion (Eq. 5.3) may not serve as a suitable criterion (in its presented form) due to a decisive dependency on the model size. Although accurate FoS predictions are made for many examples, the solution-based criterion (Eq. 5.4) is not capable to detect failure for materials with associated and non-associated flow rule with the same set of allowable errors. A modified force-based criterion (Eq. 5.5) with $\epsilon^r = 0.01$ may resolve most issues for regular slopes. Moreover, in case additional adjustments are considered for elements and nodes outside of the area of interest, model size effects can be avoided. Still, in case the area of interest is large in relation to the size of the individual slopes (e.g. for stepped slopes), model size dependencies remain, yielding inaccurate FoS predictions. More reliable results were obtained for a force-based criterion only relating residuum terms (Eq. 5.6), however, a definition of a constant and reliable allowable error ϵ^r was not possible for all examples analyzed.

$$\|\mathbf{r}^{(i)}\|_2 \leq \epsilon^r \|\mathbf{f}_{\text{ext}}^{(i)}\|_2 \quad (5.5)$$

$$\|\mathbf{r}^{(i)}\|_2 \leq \epsilon^r \|\mathbf{r}^{(i=0)}\|_2 \quad (5.6)$$

Furthermore, it was found that combinations of convergence criteria may yield more accurate FoS predictions compared to individual convergence criteria. Therefore, a combination of the solution-based criterion (Eq. 5.4) with $\epsilon^d = 0.1$, the modified force-based criterion (Eq. 5.5) with $\epsilon^r = 0.01$ and the residuum-based criterion (Eq. 5.6) with $\epsilon^r = 0.9$ could be applied. Note that although this combination of convergence criteria yields very promising FoS predictions, there is no ultimate guarantee that the FoS prediction is correct for all slope geometries and soil layer setups possible. As discussed in the subsequent sections, for a few examples, the allowable errors for the convergence criteria are not strict enough in order to force termination of the simulation due to non-convergence. Additional engineering judgment is required to identify unrealistic FoS predictions. Note that the latter fact does not allow to completely automate the determination of the FoS. Moreover, high sensitivity of the FoS on the allowable errors was observed in trial analyses.

An alternative strategy to detect failure can be followed by evaluation of the FoS versus maximum displacement curve saved in the `numgeo` simulation status file (`*.sta`) during SRFEA. Analyzing this data with displacements scaled linearly as depicted in the left subplot of Fig. 5.1, it is observed that maximum displacements increase with increasing FoS, however, it is difficult to define failure and detect the critical FoS. In contrast, for displacements plotted in logarithmic scale (right subplot in Fig. 5.1), it is observed that the FoS versus displacements curve is characterized by a decisive kink. This kink can be located analytically by evaluation of the evolution of the slope of this curve, where the critical FoS corresponds to a significant drop of the slope within a small number of FoS increments. To automate the evaluation of the FoS using this concept, the largest reduction of the slope for two consecutive sets of each two points is sought. Similar to the determination of the ultimate capacity for shallow or deep foundations based on load displacements curves, two tangents could also be fitted to the curve, where the vertical coordinate of the intersection point corresponds to the FoS. To reduce computational costs associated with this approach for the evaluation of the FoS, an additional input parameter could be defined as an upper limit of maximum displacements \hat{u}_{\max} . Once \hat{u}_{\max} is exceeded, SRFEA should be terminated, though evaluation of the FoS would still be conducted with regard to the displacement-based evaluation discussed above.

To demonstrate the applicability of the displacement-based evaluation of the factor of safety, an example slope is investigated here. For the slope inclined at $\beta = 30^\circ$ composed of a homogeneous soil with $\gamma = 20 \text{ kN/m}^3$, $\varphi = \psi = 30^\circ$ and $c = 6 \text{ kPa}$, benchmark simulations with `Plaxis2D` and `OptumG2` predicted a slope stability of $\text{FoS} = 1.49$. To conduct the displacement-based evaluation of the FoS, default convergence criteria with

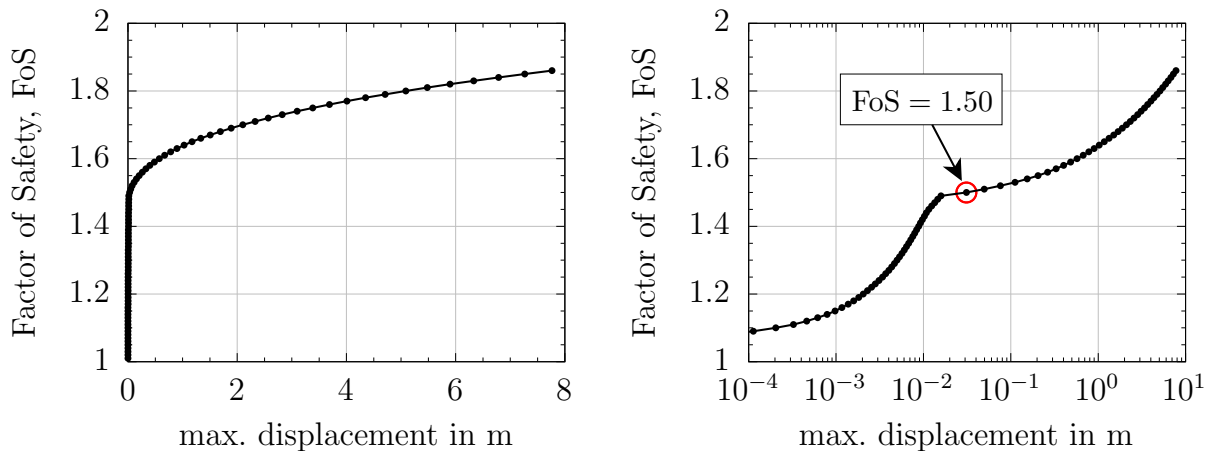


Figure 5.1: Evaluation of slope stability based on factor of safety versus maximum displacement plot

rather loose allowable errors are considered in the `numgeo` simulation to evaluate the FoS solely based on the displacement-based criterion. The FoS versus maximum displacement curve obtained with `numgeo` is depicted in Fig. 5.1 with displacements plotted in linear (left) and logarithmic (right) scale. Using the displacement-based evaluation of the FoS for this example, slope stability is evaluated as $\text{FoS} = 1.50$, which is in good agreement with the benchmark results. Note that similar FoS were also obtained using the modified force-based criterion with $\epsilon^r = 0.01$ as well as using a combination of the solution-based criterion (Eq. 5.4) with $\epsilon^d = 0.1$ and the modified force-based criterion (Eq. 5.5) with $\epsilon^r = 0.01$. A potential explanation for similar FoS obtained for this example is that the area of interest was large compared to the overall model size.

5.3. Preliminary investigations

Effect of model size

To emphasize the impact of the model size on the FoS prediction, a slope with a height of 10 m and a sloping angle of $\beta = 45^\circ$ is embedded in a large model depicted in Fig. 5.2 composed of three domains, the slope, the subsoil, and the far field with a maximum model width and height of 250 m and 60 m, respectively. The material behavior of all domains is described by the Mohr-Coulomb model with material parameters selected as unit weight $\gamma = 20 \text{ kN/m}^3$, Young's modulus $E = 30 \text{ MPa}$, Poisson's ratio $\nu = 0.2$, cohesion $c = 30 \text{ kPa}$, friction angle $\varphi = 30^\circ$ and dilation angle $\psi = 30^\circ$. To estimate a

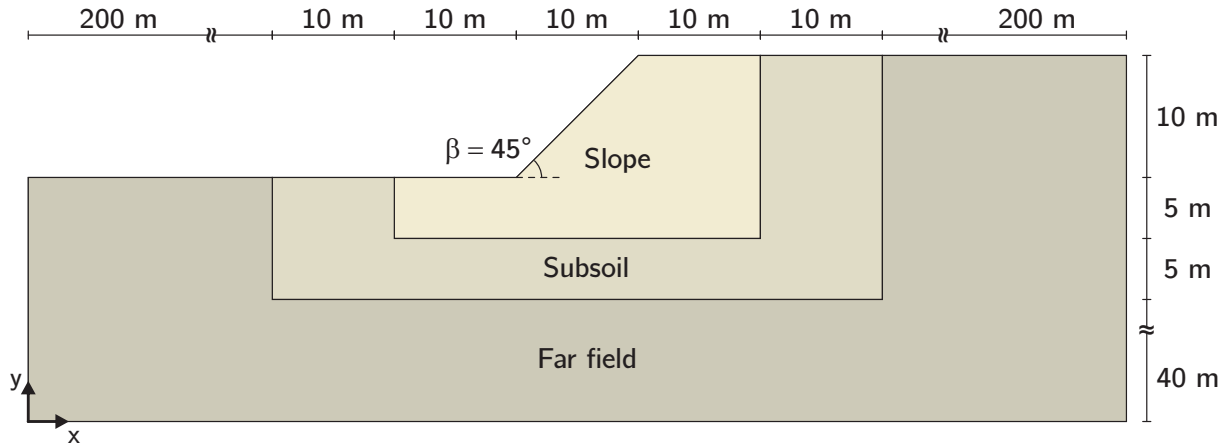


Figure 5.2: Slope model to study the effect of the model size on the FoS

reference solution of the FoS as a benchmark for the simulations with `numgeo`, stability analyses have been conducted with `Plaxis2D` and `OptumG2`. Two simulations have been performed with both software packages, where the far field area is included in the first and neglected in the second simulation. `OptumG2` yields $\text{FoS} = 1.95$ independently of the model size, while `Plaxis2D` yields $\text{FoS} = 1.92$ for the small model neglecting the far field area and $\text{FoS} = 1.93$ for the large model considering the far field area.

Note that only for this example different convergence criteria and combinations thereof are discussed. Further stability analyses presented in the following sections are evaluated with regard to the evolution of the FoS versus maximum displacement curve saved in the `numgeo` simulation status file (`*.sta`) during SRFEA.

Conducting SRFEA with the modified force-based criterion (Eq. 5.5) with $\epsilon^r = 0.01$, evaluation of the FoS using `numgeo` results in $\text{FoS} = 1.96$ and $\text{FoS} > 2.17$ for the small and the large model, respectively. It is seen that for the small model, very good agreement with the benchmark solution is obtained, while significant over-prediction of FoS is obtained for the larger model. This is due to the fact that the area of the slope highlighted in light gray (Fig. 5.2) only represents 1.21 % of the area of the total model, whereby the unbalance expressed in terms of the residuum in this area is small compared to the external forces of the total system. Note that although the large model has not obtained a failure state for a strength reduction factor of $\text{SRF} = 2.17$, massive displacements are observed with maximum values of $u_{\max} = 4.3$ m. Thus, although huge displacements of more than 40 % of the slope height are encountered, failure is not detected based on this convergence criterion. Note that even worse FoS predictions are obtained when applying the force-based criterion according to Eq. 5.3 as the norm of the residuum is compared to $\|\mathbf{f}_{\text{int}}\|_2$.

Considering the force-based criterion according to Eq. 5.5 with $\epsilon^r = 0.01$ and with adjustments of the model in terms of keeping constant the stress and deformation state in the far field area and neglecting external forces in that part, the influence of the model size vanishes and SRFEA in `numgeo` yields $\text{FoS} = 1.96$ for the large model, as well. This is achieved by applying zero incremental deformation constraints ($\Delta \mathbf{u} = \mathbf{0}$) to all nodes in the far field area and additionally neglecting the effect of body forces (gravity) on the elements in the far field area. Thus, model size effects on the FoS can be avoided when using the modified force-based criterion (Eq. 5.5) for the slope stability analysis of the area of interest, while keeping the current state of the surrounding soil. However, this concept is not applicable for all boundary value problems, for instance stepped slopes that are characterized by small individual slope sizes in relation to the overall area of interest.

Performing strength reduction analyses for the slope depicted in Fig. 5.2 utilizing the combination of solution-based criterion (Eq. 5.4) with $\epsilon^d = 0.1$, modified force-based criterion (Eq. 5.5) with $\epsilon^r = 0.01$ and residuum-based criterion (Eq. 5.6) with $\epsilon^r = 0.9$, respectively, it is observed that accurate FoS predictions are obtained for simulations including and neglecting the far field area. In both cases, a slope stability of $\text{FoS} = 1.95$ is determined without any need to fix nodal displacements or neglect body force effects in the far field area.

Performing SRFEA in `numgeo` with the default convergence criteria and rather loose allowable errors ($\epsilon^r = 0.01$, $\epsilon^d = 0.1$), large displacements are obtained (Fig. 5.3), as the detection of slope failure based on non-convergence was not successful. Though, a clear change in the slope of the FoS versus maximum displacement curve is seen for

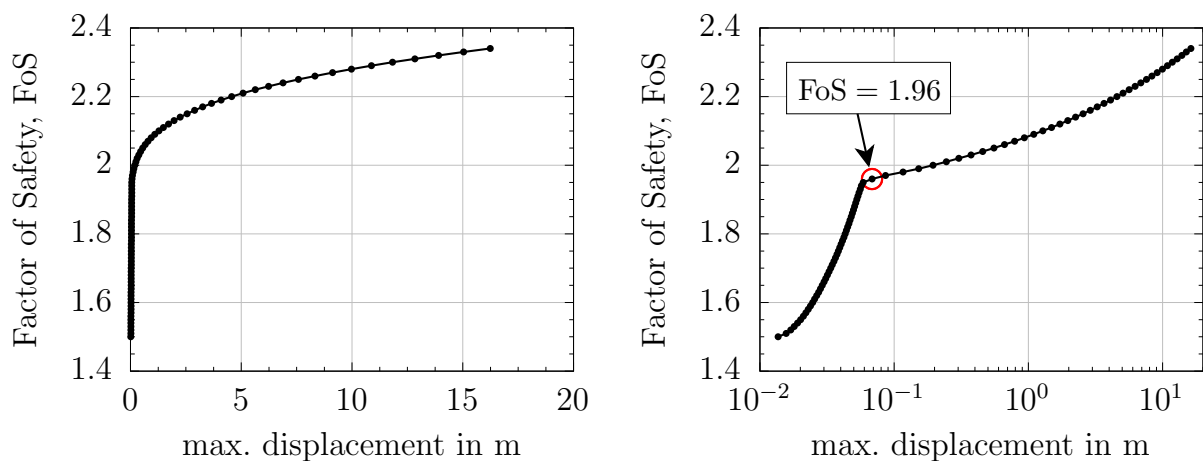


Figure 5.3: Evaluation of displacement-based FoS for the example depicted in Fig. 5.2

displacements plotted in logarithmic scale. Applying the displacement-based evaluation, an accurate estimation of the slope stability is achieved with $\text{FoS} = 1.96$.

Stepped slope

To study if the displacement-based evaluation provides accurate FoS predictions in case the area of interest is large in relation to the size of smaller individual slopes, a stepped slope is investigated, as schematically depicted in Fig. 5.4. Note that the slope has a general inclination of $\beta = \arctan(100 \text{ m}/373 \text{ m}) \approx 15^\circ$, but smaller individual slopes are inclined up to $\beta_4 = 25^\circ$. The material behavior of the soil is described by the Mohr-Coulomb model with material parameters selected as unit weight $\gamma = 20 \text{ kN/m}^3$, Young's modulus $E = 30 \text{ MPa}$, Poisson's ratio $\nu = 0.2$, cohesion $c = 1 \text{ kPa}$, friction angle $\varphi = 30^\circ$ and dilation angle $\psi = 30^\circ$. As shear strength is dominated by frictional resistance, a shallow failure surface is expected. Moreover, a local failure surface located in the proximity of the steepest slope is expected, rather than a large (global) failure surface spanning from the slope crest to the slope toe. To determine a reference solution of the FoS as a benchmark for the simulations with `numgeo`, stability analyses have been conducted for the stepped slope model with `OptumG2` and `Plaxis2D`, resulting in $\text{FoS} = 1.34$ and $\text{FoS} = 1.35$, respectively.

Strength reduction analysis with `numgeo` yields the evolution of maximum displacements with increasing factor of safety as shown in Fig. 5.5 in linear (left) and logarithmic (right) scale. Applying the displacement-based evaluation of the FoS with regard to the right plot, a slope stability of $\text{FoS} = 1.37$ is predicted. Note that for this example FoS determination would also be possible based on displacements plotted in linear scale, leading to the same FoS. In general, very good agreement between the FoS predictions of `Plaxis2D`,

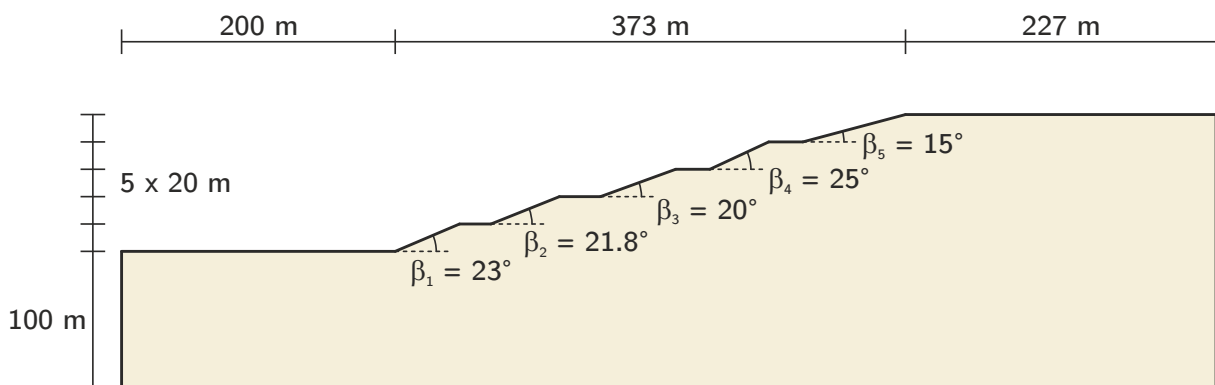


Figure 5.4: Geometry and dimensions of the stepped slope model

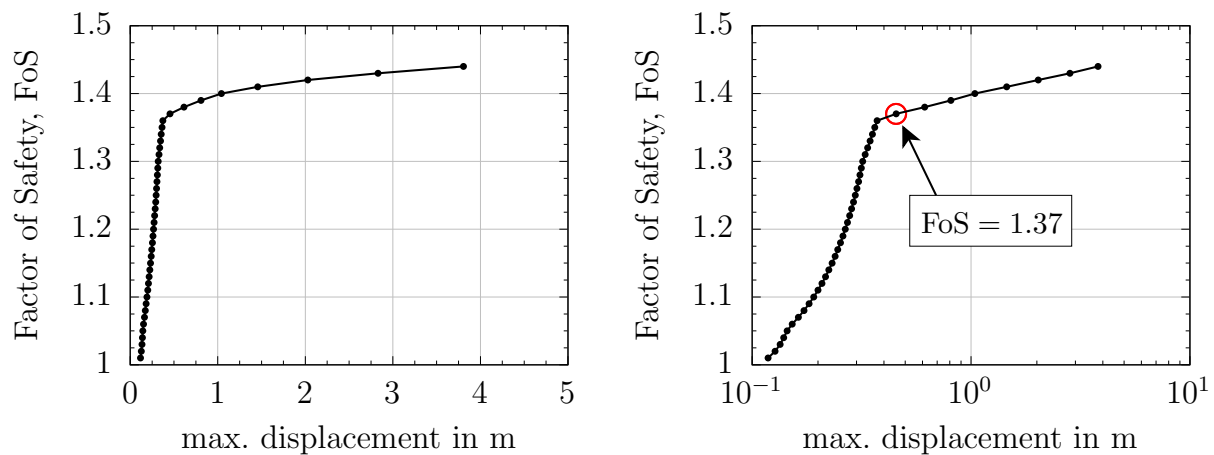


Figure 5.5: Evaluation of displacement-based FoS for the stepped slope depicted in Fig. 5.4

OptumG2 and numgeo is obtained considering that the discretization of elements in the proximity of the failure surface is of a better quality for the simulation with OptumG2 due to adaptive mesh refinement. Still, as seen in Fig. 5.6 the approximation of the failure surfaces using both FE software packages is in good agreement, as well. Note that, similar to strength reduction schemes conducted with other FE software packages, the amount of displacements obtained after SRFEA has no relevance for the slope stability problem as only the FoS is relevant for the stability judgment.

5.4. Verification

5.4.1. Homogeneous slopes

To further verify the strength reduction method implemented in this thesis, comparative analyses are conducted using results obtained with numgeo and Plaxis2D as well as simulation results published in literature. Although the main purpose in this thesis is to do slope stability analyses using the Matsuoka-Nakai model as part of the seismic slope stability assessment, verification is primarily performed using the Mohr-Coulomb model due to a lack of sufficient benchmark data available based on simulations with the MN model. The main reason for this lack of data may be explained by the fact that the Matsuoka-Nakai model has rarely been implemented in commercial FE software packages.

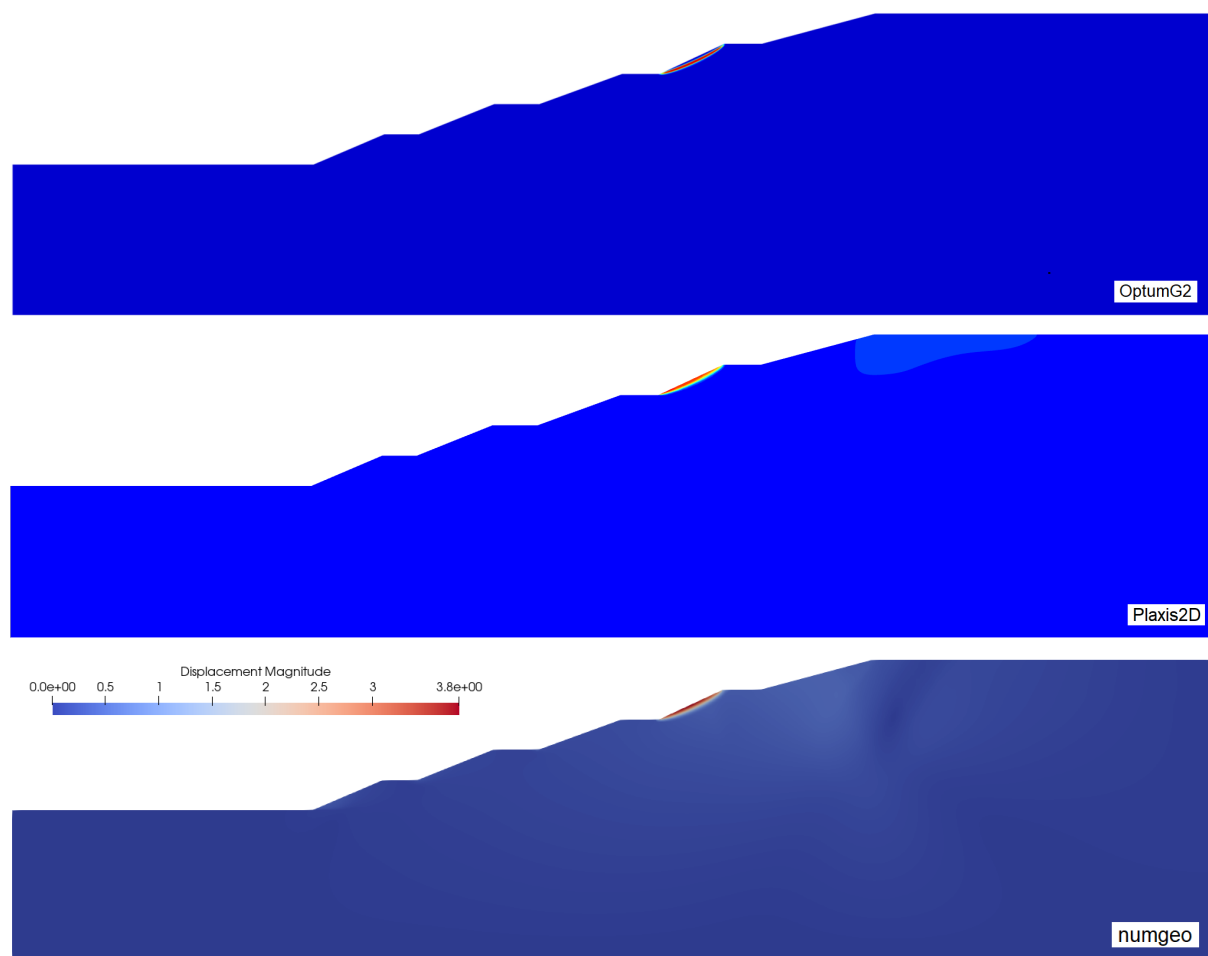


Figure 5.6: Failure surfaces obtained with `OptumG2` (plastic shear dissipation), `Plaxis2D` (displacements $|u|$) and `numgeo` (displacements $|u|$) for the stepped slope depicted in Fig. 5.4

SRFEA with MC model and associated plasticity

To verify the strength reduction method in combination with the Mohr-Coulomb model and associated plasticity, comparative analyses are conducted with `numgeo` and `Plaxis2D` for homogeneous slopes with varying sloping angles β and shear strength parameters φ and c . Note that the dilation angle is kept equal to the friction angle to account for associated plasticity (i.e. associated flow rule, AFR). Results are compared in Fig. 5.7 in terms of FoS versus normalized cohesion with different curves and subplots referring to different friction angles and sloping angles. Overall, normalized cohesion is varied in the range $0.0 < c/(\gamma \cdot H) \leq 0.3$, with γ and H denoting the soil unit weight and the slope height, respectively, while friction angles $10^\circ \leq \varphi \leq 40^\circ$ and sloping angles of $15^\circ \leq \beta \leq 60^\circ$ are considered. In `numgeo`, slope stability is evaluated based on the displacement-based

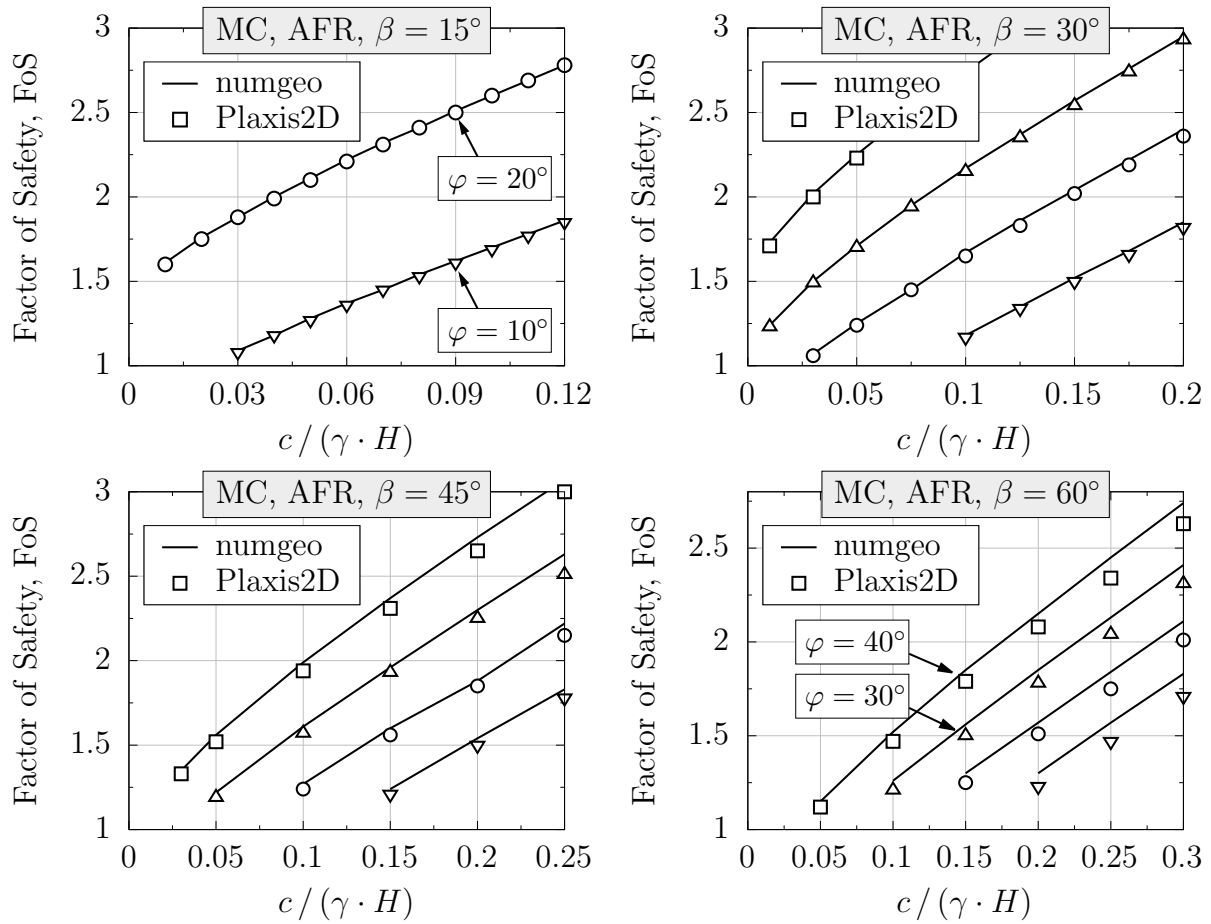


Figure 5.7: Comparison of FoS obtained with `numgeo` and `Plaxis2D` for various friction angles, normalized cohesion values and slope inclinations

criterion discussed in the previous section for all case combinations. As can be seen from this figure, good agreement between `numgeo` and `Plaxis2D` is obtained for all simulations. A decreasing agreement is apparent for increasing slope inclination, leading to slightly higher FoS using `numgeo` in particular for $\beta = 60^\circ$.

SRFEA with MC/MN model and non-associated plasticity

To verify the strength reduction method in combination with the Mohr-Coulomb and Matsuoka-Nakai model considering non-associated plasticity (i.e. non-associated flow rule, NAFR), comparative analyses are conducted utilizing results of a parametric study reported by Tschuchnigg et al. (2018). In this study, SRFEA has been conducted with `Plaxis2D` utilizing the in-built Mohr-Coulomb model and a user-material routine of the Matsuoka-Nakai model. The slope has a height of $H = 10$ m and an inclination of

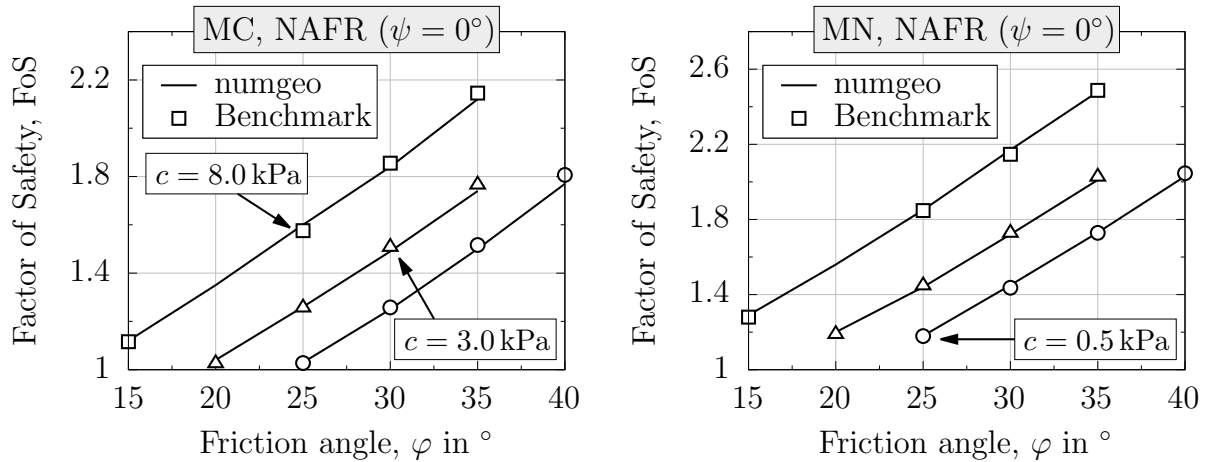


Figure 5.8: Comparison of FoS obtained with `numgeo` and reported by Tschuchnigg et al. (2018) considering the MC and MN model with non-associated plasticity

$\beta = 26.67^\circ$. While friction angle and cohesion are varied, other soil parameters are kept constant during the parametric study. The latter group includes the soil unit weight, the Young's modulus, the Poisson's ratio and the dilation angle with $\gamma = 16 \text{ kN/m}^3$, $E = 30000 \text{ MPa}$, $\nu = 0.2$ and $\psi = 0^\circ$, respectively.

The results of the parametric study presented by Tschuchnigg et al. (2018), here referred to as 'Benchmark' are compared to `numgeo` results in terms of the predicted FoS in Fig. 5.8. It is apparent from both subplots that very good agreement between the benchmark results and the ones obtained using `numgeo` are obtained for all case combinations investigated. Still, further comparative analyses should be conducted with different slope inclinations and combinations of shear parameters to further check the quality of the FoS predictions. Nevertheless, it has been demonstrated in this and the previous sections that SRFEA in `numgeo` is capable to accurately predict the factor of safety for homogeneous slopes. To check the quality of the method for layered slopes, additional benchmark problems are investigated in the following subsection.

5.4.2. Benchmark problems

In this section two benchmark problems are investigated and results are compared to previous studies in terms of FoS. Since both examples have been already presented and discussed with regard to the verification of the limit equilibrium method in Section 3.4.4, only a short summary of the main details is provided here.

The first example has been investigated, among others, by Liu et al. (2015) and Liu et al. (2020). The geometry, dimensions, soil layering and soil material parameters are depicted in Fig. 3.15. The slope consists of four inclined layers, where a thin layer of material No. 3, characterized by a significantly smaller shear strength compared to the other soil material sets, has a major influence on the shape of the failure surface. A summary of the FoS predictions obtained in various studies including Liu et al. (2015), Liu et al. (2020) and the present study (Plaxis2D) is depicted in Tab. 3.4, suggesting that the critical FoS should be found in the range of $1.05 \leq \text{FoS} \leq 1.11$. Performing SRFEA with `numgeo`, $\text{FoS} = 1.08$ is obtained, which is in good agreement with results reported in literature. Moreover, analyzing the failure surface observed in `numgeo` (Fig. 5.9) it is apparent that large amounts of the slip surface are located in layer No. 3 as the shear resistance in this layer is significantly smaller compared to the surrounding soil layers. Thus, SRFEA is also capable to accurately predict the FoS for slopes composed of multiple soil layers. Moreover, precise approximation of the failure mechanism is observed, even for boundary value problems with thin bands of weak soils. To further verify the latter statement, a second example with multiple layers and a thin weak layer is investigated.

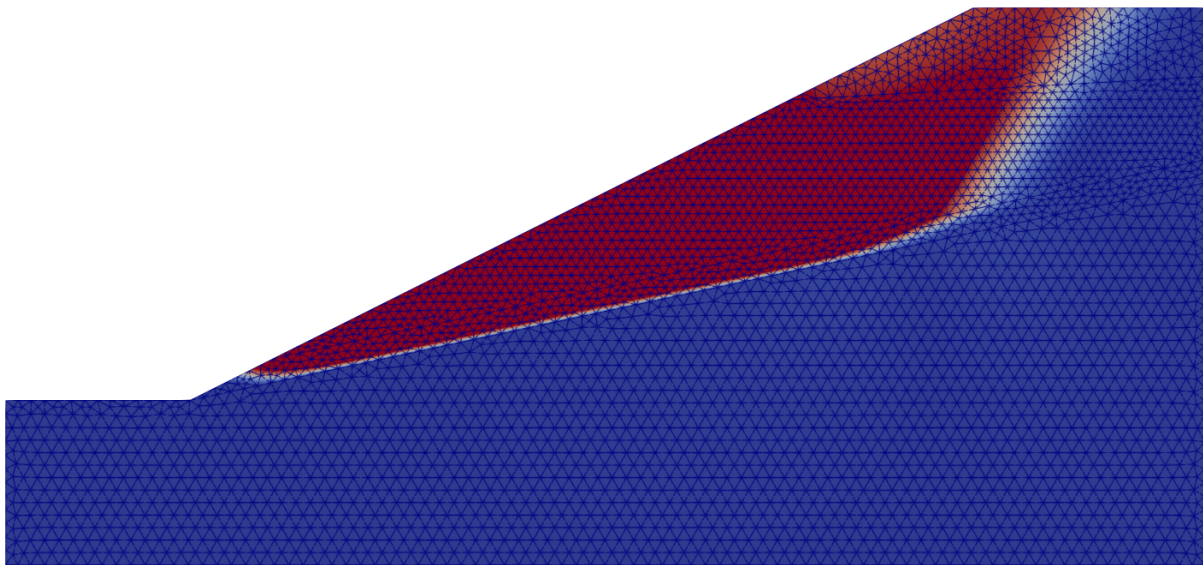


Figure 5.9: Failure surface obtained with `numgeo` (displacements $|u|$) for a slope composed of inclined layers depicted in Fig. 3.15

The second example is composed of a homogeneous slope with a horizontal thin weak layer below the slope toe. The geometry, dimensions, soil layering and soil material properties are depicted in Fig. 3.13(b). As summarized in Tab. 3.3, slope stability has been determined in the range of $1.22 \leq \text{FoS} \leq 1.36$. Further results for this benchmark can also be found in Sloan (2013). Performing SRFEA with `numgeo`, $\text{FoS} = 1.22$ is

obtained, which is in good agreement with results reported in literature, especially with the simulation results of `Plaxis2D` obtained in the present study. Analyzing the critical failure surface depicted in Fig. 5.10, it is apparent that the soil failure mass slides on the weak layer due to its low shear resistance.

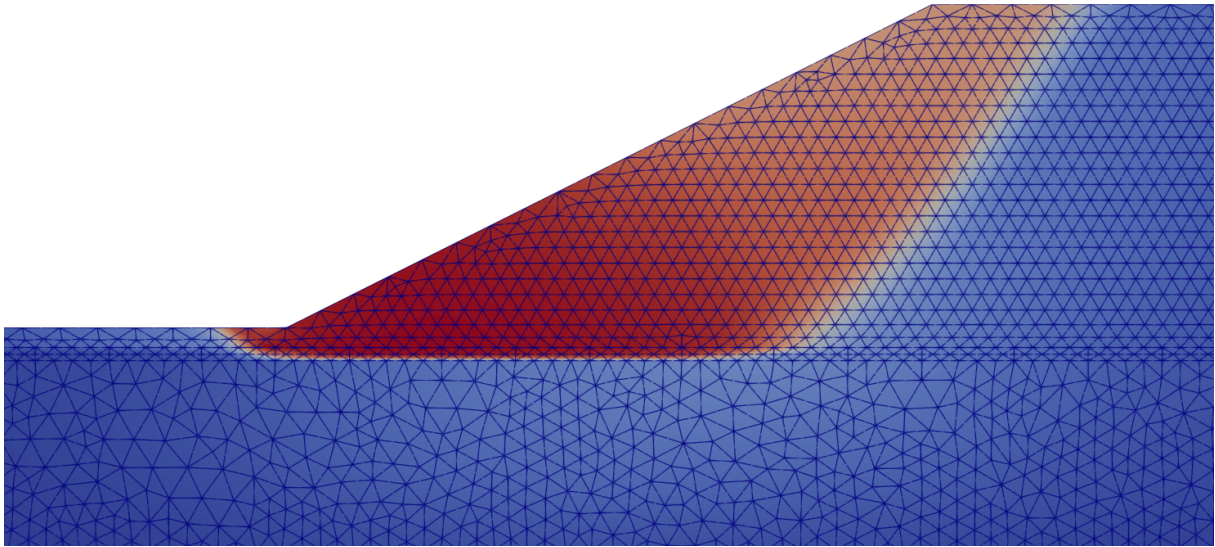


Figure 5.10: Failure surface obtained with `numgeo` (displacements $|u|$) for a homogeneous slope with a thin weak layer below the slope toe depicted in Fig. 3.13(b)

6. Approaches for the assessment of seismic slope stability

6.1. Motivation

For the assessment of the behavior of a slope subjected to seismic loading, a dynamic finite element analysis (DFEA) should be conducted, utilizing sophisticated constitutive models that enable capturing relevant effects, for instance accumulation of strains and built-up of excess pore water pressures. The DFEA provides information about displacements and potential soil liquefaction that can be used as a first estimate for the seismic slope stability. To quantitatively evaluate the seismic slope stability based on the results of the DFEA, judgment based on project specific displacements or strains is necessary, requiring substantial experience of practitioners. Since practitioners may define different threshold values, this type of slope stability assessment must be regarded as rather subjective. Utilizing well-established slope stability approaches subsequent to the DFEA, the question arises which assumptions are required to approximate spatial distributions of stresses, accumulated pore water pressures and accelerations. Note that these distributions, as schematically depicted in Fig. 6.1, vary with regard to location and time.

To overcome this issue, the aim is to develop, apply and compare different approaches for an objective assessment of seismic slope stability. In this chapter, four approaches are presented¹, including details about their motivation, (implicit) assumptions, advantages and drawbacks as well as potential for further development. These approaches are based on four different methods, namely the limit equilibrium method (LEM), the finite element limit analysis (FELA), the strain-dependent slope stability (SDSS) and the strength reduction finite element analysis (SRFEA). Note that the former two and the latter approach consider seismic effects based on modifications of the pseudo-static approach

¹Note that to emphasize details with regard to the approaches discussed in this chapter, figures linked to the boundary value problem discussed in Chapter 7 are presented.

(PSA) to incorporate inertial forces caused by accelerations. In contrast, SDSS considers seismic effects via the dynamic stress state that keeps the system in dynamic equilibrium. All approaches have in common that they are conducted subsequently to DFEA, thus, there is no influence of the choice of approach for the slope stability assessment on the dynamic simulation.

Note that large deformations after a dynamic loading may also occur due to post liquefaction flow failure (Kramer and Smith, 1997; Machaček et al., 2018; Machaček, 2020), which requires investigation of the boundary value problem for larger time spans after the seismic excitation. As excess pore water pressures might redistribute during the consolidation process, scenarios are conceivable in which significant excess pore water pressures develop in areas that did not liquefy or experience large excess pore water pressures before. Thereby, the level of safety of a slope expressed in terms of FoS might even be decreased below the most critical level of safety observed during the dynamic loading. As computational costs associated with DFEA are large, DFEA are usually performed until accelerations and velocities have decreased to a negligible level. Afterwards, transient analyses (e.g. consolidation analyses) can be conducted to determine the evolution of stresses, strains, state variables, displacements and excess pore water pressures after a seismic event. As the main difference between dynamic and transient analysis is the consideration of damping and inertial terms in the former analysis type, all approaches discussed in this chapter can also be utilized to evaluate slope stability for the latter analysis type by neglecting contributions of inertial forces.

6.2. Spatial pseudo-static analysis using LEM

A common approach to evaluate the stability of a slope subjected to seismic loading is the pseudo-static analysis (PSA) summarized in Section 2.2.1, where inertial forces are considered additionally in the slope stability analysis. Inertial forces are determined based on soil unit weight and seismic coefficients, the latter representing horizontal or vertical accelerations normalized by gravity. Application of PSA in combination with limit equilibrium methods (LEM) allows to consider seismic effects in terms of inertial forces in each slice. Thus, PSA can be performed considering either constant or spatially varying pseudo-static coefficients throughout the domain. As spatial distributions of pseudo-static coefficients are not necessarily available for every boundary value problem, most commercial LEM codes, such as `GGU-Stability`, only allow to specify constant pseudo-static coefficients for the whole domain, thus no import of external spatial distributions

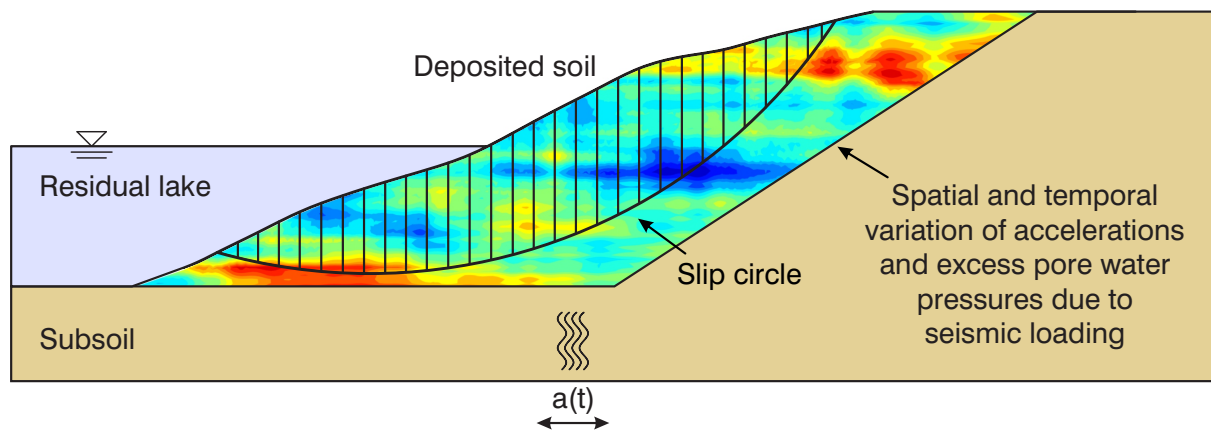


Figure 6.1: Pseudo-static analysis using the method of slices considering spatial variation of accelerations and excess pore water pressures

is possible. Other codes, such as **Quake/W** (GeoStudio, 2020), allow to conduct DFEA with a limited number of constitutive models to approximate the spatial distribution of seismic coefficients and excess pore water pressures. Note that excess pore water pressures may have a decisive impact on the slope stability and should also be considered in PSA. More accurate spatial distributions of the seismic coefficients and excess pore water pressures for use in stability analyses can be obtained from a DFEA with sophisticated constitutive models and proper finite element formulations. However, if available LEM software packages do not allow to import these distributions, the seismic slope stability assessment cannot be conducted in an accurate manner.

geoSlice presented in Chapter 3 allows for the import of either a constant value or a spatial distribution of pseudo-static coefficients (see Section 3.3), the former verified based on a comparative analysis with **GGU-Stability** summarized in Fig 3.10. In addition, spatial distributions of excess pore water pressure can be imported as well. Thereby, as depicted in Fig. 6.1, seismic slope stability assessment can be conducted utilizing spatial distributions of accelerations and excess pore water pressures, as for instance obtained from a DFEA.

Considering a specific slice, as shown in Fig. 6.2, dynamic effects are taken into account in **geoSlice** in terms of horizontal and vertical inertial forces ΔH_i and ΔV_i^\pm and the resulting accumulated excess pore water pressure force ΔU_{acc} . As it is unknown a priori whether ΔV_i directed upwards or downwards (\pm) yields more critical results, slope stability needs to be evaluated for both directions. In the last subplot of Fig. 6.2 the red and blue dots represent potential locations at which seismic coefficients (A1 - A3) and excess pore water pressures (P1 - P3) can be interpolated to allow for an appropriate determination

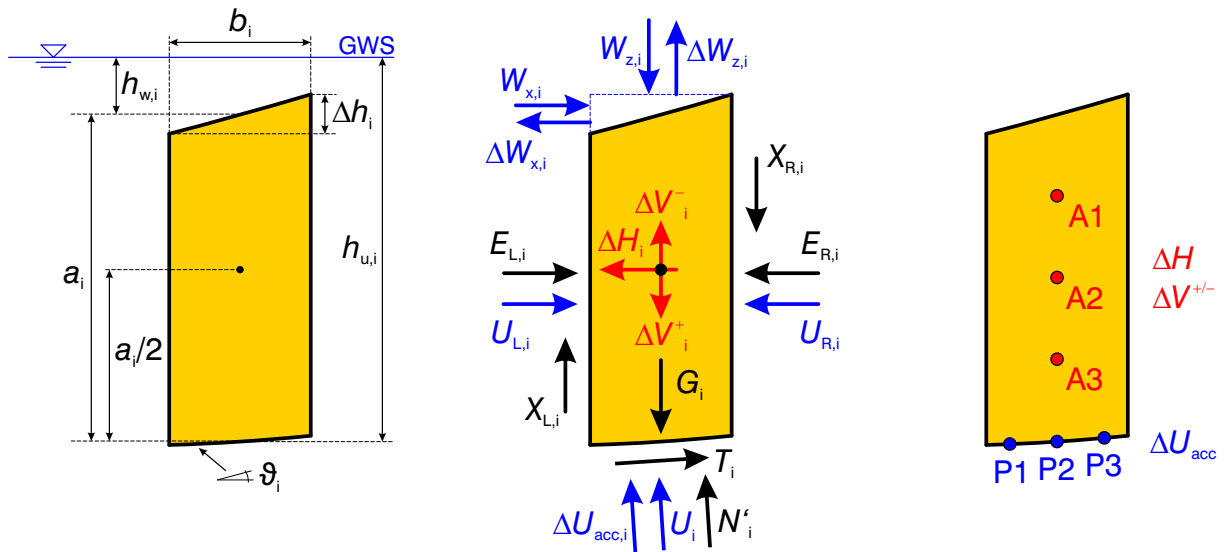


Figure 6.2: Slice details with regard to geometry (left), resulting forces (center) and location of points for interpolation of seismic coefficients A1 - A3 and excess pore water pressures P1 - P3 (right)

of average values. Note that the selection of three points each is exemplary and can be adjusted to consider more or less nodes for interpolation. However, as interpolation has to be conducted for each node in each slice for each slip surface analyzed, computational costs increase with increasing number of nodes. Thus, it is advisable to select an appropriate number of nodes based on the density of the spatial distribution of seismic coefficients and excess pore water pressures.

6.3. Cluster-based pseudo-static analysis using FELA

6.3.1. General idea

To analyze the evolution of the FoS during earthquake loading, DFEA is followed by a series of strength reduction analyses within the framework of finite element limit analysis (FELA) at predefined time intervals of the DFEA. To ensure proper evaluation of the slope stability, transfer of information from DFEA to FELA is required. The information to be transferred include the effective stress state, the friction angle and the cohesion (in case of cohesive soils) to approximate the shear strength, as well as the total stress state and the pseudo-static coefficients to reproduce the inertial forces. In a preliminary stage, different FE software packages, among others numgeo, Plaxis2D, Abaqus and OptumG2 have been

analyzed regarding their ability to perform stability analyses with a proper discretization of elements close to the failure surface. Even more critical for the decision was the software's ability to allow importing stress states as well as spatially varying inertial forces and material parameters. Based on the preliminary findings, it was concluded that the requirements are only met in a satisfactory manner by `OptumG2` (OptumG2, 2019). Although `numgeo` and `Abaqus` meet the requirements regarding the import of state variables and material properties, no adaptive mesh refinement is available. Note that other software packages, for instance `Plaxis2D`, do not allow for an import of spatially varying data and material parameters in a straightforward way. The application of `numgeo` for the dynamic earthquake analysis is necessary because most software packages do not allow for dynamic analyses together with consideration of consolidation effects, nor do they offer sophisticated constitutive soil models suitable for cyclic loading.

In `OptumG2`, stability analyses are conducted based on strength reduction in FELA. As explained in Section 2.1.4, FELA is based on the limit theorems of plasticity (Drucker et al., 1952), thus, lower and upper bound solutions are determined, bracketing the exact solution from below and above, respectively. Considering the transfer of information, `OptumG2` allows to import spatial variations of material parameters such as friction angle, cohesion, or soil unit weights. To preserve information – for instance the stress state to obtain an initial equilibrium for the stability analysis – spatial approximation of material parameters (e.g. unit weights) is considered. To accurately approximate failure mechanisms, adaptive mesh refinement can be used in `OptumG2`. A drawback of the application of `OptumG2` for the herein presented approach is that no direct import of stress states or inertial forces is possible. To overcome the latter issue, a cluster-based approach is used as indicated in Fig. 6.3. Further details about the mapping of stresses, inertial forces and friction angles as well as the consideration of a non-associated flow rule are discussed in the subsequent sections.

To evaluate the FoS for a specific time step t_{dyn} of the DFEA, the workflow depicted in Fig. 6.4 is followed to generate a FE model for the strength reduction analysis using FELA. This model – with all information written in the `OptumG2` RUN file – is created with regard to a `OptumG2` BASE file that contains information about the geometry of the slope and the clusters, the boundary conditions and the calculation type. Placeholders are used in the BASE file to enable the import of mapping information via Python scripts based on simulation results of the DFEA, for instance with respect to the friction angle or the unit weight. Additional placeholders are set with regard to the horizontal and vertical pseudo-static coefficients for each cluster. The largest effort in the generation of the

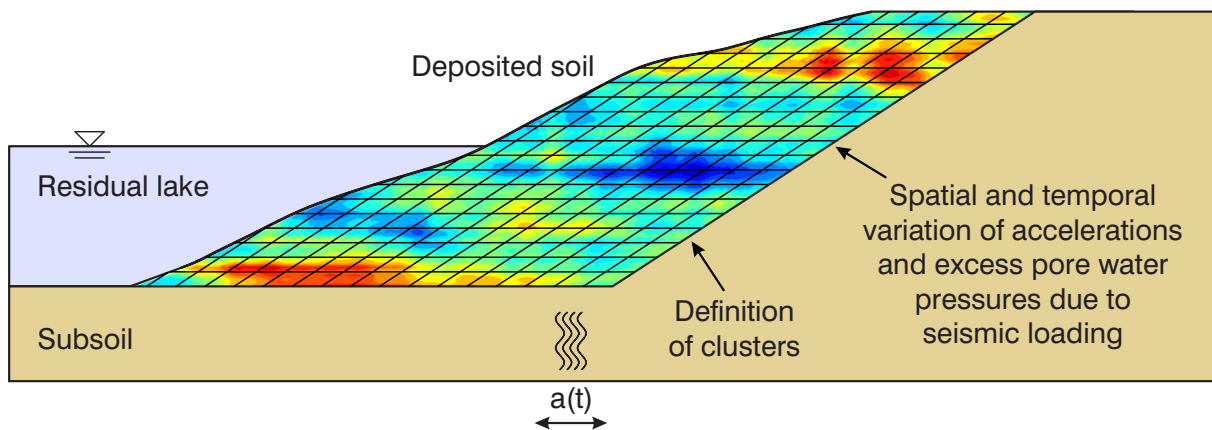


Figure 6.3: Cluster-based pseudo-static analysis using FELA considering spatial variation of accelerations and excess pore water pressures

models for the stability analysis is related to the generation of the BASE file/model and the linking between the individual clusters and the Python scripts using the placeholders. Once the BASE model is created and the preprocessing of the output data of the DFEA is conducted, the generation of RUN models is almost identical for different time steps.

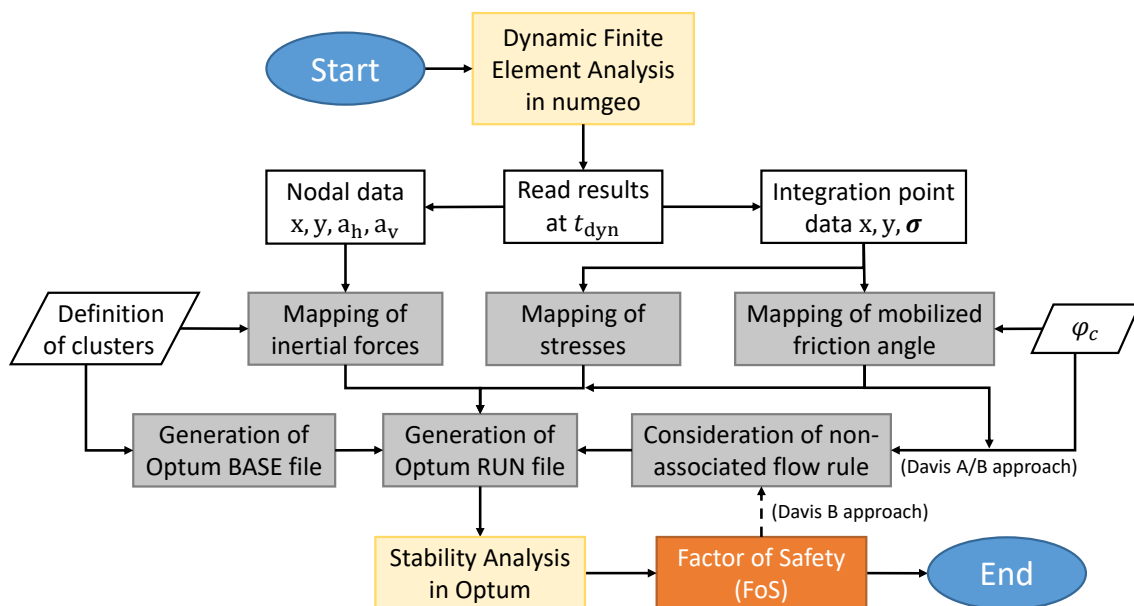


Figure 6.4: General approach for the evaluation of the seismic slope stability by cluster-based pseudo-static analysis using OptumG2

6.3.2. Mapping of stresses

The most comfortable way to map stresses between two FE models would be to use identical meshes and element types allowing for a direct transfer of state variables from the integration points of the first model to the corresponding integration points of the second model. Thereby, a direct transfer of the effective and total stress states from the DFEA to the finite element model utilized for strength reduction analysis would be achieved. However, as a direct import of stress states is not possible in **OptumG2**, a different strategy is sought. In **OptumG2**, the unit weight of the unsaturated soil γ_{unsat} and the unit weight of the saturated soil γ_{sat} can be prescribed. Considering a fully saturated slope as presented in Chapter 7, γ_{unsat} can be neglected as it has no influence on the analyses, making γ_{sat} the only available parameter for the spatial approximation of stresses. The effective unit weight γ' is automatically determined in **OptumG2** based on $\gamma' = \gamma_{\text{sat}} - \gamma_w$, where γ_w is the unit weight of water. To approximate the effective stress state with the results obtained in the DFEA, a spatial distribution of γ'_i is back-calculated from the effective stresses $\sigma'_{yy,i}$ at each integration point i of the DFEA and its overburden height h_i (Eq. 6.1). This distribution is imported into **OptumG2** in terms of $\gamma_{\text{sat}} = \gamma' + \gamma_w$.

$$\gamma'_i = \frac{\sigma'_{yy,i}}{h_i} \quad (6.1)$$

Following this approach, the spatial variation of the effective unit weight γ' obtained from the DFEA (Section 7.2.2) is depicted in Fig. 6.5 for four different time steps during seismic loading. As can be seen from this figure an almost homogeneous distribution of γ' is obtained for $t \leq 2.0$ s, because only hydrostatic pore water pressures exist. With ongoing excitation, shear waves propagate towards the slope, which results in the build-up of

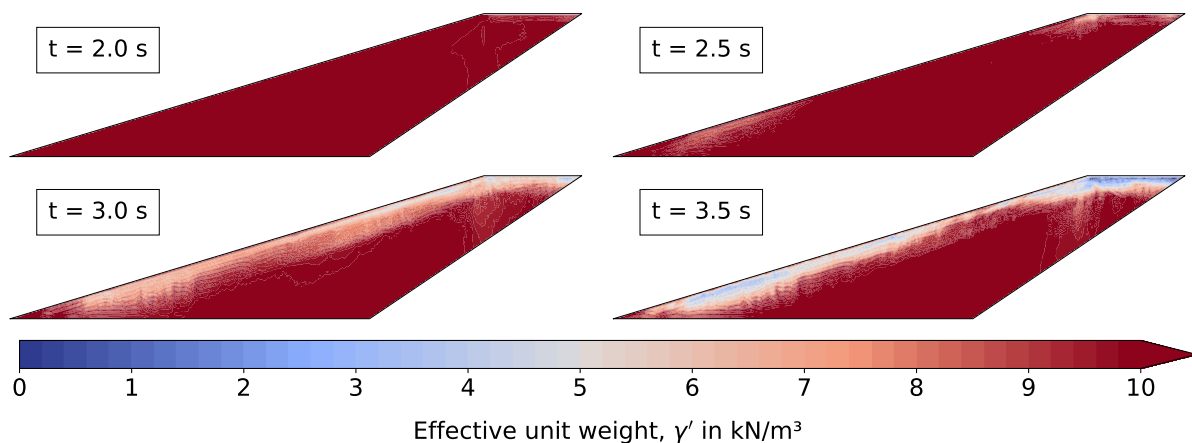


Figure 6.5: Spatial approximation of the effective unit weight for different time steps

excess pore water pressures since the loose material tends to densify under shearing. As a consequence, the effective stress and thus γ' decrease. Comparing the spatial distributions of effective unit weights for different time steps, it is apparent that a significant reduction to approx. $\gamma' = 5 \text{ kN/m}^3$ is observed along the slope surface at $t = 3.0 \text{ s}$. This is intensified at $t = 3.5 \text{ s}$ with effective unit weights approaching $\gamma' = 0 \text{ kN/m}^3$. Interestingly, it is seen that effective unit weights decrease strongest at the slope crest. Note that from a physical point of view, effective unit weights would not decrease in the same way, but would remain almost constant. The reduction in γ' solely results from the need to consider excess pore water pressures to approximate the overall effective stress state.

To evaluate if the mapping of effective unit weights yields an accurate spatial distribution of the effective stress state used in the stability analyses, a comparison of stress states obtained with `numgeo` and `OptumG2` is depicted in Fig. 6.6 in terms of depth profiles of vertical effective stresses for multiple horizontal coordinates (see Fig. 6.5) along the slope and time steps. It is apparent from this figure that good agreement between the stress states in both finite element codes is achieved. Nevertheless, it is observed that close to the slope crest ($x = 1150, 1200 \text{ m}$), the approximation of effective stresses is satisfying only close to the ground surface, whereas underestimation is seen with increasing depth. A potential explanation for this observation can be given with regard to the estimation of unit weights according to Eq. 6.1, which yields an average unit weight with regard to the

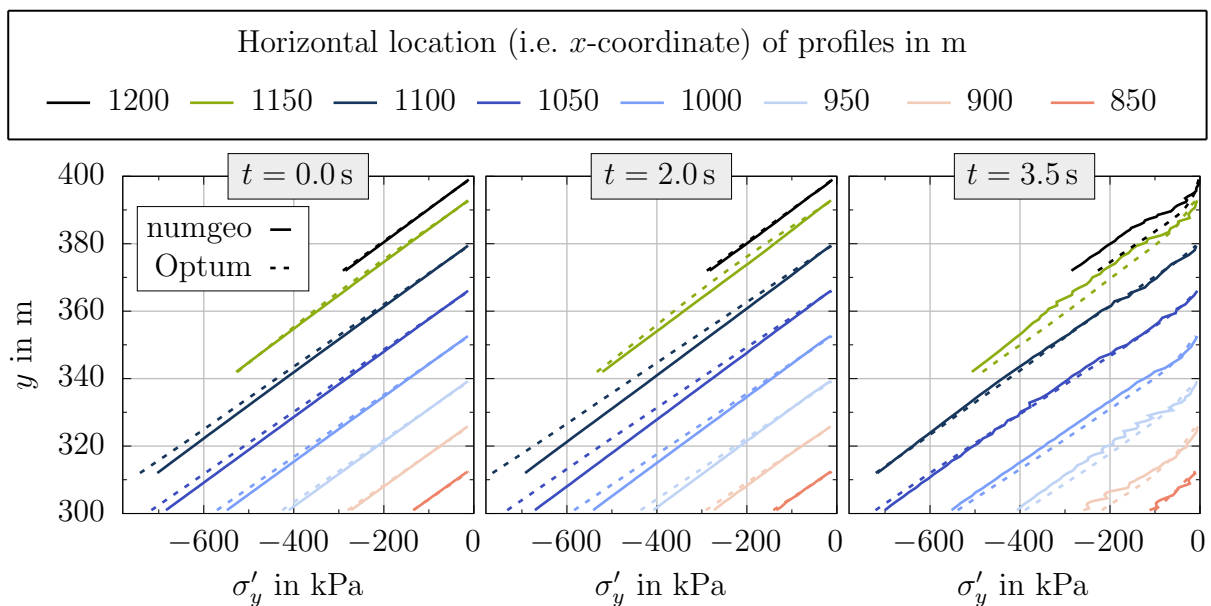


Figure 6.6: Comparison of `numgeo` and `OptumG2` regarding effective vertical stresses along vertical profiles obtained at different horizontal locations (see e.g. Fig. 7.1) and time steps

total height. A better approximation could be obtained using an incremental approach that allows the determination of unit weights with regard to stress variation in close proximity. Nevertheless, as the slip surface is expected to be located in a shallow depth, an approximation of the effective stresses is considered appropriate for the entire model.

Considering the mapping of the total stress state, it should be noted that the concept discussed above may result in an underestimation of the total stresses in those cases where excess pore water pressures are built up during the earthquake loading. However, as there is no possibility of importing excess pore water pressures in **OptumG2**, this underestimation cannot be avoided. An explanation for this underestimation can be given with regard to the total unit weight γ_{tot} that should be determined based on $\gamma_{\text{tot}} = \gamma' + \gamma_w + \Delta p^w/h_w$. However, as only a single unit weight parameter can be prescribed for saturated conditions, either the effective or the total stress state can be approximated well. For this approach, it was decided to accurately approximate the effective stress state to enable proper determination of shear resistance. Still, as the total stress state is used to determine inertial forces, underestimation of the latter is to be expected. An approach to overcome this issue is discussed in the next section.

6.3.3. Mapping of inertial forces

In contrast to material parameters (e.g. unit weights, friction angle), which can be imported to **OptumG2** in terms of unstructured table data, it is not possible to import inertial forces or pseudo-static coefficients in the same way. Instead, pseudo-static coefficients can only be assigned to predefined areas, referred to as clusters in this study. In order to enable the mapping of inertial forces, the idea is to define a collection of clusters, calculate average accelerations within them and assign corresponding pseudo-static coefficients to these clusters. The inertial forces in the horizontal and vertical direction are determined (in **OptumG2**) based on the product of pseudo-static coefficients $k_{h/v}$ and weight W according to Eq. 2.8 and Eq. 2.9, respectively.

Note that the weight W should be the total weight, such that inertial effects stem from accelerated soil-water mass. However, the total weight is underestimated in cases where excess pore water pressures are built up during the earthquake loading since the mapping concept of the effective stresses (Section 6.3.2) results in an underestimation of the total unit weight in those cases. As the total unit weight is determined as γ_{sat} instead of γ_{tot} to accurately predict γ' (see discussions above), this underestimation also influences the determination of the inertial forces. To compensate for the reduced total stresses for the

determination of the inertial forces, a factor Υ is introduced as the fraction of the total unit weight γ_{tot} and the reduced total unit weight γ_{sat} according to Eq. 6.2. This factor is multiplied with the pseudo-static coefficients to allow for a more accurate approximation of the inertial forces.

$$\Upsilon = \frac{\gamma_{\text{tot}}}{\gamma_{\text{sat}}} \quad (6.2)$$

To account for the spatially variable nature of inertial forces in the simulation, the computational model is divided into a multitude of clusters. As the geometry of the clusters (e.g. shape and size) may have a significant impact on the quality of the approximation, preliminary studies have been conducted investigating the effect of different shapes (e.g. rectangle, parallelogram) and size of clusters on the slope stability. It was found that approximations via parallelograms with the inclination of the embankment slope yield reliable results in combination with small cluster sizes that achieve higher accuracy in the approximation of the inertial forces. Note that drawbacks associated with small cluster sizes are high computational costs due to larger numbers of finite elements required for the stability analysis and potential discretization issues. In addition, the effort and complexity to generate the `OptumG2` BASE files, including linking of these clusters to the Python scripts, increases with an increasing number of clusters. Thus, a cluster size should be selected that balances accuracy and computational costs, yet yielding robust and reliable estimates of the FoS. A schematic illustration depicting an original distribution of acceleration magnitudes obtained from a DFEA together with spatial approximations using parallelograms of varying sizes is given in Fig. 6.7. Note that parallelograms exceeding the right edge of the model are cut as only the slope area is considered in the stability analysis. Analyzing the quality of the different approximations shown in this figure, it is apparent that the size of the clusters has a decisive impact on the representation of the spatial distribution of accelerations. For the stability analyses performed in Section 7.3.2, the height and base of the clusters were chosen to be $h = 0.05 \cdot H = 5.0$ m and $b = 0.10 \cdot H = 10.0$ m, respectively, where H is the height of the slope, resulting in a total number of 380 clusters. With this cluster size, a proper approximation of the spatial distribution of inertial forces is enabled using parallelograms, while computational costs of the stability analyses do not exceed the capacity of standard desktop computers.

6.3.4. Mapping of friction angle

As the hypoplastic model cannot be used to conduct strength reduction analysis in `OptumG2`, a switch of the constitutive model (i.e. model change) is required. In con-

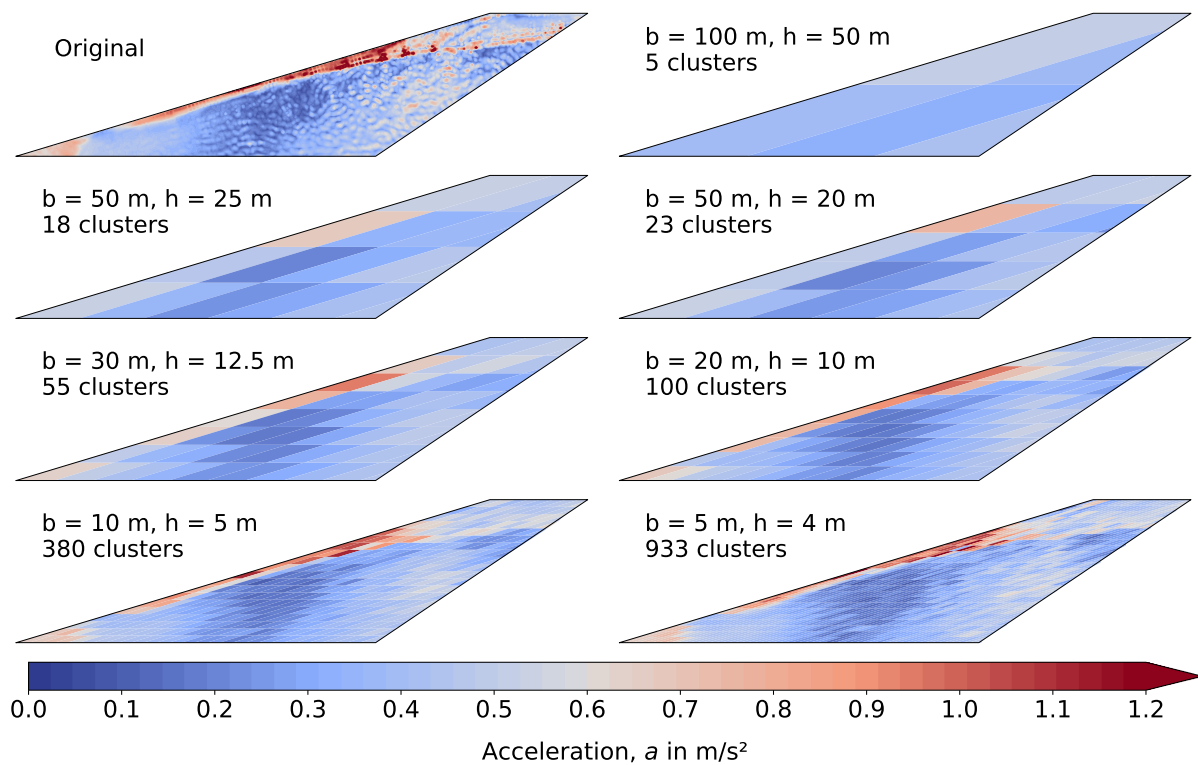


Figure 6.7: Approximation of the spatial distribution of acceleration magnitudes with different cluster sizes

trast to the hypoplastic model in which shear strength is not described by a constant friction angle, in simple elastoplastic models used for stability analyses, shear strength parameters (cohesion and friction angle) are usually constant. However, the question arises which friction angle should be used in the stability analyses. A conservative estimate would be to apply the critical friction angle φ_{crit} for the stability analyses. As the critical friction angle is a constant material parameter of the hypoplastic model, it is independent of the boundary value problem or the dynamic loading; thus, it can be used throughout the whole domain for any time step. Note that applying φ_{crit} , density (pyknosity) and confining pressure (barotropy) effects are neglected, which may result in very conservative estimates of the slope stability.

Considering the stress–dilatancy correlations proposed by Bolton (1986), the peak friction angle φ_{max} can be determined based on the critical friction angle φ_{crit} , the relative dilatancy I_R and a constant m according to Eq. 6.3. The relative dilatancy I_R is calculated from the initial relative density I_{D0} , a model parameter Q linked to the particle crushing strength σ_c , the effective mean stress p' and a model parameter R . Bolton (1986) suggests $Q = 10$ for quartz and feldspar grains, $R = 1.0$ for a wide range of sands and $m = 5$

and $m = 3$ for plane strain and triaxial conditions, respectively. More recent studies, for instance by White et al. (2008), suggest smaller values of m such as $m = 1.6$ based on analyses of the vertical bearing capacity of shallow foundations using centrifuge model tests. Choosing $m = 1.6$ and an initial relative density $I_{D0} = 0.3$, the difference between peak and critical friction angles would not be larger than $\varphi_{\max} - \varphi_{\text{crit}} = 3.2^\circ$ for mean stresses $p' \geq 1.0$ kPa. However, this difference increases up to $\varphi_{\max} - \varphi_{\text{crit}} = 10.0^\circ$ when using the original value of m suggested for plane strain conditions.

$$\varphi_{\max} = \varphi_{\text{crit}} + m \cdot I_R \quad (6.3)$$

$$I_R = I_{D0} \cdot (Q - \ln p') - R \quad (6.4)$$

Considering the Bolton approach with $m = 1.6$, the spatial distribution of the friction angle is depicted in Fig. 6.8 for four different time steps of the dynamic excitation phase. Note that, in general, increased friction angles are obtained close to the ground surface due to smaller effective mean stresses. As seen in the last sub-figure, friction angles at the slope crest further increase with increasing dynamic time as effective mean stresses decrease due to the seismic loading.

6.3.5. Consideration of a non-associated flow rule

As an associated flow rule is a prerequisite of limit analysis and accordingly also finite element limit analysis (FELA), parameter sets used for simulations with FELA are restricted to a dilation angle that equals the friction angle ($\psi = \varphi$). However, the stress-strain behavior of soils is not well captured following an associated flow rule as this leads to significant overestimation of plastic volumetric strains. Therefore, a non-associated flow rule should

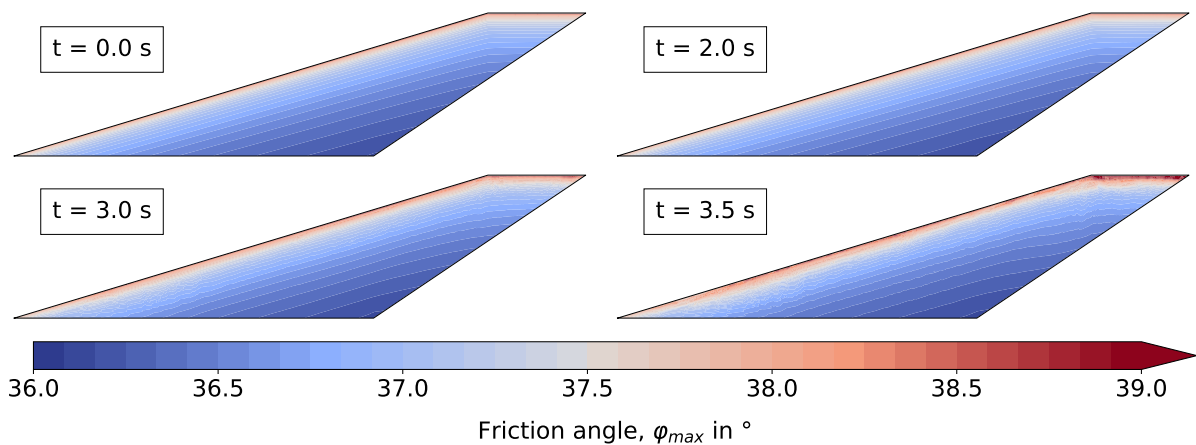


Figure 6.8: Spatial approximation of the friction angle for different time steps

be applied. Note that a non-associated flow rule refers to different yield and potential surface used in the constitutive model, which can be achieved by applying similar functions for both surfaces but using $\psi < \varphi$. It is important to understand that utilizing a non-associated flow rule, velocity and stress characteristics denoting lines of major/minor principle stresses and velocities, respectively, are not parallel anymore. Considering that it is generally accepted that the velocity characteristics do better approximate the failure surface compared to the stress characteristics, corresponding shear strength parameters should be used (Davis, 1968; Roscoe, 1970; Tschuchnigg et al., 2015a). Therefore, Davis (1968) introduced a strength reduction factor β_{failure} to derive reduced shear strength parameters (c^* , φ^*) for a given dilation angle ψ following Eqs. 6.5 - 6.7. This approach was verified by Roscoe (1970), who evaluated direct shear tests.

$$c^* = \beta_{\text{failure}} \cdot c \quad (6.5)$$

$$\tan \varphi^* = \beta_{\text{failure}} \cdot \tan \varphi \quad (6.6)$$

$$\beta_{\text{failure}} = \frac{\cos \varphi \cdot \cos \psi}{1 - \sin \varphi \cdot \sin \psi} \quad (6.7)$$

Analyzing the influence of the dilation angle on slope stability, Tschuchnigg et al. (2015b) have shown that stability analyses using an associated flow rule lead, especially for frictional soils, to over-prediction of the FoS. This over-prediction increases with increasing friction angles and decreasing dilation angles, thus with an increasing degree of non-associativity ($\Lambda = \varphi - \psi$). However, it was found that the Davis (1968) approach resulted in better but slightly conservative predictions of the FoS. Similar observations were also made for other geotechnical boundary value problems, for instance, the passive earth pressure problem (Nordal, 2008; Schmüdderich et al., 2022b). Tschuchnigg et al. (2015a) proposed extensions of the Davis approach (referred to as “Davis B” and “Davis C”) by consideration of the current FoS for the determination of the updated reduced shear strength parameters, the former extension given in Eq. 6.8. In contrast to the Davis A approach, which only required a single stability analysis, three to four iterations are required when using Davis B to converge to a constant FoS and β_{failure} .

$$\beta_{\text{failure}} = \frac{\cos \left(\arctan \left(\frac{\tan \varphi}{\text{FoS}} \right) \right) \cdot \cos \left(\arctan \left(\frac{\tan \psi}{\text{FoS}} \right) \right)}{1 - \sin \left(\arctan \left(\frac{\tan \varphi}{\text{FoS}} \right) \right) \cdot \sin \left(\arctan \left(\frac{\tan \psi}{\text{FoS}} \right) \right)} \quad (6.8)$$

The dilation angle must be known in order to conduct analyses based on the Davis A or B approaches. In general, the sine of the dilation angle can be defined in accordance with Eq. 6.9 as the ratio between the volumetric strain increment $\delta \varepsilon_{\text{vol}}$ and the deviatoric strain increment $\delta \varepsilon_{\text{q}}$. However, as the shear strain increment varies strongly during the

earthquake loading, this effect directly propagates to the dilation angle ψ , potentially resulting in a large scatter of the FoS.

$$\sin \psi = \frac{\delta \varepsilon_{\text{vol}}}{\delta \varepsilon_{\text{q}}} \quad (6.9)$$

Based on findings by Bolton (1986) that the rate of dilation is identical for triaxial and biaxial strain, Schanz and Vermeer (1996) rearranged the terms of the stress–dilatancy correlations (Bolton, 1986), to determine the dilation angle with regard to the relative dilatancy I_R (Eq. 6.4) as follows

$$\sin \psi = \frac{0.3 \cdot I_R}{2 + 0.3 \cdot I_R} \quad (6.10)$$

This definition is applied for the approach at hand to determine the spatial distribution of the dilation angle and enable analyses with the Davis approaches.

6.4. Strain-dependent slope stability for earthquake loading

6.4.1. Motivation

Evaluating the stability of slopes subjected to earthquake loading in terms of a FoS is a difficult task when not relying on pseudo-static or pseudo-dynamic approaches. As emphasized in Section 2.2.4, advanced finite element schemes and sophisticated constitutive models are required to approximate the dynamic system behavior accurately, including effects such as damping, strain accumulation or accumulation of excess pore water pressures. However, constitutive models that meet these requirements can usually not be applied to standard strength reduction analyses because the shear strength is not only controlled by the friction angle but additional material parameters must be considered. For this reason, the majority of researchers have not treated the problem of slope stability under seismic conditions evaluated in terms of FoS considering sophisticated constitutive models extensively. Most studies in this field have either focused on static problems, estimation of the FoS utilizing approximate methods such as pseudo-static or pseudo-dynamic approaches combined with simple elastoplastic constitutive models, estimation of displacements based on the analogy of a rigid sliding block, or only investigated liquefaction and deformation problems related to earthquake loading without analyzing the FoS.

In contrast, the concept of strain-dependent slope stability (SDSS) by Nitzsche and Herle (2020) enables the evaluation of the FoS considering sophisticated constitutive models. However, it only allows analyzing slope stability problems for static conditions and has some drawbacks when tackling dynamic problems. Thus, a valuable contribution to slope stability evaluation for seismic problems can be made by extension of the original SDSS (Schmüdderich et al., 2022a), which is proposed in the following. A schematic illustration of the SDSS and a flow-chart providing further details with regard to the optimization are given in Fig. 6.9 and Fig. 6.10, respectively.

In this section, discussions are provided with respect to three main aspects of adaption: the shape of the slip surface, a more precise definition of initial shear stress τ_0 used for normalization and general thoughts about the effect of specific constitutive model features on conservative and optimistic estimates of the FoS. Subsequently, a new methodology is developed to significantly enhance the computational efficiency of the strain-dependent slope stability concept by taking advantage of parallelization of element test simulations as well as adaption of different machine learning algorithms.

6.4.2. Shape of the slip surface

In the original concept of the strain-dependent slope stability, the shape of the failure mechanism is assumed to be of a wedge type with a linear slip surface. Nitzsche and Herle (2020) report that this shape has been chosen as it allows to assume that the simple shear conditions hold for any point along the slip surface. Thus, the development of shear strains in terms of direction and magnitude is identical for all points along the slip surface. By choosing other shapes of the slip surface, for instance circular or log-spiral shapes,

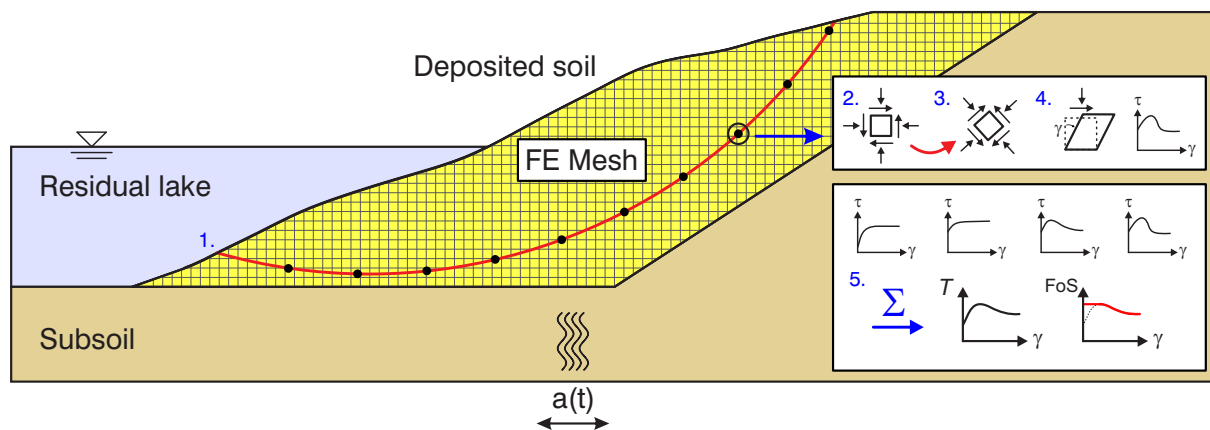


Figure 6.9: Schematic illustration of the concept of strain-dependent slope stability

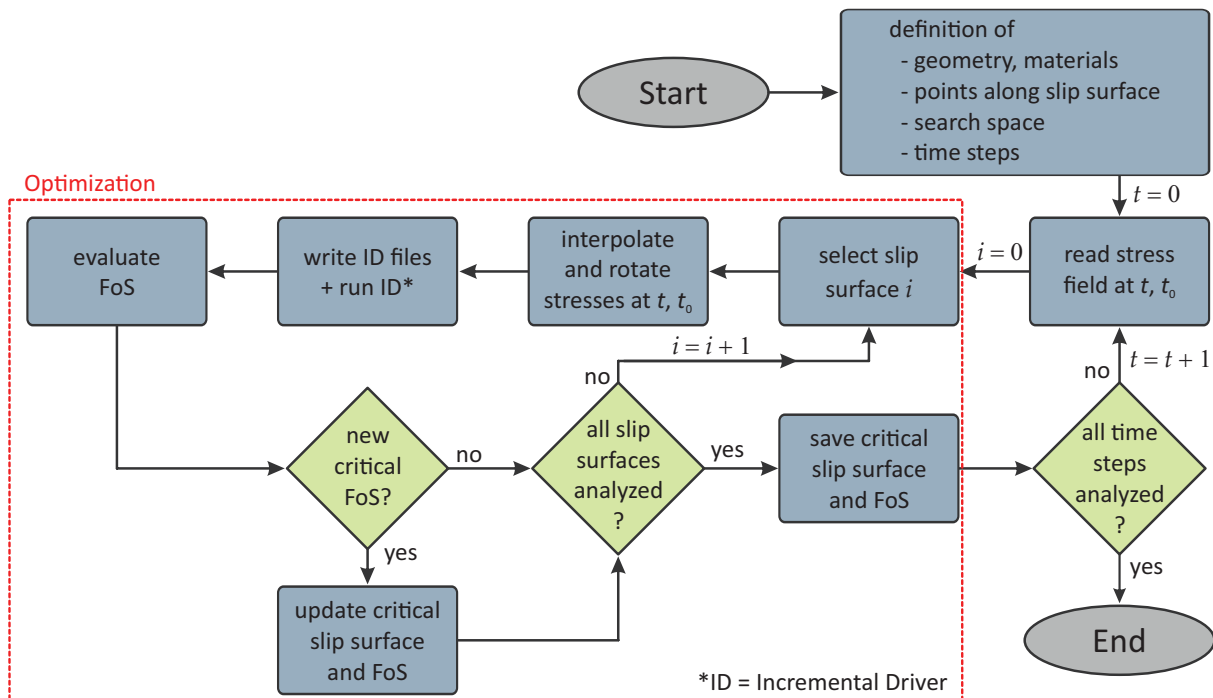


Figure 6.10: Flow chart depicting the general concept of SDSS including optimization to locate the critical slip surface

different conditions such as triaxial compression or extension could also occur along the slip surface leading to difficulties in conducting the element tests and evaluating the global mobilized shear resistance ratio $T(\gamma)$ as the summation of individual shear stress versus shear strain curves. Still, it should be noted that the assumption of a linear slip surface significantly limits the potential boundary value problems to be investigated.

In this approach, a circular slip surface is investigated (Fig. 6.9 and Fig. 6.11). Due to a rotation of the failure mechanism it is assumed that the rate of shear strains is identical in magnitude along the slip surface, whereas their direction is tangential to the slip surface. It should be noted that the assumption of a circular slip surface is, as well, not necessarily a correct approximation of real case failure mechanisms; however, for most practical cases it is a better one compared to a linear slip surface. Moreover, it enables the evaluation of slip surfaces that enter and exit within the sloping area, which is relevant for slopes with shallow slip surfaces, for instance, gentle slopes composed of sandy material subjected to earthquake loading, as will be discussed later.

Generation of slip surfaces is performed using the entry-exit method (see Section 3.3) by definition of entry, exit and radius points. Optimization to find the critical slip surface can be conducted using different optimization schemes (see e.g. Fig. 6.10), for instance

Grid Search, Particle Swarm Optimization (PSO) (Clerc, 2013) or Differential Evolution (DE) (Storn and Price, 1997). Although trial analyses showed that optimization via DE yields very accurate and reproducible results, brute grid search is chosen for the majority of the simulations in this study to enable a fair comparison between different element test simulation schemes based on identical numbers of simulations performed in every case. Further analyses utilizing machine learning approaches have been conducted with DE rather than PSO as trial analyses revealed significantly lower scatter for repeated optimization runs. Similar observations have also been reported by Macháček et al. (2022) with regard to the automatic parameter calibration of a hypoplastic soil model.

6.4.3. Reference state for normalization

Following the original concept by Nitzsche and Herle (2020), the global mobilized shear resistance ratio $T(\gamma)$ shown in Fig. 2.4 is constrained to start at $T(\gamma = 0.0) = 1.0$ for any slip surface under investigation, independent of any problem-specific boundary condition or constitutive model used to simulate the soil behavior. The reason for this is the normalization approach chosen which enforces division by the sum of the initial shear stresses which always yields unity for the beginning of the $T(\gamma)$ curve (see Eq. 2.7). Although for softening soils the residual factor of safety (FoS_{res}) may drop below unity, the maximum factor of safety will always be larger than or equal to unity ($\text{FoS}_{\text{max}} \geq 1.0$) due to the fact that the initial value of global mobilized shear resistance ratio is always equal to unity. For soil materials not showing softening behavior, the residual and maximum factor of safety will always be larger than or equal to unity ($\text{FoS}_{\text{res}} \geq 1.0$ and $\text{FoS}_{\text{max}} \geq 1.0$). Therefore, it should be very clear that using the current approach and focusing on FoS_{max} as an estimate for the safety at small shear strains, it is not possible to classify slopes as unstable. In view of a static finite element simulation using advanced constitutive models (e.g. multisurface bounding plasticity, hypoplasticity), this fact ($\text{FoS}_{\text{max}} \geq 1.0$) may be of subordinate importance as long as for unstable slopes numerical instabilities (e.g. large strains and displacements leading to distorted element shapes) during the construction, excavation or gravity loading phase of the finite element slope model prohibit finding an equilibrium state and, thereby, an appropriate initial stress field for further slope stability analysis².

²Using constitutive models without failure criterion such as linear elasticity it is also possible to obtain an initial stress field for “unstable” slopes, which would then be classified as stable using the approach at hand.

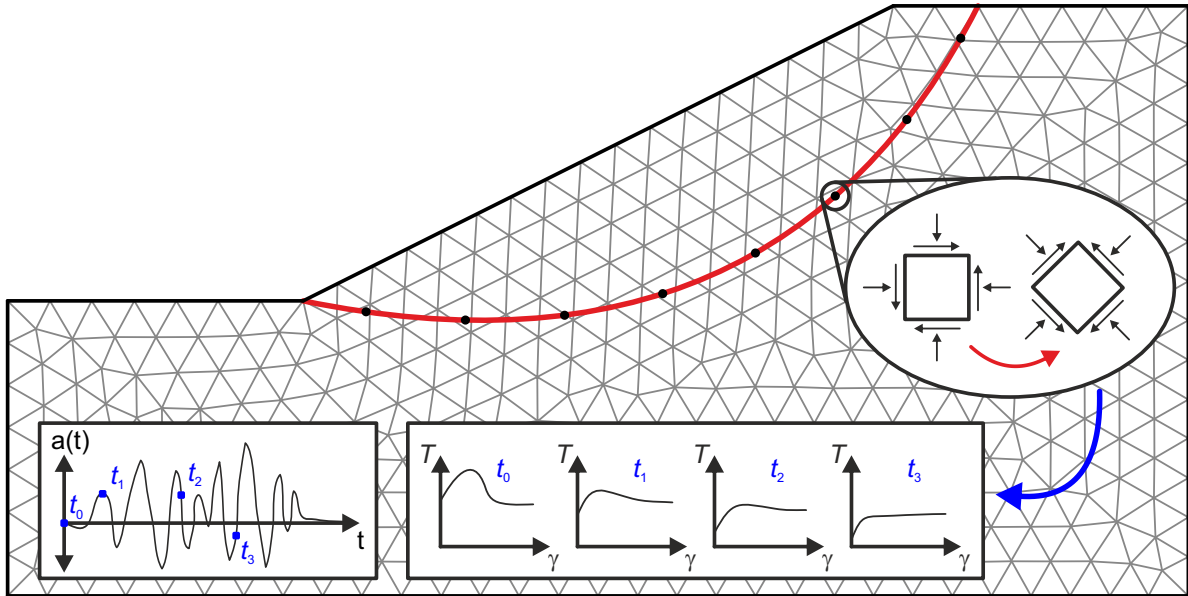


Figure 6.11: Determination of the global mobilized shear resistance ratio T for different time steps of the dynamic excitation

It should be emphasized that the equilibrium which needs to be satisfied during the finite element simulation is a dynamic equilibrium that also includes damping and inertial effects. Therefore, a priori it is not clear if a slope which is in dynamic equilibrium during an earthquake loading also satisfies the static equilibrium and should be classified stable or unstable under static conditions. In this context, the advantage of stress-based approaches including SDSS is that stresses at different points along the slip surface are elaborated independently of the overall static equilibrium, whereas strength reduction schemes have to make assumptions in a way to find a stable equilibrium, for instance approximation of inertial forces via pseudo-static approaches.

To overcome the drawbacks discussed previously, the approach proposed is to choose the initial shear stress used to derive the global mobilized shear resistance ratio $T(\gamma)$ based on the static equilibrium referred to as time step t_0 , see Fig. 6.11. Thereby, also a fair comparison of different time steps is enabled as normalization of the mobilized shear stresses is performed with respect to a fixed reference time step (t_0). The updated equation to evaluate the global mobilized shear resistance ratio T as a function of the shear strain γ and the dynamic time t_{dyn} then reads:

$$T(\gamma, t_{\text{dyn}}) = \frac{\sum_i \tau_{\text{mob},i}(\gamma, t_{\text{dyn}})}{\sum_i \tau_{0,i}(t_0)} \quad (6.11)$$

Compared to the evaluation of the global mobilized shear resistance ratio according to Eq. 2.7, the computational effort for evaluation of Eq. 6.11 is slightly larger as stresses at

each point i along the slip surface have to be determined for the current (t_{dyn}) and the reference time (t_0). However, as only the initial shear stress is required at the reference time, there is no need to also perform an element test. Thus, the increased computational effort is limited to interpolation and rotation of the stress state at the reference time. In view of the computational effort related to the computations conducted for the current time including the simulation of the element test, the additional computational effort due to evaluation of the stresses at the reference time is almost negligible.

6.4.4. Constitutive model

Nitzsche and Herle (2020) used an elastoplastic constitutive model with Mohr-Coulomb failure criterion and a strain-softening rule controlling the critical friction angle to show the effect of softening for SDSS. The current stresses at the points defining the failure surface were interpolated from an initial stress field obtained using a finite element simulation. However, no other information (e.g. additional state variables) has been transferred from the finite element model to the element test simulations, thus, plastic strains controlling the softening process have been reset to zero at the beginning of the element tests. As the constitutive model used in (Nitzsche and Herle, 2020) can not properly approximate the soil's behavior under earthquake loading, the hypoplastic model with intergranular strain (von Wolffersdorff, 1996; Niemunis and Herle, 1997) is used herein. Additional state variables such as the void ratio and the components of the intergranular strain tensor are interpolated at the points along with the stress state.

Element test simulations are performed with Incremental Driver (Niemunis, 2008). As the hypoplastic stiffness is influenced by the intergranular strain, the shear stress versus shear strain behavior under simple shear conditions is affected accordingly. To assess to what extent IGS affects the evolution of shear stresses in a simple shear test, its influence is investigated by comparison of the basic version of hypoplasticity (von Wolffersdorff, 1996) with and without the intergranular strain (IGS) extension. Simple shear tests have been simulated with mean effective stresses of $p' = 5$ kPa, $p' = 21$ kPa and $p' = 146$ kPa. To investigate the maximum potential deviation between both models, the IGS tensor is initialized with zero values ($\mathbf{h}_0 = \mathbf{0}$) leading to a large increase in the hypoplastic stiffness at small strain levels. The results are presented in terms of shear stress τ versus shear strain γ curves in Fig. 6.12. As can be seen from this figure, the stress-strain behavior under simple shear conditions is significantly influenced by IGS in terms of the general curve trend for shear strains $\gamma < 0.1$, in contrast to shear stresses at residual strains ($\gamma > 0.2$) where the effect of IGS has vanished. Moreover, it is apparent from this figure

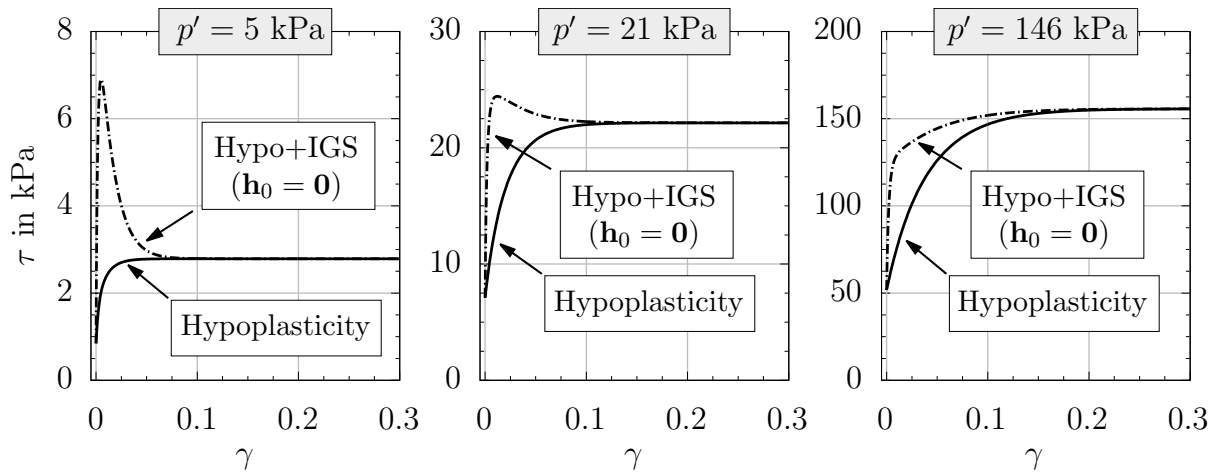


Figure 6.12: Effect of IGS on simple shear test simulations for different mean effective stresses p'

that IGS has an effect on the maximum shear stress, which is very large for small mean effective stress levels and decreases with increasing mean effective stresses. For the curves presented here, the increase in the maximum shear stress is approximately 150 % and 10 % for small and intermediate mean effective stress levels, respectively, whereas no increase in the maximum shear stress is observed for large mean effective stress levels.

In light of these findings, it should be clear that the effect of IGS on simple shear tests also has an impact on the factor of safety obtained using SDSS, at least when the FoS is determined at small shear strains or when the FoS is based on the maximum shear stress. However, as the stress points in the slope area are subjected to multiple loading and unloading cycles during the dynamic loading phase undergoing large strains, it is expected that the IGS tensor is different from a null state, leading to smaller stiffness increments during the analysis of FoS using element tests. Yet, if the orientation of the last loading cycle in the dynamic phase varies significantly from the dip angle of the slip surface, increased hypoplastic stiffness due to IGS is to be expected. Considering that, in general, the evaluation of FoS is preferably based on a slightly conservative estimate rather than a too optimistic one, IGS should thus not be considered in the stability analysis.

6.5. Spatial pseudo-static analysis using SRFEA

In contrast to the approaches proposed in the previous sections, the spatial pseudo-static analysis using SRFEA aims to conduct the DFEA and the SRFEA using the same software

package. `numgeo` software package was selected as main features relevant for this task (e.g. DFEA and sophisticated constitutive models) have been implemented and verified in advance of this study. As active coding was welcomed by the `numgeo` project leaders, elastoplastic constitutive models (Mohr-Coulomb and Matsuoka-Nakai, see Chapter 4), the strength reduction method (see Chapter 5) and further additional features have been implemented in `numgeo` within the scope of the present thesis. Details about the general approach, as well as existing and implemented features used to conduct the combined DFEA and SRFEA are provided in the subsequent paragraphs.

In general, it should be noted that advantages of performing DFEA and SRFEA in one software package include that the same interpolation schemes, element types and spatial discretization of elements are used in both analyses. In `numgeo`, a restart is required to enable a constitutive model change, for instance from Hypoplasticity with Intergranular Strain (Hypo+IGS) used in DFEA to Matsuoka-Nakai used in SRFEA, which also enables the transfer of additional information. In contrast to rough estimates or mapping concepts applied in previous approaches, the transfer of stress states and state variables as well as excess pore water pressures and displacements is enabled in the integration points and nodes, respectively. Moreover, by usage of one software package, there is a huge potential for automation of the two consecutive analyses. The following new features have been added to `numgeo` to enable DFEA with subsequent SRFEA:

Reduction: SRFEA is conducted in `numgeo` using the calculation type `*Reduction` in the step definition. Note that this keyword is followed by a line with two additional inputs, which are the initial FoS (FoS_0) used in the first increment of the SRFEA and the FoS increment (ΔFoS) that is added in each increment of the strength reduction analysis. Until now, reduction of material shear strength parameters in a SRFEA is enabled only in combination with the Mohr-Coulomb and Matsuoka-Nakai model, where an additional flag called `*Reducible Strength` needs to be activated in the material definition. For cases where strength reduction should only be applied to a section of the model, separate parameter sets need to be defined to enable strength reduction in the area of interest while keeping the original strength parameters outside of that area. Note that the initial FoS should not be selected too small ($FoS < 0.5$) in order to avoid unrealistically large friction angles.

Nodal dynamic force: It is important to note that the system is in a dynamic equilibrium during the simulation of a seismic event (e.g. earthquake loading), but slope stability analyses are commonly performed based on a static equilibrium. To maintain the dynamic state in the slope stability analysis, inertial forces are considered. In this approach, the

global nodal dynamic/inertial force vector, which is the product of the mass matrix and the acceleration vector, is saved together with the nodal and element information during the dynamic simulation. In SRFEA, this nodal inertial force vector is imported and considered as additional external force vector. To import inertial forces from a previous step, the keyword `*Nodal dynamic force` is used in the step definition.

Boundary, increment: In general, the `*Boundary` keyword is used to define boundary conditions at nodes or nodes sets with regard to the solution variables (i.e. degrees of freedom), where the latter depend on the element type. To maintain the deformed state of the finite element model after the DFEA, boundary conditions in SRFEA should be adapted in a way that displacement increments, not total displacements, are set to zero at the model boundaries. This is achieved by selecting the option `increment`. Note that setting total values rather than increments to zero would introduce incremental displacements as the coordinates of the nodes at the model boundaries in the deformed state do not necessarily match the ones in the undeformed state. The reason for this is that the dynamic signal applied in terms of displacements/velocities/accelerations or distributed loads leads to non-recoverable displacements of these nodes during the dynamic excitation phase. Moreover, the increments of pore water pressures (i.e. the rates) can be set to zero to maintain the spatial distribution of excess pore water pressures at a given time step. This is achieved by applying the `Boundary, increment` keyword for the pore water pressure (`pw`) to all nodes of the model.

Restart/Submodel: As mentioned above, SRFEA is conducted using a `*Restart` analysis that enables to change the material model and adjust the boundary conditions. A `*Restart` analysis allows to restart a finished simulation in a second analysis starting with the initial state of the first analysis. Note that this strategy is very inefficient and related to large computational costs. The reason for this is that to analyze the evolution of the FoS during dynamic loading, many DFEA have to be conducted, where each analysis is stopped at a different time, intermediate results are saved and SRFEA is conducted via restart. Considering a constant frequency over the full DFEA for which SRFEA should be conducted, an equivalent of approx. $n/2$ DFEA analyses need to be performed, where n is the number of SRFEA analyses. Thus, as an example, investigating the evolution of FoS for 500 time steps of the DFEA, computational costs of the dynamic analyses can be approximated by around 250 times the computational costs of a single DFEA. As an alternative, `*Submodel` analyses can be conducted, which enable to conduct restart analyses at predefined total time steps or frequencies. Note that the main advantage of `*Submodel` analyses compared to `*Restart` analyses is that the original simulation, i.e.

the DFEA, is not terminated but on hold. Once the SRFEA is finished at a specified time of the dynamic loading, the original simulation is resumed. Thereby, not considering the time required for writing the restart files, the computational costs related to the DFEA performed during submodel analyses are identical to the computational costs of a single DFEA. For this reason, the spatial pseudo-static analysis using SRFEA is conducted in terms of DFEA and SRFEA coupled via submodel analyses considering the additional features mentioned above. Note that the implementation of both features – `*Restart` and `*Submodel` – into `numgeo` was not part of this work.

6.6. Major differences of the proposed approaches

To enhance the comprehensibility of the discussions in the subsequent chapters, in which the seismic slope stability is assessed for different boundary value problems, major differences of the approaches presented in this chapter are emphasized beforehand. Since the names used for the approaches are rather long, the following short forms are used in this section: (PSA-)LEM, (PSA-)FELA, SDSS and (PSA-)SRFEA. Major differences of LEM, FELA, SDSS and SRFEA are discussed with regard to the approximation of stresses, inertial forces, equilibrium, shear strength and failure mechanisms.

Approximation of stresses: In LEM, total vertical stresses are determined with respect to the overburden height and the (un-)saturated unit weight of the soil (see Section 6.2). Depending on the method applied, lateral stresses and shear stresses are estimated differently. Effective stresses are calculated by subtraction of hydrostatic pore water pressures p^w and excess pore water pressures Δp^w from the total stresses, where p^w is calculated based on the phreatic level and Δp^w can be back-calculated from DFEA results at the nodes and interpolated for the slice bases. In the FELA approach, stress distributions can not be prescribed directly, but via corresponding unit weights. Total stresses are determined based on the overburden height and the (un-)saturated unit weight of the soil and lateral stresses are calculated based on the vertical stresses and the lateral earth pressure coefficient. Shear stresses are calculated in a way to satisfy equilibrium conditions. Effective stresses are calculated by subtraction of hydrostatic pore water pressures p^w from the total stresses. Note that excess pore water pressures Δp^w can not be considered separately. Thus, for cases where $\Delta p^w > 0$, either the total or the effective stresses can be approximated properly (see Sections 6.3.2 and 6.3.3). By ensuring a proper approximation of effective stresses in case of $\Delta p^w > 0$, total stresses are underestimated, which is compensated by consideration of increased seismic coefficients.

In SDSS and SRFEA, accurate distributions of total and effective stresses are used, since no mapping concept is required.

Inertial forces: In pseudo-static approaches (PSA, see Section 2.2.1), dynamic effects are considered in terms of inertial forces, which are the product of mass and seismic coefficients, the latter denoting accelerations normalized by gravity. At each dynamic time step of interest during the DFEA, accelerations are saved for each node and seismic coefficients are calculated. Inertial forces are obtained in a subsequent step during the execution of the different approaches. In LEM and FELA, horizontal inertial forces are orientated in driving direction, whereas in SRFEA, horizontal inertial forces are orientated according to the DFEA. Furthermore, average inertial forces for each cluster are determined in FELA, which might filter out very large values considered in LEM and SRFEA. As SDSS is not based on PSA but only considers stresses and state variables, no inertial forces are considered.

Equilibrium: Depending on the method selected, in LEM, FoS is determined based on the global equilibrium of horizontal forces and/or momentum. However, it is not checked whether the overall system satisfies equilibrium conditions. Similar to LEM, in SDSS, no equilibrium conditions are enforced. This also refers to the fact that stresses can not be redistributed in SDSS, for instance from one element to another element along the slip surface. In FELA, equilibrium conditions need to be satisfied throughout the domain to obtain a rigorous solution. However, as stresses and inertial forces are roughly estimated, it can not be ensured that the equilibrium agrees well with the dynamic equilibrium obtained in the DFEA at every time step. In SRFEA, the aim was to accurately maintain equilibrium by consideration of inertial forces and adjusted boundary conditions. However, further elaboration is required to verify this approach in depth.

Shear strength: In LEM and FELA, the Mohr-Coulomb (MC) failure criterion is used, which, compared to the Matsuoka-Nakai (MN) failure criterion, allows for smaller deviatoric stresses under plane strain conditions. In LEM, consideration of the MN criterion is rather difficult as the full stress tensor needed to be transferred to LEM. Alternatively, choosing a fixed Lode angle (e.g. $\theta = 0^\circ$) an equivalent MC friction angle could be applied in accordance with the MC model, utilizing design charts as suggested by Griffiths and Huang (2009) or Jiang and Wang (2011). In FELA, the maximum friction angle following the Bolton (1986) approach is applied which considers a dependency of the friction angle on the mean effective stress. Thereby, larger friction angles are obtained for smaller stress levels. In SDSS, the soil shear strength relevant for the stability analyses is related to the mobilized shear strength at a given shear strain. Applying sophisticated constitutive

models, advanced effects, as for instance those of loading history, can be considered by transfer of state variables. SRFEA can be performed with the MC model or the MN model, where the latter is preferred in this work as Hypoplasticity used for the DFEA incorporates the Matsuoka-Nakai limit surface. Note that LEM, FELA and SRFEA could further be extended in a way to allow for spatially inhomogeneous distributions of the shear strength parameters, for instance by considering a spatial distribution of the MN friction angle rather than a homogeneous distribution. For MC models, an additional factor to account for the equivalent MC friction angle could be used.

Failure mechanism: In LEM and SDSS, the shape of the failure mechanism needs to be selected prior to the stability analyses. Thereby, the critical failure mechanism may not be approximated accurately. Note that for LEM, post optimization (see Section 3.3) allows to detect critical slip surfaces with shapes different from the initial circular shape. However, using a similar post optimization in SDSS to consider non-circular slip surfaces (e.g. composite slip surfaces), assumptions need to be made with regard to the magnitude of shear strain experienced at different nodes. A potential solution to overcome this issue would be the adaption of a hodograph to ensure kinematic compatibility. In contrast, in FELA and SRFEA, the shape of the failure mechanism is not prescribed, but is the result of the optimization process and the strength reduction method, respectively.

7. Saturated opencast slope subjected to seismic loading

7.1. Motivation

As an application of the proposed methods, the stability of an opencast mine slope under earthquake loading is investigated. When opencast mines are decommissioned, the residual pits are frequently refilled with soil or water, resulting in so-called residual lakes. The enclosing slopes of such lakes are often made of uncompacted material obtained from the excavation pit whose pores are filled with water. Depending on the drainage conditions, cyclic shearing of the grain skeleton induced by earthquakes may lead to a build-up of excess pore water pressures, accompanied by a reduction of effective stress and, consequently, to a decrease of shearing resistance of the soil. The seismic stability assessments of such slopes are therefore complex and non-linear problems, often addressed using pseudo-static approaches that neglect material-induced failures and the role of pore-fluids. They are thus ideally suited to present the advantages and applicability of the proposed methods introduced in the previous chapter.

7.2. Dynamic finite element analysis

7.2.1. Finite element model

The finite element software `numgeo` was used for the analysis of the dynamic excitation of a water-saturated slope of an open pit mine, where the model is schematically shown in Fig. 7.1. The model represents an idealized slope of an open pit and consists of two sections, namely the “Slope” and the “Subsoil”. The embankment was created by the deposition of the waste material during the operation of the open cast mine and consists of loose sand ($D_{r0} = 0.3$). The subsoil section represents the natural material, composed

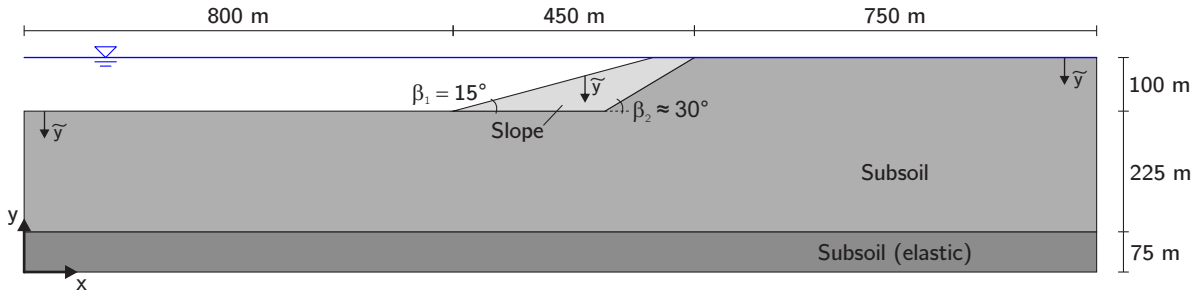


Figure 7.1: Geometry and dimensions of the finite element model

of dense sand ($D_{r0} = 0.7$). The FE model consists of about 22,000 elements in total and approx. 65,000 nodes. The finite element mesh was generated with a mean nodal distance of $\Delta x = \Delta y \approx 1.5$ m in the area of the slope and the "Subsoil" beneath it. To improve the numerical performance and increase the numerical damping to reduce reflections of waves from the outer boundaries back into the model, the nodal distance in the horizontal direction was increased with increasing distance from the "Slope" up to $\Delta x \approx 20$ m for the outermost elements. To account for changes in pore water pressure and consolidation effects during and after the earthquake loading, the solid displacements \mathbf{u} and the pore water pressure p^w were discretized at the nodes (so-called u-p elements). The simulations were performed in an updated Lagrangian framework, using the Zaremba-Jaumann stress rate.

The hypoplastic constitutive model of von Wolffersdorff (1996) with intergranular strain (IGS) extension (Niemunis and Herle, 1997) was used to simulate the material behavior of the "Slope" and the "Subsoil". The material parameter sets used for the "Slope" and the "Subsoil" are summarized in Tab. 7.1 and Tab. 7.2 for the hypoplastic model and IGS, respectively. As depicted in Fig. 7.1, the bottom layer labeled "Subsoil (elastic)" was modeled as a linear elastic material. The selection of an elastic material model was made as it allows for a direct determination of a constant shear wave velocity based on the elastic properties, which is essential for the definition of the compliant base boundary condition applied to the bottom of the model (see explanations given later in this section).

Table 7.1: Parameters of the Hypoplastic model for "Slope" and "Subsoil"

Soil	φ_c [°]	h_s [GPa]	n	e_{d0}	e_{c0}	e_{i0}	α	β
Slope	35.9	0.25	0.23	0.426	0.722	0.83	0.0	2.9
Subsoil	32.8	5.8	0.28	0.568	0.866	0.996	0.13	1.05

Table 7.2: Parameters of Intergranular Strain for "Slope" and "Subsoil"

Soil	m_T	m_R	R	β_R	χ
Slope	3.0	7.0	10^{-4}	0.1	1.25
Subsoil	5.0	5.0	10^{-4}	0.2	1.0

Following the concept of Wegener and Herle (2012) to determine the shear modulus of the hypoplastic model with IGS (see also Sec. 2.3.4) and by forcing minor differences in shear stiffness at the transition from the elastic to the hypoplastic layer, the elastic material parameters have been back-calculated as a Young's modulus of $E = 609.4$ MPa and a Poisson's ratio of $\nu = 0.3$. Independent of the layer, a constant hydraulic conductivity of $k = 5 \cdot 10^{-4}$ m/s was set into approach.

The simulation was performed in the following steps:

1. Application of gravity while prescribing the solid displacements at all nodes as zero. In addition, the pore water pressure was prescribed at each node according to a hydrostatic distribution, considering the phreatic level as given in Fig. 7.1. The initial void ratio follows Bauer's equation (Bauer, 1996):

$$e_0(x, \tilde{y}) = e(\sigma'_{ii,0} = 0, D_{r0}) \cdot \exp \left[- \left(\frac{-\sigma'_{ii,0}}{3h_s} \right)^n \right], \quad (7.1)$$

where the parameters h_s and n given in Tab. 7.1 are used and \tilde{y} denotes the depth below the ground surface presented in Fig. 7.1. A lithostatic initial stress distribution was prescribed, considering the variable overburden height in the area of the slope. However, no shear stresses, which are required to obtain a static equilibrium of the slope, were prescribed, since they are unknown. The reaction forces at each node were saved following the application of gravity. Note that no deformations occurred in this step.

2. Application of the reaction forces as external forces to each node in the initial increment, considering a gradual decrease within 100 increments to zero. The displacements of the bottom boundary were constrained in the vertical direction, while the lateral boundaries were constrained in the horizontal direction. The pore water pressure was still prescribed according to a hydrostatic distribution in this step. Initially, when the complete reaction forces are acting, the model is in perfect equilibrium and no deformations occur. Then the reaction forces are incrementally reduced, deformations occur and the stresses change such that static equilibrium is

achieved. The reason for reducing the reaction forces gradually is due to the non-linearity of the hypoplastic model, which necessitates an incremental application of changes in loading. At the end of the step, the externally applied reaction forces are zero. To account for the dead weight of the free water table in the residual lake, an additional surface load was applied in this step and kept constant for the following step. In addition, a surface pressure of 1 kPa was applied perpendicular to the entire ground surface in order to avoid very small mean effective stresses leading to numerical problems with the hypoplastic model. The reaction forces at the lateral boundaries were saved at the end of the step.

3. Excitation of the model base in horizontal direction in a dynamic step. In order to avoid any reflections by waves traveling back to the bottom, the excitation was applied by a compliant base boundary condition. In this case, the excitation is applied by a von Neumann rather than a Dirichlet boundary condition (Machaček, 2020). The imposed velocity-time history in the horizontal direction at the bottom of the model is described by a rising sine function shown in Fig. 7.2. The Hilber-Hughes-Taylor time integration scheme ($\alpha = -0.05$) was used and a fixed time increment of 10^{-3} s was set. A constant hydrostatic pore water pressure was assigned to all nodes at the top and the sides of the model, allowing for drainage. The reaction forces of the lateral boundaries were imposed at the beginning of the step and kept constant throughout the step. Except for the bottom of the model, which was constrained in the vertical direction, no Dirichlet boundary conditions were applied to the solid displacement.

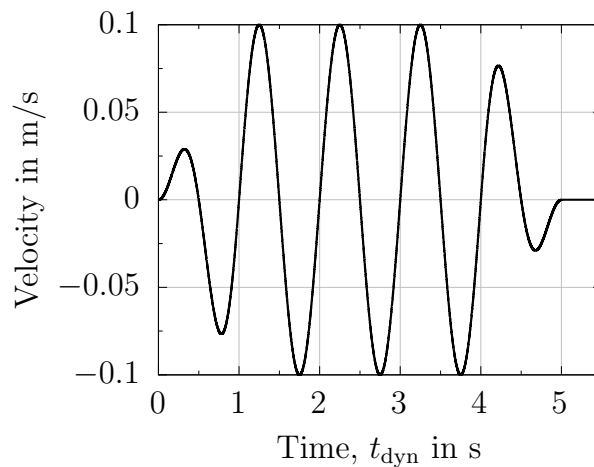


Figure 7.2: Cyclic signal applied at the bottom of the FE model

7.2.2. Results

Prior to the evaluation of the seismic slope stability in terms of a factor of safety, the results of the DFEA are discussed. The simulation was terminated at approximately 5.5 s of dynamic excitation due to excessive deformations, indicating a failure of the slope.

The slope's tendency to become unstable near the end of the simulation can also be seen by evaluating the maximum lateral and vertical accelerations, velocities, and displacements in the slope area as depicted in Fig. 7.3. It is apparent from the accelerations and velocities shown in this figure that the dynamic evolution of the slope stability can be split and analyzed into three segments. During the first second of earthquake excitation ($t_{\text{dyn}} \leq 1.0$ s), the slope is not influenced as the dynamic signal is still propagating upwards towards the slope area. For $1.0 \leq t_{\text{dyn}} \leq 3.5$ s, a semi-stable state is observed indicated by moderate to large accelerations and velocities with peak values up to $a_{x/y} \approx 2 \text{ m/s}^2$ and $v_{x/y} \approx 0.5 \text{ m/s}$, respectively. Ultimately, for $t_{\text{dyn}} \approx 3.6$ s, accelerations and velocities increase rapidly, whereby increasing displacements are observed shortly after, as well. Although a FoS can not be determined in DFEA without specifying threshold accelerations, velocities or displacements, it is expected that an unstable state of the slope is reached latest at $t_{\text{dyn}} \approx 3.6$ s.

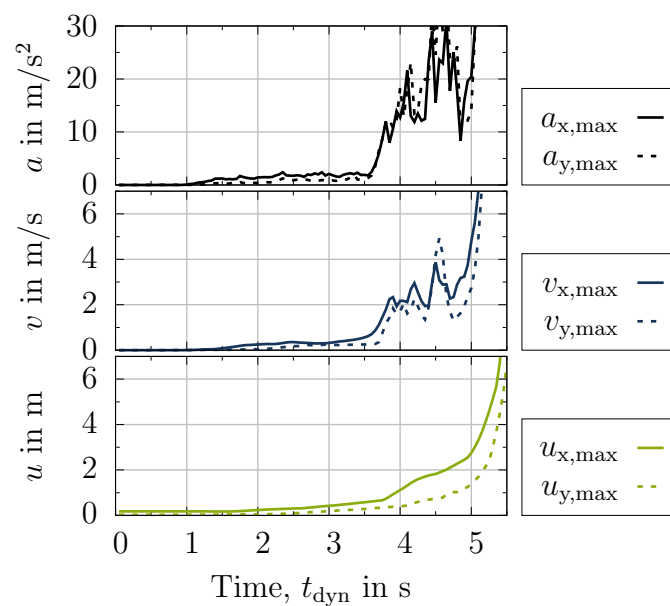


Figure 7.3: Evolution of maximum accelerations, velocities and displacements in slope area with time

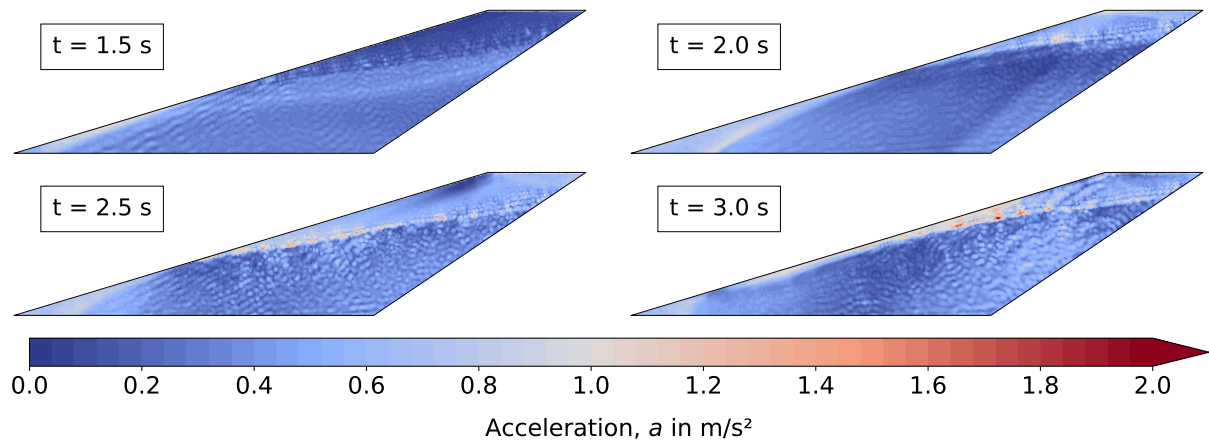


Figure 7.4: Acceleration magnitudes in the slope at different time steps

To identify critical locations in the slope area that are prone to slope failure events, spatial distributions of acceleration magnitudes are evaluated in Fig. 7.4 for four different time steps. As can be seen from this figure, maximum accelerations were detected close to the slope toe for $1.5 \text{ s} \leq t_{\text{dyn}} \leq 2.0 \text{ s}$ and at larger elevations along the slope for later time steps. Note that for all time steps investigated the critical accelerations were located in shallow depth. For $t_{\text{dyn}} = 3.0 \text{ s}$, acceleration magnitudes larger than 1 m/s^2 are detected along the slope surface in the range of $900 \text{ m} \leq x \leq 1100 \text{ m}$. Taking into consideration that slope failure is also triggered by the accumulation of excess pore water pressures that lead to a reduction of effective stresses, spatial distributions of normalized excess pore water pressures are analyzed in Fig. 7.5. It is apparent from this figure that – in contrast to the evolution of accelerations – no significant excess pore water pressure was built-up within the first two seconds. Although not depicted here explicitly, it should be

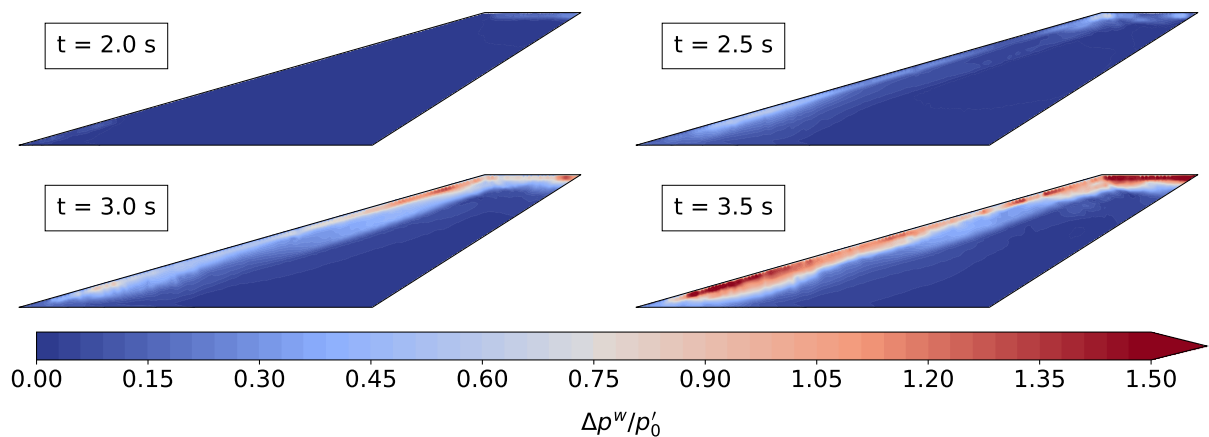


Figure 7.5: Normalized excess pore water pressures in the slope at different time steps

noted that also effective normal stresses only show small variations within the same time period. Still, for $t_{\text{dyn}} \geq 2.5$ s it is observed that excess pore water pressures accumulated along the slope surface. Further significant increase of Δp^w is seen with increasing time, showing critical locations with high excess pore water pressures close to the slope toe and at the slope crest. Note that values of $\Delta p^w/p'_0 > 1.0$ seen in this figure are possible due to changing mean stresses resulting from the seismic loading.

7.3. Assessment of seismic slope stability

As reported in Section 7.2.2, the dynamic finite element analysis (DFEA) was terminated at approx. 5.5 s of the excitation phase. However, it should be noted that the termination of DFEA might not be a precise indicator of the loss of stability. This is because in dynamic analyses, a material failure does not necessarily lead to the termination (non-convergence) of the analysis. The inertial forces prevent the system from becoming kinematic. Analogous to any other analysis involving large deformations, the simulation can run well beyond the point of failure. Subsequent slope stability analyses are essential for a quantitative assessment of seismic slope stability in terms of a factor of safety (FoS).

7.3.1. Spatial pseudo-static analysis using LEM

To evaluate the seismic slope stability, the spatial pseudo-static analysis (PSA) using the limit equilibrium method (LEM) presented in Sec. 6.2 is applied to the current boundary value problem. Stability analyses are conducted for the slope area defined in Fig. 7.1 with time increments of $\Delta t_{\text{dyn}} = 0.05$ s until $t_{\text{dyn}} = 5.5$ s at which the DFEA was terminated. For each time increment, respective spatial distributions of horizontal and vertical seismic coefficients are imported into `geoSlice`. The effect of accumulated excess pore water pressures Δp^w on the evolution of the FoS is investigated by performing simulations with and without import of it. As depicted in Fig. 6.2, for each distribution (inertial forces and excess pore water pressure), three nodes per slice are utilized for interpolation of representative values. LEM is performed in accordance with Bishop (1955) and Janbu (1954) for slip surfaces of circular shape. For four case combinations of excess pore water pressure and stability method, analyses were performed for 111 different time steps. To limit computational costs associated with the stability analyses, the shape of potential slip surface was restricted in a way that very shallow and small shapes were neglected by making use of *MinWidth* and *MinHeight* (see Sec. 3.3). Based on experiences gained

during trial analyses, brute grid optimization was chosen over differential evolution as the spatial distribution of seismic coefficients and excess pore water pressures renders the optimization problem a highly non-linear one. The material properties of the slope have been selected in accordance with the DFEA as follows: unit weight of the saturated soil $\gamma_{\text{sat}} = 20.2 \text{ kN/m}^3$, friction angle $\varphi = 39.89^\circ$ and cohesion $c = 0.1 \text{ kPa}$.

In contrast to SDSS and SRFEA utilizing Matsuoka-Nakai as limit or yield surface, respectively, stability analyses based on LEM are conducted applying the Mohr-Coulomb failure criterion in the slip surface (see Section 2.1.1). For plane strain problems with Lode angles of $0^\circ \leq \theta \leq 10^\circ$, for instance the 2D slope stability problem, applying MC results in smaller allowable deviatoric stresses compared to Matsuoka-Nakai, which ultimately leads to smaller FoS. In this section, an equivalent Mohr-Coulomb friction angle (Griffiths and Huang, 2009; Jiang and Wang, 2011) of $\varphi = 39.89^\circ$ evaluated at a Lode angle of $\theta = 0^\circ$ is determined to compensate effects related to differences between the Mohr-Coulomb and Matsuoka-Nakai surfaces. Moreover, a stabilizing distributed load was used in the DFEA, which was also considered in FELA, SDSS and SRFEA. To ensure comparable assumptions, a distributed load of 1 kPa acting perpendicular to the slope is applied also in the LEM analysis.

The results of the stability analyses with spatial PSA and LEM are depicted in Fig. 7.6. It is apparent from this figure that the applied seismic signal has a decisive impact on the FoS of the saturated opencast mine slope. Considering analyses with Bishop's method and

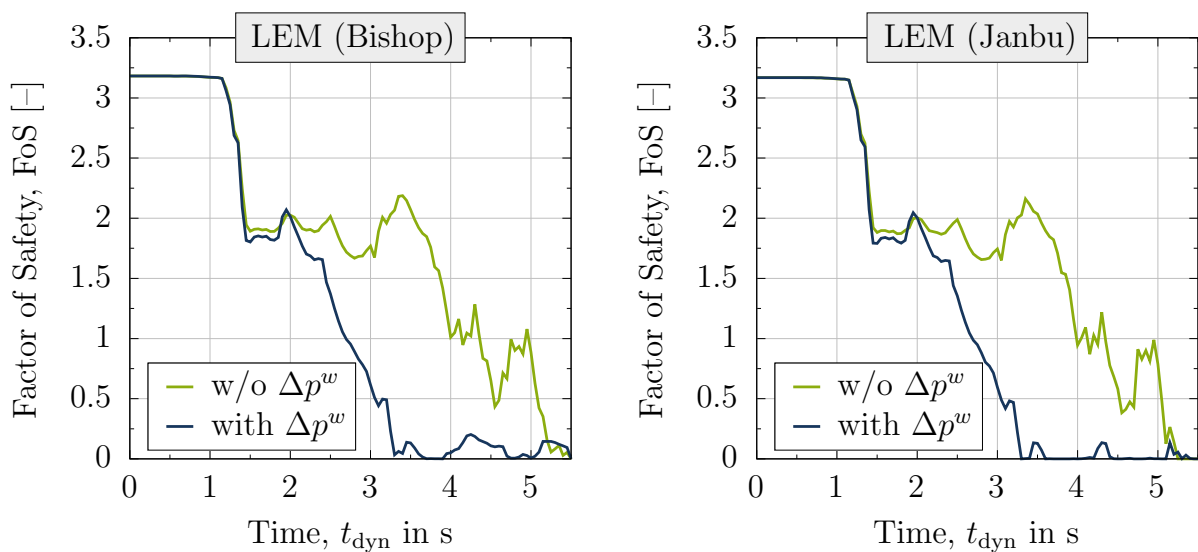


Figure 7.6: Evolution of FoS with spatial pseudo-static analysis using LEM considering the effect of excess pore water pressure and different LEM methods

with excess pore water pressures (left subplot, blue curve), the evolution of the FoS with increasing dynamic time can be summarized as follows: initially, for static conditions ($t_{\text{dyn}} = 0$ s), a slope stability of FoS ≈ 3.18 is determined that remains unchanged for $t_{\text{dyn}} \leq 1.1$ s. As soon as the shear waves enter the slope area, their impact can also be seen on the FoS evolution curve by a fast drop down to FoS ≈ 1.8 for $1.1 \text{ s} \leq t_{\text{dyn}} \leq 1.5$ s. After a slight recovery, a steady decrease of the FoS down to zero is observed for $2.0 \text{ s} \leq t_{\text{dyn}} \leq 3.2$ s, which remains at FoS ≤ 0.2 until the end of the DFEA. A similar trend is obtained for analyses applying Janbu's method (right subplot, blue curves) considering circular slip surfaces. Comparing analyses with and without Δp^w it is seen that excess pore water pressures have a strong impact on the evolution of the FoS. Although all curves ultimately reach FoS ≈ 0.0 , major differences are observed for $2.0 \text{ s} < t_{\text{dyn}} \leq 5.0$ s, where simulations without Δp^w result in non-conservative estimates of the slope stability. This refers to the absolute FoS values as well as the critical time at which the FoS curve drops below unity.

7.3.2. Cluster-based pseudo-static analysis using FELA

Finite element model

Slope stability analyses were conducted in terms of strength reduction analyses with finite element limit analysis (FELA) for the slope section of the finite element model (Fig. 7.1) used in the DFEA. The geometry and dimensions of the model are shown in Fig. 7.7. The model's mechanical boundary conditions were chosen so that deformations are restricted in normal and tangential directions at the bottom and the inclined edge at the right side of the model. To incorporate spatial variations of inertial forces, clusters were introduced in accordance with the discussions provided in Section 6.3.3. Identical to the DFEA, the water level is assumed to be at the slope crest level for all stability analyses.

As the hypoplastic model with intergranular strain cannot be used in combination with typical strength reduction schemes, an elastic perfectly plastic material model with Mohr-Coulomb yield surface is utilized. The Young's modulus E and the Poisson's ratio ν describing the isotropic elasticity were selected constant throughout the analyses ($E = 30$ MPa, $\nu = 0.25$) as their effect is negligible in strength reduction finite element limit analysis. As discussed in Section 6.3.2, spatial variations of the effective and total unit weights were considered, where the initial values of $\gamma'_0 = 10.2 \text{ kN/m}^3$, $\gamma_{\text{sat},0} = 20.2 \text{ kN/m}^3$ were selected in accordance with the DFEA. The unsaturated unit weight γ_{unsat} was unchanged in this study as it did not have an effect on the simulation due to a constant

water level at the slope crest level. The shear strength is defined with respect to the cohesion and the friction angle, the former chosen to be constant ($c = 0.1 \text{ kPa}$). A value close to zero has been selected as the slope is composed of loosely deposited sandy material. However, a non-zero value helps to avoid numerical instabilities and very shallow failure surfaces. As the shear strength due to friction is not constant in hypoplasticity, the approach discussed in Section 6.3.4 is followed, yielding a spatial distribution of the friction angles obtained from the DFEA in accordance with Bolton's approach (Bolton, 1986). Due to the prerequisite of an associated flow rule in FELA, the dilation angle was chosen equal to the friction angle ($\psi = \varphi$) throughout all safety analyses. To investigate the effect of a non-associated flow rule on the factor of safety for different time steps of the earthquake loading, simulations following the Davis A and B approaches (Davis, 1968; Tschuchnigg et al., 2015a) were conducted additionally with dilation angles obtained in accordance with Section 6.3.5. Although its effect on the factor of safety should be negligible, the lateral earth pressure coefficient K_0 was chosen with respect to the friction angle via $K_0 = 1 - \sin \varphi_{\text{crit}}$ in accordance with (Jaky, 1944).

In the strength reduction analysis based on FELA, rigorous lower and upper bound solutions are obtained by selection of correct element types (Sloan, 2013). In this thesis 3-node and 6-node triangular elements have been used for lower and upper-bound simulations, respectively. Furthermore, adaptive mesh refinement has been applied to improve computational effort and enhance the accuracy for the determination of the critical failure mechanism. In general, adaptive mesh refinement is a powerful tool used to reduce computational costs and to accurately evaluate limit states in terms of the critical shear strength in slope stability problems or the limit load in active or passive earth pressure or bearing capacity problems. Utilizing adaptive mesh refinement, the approximation of the failure mechanism is enhanced by adjustment of element sizes based on an indicator of

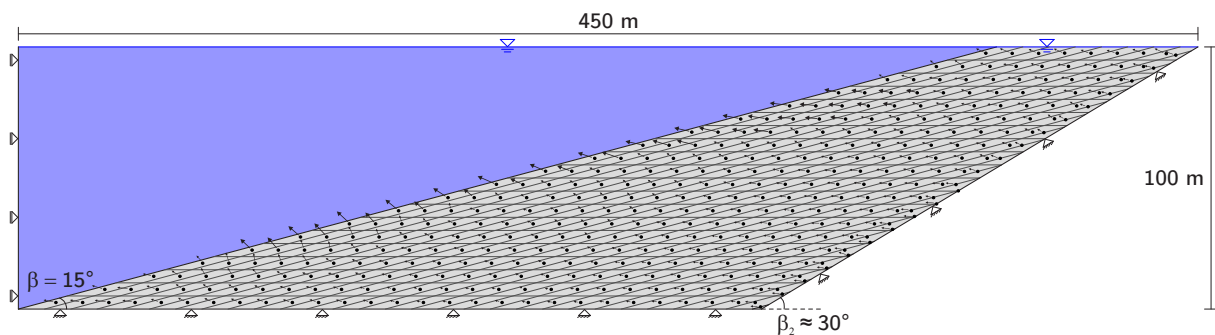


Figure 7.7: Schematic representation of the slope geometry, dimensions and spatial distribution of inertial forces using the cluster approach with parallelograms

plasticity in the system, for instance, the plastic shear dissipation. Thereby, element sizes are decreased or increased in areas with large or small shear dissipation, respectively. The optimal-mesh-adaptive technique was proposed by Almeida et al. (2000) and, among others, further developed by Lyamin et al. (2005). Advantages of adaptive mesh refinement were shown for many geotechnical applications, such as slope stability analyses (Oberhollenzer et al., 2018; Mahmoudi et al., 2020), the earth pressure problem and retaining walls (Lyamin et al., 2013; Krabbenhoft, 2019; Schmüdderich et al., 2020d, 2022b) or the bearing capacity problem (Lyamin et al., 2013; Schmüdderich et al., 2020a,b, 2021).

Effect of excess pore water pressure and orientation of inertial forces

A parametric study investigating the effect of excess pore water pressure and orientation of inertial forces on the stability of the slope presented in Section 7.2.1 was conducted following the concept presented in Section 6.3. The two effects were investigated by evaluation of the slope stability for simulations with and without (w/o) excess pore water pressures Δp^w and vertical components of inertial forces directed upwards or downwards. Similar to pseudo-static analyses performed with the limit equilibrium method, the latter effect was studied as it is unknown a priori whether upwards or downwards-directed inertial forces yield the critical FoS. The FoS is evaluated with a time interval of $\Delta t = 0.05$ s. In total, stability analyses of the full-time series (111 time steps), with each a lower and upper bound analysis, were conducted for all case combinations.

The results of the stability analyses are presented in terms of FoS versus time during the dynamic excitation t_{dyn} in Fig. 7.8, with the different colors indicating analyses with and without excess pore water pressures and separate sub-figures denoting different vertical orientation of inertial forces. Note that the FoS values reported herein are evaluated as the mean values from lower and upper bound finite element analyses. As can be seen from this figure, the stability of the static case (i.e. initial time step) of $\text{FoS} \approx 2.84$ is obtained for all cases. This is slightly larger compared to the fast estimate of $\tan \varphi_c / \tan \beta = \tan 35.9^\circ / \tan 15^\circ = 2.70$ for an infinite planar slope failure. Analyzing the overall trend of the slope stability versus time for all cases, it is observed that all curves yield $\text{FoS} = 2.84$ for $t_{\text{dyn}} \leq 1.0$ s, show a decisive drop down to $\text{FoS} \approx 1.7$ for $1.0 \text{ s} \leq t_{\text{dyn}} \leq 1.5$ s, remain at this level until $t_{\text{dyn}} \approx 2.5$ s, separate thereafter, but ultimately yield $\text{FoS} \leq 0.5$ at $t_{\text{dyn}} = 5.5$ s. Although these trends are clearly identified, scattering is observed for consecutive time steps, which may result from the dynamic loading, the cluster approach and changes in the shape of the critical failure mechanism. All cases predict slope failure by defining the stability loss as the first drop below $\text{FoS} = 1.0$. However, the dynamic

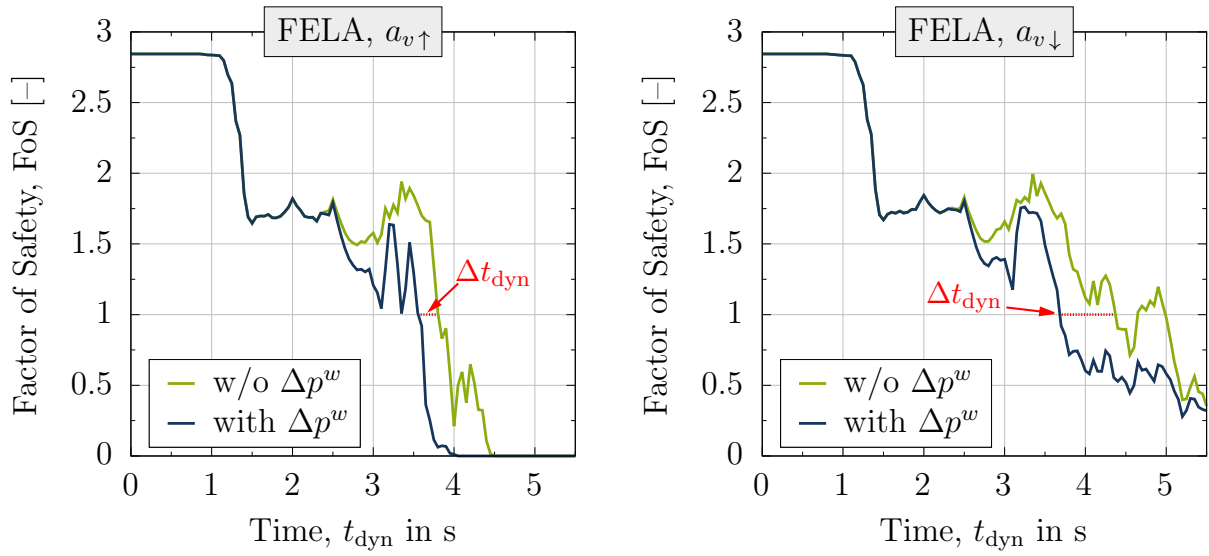


Figure 7.8: Evaluation of FoS with respect to excess pore water pressure and orientation of inertial forces

time at the loss of stability varies between $t_{\text{dyn}} = 3.5\text{ s}$ and $t_{\text{dyn}} = 4.5\text{ s}$. Considering cases with excess pore water pressures only, a critical dynamic time of $3.5\text{ s} \leq t_{\text{dyn}} \leq 3.7\text{ s}$ is observed. The latter observation is in good agreement with the results of the DFEA depicted in Fig. 7.3, where an evaluation of maximum accelerations shows that the slope turns into an unstable state indicated by a significant increase of $a_{x/y,max}$ for $t_{\text{dyn}} \geq 3.5\text{ s}$.

Although the effects of excess pore water pressure and direction of vertical inertial forces on the FoS can clearly be seen, it should be noted that – for this boundary value problem and the dynamic loading applied – the effect of the horizontal component of the inertial forces dominates over the other effects as it dictates the evolution of the FoS with respect to the loading time under dynamic conditions. Still, as significant differences can be seen in the evolution of the slope stability with regard to the different cases, individual assessment of the effects is conducted, as well. Comparing the evolution of FoS with dynamic time for a_v directed upwards with the one pointing downwards, it is clear that the former predicts significantly lower slope stability with FoS approaching zero for $4.0\text{ s} \leq t_{\text{dyn}} \leq 5.0\text{ s}$. In contrast, an almost steady decline of FoS with dynamic time is seen for the latter case, approaching $0.25 \leq \text{FoS} \leq 0.5$ at $t_{\text{dyn}} = 5.5\text{ s}$. Note that the impact of the orientation of the vertical component of the inertial forces is negligible for $t_{\text{dyn}} < 3.0\text{ s}$. A potential explanation for this can be given with regard to the dynamic signal applied, which is orientated parallel to the bottom edge of the DFEA model (i.e. in the horizontal direction). As vertical accelerations develop mainly from reflections at the slope surface,

the earthquake signal needs to first reach the ground surface before any impact on the FoS curves can be detected.

Similarly, it can be seen from Fig. 7.8 that excess pore water pressures have a decisive impact on the slope stability for $t_{\text{dyn}} > 2.5$ s, where non-conservative FoS predictions are obtained in case excess pore water pressures are neglected in the stability analyses. The largest deviation between curves considering and ignoring Δp^w is obtained at $t_{\text{dyn}} \approx 3.7$ s with maximum values ranging between $\Delta\text{FoS} = 0.79$ and $\Delta\text{FoS} = 1.40$. Note that the largest differences are obtained for simulations with the vertical component of the inertial forces directed upwards. Considering the point of time related to the loss of stability, a time difference ranging between $\Delta t_{\text{dyn}} \approx 0.25$ s and $\Delta t_{\text{dyn}} \approx 0.7$ s is obtained. Thus, neglecting excess pore water pressures may result in significantly larger FoS and later (if at all) observation of the loss of stability.

Assessment of the quality of the FELA results

The quality of the FELA results can be evaluated by quantification of the gap between the lower and upper bound solution in terms of the worst case error defined as $\varepsilon_{\text{wc}} = (\text{UB} - \text{LB}) / (\text{UB} + \text{LB})$ (Krabbenhoft, 2018; Schmüdderich et al., 2020d) with LB and UB denoting the lower and upper bound results, respectively. However, this measure may produce misleading results in case limit loads or factors of safety approach very small values. Therefore, assessment of the quality of the FELA results is conducted based on the absolute rather than the relative error by evaluation of the distance between the mean value and the lower/upper bound solution. The evolution of the absolute error $\Lambda = (\text{UB} - \text{LB}) / 2$ with respect to the dynamic loading time is shown in Fig. 7.9 for all case combinations.

In this figure, different colors refer to simulations with and without excess pore water pressures, while different subplots are used to denote the influence of the direction of the vertical inertial forces. It is apparent from this figure that the lower and upper bound solutions are in good agreement indicated by a small Λ value for $t_{\text{dyn}} \leq 1.0$ s. Since the shear waves did not reach the slope body within this time span, the equilibrium state is still comparable to the static case without any impact of accelerations or excess pore water pressures. For $t_{\text{dyn}} \geq 2.0$ s, the gap between the lower and upper bound solution varies with time and shows decisive differences in short time spans. This observation may be explained by the temporal and spatial variation of excess pore water pressures and inertial forces as a result of the dynamic excitation as well as reflections of the shear waves from the (inclined) ground surface back into the model.

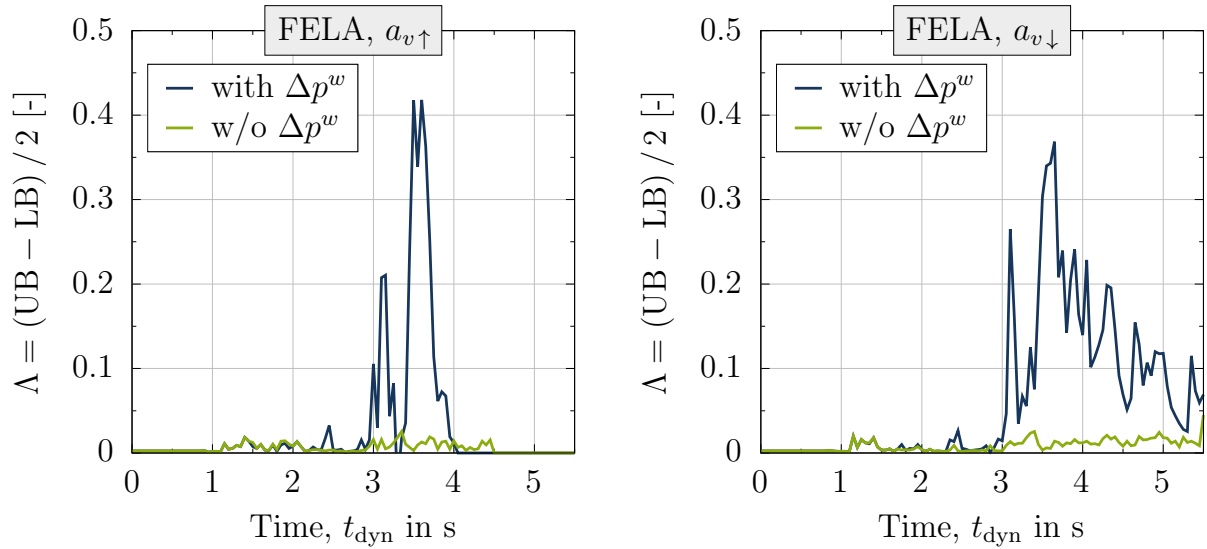


Figure 7.9: Evolution of the gap between lower and upper bound solution in terms of the deviation Λ from the mean value

In contrast to analyses conducted without (w/o) consideration of excess pore water pressures Δp^w , which resulted in $\Lambda < 0.05$, deviations of up to $\Lambda \approx 0.4$ are observed for analyses with consideration of excess pore water pressures Δp^w . Thus, excess pore water pressures not only reduce the FoS, but also lead to a larger gap between lower and upper bound solutions. Note that very large Λ values are mostly related to a sudden drop of the lower bound solution, whereas the upper bound solution follows the same trend with a small time delay. This can also be seen by the sudden decrease of Λ as soon as the maximum is reached.

Effect of non-associated flow rule

As limit analysis and finite element limit analysis (FELA) need to fulfill the requirements of the normality rule, an associated flow rule is considered as a prerequisite. However, as discussed in Section 6.3.5, this assumption may lead to a non-conservative estimation of the stability of the slope. To overcome this limitation and indirectly consider a non-associated flow rule with a dilation angle smaller than the friction angle, the Davis (Davis, 1968) approach – referred to as 'Davis A' – and the Davis B approach (Tschuchnigg et al., 2015a) are applied. To evaluate the importance of a non-associated flow rule on the slope stability for this boundary value problem, FoS values obtained based on the Davis A and B approach are compared to the original simulations (FELA with associated flow rule, AFR) for 7 different time steps considering analyses with excess pore water pressures and

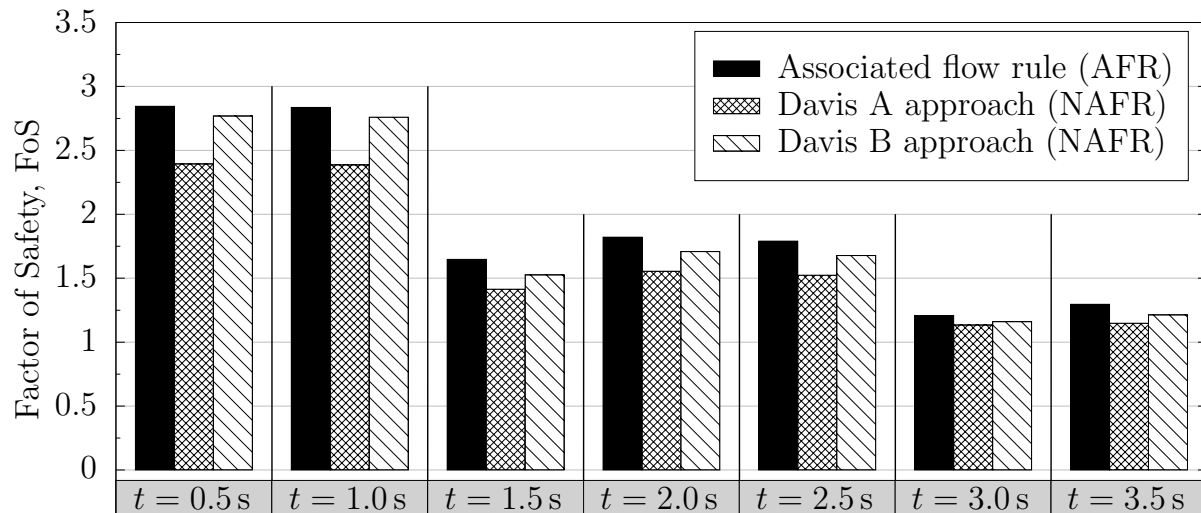


Figure 7.10: Influence of the flow rule (associated, non-associated) on the FoS

vertical inertial forces directed upwards. The comparison depicted in Fig. 7.10 reveals that, compared to the analyses with AFR, smaller FoS values are obtained applying the Davis A approach, leading to maximum deviations of $\Delta\text{FoS} = 0.45$. However, as previous studies (Tschuchnigg et al., 2015b, 2019; Schmüdderich et al., 2022b) showed that the latter approach might be very conservative when compared to actual finite element analyses using a non-associated flow rule, the present results should also be considered conservative. A more appropriate estimation of the FoS with regard to a non-associated flow rule is obtained following the Davis B approach. Comparing the results of Davis B and AFR, it is apparent that the indirect consideration of a non-associated flow rule leads to smaller FoS values, deviating by $0.05 \leq \Delta\text{FoS} \leq 0.12$. Setting the non-associated flow rule into context with the effects discussed above, it is seen that – for the boundary value problem investigated here – the influence of the former is of subordinate importance as inertial forces and excess pore water pressures primarily dictate the FoS versus time evolution. Nevertheless, considering a non-associated flow rule will always result in smaller FoS, where the gap between AFR and NAFR increases with increasing difference between friction angle and dilation angle (Tschuchnigg et al., 2015b,a).

7.3.3. Strain-dependent slope stability for earthquake loading

Slope stability analyses are conducted applying the modified concept of strain-dependent slope stability (SDSS) developed in Section 6.4 to the boundary value problem investigated in Sections 7.2.1 and 7.2.2 considering the first 5.5 seconds of the dynamic loading phase

($0.0 \text{ s} \leq t_{\text{dyn}} \leq 5.5 \text{ s}$). As a first step, element test simulations are performed with the basic version of the hypoplastic model, where the transfer of information from the finite element model to the element tests included the spatial distribution and temporal evolution of stresses and void ratios. The evaluation is based on the maximum factor of safety (FoS_{max}). For the determination of FoS_{max} every $\Delta t_{\text{dyn}} = 0.05 \text{ s}$, the time series depicting the evolution of FoS_{max} with the dynamic time requires stability analyses for 111 time steps. Considering a grid search algorithm with approximately 3,500 potential slip surfaces analyzed to find the critical slip surface and a discretization of the slip surface using 15 points, a total of $5.8 \cdot 10^6$ element test simulations are performed using the Incremental Driver software (Niemunis, 2008). Additional simulations with $\Delta t_{\text{dyn}} = 0.5 \text{ s}$ are performed to investigate the influence of the intergranular strain extension (IGS) on the strain-dependent slope stability. Therefore, three different assumptions are compared: stability analyses via simulation of element tests using (1) the basic hypoplastic model, (2) the hypoplastic model with the IGS tensor initialized with zero values ($\mathbf{h}_0 = \mathbf{0}$) and (3) the hypoplastic model with IGS utilizing the IGS tensor as obtained from the finite element slope model for the current time step of the dynamic loading phase. In the latter case, additional transfer of information from the finite element model to the element tests included the IGS tensor. In summary, $2 \times 630,000 = 1.26 \cdot 10^6$ additional element test simulations are conducted to analyze the effect of IGS on the strain-dependent slope stability.

The results of the full time series are presented in Fig. 7.11 in terms of the maximum factor of safety (FoS_{max}) obtained using the modified concept of strain-dependent slope stability versus the time step of the dynamic loading phase. As can be seen from the solid line in this figure, the FoS_{max} considering the basic version of the hypoplastic model is almost constant for $t_{\text{dyn}} \leq 2.0 \text{ s}$, reduces significantly for $t_{\text{dyn}} \geq 2.0 \text{ s}$, drops below the critical value of $\text{FoS} = 1.0$ at $t_{\text{dyn}} \approx 3.0 \text{ s}$, and reduces further with a decreasing rate down to $\text{FoS} = 0.5$ at $t_{\text{dyn}} = 5.5 \text{ s}$. These results of the FoS_{max} are in good agreement with the development of excess pore water pressures depicted in Fig. 7.5, which also indicates that the effect of the dynamic loading is small for $t_{\text{dyn}} \leq 2.0 \text{ s}$, whereas it increases significantly between $2.0 \text{ s} \leq t_{\text{dyn}} \leq 3.0 \text{ s}$. Moreover, as the rate of displacements increases with time for $2.5 \text{ s} \leq t_{\text{dyn}} \leq 4.5 \text{ s}$ (Fig. 7.3), strong evidence is given that this is accompanied by a continuous decrease in FoS , which can also be seen in Fig. 7.11.

Analyzing the general trend of the FoS_{max} obtained using the hypoplastic model, it is apparent from Fig. 7.11 that the evolution of the FoS with respect to time is not resembled by a smooth curve, but rather shows small variations. A potential reason for this trend

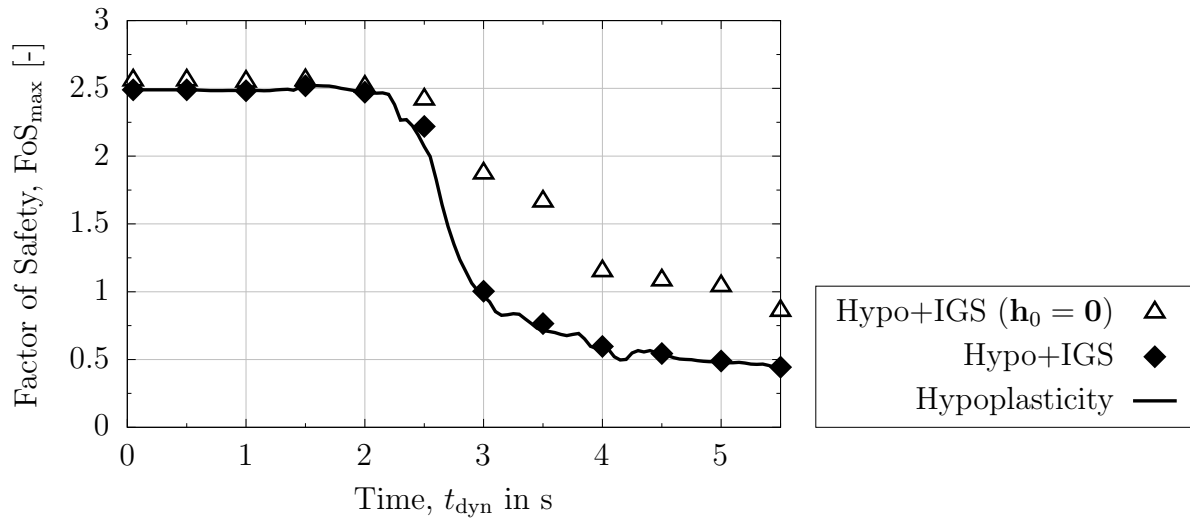


Figure 7.11: FoS at different times of the dynamic simulation for different specifications of the IGS in the simple shear tests

can be given with respect to the results depicted in Fig. 7.5 also showing fluctuations of the excess pore water pressure, which indicate fluctuations of the stress states used for the stability analyses. As the stresses slightly increase or decrease, it is expected that this fluctuation also propagates to the FoS. Moreover, it should be noted that the location and size of the critical slip surface vary due to the evolution of the excess pore water pressures and mean effective stresses. This fact increases the complexity for locating the critical slip surface using a simple grid optimization as it was done in creating Fig. 7.11, where based on a predefined grid always the same slip surfaces are analyzed for each time step. Thus, if the critical slip surface is not well captured by the slip surfaces analyzed, an overestimation of the FoS is expected. As the number of slip surfaces used for each analysis had to be limited due to the computational costs related to the concept of SDSS, it is possible that the critical slip surface associated with a (slightly) smaller FoS is not found exactly. However, this drawback can be overcome by utilizing machine learning algorithms combined with advanced optimization techniques, as will be discussed in Chapter 9.

Comparable to the basic hypoplastic model, a similar trend is observed if the IGS tensor is initialized in the Incremental Driver simulations with the values obtained from the finite element simulation for the current time step of the dynamic loading phase (solid diamond symbols). This indicates that the magnitude of the strain level has almost reached the maximum mobilized value of IGS (i.e. parameter R) during the dynamic loading phase. Hence, the hypoplastic stiffness is only slightly increased due to the contribution of IGS,

leading to a marginal increase in the maximum shear stress and the maximum factor of safety. Moreover, good agreement between all cases is seen for $t_{\text{dyn}} \leq 2.0$ s. However, significant differences are evident for $t_{\text{dyn}} \geq 2.0$ s for the case of an IGS tensor initialized with null values ($\mathbf{h}_0 = \mathbf{0}$). An explanation for these differences has already been given in Sections 6.4 and 7.2.2. As excess pore water pressures increase due to the dynamic loading, effective stresses reduce. Thereby, simple shear tests are performed at a smaller stress level where IGS initialized with null values leads to significantly larger maximum shear stresses. The gap between the FoS_{max} obtained with the basic version of the hypoplastic model and the one with IGS initialized with null values develops in accordance with the trend of the excess pore water pressures that are small for $t_{\text{dyn}} \leq 2.0$ s and increase thereafter.

To further elaborate on the results presented in Fig. 7.11, the evolution of the global mobilized shear resistance ratio (T) and the factor of safety (FoS) with applied shear strain (γ) is analyzed for the critical slip surfaces at five selected time steps ($t_{\text{dyn}} = 1.5$ s, 2.5 s, 3.0 s, 3.5 s, 4.5 s). The main objective here is to identify how IGS influences the shape of the FoS versus γ curves, as exemplary depicted in Fig. 2.5(a) and (b) for purely contractive behavior and contractive behavior followed by strain softening, respectively. Moreover, these curves allow for evaluation of the difference between the maximum and the residual factor of safety (FoS_{max} , FoS_{res}). The results associated with the stability analyses discussed in Fig. 7.11 are presented in Fig. 7.12 in terms of (a,c) $T(\gamma)$ and (b,d) $\text{FoS}(\gamma)$ for element test simulations with (a,b) the basic hypoplastic model and (c,d) the hypoplastic model with IGS initialized as $\mathbf{h}_0 = \mathbf{0}$. It is apparent from Fig. 7.12(b) that the FoS versus γ curve using the basic hypoplastic model can be approximated well with a constant line indicating negligible differences between the maximum and residual factor of safety. An explanation for this trend can be given with regard to the evolution of the global mobilized shear resistance ratio (T) depicted in Fig. 7.12(a), which is monotonously increasing until reaching the critical state.

In contrast, Fig. 7.12(d) shows a significant decrease of the FoS for element tests using the hypoplastic model with IGS initialized with null values ($\mathbf{h}_0 = \mathbf{0}$) for shear strains in the range of $0 \leq \gamma \leq 0.05$ and time steps $t_{\text{dyn}} \geq 3.0$ s. As large differences between FoS_{max} and FoS_{res} are obtained in these analyses, it should be noted that minor shear strains result in a large reduction of the factor of safety. An explanation for the FoS trend can be given with respect to the T versus γ curve displayed in Fig. 7.12(c) showing a very stiff initial response in the simple shear tests as a result of increased hypoplastic stiffness due to IGS followed by a rapid decrease of T with increasing shear strain until reaching the

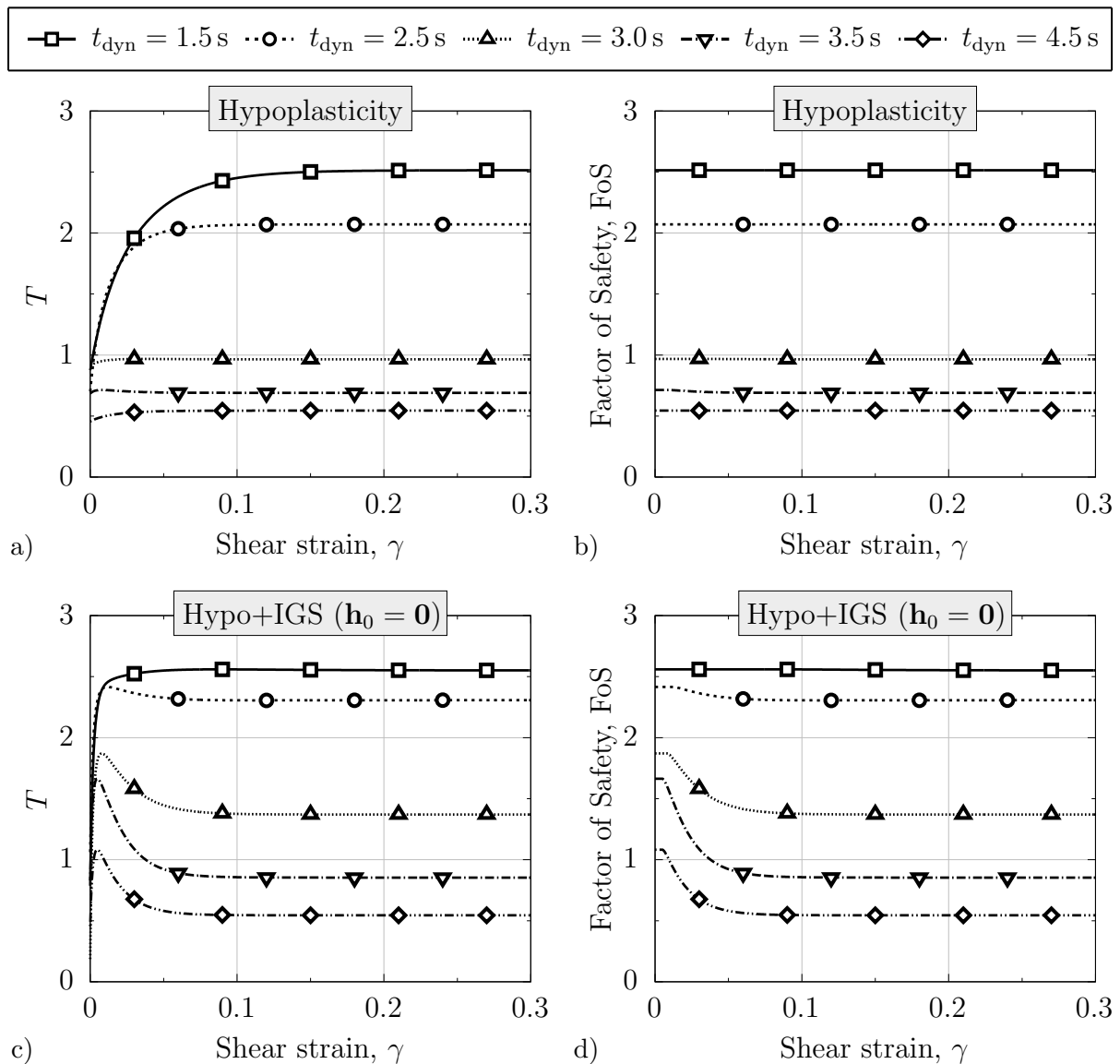


Figure 7.12: Global mobilized shear resistance ratio (T) and factor of safety (FoS) curves with respect to applied shear strain (γ) considering (a,b) the basic hypoplastic model and (c,d) the hypoplastic model with IGS initialized with null values ($\mathbf{h}_0 = \mathbf{0}$) for different time steps during the dynamic excitation phase

critical state. It should be noted that T_{res} and FoS_{res} obtained in these simulations are slightly larger compared to simulations without IGS (Fig. 7.12(a,b)) since the objective function in the optimization was linked to FoS_{max} rather than to FoS_{res} .

With respect to the discussion in Section 6.4.4 on the expected influence of the intergranular strain extension on the factor of safety considering the concept of strain-dependent slope stability, it was shown with this academic example that consideration of IGS can

lead to a non-conservative estimate of FoS_{\max} . As computational costs for element test simulations with IGS are also significantly larger compared to simulations without IGS ($\approx 50\%$ in time), IGS should not be considered for the analysis of the SDSS. However, for the dynamic FE simulations, which are the basis for these stability analyses, the consideration of the IGS is mandatory to capture the soil behavior under cyclic loading. Moreover, it is worth noting that the FoS curve trends discussed here are not only influenced by the state variables (e.g. stress state, void ratio, IGS tensor) but also by the parameter sets used for the constitutive model. Thus, slight variations of these curve trends are to be expected for different parameter sets.

7.3.4. Spatial pseudo-static analysis using SRFEA

To evaluate the evolution of the FoS based on the spatial pseudo-static analysis using SRFEA, submodel analyses (see Section 6.5) are conducted, in which the DFEA is put on hold whenever a SRFEA is performed. For the SRFEA, the current stress state, (excess) pore water pressures and inertial forces are imported from the DFEA. During the SRFEA, (excess) pore water pressures and inertial forces are kept constant. The material behavior is approximated using the Matsuoka-Nakai model with the friction angle chosen to be identical to the critical friction angle (Tab. 7.1). SRFEA is performed for time intervals of $\Delta t_{\text{dyn}} = 0.05$ s considering an initial factor of safety of $\text{FoS}_0 = 0.5$ and an incremental increase of $\Delta \text{FoS} = 0.01$. The critical FoS was obtained based on a sudden change in the FoS versus displacement plot with displacements displayed in logarithmic scale, following the approach discussed in Section 5.2. To avoid unrealistically large friction angles in the stability analyses, SRFEA was conducted with $\text{FoS}_0 = 0.5$, thus, theoretical FoS values below this threshold ($\text{FoS} \leq 0.5$) will be displayed as $\text{FoS} = 0.5$. To study the influence of the inertial forces, the full FoS time history is investigated with and without consideration of inertial forces.

The results of the stability analyses with SRFEA are depicted in Fig. 7.13 in terms of FoS versus t_{dyn} . As can be seen from this figure the seismic excitation has a significant impact on the stability of the opencast slope. Focusing on the simulations without inertial forces (green curve, left subplot), under static conditions ($t_{\text{dyn}} = 0.0$ s), the opencast slope can be classified as stable with $\text{FoS} \approx 3.25$. Besides small fluctuations in FoS, this level of safety remains unchanged up to $t_{\text{dyn}} = 1.7$ s. After a drop to $\text{FoS} = 3.0$ ($t_{\text{dyn}} = 1.85$ s) and an increase up to $\text{FoS} = 3.36$ ($t_{\text{dyn}} = 2.05$ s), a steady decrease of the FoS is observed down to $\text{FoS} \approx 0.5$ ($t_{\text{dyn}} = 3.65$ s). Thereafter, the level of safety remains unchanged, though, it should be clear that $\text{FoS} < 0.5$ can not be reached as $\text{FoS}_0 = 0.5$

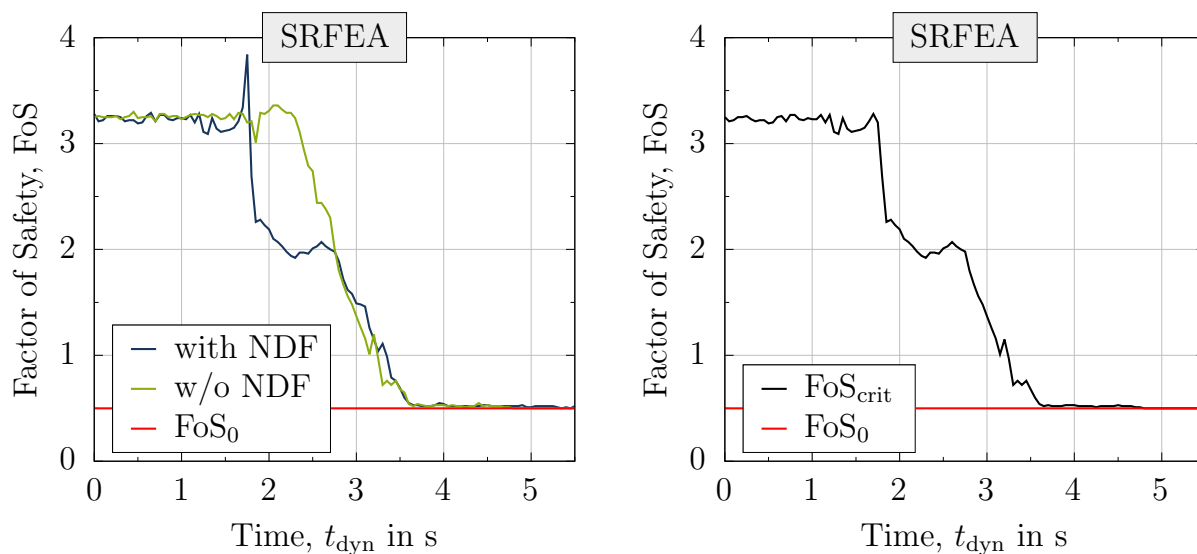


Figure 7.13: Evolution of FoS with spatial pseudo-static analysis using SRFEA: (left) influence of consideration of inertial forces on FoS and (right) critical FoS based on simulations with and without inertial forces

was selected. Significant deviations between the simulations with and without inertial forces are observed for $1.7 \leq t_{\text{dyn}} \leq 2.8$ s, where (except for a peak at $t_{\text{dyn}} \approx 1.8$ s) the former simulations result in lower FoS predictions. For $t_{\text{dyn}} \geq 2.8$ s similar FoS trends are obtained in both simulations due to a higher importance of accumulated excess pore water pressures, which are considered in both simulations. Overall, it can be concluded that once an unstable state is obtained, the opencast slope remains unstable until the DFEA was terminated.

7.3.5. Discussion

To enable a direct comparison of the results obtained using LEM, SDSS, FELA and SRFEA, the evolution of the FoS during the dynamic loading is summarized in Fig. 7.14. Note that differences in the results of the four seismic slope stability approaches are obtained with regard to the static FoS ($t_{\text{dyn}} = 0.0$ s), the point in time from which the slope stability is affected by the seismic loading, the time at which $\text{FoS} < 1.0$ and the FoS at the end of the simulation. As for this example the frequency of the input signal is rather small, no significant oscillations in the FoS are observed¹.

¹Note that significant larger oscillations in the FoS are observed for seismic stability analyses conducted for centrifuge model tests discussed in Chapter 8 due to input signals with higher frequencies.

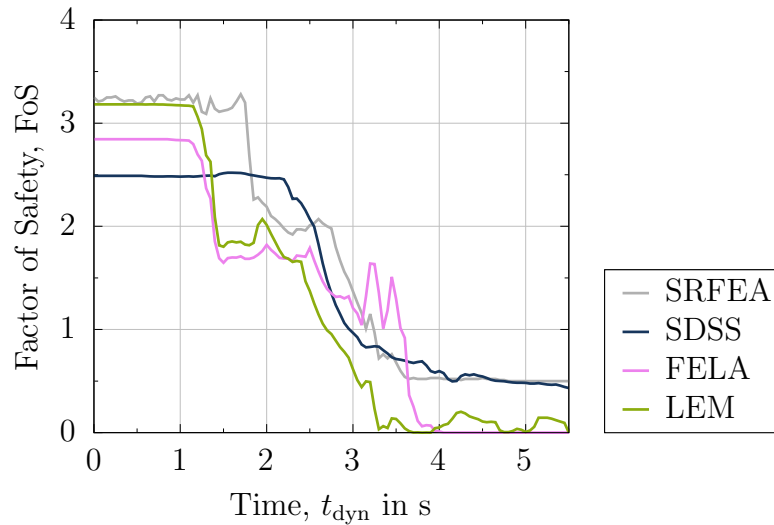


Figure 7.14: Comparison of the FoS predictions for the opencast slope based on LEM, FELA, SDSS and SRFEA

Analyzing the initial stability of the slope, it is apparent from Fig. 7.14 that LEM and SRFEA predict almost identical FoS, whereas FELA and SDSS predict significantly smaller FoS. The good agreement of LEM and SRFEA can be explained by the fact that the latter uses the Matsuoka-Nakai (MN) model and the former applies an equivalent Mohr-Coulomb (MC) friction angle φ_{MC} that ensures a similar size of the yield surface of MC and MN at a Lode angle of $\theta = 0^\circ$ corresponding to plane strain conditions. As the FELA is based on the Bolton (1986) approach, a different friction angle – in this case, a smaller one compared to φ_{MC} – is used in combination with the MC model, which results in less shear resistance along the slip surface and a smaller FoS. Although it could be expected that SDSS predicts a similar FoS compared to LEM and SRFEA, it is observed that SDSS yields the smallest FoS under static conditions. A possible reason for this observation are large deformations occurring prior to the dynamic excitation of the slope that lead to large shear strains and shear stresses during the iterations to achieve a static equilibrium².

Considering the time from which the slope stability is affected by the seismic loading, it is noted that FoS predictions of LEM and FELA are influenced first at $t_{dyn} \approx 1.15$ s and SRFEA is affected shortly after ($t_{dyn} \approx 1.25$ s), while SDSS is not influenced significantly before $t_{dyn} \approx 2.25$ s. The differences in the time from which the slope stability is affected by the seismic loading are directly related to the way in which the different approaches

²Note that better agreement of FoS values under static conditions are obtained for the centrifuge models investigated in Chapter 8 using LEM, SRFEA and SDSS

are influenced by accelerations/inertial forces and excess pore water pressures Δp^w . As the dynamic signal reaches the slope before significant Δp^w could accumulate, stability approaches considering inertial forces show an earlier impact of the seismic excitation. Moreover, as LEM and FELA consider inertial forces with their horizontal components always directed in driving direction, smaller FoS values are predicted compared to SRFEA that considers inertial forces directed in the way that dynamic equilibrium is achieved. As in SRFEA inertial forces may be directed in driving and stabilizing direction at different locations at the same time, rather than only directed in driving direction, destabilizing effects are smaller compared to LEM and FELA. In contrast to the former three approaches, SDSS does not explicitly consider inertial forces but only the current stress state. The FoS determined with SDSS is rather influenced by Δp^w that accumulated for $t_{\text{dyn}} > 2.0$ s and ultimately led to a decisive reduction of effective stresses. Note that Δp^w also significantly affected the FoS obtained with LEM, FELA and SRFEA.

Investigating the time at which slope stability drops below $\text{FoS} = 1.0$, differences are obtained for the different approaches. In LEM, the opencast slope is classified unstable at $t_{\text{dyn}} = 2.6$ s, while FELA almost reaches an unstable state ($\text{FoS} = 1.04$) at $t_{\text{dyn}} = 3.1$ s but ultimately predicts an unstable state for $t_{\text{dyn}} \geq 3.6$ s. SDSS and SRFEA predict a drop below $\text{FoS} = 1.0$ at $t_{\text{dyn}} = 3.0$ s and $t_{\text{dyn}} = 3.25$ s, respectively. Although, despite the initial offset, the general FoS curve trends of LEM and FELA are comparable within the first 2 seconds, FELA yields larger FoS predictions compared to LEM as soon as acceleration amplitudes increase and the spatial distribution of accelerations becomes more heterogeneous throughout the slope. As in FELA seismic coefficients are averaged throughout the clusters, which are required to create spatial distributions of accelerations, local peak values (minimum or maximum) are damped or even filtered out, leading to smaller inertial forces that could destabilize the slope. Still, it should be noted that FoS values obtained using FELA drop to zero as accelerations increase rapidly at $t_{\text{dyn}} \approx 3.7$ s (see Fig. 7.3). Comparing FoS predictions by FELA and SRFEA, it is clear that FELA yields smaller FoS values for most of the seismic excitation time, which mostly results from a Mohr-Coulomb friction angle smaller than φ_{MC} and horizontal inertial forces that are always directed in driving direction. Still, SRFEA yields smaller FoS predictions for $3.1 \text{ s} \leq t_{\text{dyn}} \leq 3.7 \text{ s}$, which results from damped peak accelerations due to averaging in the clusters and less accurate excess pore water pressures estimates in FELA.

Analyzing the FoS at the end of the simulation, it is seen that all approaches clearly predict a slope failure with $\text{FoS} \leq 0.5$. Though, it is observed that, except for SRFEA, approaches considering inertial forces yield very small FoS values for $t_{\text{dyn}} \geq 4.0$ s, while

SDSS ends up at FoS ≈ 0.5 . Note that SRFEA yields FoS = 0.5 corresponding to the initial FoS value in the strength reduction procedure, which should be interpreted in a way that the slope fails at this FoS or even smaller ones. Thus, selecting smaller initial FoS may result in smaller FoS predictions using SRFEA, which agree better with LEM and FELA predictions.

To evaluate the quality of the FoS predictions obtained using the four stability approaches and to categorize the results from conservative to optimistic, discussion regarding limitations of the individual approaches is required. This discussion is necessary as the boundary value problem under investigation is a synthetic one, where no experimental results can be taken into consideration. Note that all four approaches applied here have their individual advantages and drawbacks that may have different effects on the FoS predictions for different boundary value problems under investigation.

In LEM, shear strength is approximated using the Mohr-Coulomb criterion with a friction angle calibrated using the concept of equivalent Mohr-Coulomb friction angle (Griffiths and Huang, 2009; Jiang and Wang, 2011) considering a fixed Lode angle of $\theta = 0^\circ$. However, as θ is not constant throughout the domain, the actual Lode angle may differ from $\theta = 0^\circ$ at different locations within the slope. Though, it should be clear that for this example, the major impact on the FoS should be attributed to the inertial forces and the excess pore water pressures. LEM with spatial distributions of accelerations/inertial forces and excess pore water pressures as utilized here can be considered to yield conservative estimates to the FoS as horizontal inertial forces are always directed in driving direction. Classification of the FELA-based approach should be considered conservative in case sufficiently small clusters are used to approximate the spatial distribution of inertial forces. The main reason for this is that, similar to LEM, horizontal inertial forces are always considered pointing in driving direction. Still, in case cluster sizes are too large, over-estimation of the FoS is possible due to damped peak accelerations as a result of the averaging approach within the clusters. SRFEA can be considered to yield rather realistic FoS predictions due to consideration of accurate stress states and excess pore water pressures, inertial forces orientated in accordance with the dynamic equilibrium and soil shear strength based on the Matsuoka-Nakai failure criterion. Note that SRFEA might yield slightly conservative results as the critical friction angle φ_c is considered in the strength reduction method, which might be smaller than the current mobilized friction angle. Still, it should be clear that the Matsuoka-Nakai model cannot predict an accurate stress-strain behavior and take into account stress history, barotropy and pyknotropy compared to more sophisticated constitutive models, for instance the hypoplastic model.

As the latter constitutive model is utilized in SDSS and relevant state variables are transferred from the DFEA to the SDSS, the FoS predictions can be considered rather realistic. Note that up to now, SDSS has only been applied in combination with wedge or circular slip surfaces which may result in over-prediction of the FoS for layered soils, especially for boundary value problems with thin weak layers as discussed in Sections 3.4.4 and 5.4.

Besides the similarities and differences in the approaches for the assessment of the slope stability under seismic loading, evaluation of computational costs related to the different approaches should also be considered. For this boundary value problem considering a single time step, it is observed that LEM only requires a few seconds, whereas FoS predictions based on FELA require 30 minutes, and SRFEA and SDSS take up to 2 and 4 hours, respectively. Note that the computational costs related to LEM and SDSS increase with increasing numbers of slip surfaces to be investigated. In SDSS, the largest computational costs can be attributed to the simulation of element tests, which is further addressed in Chapter 9. In FELA and SRFEA, computational costs are mainly influenced by the number of elements, thus, the number of nodes and integration points. Thus, for boundary value problems discretized with less elements, computational costs associated with FELA and SRFEA are reduced, as will also be discussed with respect to stability analyses conducted for centrifuge model tests in Chapter 8.

8. Centrifuge model tests

8.1. Overview

To demonstrate the applicability and robustness of the methods proposed in Chapter 6, the stability of two centrifuge model tests under earthquake loading is investigated. The first centrifuge model test has been performed within the framework of the *Verification of Liquefaction Analyses by Centrifuge Studies* (VELACS). In model scale, it is a non-symmetric dam of 10 cm height with two differently inclined slopes of 1:3 and 1:1.75. The second centrifuge model test (LEAP-UCD-2017) belongs to the series of *Liquefaction Experiments and Analysis Projects* (LEAP), where centrifuge tests with identical material and test setups have been conducted worldwide at different facilities. Information about the test setups for both centrifuge model tests are provided in the following sections. Among others, more in depth information about the VELACS and the LEAP model tests can also be found in Muraleetharan et al. (2004) and Kutter et al. (2020), respectively.

To assess the evolution of the stability of both centrifuge model tests during the dynamic excitation, two consecutive steps are performed, which include dynamic finite element analyses (DFEA) and subsequent evaluation of the factor of safety (FoS) using the stability approaches introduced in Chapter 6¹. Note that as the focus of this work is the assessment of the slope stability rather than performing the DFEA, the latter are conducted in accordance with previous studies (Machaček et al., 2018; Machaček, 2020; Triantafyllidis et al., 2022). For this reason, only selected details and explanations about the finite element models, constitutive models and calculation phases applied in the DFEA are summarized in the respective sections, whereas the reader is referred to the previous studies for additional detailed information.

¹Note that the cluster-based pseudo-static analysis using FELA is not applied to assess the slope stability for the centrifuge model tests since the applicability of the approach has already been shown in Chapter 7.

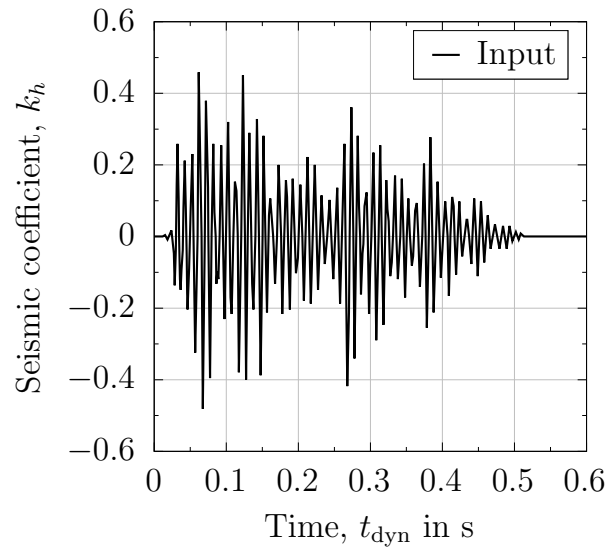


Figure 8.2: Input motion at the bottom of the VELACS model

in Table 8.1. The FE model consists of about 1089 elements and 3417 nodes. The finite element mesh was generated as a quad-dominated mesh (1055 quad elements with each eight nodes and nine IPs², 34 triangular elements with each six nodes and three IPs) with a mean nodal distance of $\Delta x \approx 2.5$ mm and $\Delta y \approx 2.0$ mm. To account for changes in the pore water pressure and consolidation effects during and after the earthquake loading, so-called u-p elements are used, discretizing the solid displacements \mathbf{u} and the pore water pressure p^w at the nodes. The simulations are performed in an updated Lagrangian framework, using the Zaremba-Jaumann stress rate. In accordance with Machaček et al. (2018), viscous stresses are considered to stabilize the stress-strain behavior at small stress states. In this simulation, viscous stresses are limited to 2 kPa.

The simulation was performed in the following steps:

Geostatic: Application of gravity with a magnitude of 1 g while the displacements of the bottom boundary were constrained in horizontal and vertical direction. In addition, the pore water pressure was prescribed at each node according to a hydrostatic distribution, considering the phreatic level as given in Fig. 8.1. In accordance with the degree of saturation reported in the literature, $S^w = 0.98$ is assumed with a corresponding fluid bulk modulus of $K^w = 5.0$ MPa. The initial void ratio follows Bauer's equation (Bauer, 1996). A lithostatic initial stress distribution was prescribed, considering the variable overburden height in the dam. As shear stresses are unknown a priori, they develop during the iteration process as they are required to obtain a static equilibrium of the

²Integration points

Table 8.1: Parameters of the Hypoplastic model ($\varphi_c - \beta$) with intergranular strain (IGS, $m_T - \chi$) for Nevada sand (Triantafyllidis et al., 2022)

φ_c	ν	h_s	n	e_{d0}	e_{c0}	e_{i0}	α	β	m_T	m_R	R	β_R	χ
[°]	[-]	[MPa]	[-]	[-]	[-]	[-]	[-]	[-]	[-]	[-]	[-]	[-]	[-]
31	0.24	755	0.328	0.511	0.883	1.05	0.34	0.9	4.5	9.0	10^{-4}	1.4	0.48

model. To account for the dead weight of the free water table, an additional surface load was applied in this step and kept constant for the following steps. In addition, a surface pressure of 1 kPa was applied perpendicular to the ground surface to avoid very small mean effective stresses leading to numerical problems with the hypoplastic model.

Spin-up: Gravity is increased from 1 g to 50 g in small increments to approximate the spin-up phase. Note that the unit weight of the soil and the water are affected by the increased gravity. To account for the latter, increasing pore water pressure was prescribed at each node in accordance with the increased gravity. Moreover, increased water pressure of the free water above the soil top surface (i.e. dead weight of the free water table) is considered in accordance with the increased gravity.

Dynamic loading: Excitation of the model base in horizontal direction in a dynamic step. In this case, the excitation is applied by a Dirichlet boundary condition, imposing the acceleration-time history in the horizontal direction at the bottom of the model in accordance with Fig. 8.2. The Hilber-Hughes-Taylor time integration scheme ($\alpha = -0.05$) was used and a fixed time increment of $5 \cdot 10^{-5}$ s was set. A constant hydrostatic pore water pressure was assigned to all nodes at the top of the model, allowing for drainage. Except for the bottom of the model, which was constrained in the vertical direction, no further Dirichlet boundary conditions were applied to the solid displacement.

Results

To assess whether the DFEA using Hypoplasticity with Intergranular Strain (IGS) is capable to reproduce the results of the centrifuge model test, comparisons of vertical displacements, acceleration and excess pore water pressure time histories at the positions of the respective sensors depicted in Fig. 8.1 are undertaken. For this, the vertical displacements measured at the center point of the crest (LVDT 1), the acceleration time histories

recorded at the accelerometers ACC 3, ACC 6, ACC 7 and ACC 8 as well as the excess pore water pressure time histories back-calculated from the pore pressure transducers PPT A – PPT F summarized in Muraleetharan et al. (2004) are considered.

The evolution of vertical displacements u_y at the center point of the crest (LVDT 1) obtained from the experiment and the numerical simulation during the dynamic excitation are depicted in Fig. 8.3. Note that displacements related to the installation and spin-up process are not included in this plot. For the experiment as well as the numerical simulation, no displacements are obtained up to $t \approx 0.03$ s as the dynamic loading of the VELACS model starts with very small amplitudes (Fig. 8.2). As soon as the amplitudes of the dynamic signal increase, displacements increase as well, showing an almost linear evolution with ongoing dynamic loading until $t \approx 0.4$ s. Afterwards, the displacement rate decreases. For $t > 0.45$ s almost no change in displacements is seen in the experiment while small changes are still observed in the numerical simulation. An explanation for this can be given with regard to the dissipation of excess pore water pressures that is slower in the numerical simulation, as discussed in the subsequent paragraphs. Overall, good agreement of the displacements obtained in the experiment and the numerical simulation is seen during the entire time of the test. Considering the assessment of the stability, a factor of safety could be defined with regard to a threshold displacement. However, this assessment should be considered rather subjective. Still, as the final displacements

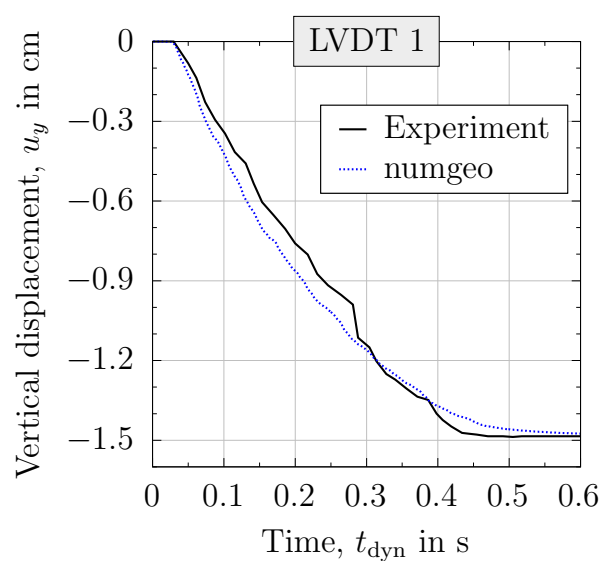


Figure 8.3: Comparison of vertical displacements obtained from `numgeo` with measurement at LVDT 1 from the experiment (Muraleetharan et al., 2004)

of 1.5 cm are equivalent to an average of 15% vertical strain, it should be clear that this magnitude of strain is certainly beyond any acceptable threshold values.

Analyzing the horizontal accelerations in terms of seismic coefficients from the experiment and the numerical simulation, it is apparent from Fig. 8.4 that very good agreement is obtained close to the bottom of the model (ACC 3) with some spikes for which larger values are obtained in the experiment compared to the numerical simulation. Slight deviations in the acceleration time histories are seen for accelerometers at the left and right slope surfaces (ACC 6 and ACC 7) with larger magnitudes recorded in the experiment. Close to the dam crest at accelerometer ACC 8, larger accelerations are obtained in the

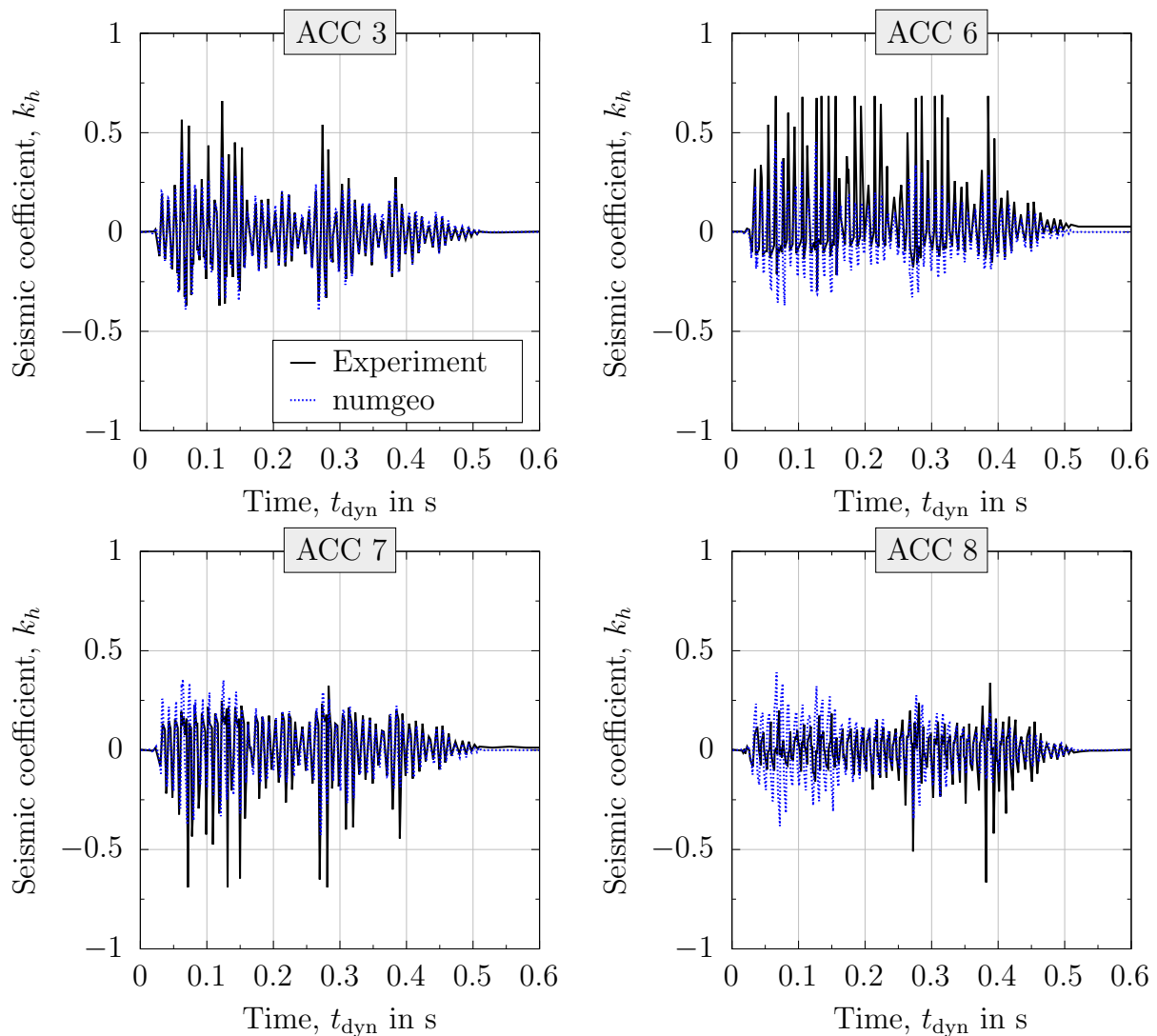


Figure 8.4: Comparison of accelerations obtained from numgeo with measurements ACC 3, ACC 6 - ACC 8 from the experiment (Muraleetharan et al., 2004)

numerical simulation, especially for $t_{\text{dyn}} \leq 0.2$ s. Regarding the assessment of the slope stability during the dynamic loading with pseudo-static analyses, it should be noted that underestimation of accelerations (or seismic coefficients) may also result in overestimation of the FoS.

Comparing excess pore water pressures in Fig. 8.5, larger differences can be seen between the experiment and the numerical simulation, where Δp^w recorded in the experiment shows a faster build-up and a faster dissipation of excess pore water pressure as well as larger magnitudes. In contrast to pore pressure transducers PPT A - PPT C that yield $\Delta p^w = 0$ for $t_{\text{dyn}} \geq 0.5$ s, it is apparent from the results of PPT D - PPT F that increased pore water pressures of about $2.0 \text{ kPa} \leq \Delta p^w \leq 4.0 \text{ kPa}$ remain after the test. This can be explained with regard to deformation of the soil and the transducers placed inside the dam, as due to the displacements, the transducers are finally located at a deeper position, at which hydrostatic pore water pressures are larger. Note that, in general, lower excess pore water pressures are obtained in the numerical simulation compared to the experiment. With regard to the assessment of the slope stability, this means larger effective stresses, leading to larger shear resistance and, potentially, a higher FoS prediction. Thus, the FoS predictions should be considered optimistic rather than conservative.

Besides the comparison of the predicted and measured accelerations and excess pore water pressures, accelerations obtained from DFEA are analyzed in terms of maximum positive and negative seismic coefficients (see Eq. 2.8) obtained in the whole soil domain during the dynamic loading. The time histories of the maximum horizontal and vertical seismic coefficients are depicted in Fig. 8.6. A clear similarity between the input seismic coefficients (Fig. 8.2) and the peak horizontal and vertical seismic coefficients in the soil domain (Fig. 8.6) is observed. Still, larger seismic coefficients are obtained in the soil domain compared to the input signal. This is due to amplification of the accelerations in the soil domain and reflections at the top surface and the model boundaries. Overall, an amplification of about 50% is seen for k_h , while large vertical seismic coefficients are obtained, as well, with peak values ranging up to $k_{v,\text{min}/\text{max}} \approx 0.4$.

8.2.2. Assessment of seismic slope stability

Spatial pseudo-static analysis using LEM

In contrast to SDSS and SRFEA utilizing Matsuoka-Nakai as limit or yield surface, respectively, stability analyses based on LEM are conducted applying the Mohr-Coulomb

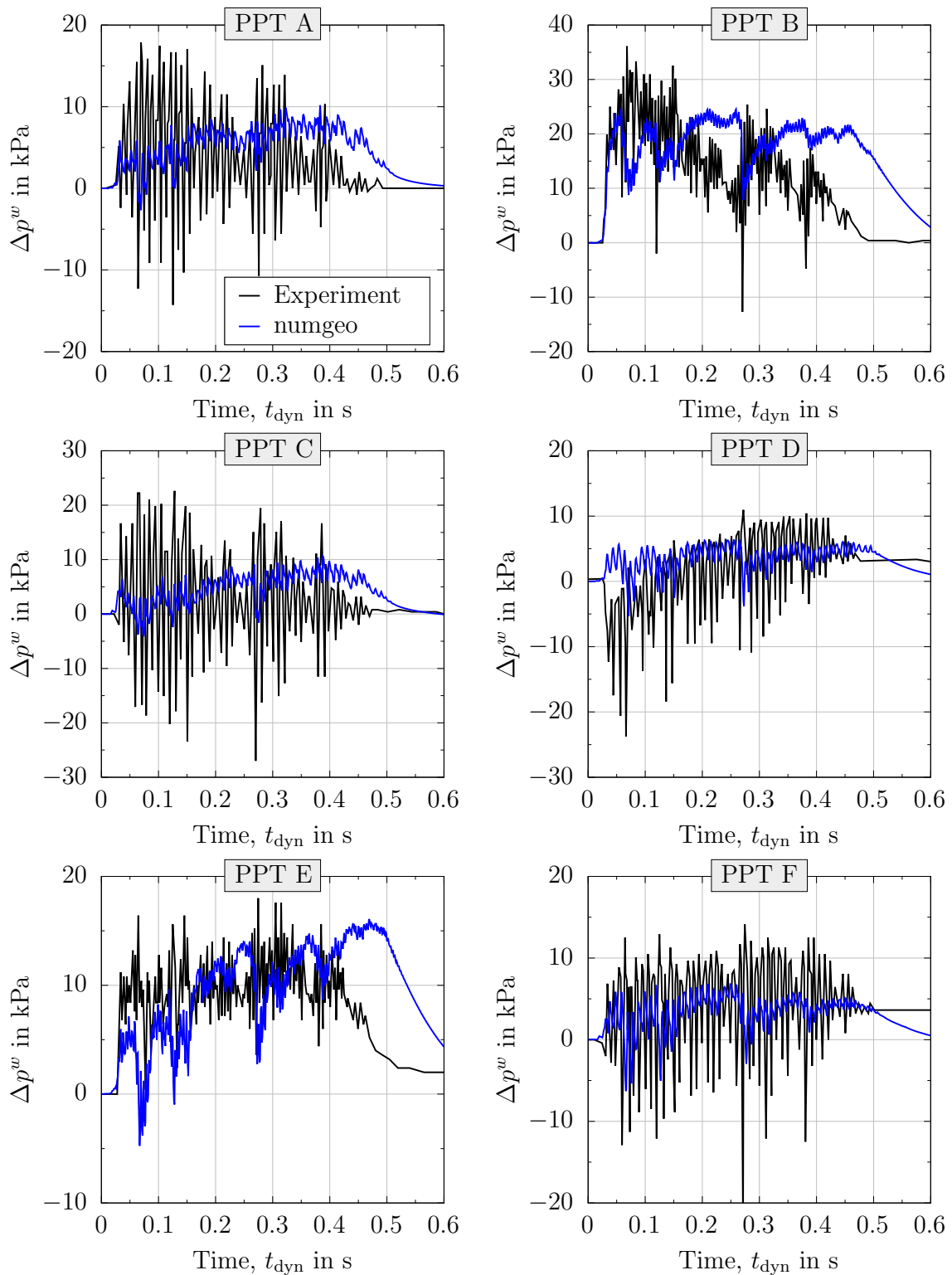


Figure 8.5: Comparison of excess pore water pressures obtained from numgeo with measurements PPT A - PPT F from the experiment (Muraleetharan et al., 2004)

failure criterion in the slip surface (see Section 2.1.1). For plane strain problems with Lode angles of $0^\circ \leq \theta \leq 10^\circ$, for instance the 2D slope stability problem, applying MC results in smaller allowable deviatoric stresses in the latter case, which ultimately leads to smaller FoS. In this section, an equivalent Mohr-Coulomb friction angle (Griffiths and Huang, 2009; Jiang and Wang, 2011) of $\varphi = 34.75^\circ$ evaluated at a Lode angle of $\theta = 0^\circ$ is set into approach to compensate effects related to differences between the Mohr-Coulomb and Matsuoka-Nakai surfaces. Moreover, a stabilizing distributed load of 1 kPa was used in the DFEA, which was also considered in SDSS and SRFEA to ensure comparable assumptions.

As a rough estimate of the slope stability applying the PSA with LEM, a constant seismic coefficient can be assumed for the whole soil domain. Following Hynes-Griffin and Franklin (1984) and Kramer and Smith (1997), an acceptable approach would be to calculate the horizontal seismic coefficient according to $k_h = 0.5 \cdot a_{\max}/g$, where a_{\max} is the maximum bedrock acceleration. Hleibieh and Herle (2019a) suggested to determine k_h based on 60% of the maximum acceleration as a result of amplification within the soil domain. Additionally, in line with Hleibieh and Herle (2019a), a vertical seismic coefficient is assumed in the order of $k_v \approx 1/3 \cdot k_h$. In both approaches, a homogeneous distribution of the seismic coefficient is assumed and accumulated excess pore water pressures resulting from the dynamic loading are neglected. For the input motion used in the excitation phase of the VELACS model (Fig. 8.2), following the above mentioned recommendations would result in $k_h = 0.240$ (Hynes-Griffin and Franklin, 1984; Kramer and Smith, 1997) up to

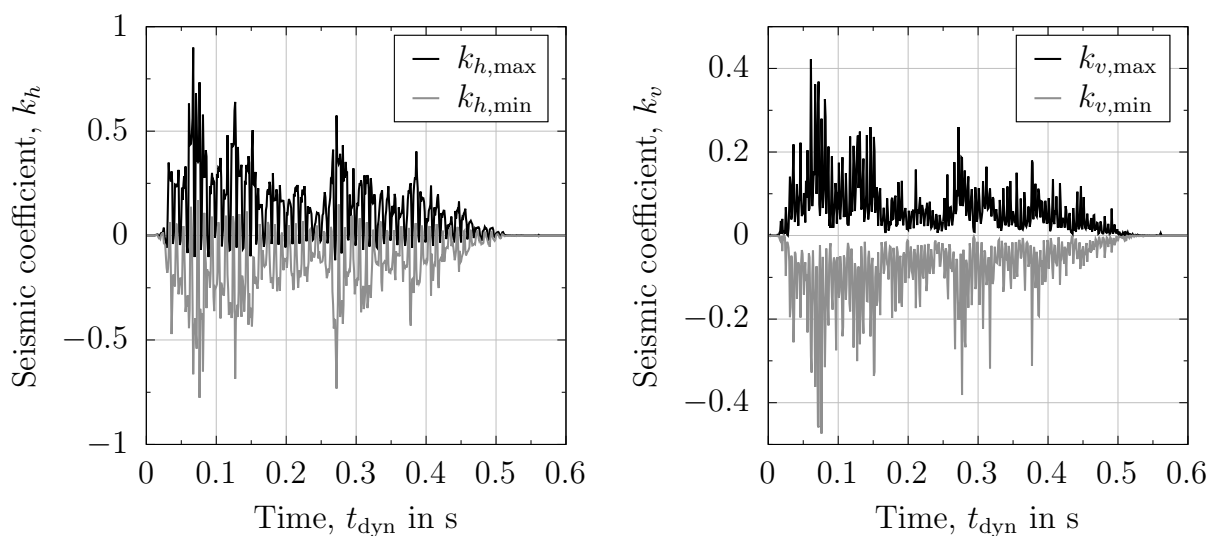


Figure 8.6: Peak (min/max) seismic coefficients in the soil domain during dynamic loading of the VELACS model

$k_h = 0.289$ and $k_v = 0.096$ (Hleibieh and Herle, 2019a). Applying these seismic coefficients in PSA with LEM (Bishop) using `geoSlice`, $\text{FoS} = 0.647$ and $\text{FoS} = 0.477$ are obtained, respectively. Therefore, the VELACS model dam would be classified as instable. Note that based on these approaches it is not possible to determine the evolution (time history) of the stability of the dam as the spatial and temporal distribution of the accelerations are not taken into consideration.

To analyze the VELACS model with regard to the evolution of the slope stability during dynamic loading, spatial pseudo-static analyses with LEM introduced in Section 6.2 are conducted. With time increments of $\Delta t = 0.001$ s and two potential directions of failure (i.e. slip surfaces along the left and right face of the slope), 1200 stability analyses are performed in total. Spatial distributions of seismic coefficients and excess pore water pressures are accounted for using three nodes for interpolation. Horizontal seismic coefficients (inertial forces) are always considered as acting in the direction of the driving forces and vertical seismic coefficients are varied to automatically determine the critical direction. To account for the increased gravity, corresponding unit weights of the soil and the water are determined.

The results of the spatial pseudo-static analyses using LEM are depicted in Fig. 8.7 in terms of FoS versus dynamic time for the left and right slope face individually and for the critical slip surface, where the latter refers to the lower FoS of the former two. Analyzing the stability under static conditions (at $t_{\text{dyn}} = 0.0$ s), it can be seen that the stability of

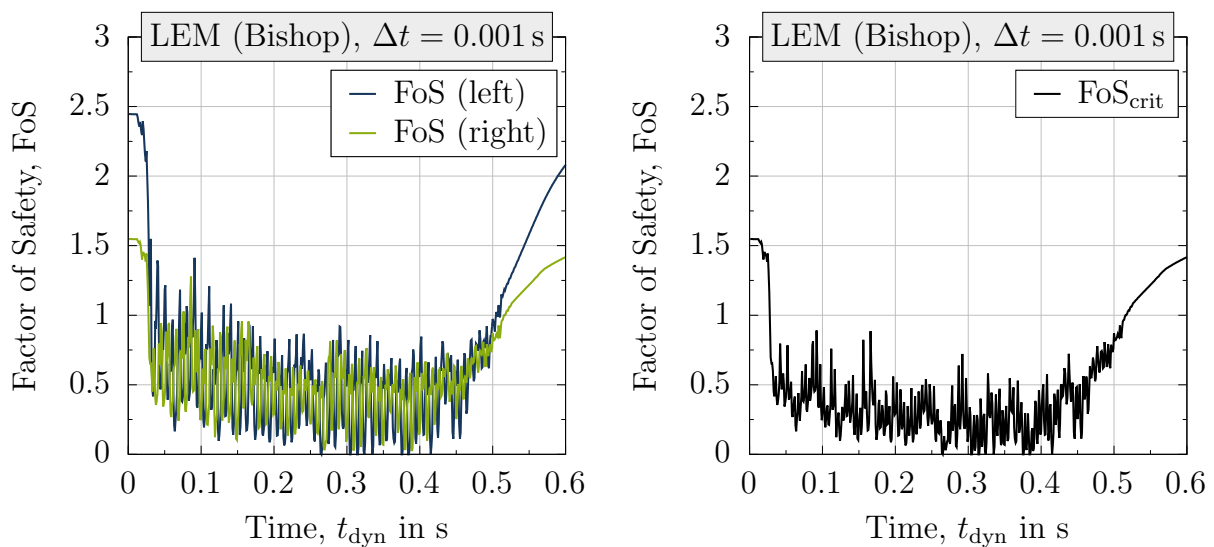


Figure 8.7: Evaluation of the FoS of the left and right face of the VELACS model dam based on spatial PSA+LEM considering time increments of $\Delta t = 0.001$ s

the left and right slope with $\text{FoS} = 2.45$ and $\text{FoS} = 1.55$ indicate that the model dam is stable initially. Note that the right face yields a smaller FoS compared to the left face since the inclination of the former slope is larger. As soon as the dynamic excitation starts and the shear waves approach the dam top surface, a significant reduction of the FoS is observed for both faces. Note that due to a rapid variation of the accelerations in the model, the FoS undergoes rapid changes, as well, where, depending on the spatial distribution of accelerations, the critical slip surface associated with the lowest FoS is found at the left or the right face of the dam. Furthermore, it is seen that the amplitude of the FoS variation slightly decreases with increasing dynamic time. This trend is in good agreement with the applied input signal (Fig. 8.2) and the amplified peak accelerations observed in the dam (Fig. 8.6), however, it may also be associated with the accumulation of excess pore water pressures (Fig. 8.5) that further destabilize the dam by decreasing effective stresses. After the dynamic loading finished at $t_{\text{dyn}} \approx 0.5$ s and also accelerations in the dam decreased (Fig. 8.4), the FoS increases with increasing time as a result of dissipation of excess pore water pressure. Note that the initial level of safety is not fully recovered at $t_{\text{dyn}} = 0.6$ s as Δp^w has not decreased to zero in the whole model (see e.g. PPT B/E in Fig. 8.5).

Evaluation of the right subplot of Fig. 8.7 allows to state that the VELACS model reaches an unstable state ($\text{FoS} < 1.0$) as soon as the dynamic excitation begins. As the FoS does not recover a stable state after the first drop until the dynamic loading finished, approaches based on the permanent-displacement analysis (e.g. Newmark's method) would predict large displacements as a result of accelerations exceeding the yield acceleration. To be more specific, a yield acceleration of $a_y \approx 54 \text{ m/s}^2$ is determined using LEM for this model (model scale) and a slope failure towards the right side. Applying Newmark's method, a similar displacement versus time trend as depicted in Fig. 8.3 is seen with a maximum displacement of about 1 cm. This is in good agreement with the displacements observed in the experiment (Muraleetharan et al., 2004) that ultimately led to a decrease in the height of the model dam in the experiment of about 1.5 cm, corresponding to 15% of the model dam height.

Strain-dependent slope stability for earthquake loading

To assess the stability of the VELACS model considering an advanced constitutive model and an accurate spatial distribution of the effective stress state and the state variables, the extended strain-dependent slope stability (SDSS) described in Section 2.1.6 and Section 6.4 is utilized. Similar to the DFEA, the hypoplastic model in the version of von

Wolffersdorff (1996) is applied, however, in line with the discussions in Section 6.4, intergranular strain (IGS) proposed by Niemunis and Herle (1997) is deactivated in SDSS to avoid overestimation of the shear stresses and the FoS. For this reason, in addition to the stress tensor only the void ratio is transferred from the DFEA model to the element test simulations. SDSS is conducted in terms of direct simple shear (DSS) tests for 15 nodes along a potential slip surface, where the stress tensor at each node is rotated onto the slip surface before the DSS test is performed. Evaluation of the global mobilized shear resistance ratio $T(\gamma)$ is conducted in accordance with Eq. 6.11, where the summation of the shear stress versus shear strain curves is normalized by the sum of the initial shear stresses at $t_{\text{dyn}} = 0.0$ s, which resembles the static equilibrium. The FoS curve is obtained in accordance with the descriptions in Section 2.1.6. Similar to the seismic slope stability assessment conducted for the opencast slope using SDSS (Section 7.3.3), slope stability is assessed in terms of FoS_{max} . Note that different to the aforementioned slope, two different directions of failure need to be investigated for the VELACS dam model. For this reason, SDSS had to be applied for both the left and the right face of the VELACS model. As the computational costs associated with SDSS are significantly larger compared to LEM (≈ 2 orders of magnitude), stability analyses are conducted for time increments of $\Delta t = 0.005$ s, resulting in 121 analyses per face (i.e. per direction of failure).

The results of the analyses applying SDSS are presented in Fig. 8.8 in terms of the FoS versus dynamic time for the individual assessment of the left and right slope (first subplot) and the critical slope (second subplot). It can be seen from this figure that,

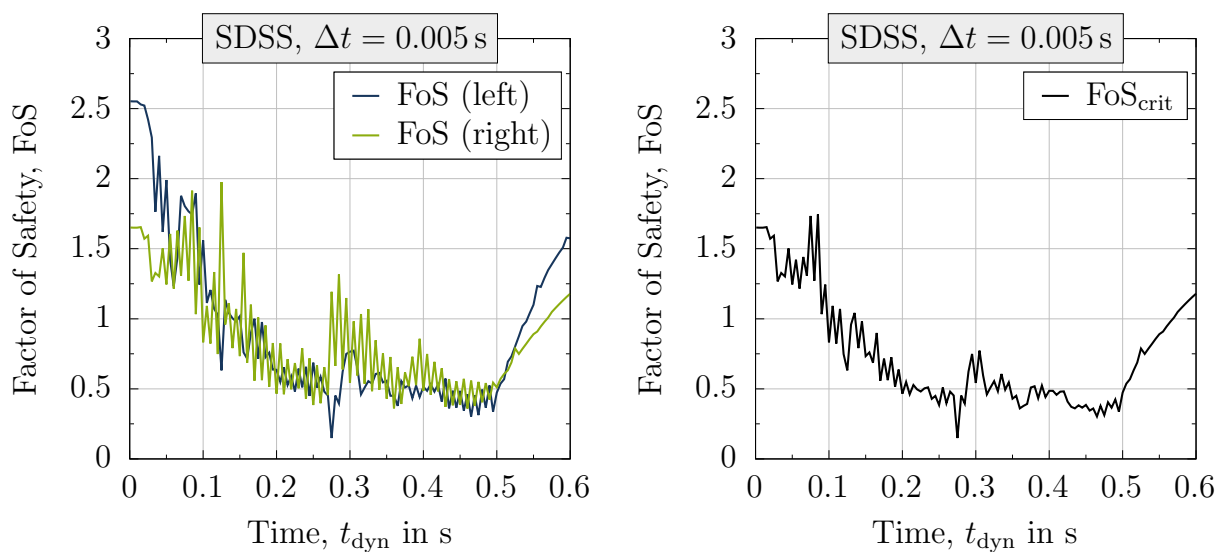


Figure 8.8: Evaluation of the FoS of the left and right face of the VELACS model dam based on SDSS considering time increments of $\Delta t = 0.005$ s

initially ($t_{\text{dyn}} = 0.0$ s), the right face yields a smaller FoS compared to the left face since the inclination of the former slope is larger. During the dynamic loading, the initial difference between the stability of the left and the right face is not maintained but reduces significantly. This observation may be related to the fact that the slopes are differently affected by the dynamic loading due to the type of the input motion. Note that the critical FoS is not always associated with the same face (i.e. always the left or right slope), but changes for different time steps. Analyzing the critical FoS, it is observed that the dynamic loading destabilizes the VELACS model significantly with a drop of the FoS below unity at $t_{\text{dyn}} \approx 0.1$ s. Despite slight temporary re-increases of the slope stability, an overall decreasing trend of the FoS is seen with a minimum of $\text{FoS} = 0.38$ at $t_{\text{dyn}} \approx 0.25$ s. After reaching this minimum, slight increases and decreases of the FoS are observed for $0.25 \text{ s} \leq t_{\text{dyn}} \leq 0.46 \text{ s}$. As soon as the amplitude of the dynamic signal reduced and finally vanished ($t_{\text{dyn}} \geq 0.5$ s), the FoS is partly recovered as a result of dissipating excess pore water pressures and increasing effective stress levels. Note that the initial FoS is not reached as a result of a modified stress state and remaining excess pore water pressures $\Delta p^w > 0$ in the model at $t_{\text{dyn}} = 0.6$ s. In line with the high frequency oscillations of the input signal, it is observed that also the FoS predictions with SDSS are characterized by oscillations, though, the amplitude of these oscillations is smaller compared to those obtained with LEM.

In general, evaluation of the seismic slope stability based on the concept of strain-dependent slope stability indicates that the VELACS centrifuge model test reaches and contains a state of failure shortly after the dynamic loading started. This observation is in good agreement with the results obtained with LEM. Note that higher frequencies and amplitudes of the oscillations of the FoS during the dynamic loading might be seen when decreasing the time interval of the stability analyses.

Spatial pseudo-static analysis using SRFEA

To evaluate the evolution of the FoS based on the spatial pseudo-static analysis using SRFEA, submodel analyses (see Section 6.5) are conducted, in which the DFEA is put on hold whenever a SRFEA is performed. For the SRFEA, the current stress state, (excess) pore water pressures and inertial forces are imported from the DFEA. During the SRFEA, (excess) pore water pressures and inertial forces are kept constant. The material behavior is approximated using the Matsuoka-Nakai model with the friction angle chosen to be identical to the critical friction angle (Tab. 8.1). SRFEA is performed for time intervals of $\Delta t = 0.001$ s considering an initial factor of safety of $\text{FoS}_0 = 0.5$ and an incremental

increase of $\Delta\text{FoS} = 0.01$. The critical FoS was obtained based on a sudden change in the FoS versus displacement plot with displacements displayed in logarithmic scale, following the approach discussed in Section 5.2. Technically, SRFEA could also be started with smaller FoS values, however, a value of 0.5 was selected here to avoid unrealistically large friction angles. For this reason, it should be clear that values of $\text{FoS} \leq 0.5$ will be displayed as $\text{FoS} = 0.5$, since in those cases slope failure has been detected either way.

The results of the analyses applying SRFEA are presented in Fig. 8.9 in terms of the FoS versus dynamic time for two cases, where inertial forces (denoted in the plot as nodal dynamic forces, NDF) are considered in one case and ignored in the other case. Focusing on the initial FoS after the spin-up at first, SRFEA yields $\text{FoS} = 1.6$, which is comparable to the one obtained using LEM ($\text{FoS} = 1.55$). During dynamic loading, significant oscillations of the FoS were observed in this figure that can be attributed to large oscillations in the dynamic signal, which leads to oscillations in the inertial forces as well as in the excess pore water pressure. Note that significant differences in the predicted FoS are obtained for simulations considering and neglecting inertial forces, where the former predominantly yield smaller (i.e. more critical) factors of safety. Thus, neglecting the contribution of inertial forces may yield to non-conservative FoS estimates.

Considering the evolution of the critical FoS defined as the minimum FoS for simulations with and without inertial forces displayed in the right subplot, it is apparent that initially, the VELACS model is in a stable state for the first time steps investigated. However, at $t \approx$

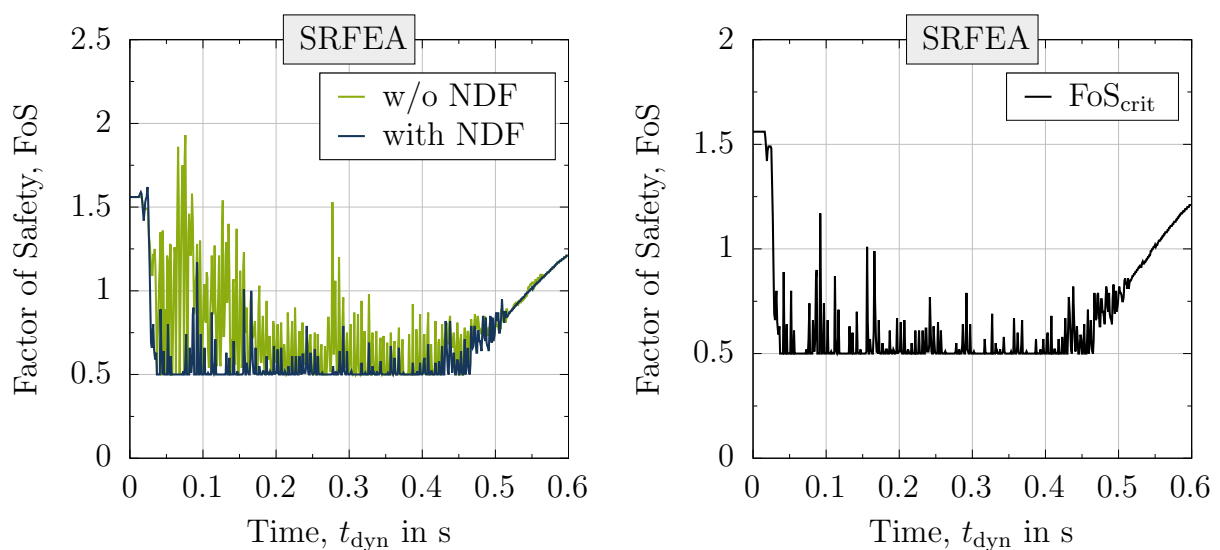


Figure 8.9: Evaluation of the FoS of the VELACS model dam based on SRFEA considering time increments of $\Delta t = 0.001$ s with or without considering inertial forces (NDF)

0.03 s a sudden decrease of the safety is obtained down to $\text{FoS} = 0.66$ with further reduction within the following time increments down to $\text{FoS} = 0.5$ at $t \approx 0.037$ s. Afterwards, large oscillations of the FoS are detected. For $0.03 \text{ s} \leq t \leq 0.54 \text{ s}$, the VELACS model is classified as unstable for (almost) the entire time span. Note that a continuous increase in the FoS is seen for $t \geq 0.45$ s as a result of vanishing inertial forces and increasing effective stresses, the latter related to the dissipation of excess pore water pressures. Compared to the results of the LEM, larger FoS values are predicted using the SRFEA for most of the time steps. These differences may be attributed to the consideration of inertial forces. In contrast to LEM, inertial forces in SRFEA are not strictly directed into driving direction but in line with the DFEA to ensure the analysis of an equilibrium state that is very similar to the dynamic equilibrium.

Discussion

To enable a direct comparison of the results obtained using LEM, SDSS and SRFEA, the evolution of the FoS during the dynamic loading, individually plotted in Fig. 8.7, Fig. 8.8 and Fig. 8.9, respectively, is summarized in Fig. 8.10. It is obvious from this figure that the three approaches do not yield identical predictions of FoS versus t_{dyn} , however, further elaboration is needed to enable an assessment of the approaches. For this reason, discussion is conducted with regard to similarities, differences, reliability and computational costs.

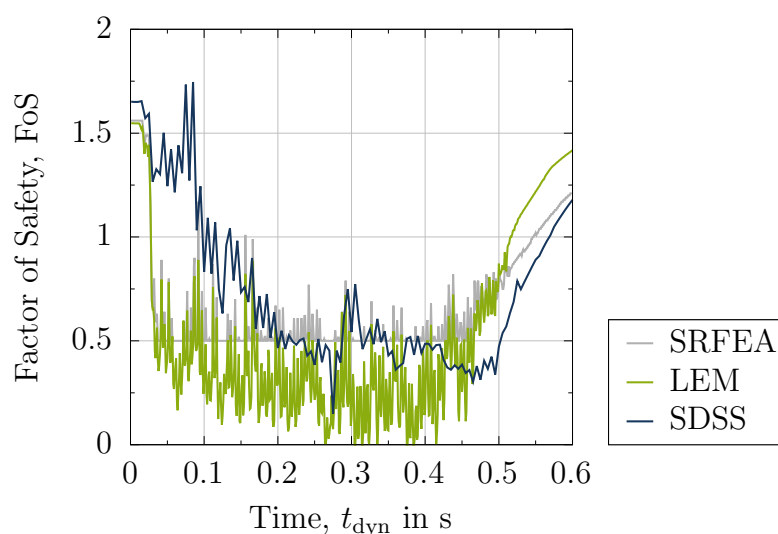


Figure 8.10: Comparison of the FoS of the VELACS model based on LEM, SDSS and SRFEA

As can be seen from Fig. 8.10, all approaches result in similar FoS under static conditions ($t = 0.0$ s). Moreover, all approaches show a decisive drop of the FoS at $t \approx 0.03$ s, which agrees well with the time at which the amplitude of the dynamic signal increased to $k_h \geq 0.2$ for the first time. During the dynamic loading, LEM yields small FoS values, whereas SDSS and SRFEA predict larger FoS values. Note that FoS in SRFEA are restricted to $\text{FoS} \geq 0.5$ to avoid unrealistically large friction angles in the constitutive model routine. Using a smaller initial FoS in SRFEA, it is possible that also smaller FoS values would be detected. Still, it is noteworthy that all approaches classify the VELACS model as unstable for at least 75% of the test duration. Considering the last 0.1 s of the centrifuge test, it is observed that FoS determined based on all approaches increases significantly as a result of (almost) zero accelerations and dissipation of excess pore water pressures Δp^w . The FoS at the beginning of the dynamic loading is not fully recovered at $t = 0.6$ s due to $\Delta p^w \geq 0$ kPa in the model (see e.g. PPT B/E in Fig. 8.5).

To evaluate the reliability related to the different approaches and to categorize them from conservative to optimistic, stress states, shear strength and approximation of the critical slip surface are discussed. In LEM, the shape of the slip surface is prescribed and the total stress state is approximated only roughly. The effect of excess pore water pressures is captured accurately, while shear strength is approximated based on the concept of the equivalent Mohr-Coulomb friction angle (Griffiths and Huang, 2009; Jiang and Wang, 2011). The impact of inertial forces is overestimated by considering horizontal seismic coefficients that always act in driving direction. As for slopes without soil layering (see e.g. Section 3.4.4) the last two aspects are more important than the former two, LEM is regarded to yield conservative estimates for the VELACS model. In SDSS, effective (and total) stress states are captured accurately and shear strength is approximated realistically due to the use of advanced constitutive models for the stability analyses. The shape of the slip surface and the discretization of nodes along the slip surface need to be prescribed, where the former requires an optimization to detect the critical slip surface and sensitivity analyses with regard to the latter should be conducted to evaluate the impact of the discretization on the FoS. Note that in contrast to SRFEA, stress redistribution during the stability analysis is not possible in SDSS as each node is considered isolated. Furthermore, stresses and strains after the element tests are not transferred back to the finite element model and overall equilibrium is not checked. SDSS is considered to give a more reliable prediction of the stability of the VELACS model in comparison with LEM as the spatial distribution of stresses is more accurate and shear strength is defined based on an advanced constitutive model taking into account the current stress state, the loading history and the soil density.

In SRFEA, an accurate distribution of stresses is considered and equilibrium is ensured during the strength reduction procedure. Setting these aspects into context with the previous approaches, the former is only captured in SDSS and the latter is neither considered in LEM nor in SDSS. Comparable to LEM and SDSS, ultimate shear strength in SRFEA is governed based on the Matsuoka-Nakai (MN) model that also accounts for the intermediate principal stress. Predictions based on SRFEA are considered to be slightly more accurate compared to LEM as shear strength in the latter approach is approximated based on the equivalent MC friction angle. However, as the MN model with perfect plasticity (i.e. without hardening and softening) used in SRFEA does not take into consideration the effect of the strain level on the ultimate shear strength, for instance by a strain-softening rule related to plastic strains, the description of shear strength should be regarded more accurate in SDSS as strain-dependency is considered and more sophisticated constitutive models can be applied. In contrast to LEM and SDSS, the approximation of the critical slip surface in SRFEA does not require predefined slip surfaces but the location and the shape of the critical slip surface are part of the outcome of the strength reduction procedure. Note that for slopes composed of a single material (i.e. no soil layering) and homogeneously distributed material parameters (i.e. no variation within soil domain), the shape of the critical slip surface should be of subordinate importance provided a circular shape was assumed. Therefore, comparable to the SDSS, SRFEA is considered to give a reliable prediction of the stability of the VELACS model.

Besides the similarities and differences in the approaches for the assessment of the slope stability under seismic loading, evaluation of computational costs related to the different approaches should also be considered. In general, stability analyses based on LEM are very fast. Although, depending on the optimization technique, the number of slip surfaces to be investigated may vary significantly, LEM analyses require only a few seconds to predict the FoS. This also holds for the assessment of the stability of the VELACS model, where slip surfaces considering a failure both along the left and the right slope face needed to be analyzed. Note that the consideration of spatial distributions of accelerations (inertial forces) and excess pore water pressures increases the computational costs associated with LEM, though, this approach is still fast when compared to SDSS and SRFEA. Performing SDSS with a basic grid optimization technique, the number of simulations to be conducted is independent of the level of safety, but it is only related to the number of slip surfaces specified. Similar to LEM, the left and the right slope of the VELACS model need to be analyzed independently. Considering analyses for both slopes, SDSS requires approximately 1 hour to evaluate the stability for one time step. In SDSS, the largest fraction of the computational costs is related to the simulation of

the element tests, which is also addressed in Chapter 9. Depending on the level of safety and, thereby, the number of increments conducted, SRFEA requires a few seconds up to 2 minutes for each time step. Note that the time to conduct SRFEA is strongly related to the number of nodes, elements and integration points in the model. As the number of elements used to discretize the VELACS model is rather small, SRFEA is significantly faster in comparison to SDSS.

8.3. Liquefaction Experiments and Analysis Projects (LEAP)

8.3.1. Dynamic finite element analysis

Finite element model

The Liquefaction Experiments and Analysis Projects (LEAP) aim to investigate the repeatability and reliability of experimental data obtained from centrifuge model tests at different facilities. It is a series of centrifuge model tests that started with LEAP-GWU-2015, followed by LEAP-UCD-2017 and LEAP-ASIA-2019, where the focus here is on the second event. In total, 24 centrifuge tests were performed at 9 centrifuge facilities located in various countries around the world. The results of the experimental and numerical analyses related to LEAP-UCD-2017 are summarized in Kutter et al. (2020). The slope under investigation is inclined by 5° and is composed of medium dense Ottawa sand. According to Kutter et al. (2020), a degree of saturation in the range of $0.994 \leq S^w \leq 0.998$ was obtained. A schematic illustration of the centrifuge model test is depicted in Fig. 8.11. Among the 9 facilities, centrifuge model tests were also conducted at National Central University (NCU) in Taiwan with the results used as a benchmark for the numerical analyses conducted in this chapter. Note that further numerical analyses of the LEAP centrifuge model test were conducted by Triantafyllidis et al. (2022).

The finite element software `numgeo` was used for the analysis of the dynamic excitation of the LEAP centrifuge model test. As the simulation was performed in prototype scale, no increased gravity was considered. The mechanical behavior of Ottawa sand was modeled using Hypoplasticity with Intergranular Strain (IGS) with the parameters provided in Table 8.2. The FE model consists of about 822 elements and 2,620 nodes. The finite element mesh was generated as a quad-dominated mesh (810 quad elements, 12 triangular elements) with a mean nodal distance of $\Delta x = \Delta y \approx 0.15$ m. To account for changes in

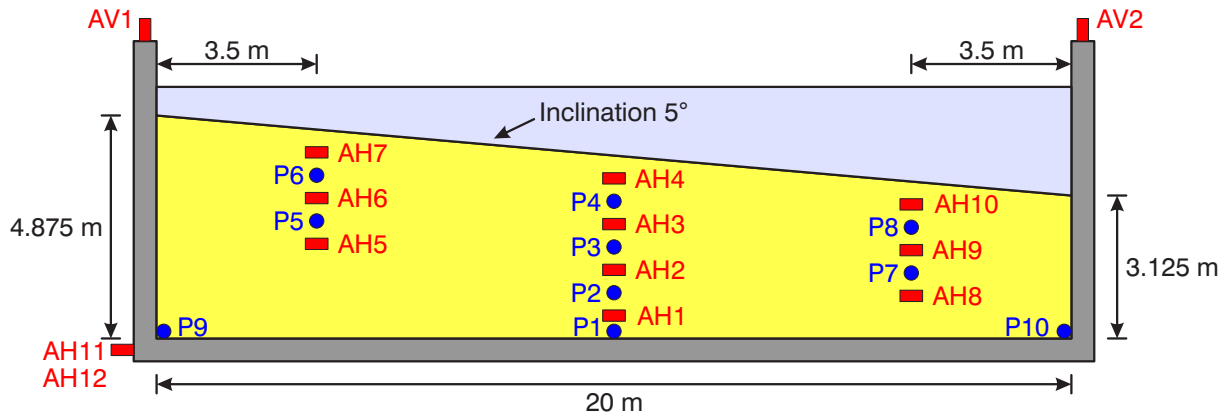


Figure 8.11: Geometry and dimensions of the LEAP model in prototype scale

the pore water pressure and consolidation effects during and after the earthquake loading, u-p elements were used, discretizing the solid displacements \mathbf{u} and the pore water pressure p^w at the nodes. Similar to the VELACS model, in this simulation, viscous stresses limited to 2 kPa were considered to stabilize the stress-strain behavior at small stress states.

The simulation was performed in the following steps:

Geostatic: Application of gravity while the displacements of the bottom boundary were constrained in the horizontal and vertical direction. Additionally, displacements at the lateral boundaries were constrained in horizontal direction. The pore water pressure was prescribed at each node according to a hydrostatic distribution, considering the phreatic level as given in Fig. 8.11. The initial void ratio follows Bauer's equation (Bauer, 1996). A lithostatic initial stress distribution was prescribed, considering the variable overburden height in the slope. As shear stresses are unknown a priori, they are obtained during the iteration process as they are required to obtain a static equilibrium of the model. To account for the dead weight of the free water table, an additional surface load was applied in this step and kept constant for the following steps. In addition, a surface traction of 1 kPa was applied perpendicular to the ground surface

Table 8.2: Parameters of the Hypoplastic model ($\varphi_c - \beta$) with intergranular strain (IGS, $m_T - \chi$) for Ottawa sand (Triantafyllidis et al., 2022)

φ_c	ν	h_s	n	e_{d0}	e_{c0}	e_{i0}	α	β	m_T	m_R	R	β_R	χ
[°]	[-]	[MPa]	[-]	[-]	[-]	[-]	[-]	[-]	[-]	[-]	[-]	[-]	[-]
32	0.2	304.8	0.54	0.508	0.777	0.894	0.145	3.5	2.5	3.5	10^{-4}	1.3	1.0

to avoid very small mean effective stresses leading to numerical problems with the hypoplastic model.

Release pore water pressure boundary condition: To allow for changes in the pore water pressure during the dynamic loading step, the pore water pressure boundary condition is removed in this step. This applies to all nodes except for those at the top surface, for which the hydrostatic pore water pressure boundary condition is kept to allow for drainage at the top surface

Dynamic loading: Excitation of the model base and the model sides in horizontal direction in a dynamic step. In this case, the excitation is applied by a Dirichlet boundary condition, imposing the acceleration-time history in the horizontal direction at the bottom and at the sides of the model in accordance with Fig. 8.12. The Hilber-Hughes-Taylor time integration scheme ($\alpha = -0.05$) was used and a fixed time increment of $5 \cdot 10^{-3}$ s was set. A constant hydrostatic pore water pressure was assigned to all nodes at the top of the model, allowing for drainage. Except for the bottom of the model, which was constrained in the vertical direction, no further Dirichlet boundary conditions were applied to the solid displacement.

The input signal used in the numerical analyses refers to the NCU-3 test in Kutter et al. (2020). Note that the target input signal defined as a sine function scaled by an increasing ramp (up to 10 s) and a decreasing ramp (after 10 s) and the one measured outside of the model (AH11, AH12) differ significantly (Fig. 8.12). The measured signal is characterized by larger peak amplitudes and additional higher frequency fluctuations compared to the

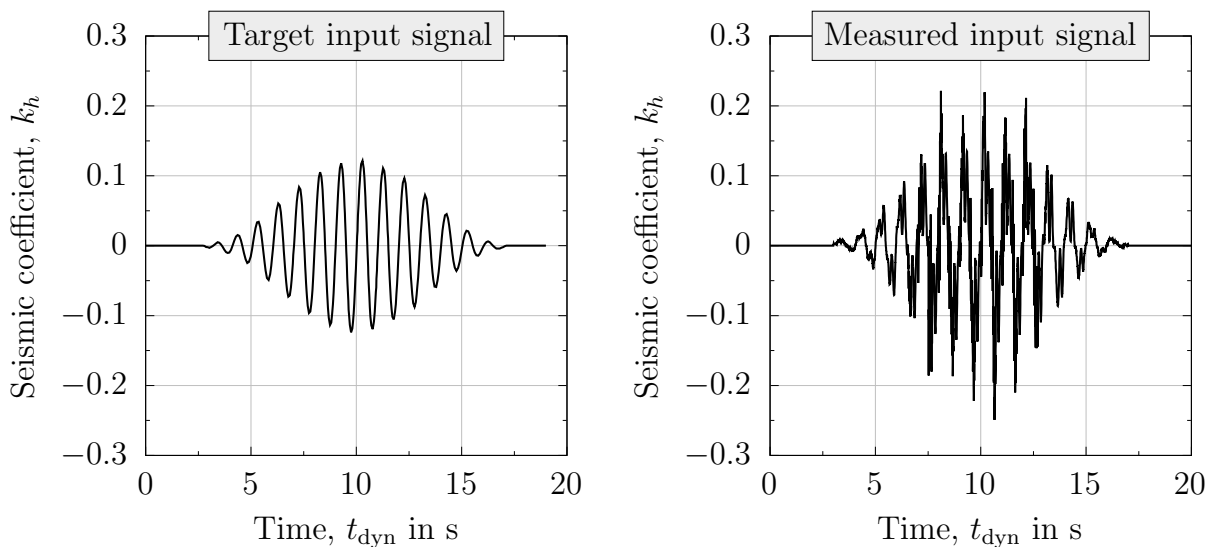


Figure 8.12: Target and measured input signal at the bottom of the LEAP model

sine function. Based on numerical analyses with the target and the measured signal, Triantafyllidis et al. (2022) reported that the values of the excess pore water pressure Δp^w were significantly underestimated with the former, while better agreement was obtained with the latter signal. For this reason, the measured signal was applied in the numerical simulations.

Results

To assess whether the DFEA using Hypoplasticity with Intergranular Strain (IGS) is capable to reproduce the results of the centrifuge model test, a comparison of acceleration and excess pore water pressure time histories at the position of the respective sensors (Fig. 8.11) is undertaken. For this, the acceleration time histories recorded at the accelerometers AH1, AH2, AH5 and AH8 as well as the excess pore water pressure time histories back-calculated from the pore pressure transducers P1, P2 and P4 – P7 summarized in Kutter et al. (2020) are considered. Note that vertical displacements are not compared due to the lack of measurements. Horizontal displacements have not been recorded but back-calculated by double integration of the difference of the accelerations recorded at AH1 and AH4.

Analyzing the accelerations in terms of seismic coefficients from the experiment and the numerical simulation, it is apparent from Fig. 8.13 that good agreement is obtained for AH1 and AH8, which are the two accelerometers inside the soil domain located closest to the bottom of the model. With increasing elevation, as depicted for instance for AH2 and AH5, the differences between the experiment and the numerical simulation are more obvious, as peak values are not well captured. Although not explicitly shown here, discrepancies further increase with increasing elevation, thus, with decreasing overburden height. In general, the numerical simulation predicts smaller seismic coefficients compared to the recorded data of the experiment. Regarding the assessment of the slope stability during the dynamic loading with pseudo-static analyses, it should be noted that underestimation of accelerations (or seismic coefficients) may result in overestimation of the FoS.

Comparing excess pore water pressures in Fig. 8.14, differences can be seen between the experiment and the numerical simulation. Although a similar fast build-up of Δp^w is recorded in the experiment and the numerical simulation, larger magnitudes and a slower dissipation of excess pore water pressure are obtained in the experiment. The difference in the maximum excess pore water pressures at the pore pressure transducers P1, P2 and

P4 – P7 is found to be up to 10 kPa for $5 \text{ s} \leq t_{\text{dyn}} \leq 15 \text{ s}$. At P7, even larger differences are seen for $t_{\text{dyn}} \geq 15 \text{ s}$. Note that, in general, lower excess pore water pressures are obtained in the numerical simulation compared to the experiment. With regard to the assessment of the slope stability, increased effective stresses are considered, leading to larger shear resistance and, potentially, a higher FoS prediction. Thus, the FoS predictions should be considered optimistic rather than conservative.

The evolution of horizontal displacements u_x obtained from the experiment and the numerical simulation during the dynamic excitation is depicted in Fig. 8.15. For the experiment as well as the numerical simulation, no displacements are obtained up to $t \approx 7.5 \text{ s}$,

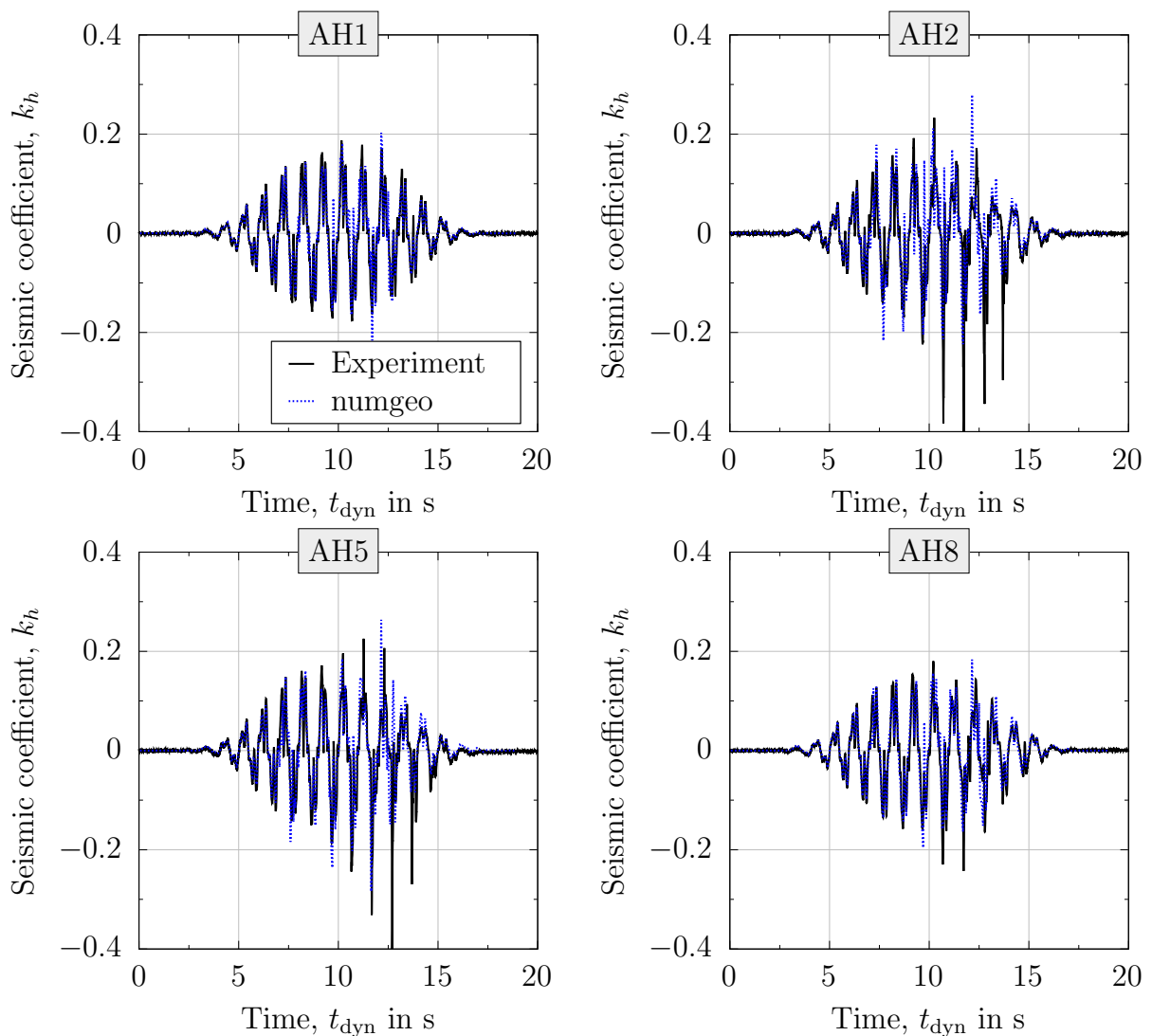


Figure 8.13: Comparison of accelerations obtained from `numgeo` with measurements AH1, AH2, AH5 and AH8 from the experiment (Kutter et al., 2020)

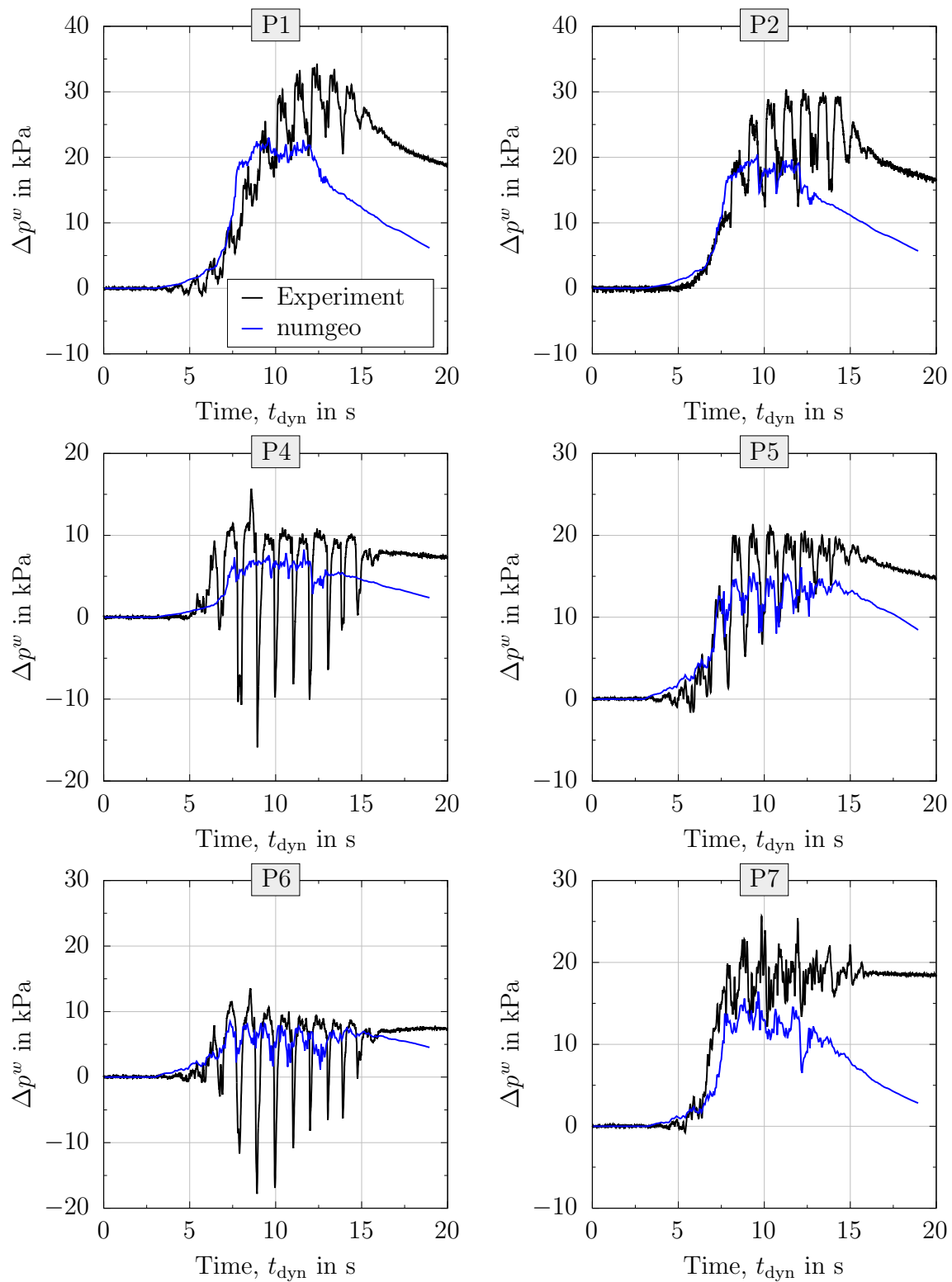


Figure 8.14: Comparison of excess pore water pressures obtained from numgeo with measurements P1, P2 and P4 – P7 from the experiment (Kutter et al., 2020)

although the dynamic loading of the LEAP model started at $t \approx 4$ s (Fig. 8.12). A potential explanation for this can be given with regard to the concept of yield acceleration, below which no significant displacements are accumulated. As soon as the amplitudes of the dynamic signal increase, displacements increase as well, showing large difference between the experiment and the numerical simulation, where large displacements are accumulated in the former and only a comparatively small magnitude of displacements is observed in the latter case. Note that overall a poor agreement of the displacements obtained in the experiment and the numerical simulation is seen from $t \approx 7.5$ s up to the end of the test. Triantafyllidis et al. (2022) reported a similar poor agreement between the experiment and simulations with Hypoplasticity with IGS but also noted that better predictions were obtained with the Sanisand model (Dafalias and Manzari, 2004). Considering the reports summarized in Kutter et al. (2020) it should be noted that large variations related to the LEAP-UCD-2017 project were obtained in both, the experimental results of centrifuge model tests conducted at different facilities and the numerical simulations. Although the displacements are not well captured with Hypoplasticity with IGS, the applicability of the approaches for the assessment of the stability of slopes under seismic loading is shown in the following section.

Besides the comparison of accelerations and excess pore water pressures at the accelerometers and pore pressures transducers, accelerations are also analyzed in terms of maximum positive and negative seismic coefficients obtained in the whole soil domain during the

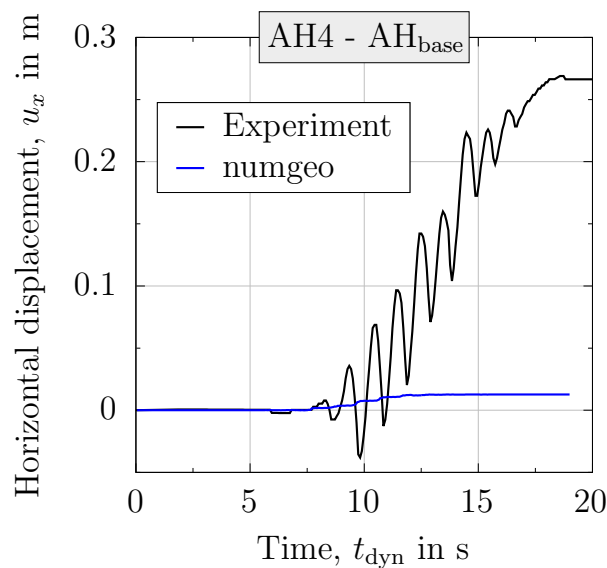


Figure 8.15: Comparison of horizontal displacements obtained from `numgeo` with back-calculated data from the experiment (Kutter et al., 2020)

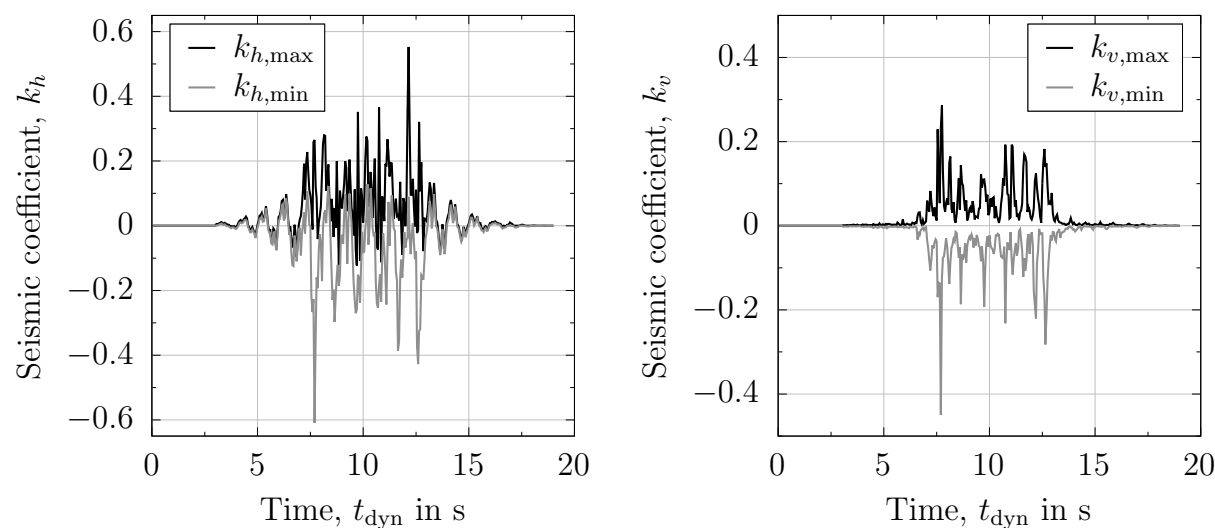


Figure 8.16: Peak (min/max) seismic coefficients in the soil domain during dynamic loading of the LEAP model

dynamic loading. The time histories of the maximum horizontal and vertical seismic coefficients are depicted in Fig. 8.16. While the input seismic coefficients (Fig. 8.12) and the peak horizontal and vertical seismic coefficients in the soil domain (Fig. 8.16) are similar, larger seismic coefficients are obtained in the soil domain compared to the input signal. This is due to amplification of the accelerations in the soil domain and reflections at the top surface and the model boundaries. Overall, an amplification of about 50% to 100% is seen for k_h , while large vertical seismic coefficients are obtained as well, with peak values ranging up to $k_{v,\min/\max} \approx 0.3$. Note that spikes with even larger magnitudes are observed for k_h as well as for k_v .

8.3.2. Assessment of seismic slope stability

Spatial pseudo-static analysis using LEM

Similar to the assessment of the seismic slope stability of the VELACS model based on LEM, stability analyses based on LEM are conducted using an equivalent Mohr-Coulomb friction angle (Griffiths and Huang, 2009; Jiang and Wang, 2011) of $\varphi = 35.81^\circ$ to compensate effects related to differences between the Mohr-Coulomb and Matsuoka-Nakai surfaces and a distributed load of 1 kPa acting perpendicular to the slope. Moreover, rough estimates of the FoS are determined considering homogeneous seismic coefficients for the entire soil domain with the magnitude determined as a portion of the peak values

of the dynamic input signal (Hynes-Griffin and Franklin, 1984; Kramer and Smith, 1997; Hleibieh and Herle, 2019a). For the LEAP model, applying $k_h = 0.125$ (Hynes-Griffin and Franklin, 1984; Kramer and Smith, 1997) and $k_h = 0.149$ and $k_v = 0.05$ (Hleibieh and Herle, 2019a) in a PSA with LEM (Bishop) using `geoSlice` yields $\text{FoS} = 2.42$ and $\text{FoS} = 1.96$, respectively. Thus, the LEAP model is classified stable in both cases, though spatial and temporal distribution of the accelerations are not taken into consideration and excess pore water pressures are neglected.

To analyze the LEAP model in terms of the evolution of the slope stability during dynamic loading, spatial pseudo-static analyses with LEM introduced in Section 6.2 are conducted. With time increments of $\Delta t = 0.05$ s, 380 stability analyses are performed in total. Spatial distributions of seismic coefficients and excess pore water pressures are accounted for using three nodes for interpolation. Horizontal seismic coefficients (inertial forces) are always considered acting in the direction of the driving forces and vertical seismic coefficients are varied to automatically determine the critical direction. The full time series is investigated four times to analyze the impact of excess pore water pressures and the optimization concept, where the latter refers to differences in the horizontal expansion of the slip surface, which is free in the first case ('global optimization') and restricted to the maximum size for the second case ('fixed entry/exit points'), as emphasized in Fig. 8.17.

The results of the spatial pseudo-static analyses using LEM are depicted in Fig. 8.18 in terms of FoS versus dynamic time for analyses with and without Δp^w as well as the two optimization concepts. Analyzing the stability under static conditions (at $t_{\text{dyn}} = 0.0$ s), it can be seen that the stability of the slope is $\text{FoS} = 9.4$. As soon as the dynamic excitation starts and the shear waves approach the ground surface, a significant reduction of the FoS is observed. Note that due to the oscillations of the input signal, the FoS undergoes rapid changes, though, an almost monotonously decreasing trend of the FoS is observed for $3.0 \text{ s} \leq t_{\text{dyn}} \leq 7.2 \text{ s}$. As seismic coefficients decrease after the peak dynamic loading (e.g. for $8.0 \leq t_{\text{dyn}} \leq 13.0 \text{ s}$), corresponding inertial forces to be considered in LEM decrease as

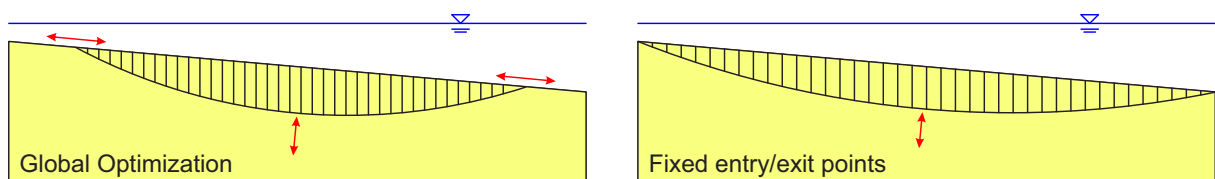


Figure 8.17: Schematic illustration of two optimization concepts used for the assessment of the FoS via spatial pseudo-static analysis using LEM

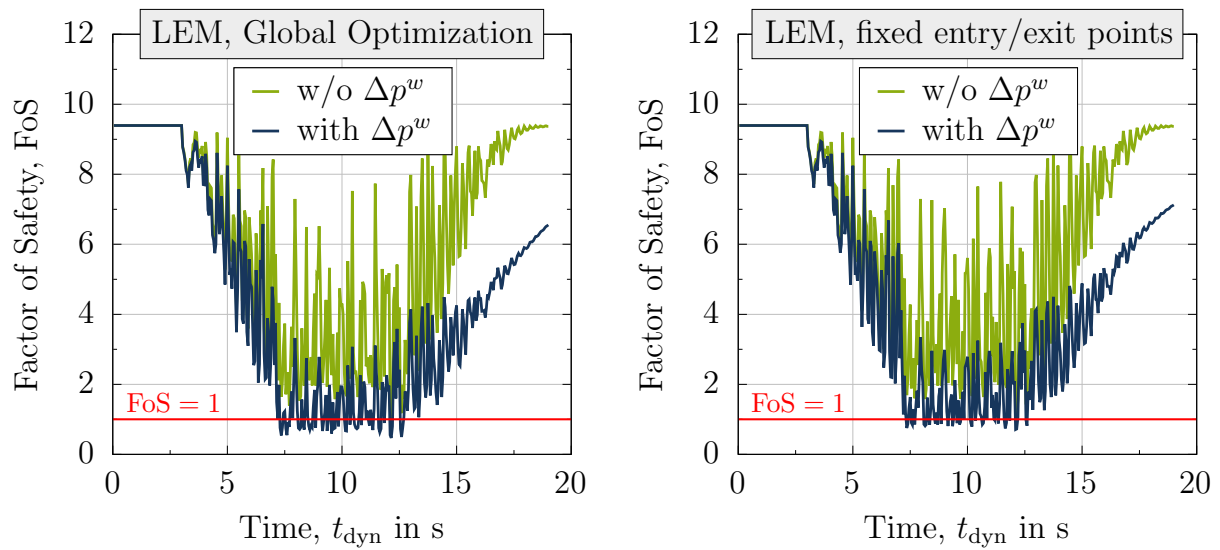


Figure 8.18: Impact of excess pore water pressures and optimization concept on the FoS for the LEAP model based on spatial PSA+LEM considering time increments of $\Delta t = 0.05$ s

well, leading to increasing FoS values. At the end of the test, at $t_{\text{dyn}} = 19$ s, accelerations have vanished (Fig. 8.13), which results in FoS values similar to the static case.

Due to the accumulation of excess pore water pressures (Fig. 8.14), the model is further destabilized by decreasing effective stresses. In addition, a delay in the increase of the FoS can be seen after the peak dynamic loading when comparing analyses with and without Δp^w . This can be explained by slowly dissipating excess pore water pressures still present at $t_{\text{dyn}} = 19$ s. Considering the two optimization concepts under investigation, it is apparent from Fig. 8.18 that slightly smaller FoS values are obtained in case entry and exit points of the slip surface are varied in addition to the radius. However, the general trend is very similar for both cases, which allows to state that a proper consideration of spatial distributions of accelerations/seismic coefficients and excess pore water pressures is of higher importance.

With regard to the initial analyses based on homogeneously distributed seismic coefficients, it should be noted that the predicted factors of safety (FoS = 2.42 and FoS = 1.96) can be considered reasonable estimates for cases where no accumulated excess pore water pressures Δp^w are to be expected. However, as the consideration of Δp^w leads to a decisive reduction of the slope stability with FoS < 1.0 for short terms, this effect should not be neglected. Still, as the FoS only indicates an unstable state for a short period of time, small permanent displacements are to be expected, which is in line with the displacements

observed in the numerical simulation but in contrast to the displacements obtained from the experiment (Kutter et al., 2020).

Strain-dependent slope stability for earthquake loading

To assess the stability of the LEAP model considering an advanced constitutive model as well as an accurate spatial distribution of the effective stress state and the state variables, the SDSS described in Section 2.1.6 and Section 6.4 is utilized. Similar to the DFEA, the hypoplastic model in the version of von Wolffersdorff (1996) is applied, however, in line with the discussions in Section 6.4, intergranular strain (IGS) (Niemunis and Herle, 1997) is deactivated in the element tests to avoid overestimation of the shear stresses and the FoS. For this reason, in addition to the stress tensor only the void ratio is transferred from the DFEA model to the element test simulations. SDSS is conducted in terms of direct simple shear (DSS) tests for 15 nodes along a potential slip surface, where the stress tensor at each node is rotated onto the slip surface before the DSS test is performed. Evaluation of the global mobilized shear resistance ratio $T(\gamma)$ is conducted in accordance with Eq. 6.11, where the summation of the shear stress versus shear strain curves is normalized by the sum of the initial shear stresses at $t_{\text{dyn}} = 0.0\text{ s}$, which resembles the static equilibrium. The FoS curve is obtained in accordance with the descriptions in Section 2.1.6. Similar to the seismic slope stability analyses conducted for the opencast slope and the VELACS model using SDSS (Section 7.3.3 and Section 8.2.2), slope stability is assessed in terms of FoS_{max} . As the computational costs associated with SDSS are significantly larger compared to LEM, stability analyses are conducted for time increments of $\Delta t = 0.25\text{ s}$, resulting in 77 analyses.

The results of the analyses applying SDSS are presented in Fig. 8.19 in terms of the factor of safety versus dynamic time. It is apparent from this figure that the safety of the slope is very large initially but a decisive decrease for $3\text{ s} \leq t_{\text{dyn}} \leq 7.5\text{ s}$ down to $\text{FoS} \approx 3.4$ is observed. Within the following four seconds the slope stability varies between $\text{FoS} \approx 3.2$ and $\text{FoS} \approx 5.0$, until it increases again. For $t_{\text{dyn}} \geq 15\text{ s}$ up to the end of the test, a steady increase of the FoS is observed, which can be attributed to dissipating excess pore water pressures and increasing effective stress levels. Note that decreasing accelerations do not have a direct impact on the SDSS as only the effective stress state and the void ratio are considered. In general, it can be stated that the evaluation of the seismic slope stability based on the concept of strain-dependent slope stability indicates that the LEAP centrifuge model test shows a decisive reduction in the FoS but does not reach a state of failure.

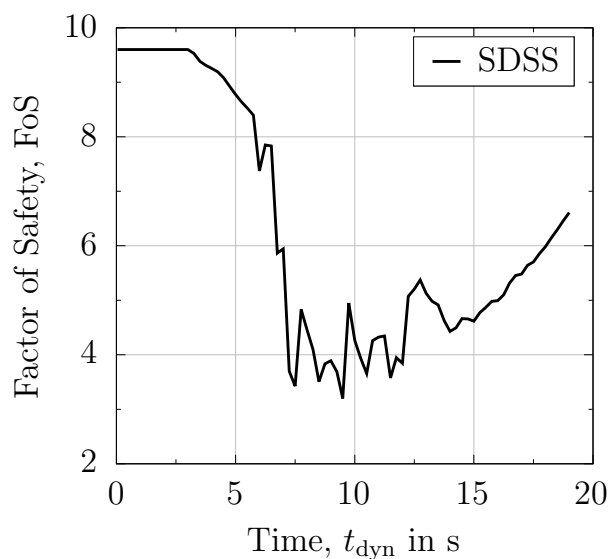


Figure 8.19: Evaluation of the FoS for the LEAP model based on SDSS considering time increments of $\Delta t = 0.25$ s

Spatial pseudo-static analysis using SRFEA

To evaluate the evolution of the FoS based on the spatial pseudo-static analysis using SRFEA, DFEA and SRFEA were conducted using submodel analyses. For the SRFEA, the current stress state, (excess) pore water pressures and inertial forces are transferred from the DFEA to the SRFEA. During the SRFEA, (excess) pore water pressures and inertial forces remain unchanged. The material behavior is described using the Matsuoka-Nakai model with the friction angle chosen to be identical to the critical friction angle (Tab. 8.2). SRFEA is performed for time intervals of $\Delta t = 0.05$ s considering an initial factor of safety of $\text{FoS}_0 = 0.5$ and an incremental increase of $\Delta \text{FoS} = 0.01$. The critical FoS was obtained based on a sudden change in the FoS versus displacement plot with displacements displayed in logarithmic scale, following the approach discussed in Section 5.2. SRFEA was started at a value of $\text{FoS} = 0.5$ to avoid unrealistically large friction angles. As $\text{FoS} = 0.5$ was chosen as lower bound, $\text{FoS} = 0.5$ would also be reported for cases where the actual slope stability based on SRFEA might be smaller and equilibrium could not even be obtained for a friction angle of $\varphi = \arctan[\tan(\varphi_c)/0.5] = 51.3^\circ$.

The results of the SRFEA are presented in Fig. 8.20 in terms of the FoS versus dynamic time, where inertial forces (denoted in the plot as nodal dynamic forces, NDF) are considered in one case and neglected in the other case. Focusing on the initial FoS, in both cases SRFEA yields $\text{FoS} \approx 9.4$, which is similar to the one obtained using LEM. During the dynamic loading for $3.5 \text{ s} \leq t \leq 7.9 \text{ s}$, the evolution of the FoS is characterized

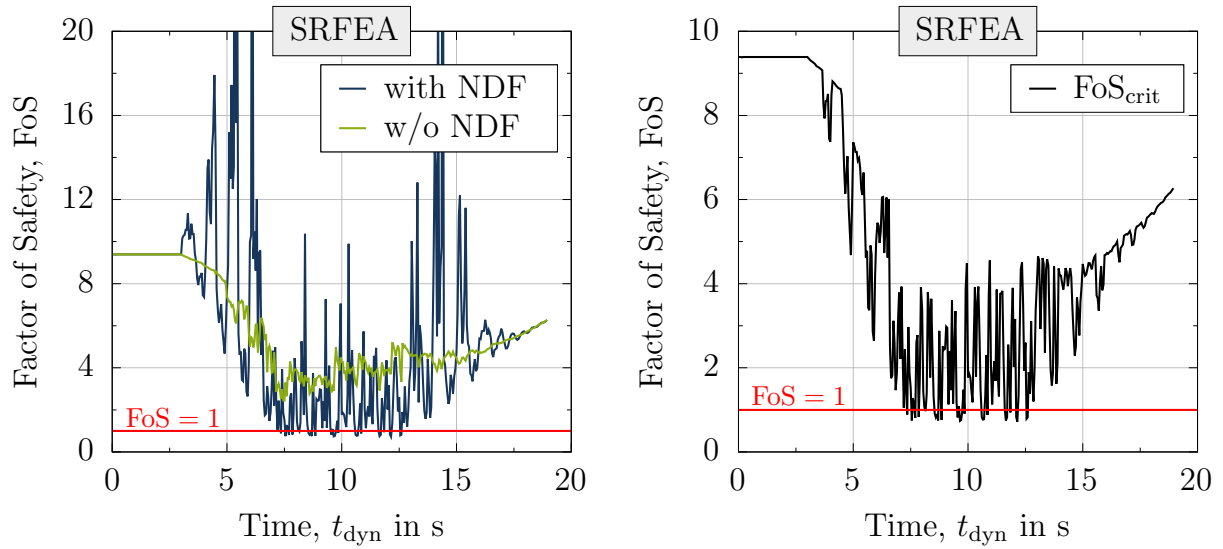


Figure 8.20: Evaluation of the FoS for the LEAP model based on SRFEA considering time increments of $\Delta t = 0.05$ s

by high frequency oscillations in accordance with the dynamic signal. Note that there are significant differences between FoS values obtained with and without consideration of inertial forces, where the former also yields $\text{FoS} \geq 20$ for a few time steps, whereas the latter shows an almost steady decreasing trend of the FoS. Further elaboration of these large FoS values when considering inertial forces is provided in the following paragraph. Considering the critical FoS displayed in the right subplot, for $t \leq 12.5$ s, oscillations of the slope stability in the range of $0.7 \leq \text{FoS} \leq 4.6$ are observed, while the mean value remains almost constant at $\overline{\text{FoS}} \approx 2.5$. For $t \geq 12.5$ s, an increasing trend of the FoS is observed with the magnitude of oscillations decreasing in line with the dynamic input signal. Note that the continuous increase in the FoS is a result of vanishing inertial forces and increasing effective stresses, the latter related to the dissipation of excess pore water pressures. In general, the LEAP model can be classified as stable for (almost) the entire time span, where only for very short time spans $\text{FoS} \leq 1.0$ is obtained.

In contrast to the boundary value problems (opencast slope, VELACS model) investigated with SRFEA in Sections 7.3.4 and 8.2.2, very large FoS values are frequently obtained for the LEAP model when considering inertial forces. To illustrate this case, two time steps at $t_{\text{dyn}} = 4.9$ s and $t_{\text{dyn}} = 5.45$ s are investigated in more detail. SRFEA with consideration of inertial forces yields $\text{FoS} = 4.68$ and $\text{FoS} = 22.36$, while LEM yields $\text{FoS} = 4.85$ and $\text{FoS} = 4.78$ for both time steps, respectively. The reason for very large FoS values obtained with SRFEA in this case can be attributed to horizontal inertial forces, which are primarily directed in stabilizing direction. As the stabilizing effect of the inertial

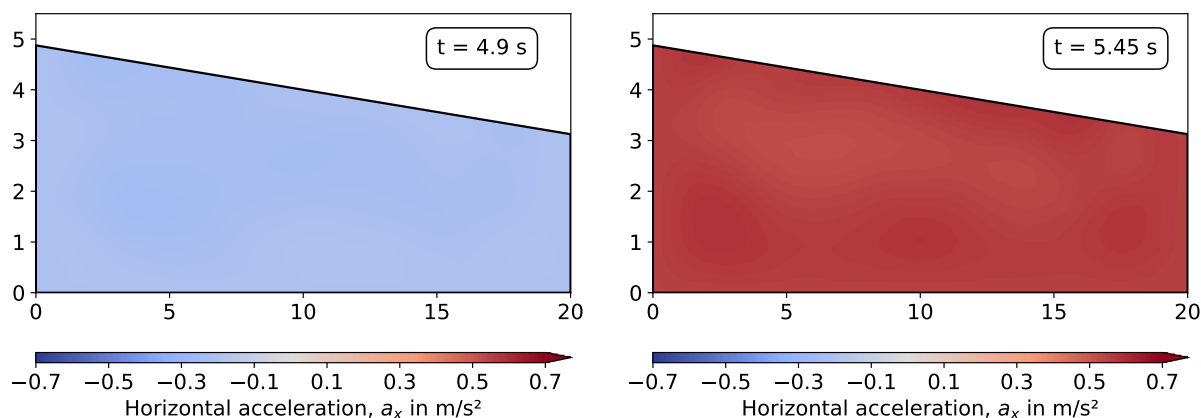


Figure 8.21: Distribution of horizontal accelerations at two different time steps during the dynamic excitation

forces is almost large enough to keep the system in equilibrium with no contribution of resisting frictional forces, due to a slope inclination which is very small ($\beta = 5^\circ$), the FoS during the strength reduction procedure can be increased up to very large values without a significant accumulation of displacements and development of a failure surface. To further emphasize the differences in the two time steps under investigation, the spatial distributions of accelerations for $t_{\text{dyn}} = 4.9\text{ s}$ and $t_{\text{dyn}} = 5.45\text{ s}$ are depicted in Fig. 8.21. It can be seen from this figure that accelerations are directed in negative horizontal direction for $t_{\text{dyn}} = 4.9\text{ s}$ and in positive horizontal direction for $t_{\text{dyn}} = 5.45\text{ s}$. As inertial forces act in opposite direction of the accelerations, inertial forces act in driving direction in the former case and in stabilizing direction in the latter case. Thus in SRFEA, consideration of inertial forces leads to a reduction of FoS at $t_{\text{dyn}} = 4.9\text{ s}$, but to an increase in FoS at $t_{\text{dyn}} = 5.45\text{ s}$. This explanation is also in good agreement with the results of an LEM analysis at $t_{\text{dyn}} = 5.45\text{ s}$ considering inertial forces in stabilizing direction, which led to FoS = 27.2 instead of FoS = 4.78 considering inertial forces directed in driving direction.

Discussion

To evaluate the results obtained using LEM, SDSS and SRFEA, the evolution of the FoS during the dynamic loading, individually plotted in Figs. 8.18, 8.19 and 8.20, respectively, is summarized in Fig. 8.22. Very good agreement of the FoS obtained with all three approaches is observed at the start and the end of the test. Considering the overall evolution of the FoS, it is apparent from Fig. 8.22 that all approaches show a decisive decrease of the FoS until $t \approx 7.0\text{ s}$, which agrees well with the time at which the amplitude of the dynamic signal increased to about $k_h \approx 0.2$ for the first time. For $7.0\text{ s} \leq t \leq 12.5\text{ s}$,

the FoS (in case of SDSS) or the mean value of the FoS (in case of LEM and SRFEA) is almost constant and increases thereafter as a result of small to negligible accelerations and dissipation of excess pore water pressures Δp^w . Note that the initial FoS is not fully recovered at $t = 19.0$ s as $\Delta p^w \geq 0$ kPa in the model. In general, decisive oscillations of the FoS are observed in LEM and SRFEA, resulting from the high frequency input signal. Note that oscillations of the FoS with smaller amplitudes are obtained with LEM in comparison to SRFEA. A potential reason for this can be given with regard to the direction of inertial forces in LEM that are always oriented in driving direction. In SDSS, oscillations with smaller frequencies are observed. This may be due to larger time intervals investigated as well as due to neglecting inertial forces that change rapidly during the seismic excitation. Overall, LEM and SRFEA show a pronounced decrease in the FoS as soon as the dynamic signal reaches the slope, whereas SDSS predicts a delayed reduction in the FoS. Moreover, it is noteworthy that only LEM classifies the LEAP model as unstable for a short period of time, whereas SRFEA only predicts a few spikes with $\text{FoS} \leq 1.0$ and SDSS classifies the slope as stable.

Considering the discussion about the approaches with regard to the stability of the VELACS model, similar conclusions can be drawn for the LEAP centrifuge model test. As inertial forces are always directed in driving direction, the LEM approach yields slightly conservative estimates of the FoS. SDSS and SRFEA consider accurate stress distributions as obtained from DFEA and make use of the Matsuoka-Nakai surface to describe the soil's shear strength, which is more accurate compared to the concept of the equivalent Mohr-Coulomb friction angle (Griffiths and Huang, 2009; Jiang and Wang, 2011). As the

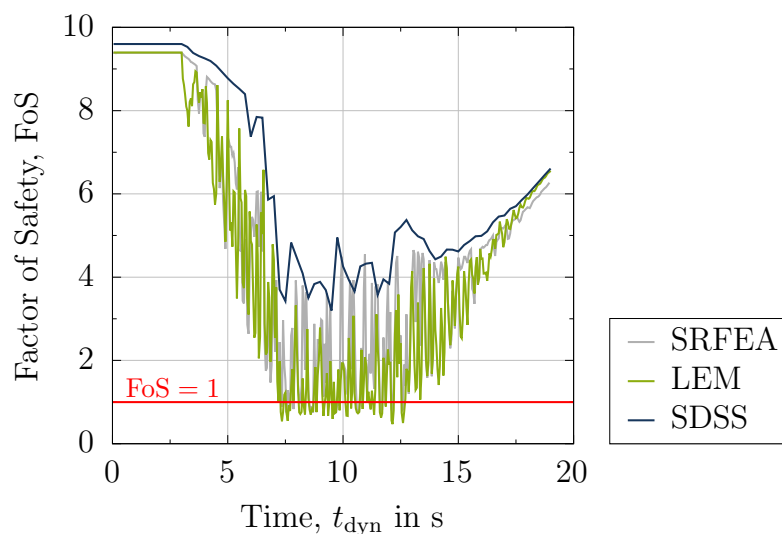


Figure 8.22: Comparison of the FoS of the LEAP model based on LEM, SDSS and SRFEA

dynamic input signal is characterized by rapid changes of the acceleration, it is expected that the time history of the FoS shows similar tendencies, though, the magnitude of the oscillations can be questioned. Following pseudo-static approaches, larger oscillations as a result of the consideration of inertial forces are seen, whereas significantly less oscillations are observed for SDSS that uses the current stress state and the state variables to determine slope stability rather than inertial forces.

9. Enhanced strain-dependent slope stability using machine learning

9.1. Motivation

In the SDSS approach, the search for the critical slip surface requires evaluation of element tests for many potential slip surfaces each with multiple points along the slip surface. Depending on the optimization scheme chosen for this search and the desired accuracy for identifying the critical location of the slip surface, 10,000 to 100,000 element test simulations may be a realistic choice. Assuming that a single element test simulation takes 1.5 seconds, which is an optimistic estimate, the total evaluation time for a single time step considering the number of element tests given above would be 4.17 hours to 1.74 days, respectively. As a single element test simulation does not fully exploit the CPU, in a first attempt multiple element test simulations have been started in parallel. In fact, parallel simulation of element tests reduces computational time required for a single element test to approximately 0.5 seconds. However, the number of element tests performed within a parallel scheme can not be increased too much as the efficiency reduces if too many parallel simulations are performed.

Taking into consideration that the evolution of the shear stress during a simple shear test (Fig. 6.12) for a given hypoplastic parameter set is only dependent on the current stress state and the additional state variables (void ratio, intergranular strain tensor), the idea is to use machine learning techniques and train a machine learning algorithm to mimic the actual simulation of an element test. Considering the general concept of the strain-dependent slope stability, application of machine learning is utilized according to the general procedure depicted in Fig. 9.1. Reducing the additional state variables to be considered in this approach to the void ratio based on the discussion given in Section 6.4.4, the number of input parameters for the machine learning process reduces to five parameters: the normal stresses $\sigma_{\bar{x}\bar{x}}$, $\sigma_{\bar{y}\bar{y}}$ and $\sigma_{\bar{z}\bar{z}}$ and the shear stress $\tau_{\bar{x}\bar{y}}$ in the rotated configuration and the void ratio e . It should be noted that further reduction of the number

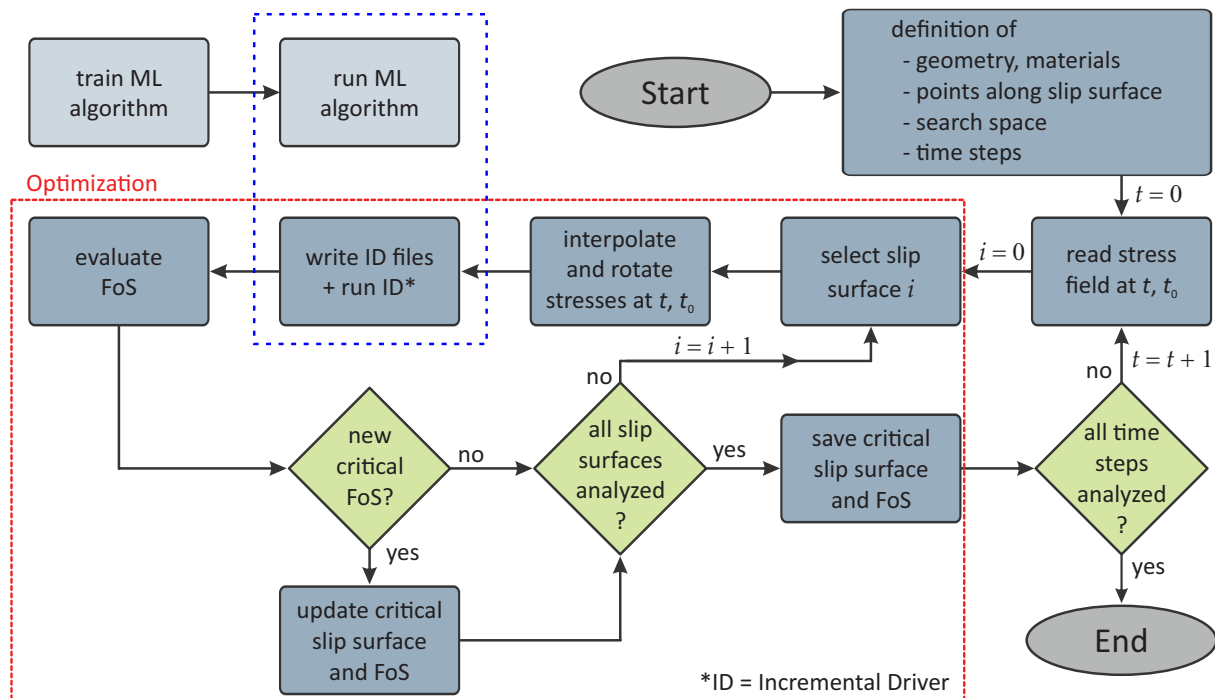


Figure 9.1: Flow chart depicting the general concept of SDSS with ML algorithms

of input parameters could be considered by identification of the most relevant input parameters beforehand. This can be achieved by local and global sensitivity analyses, as discussed for instance in Saltelli et al. (2008), Zhao et al. (2019) and Schmüdderich et al. (2020c). Note that the applicability of the approach is demonstrated for the saturated opencast mine slope subjected to seismic loading investigated in Chapter 7 with the only difference that the `nlgeom`¹ feature was not active.

9.2. Sampling strategy

To train a machine learning algorithm for the problem at hand, sampling of training data including definition of parameter ranges and constraints is of high importance. To define parameter ranges for the sampling, evaluation of representative input parameter combinations based on the sloping area of the finite element slope model is conducted. Collecting information from the slope model (e.g. stress states and multiple rotations of it together with the void ratio), a data base composed of 7.3×10^6 unique input parameter

¹`nlgeom` is an optional feature in `numgeo` to consider non-linear geometrics. The current configuration is used for the determination of all quantities and integration is carried out in the deformed state.

sets is obtained. Projecting this data onto 2D planes, convex hulls² of representative combinations can be examined for each combination of input parameters (e.g. $\sigma_{\bar{x}\bar{x}} - \sigma_{\bar{y}\bar{y}}$ or $\tau_{\bar{x}\bar{y}} - e$), yielding convex hulls for 10 different 2D projections in total. These hulls, as exemplarily shown together with a subset ($\approx 3 - 4\%$) of the data points in Fig. 9.2, are further elaborated as constraints within the sampling process.

In general, a sampling method needs to ensure that samples are well-distributed over the input parameter space, keeping a minimum distance between individual samples to avoid potential singularities in the machine learning algorithm. Among many others, popular

²Projections including the void ratio e have been approximated by concave hulls as depicted in Fig. 9.2(d).

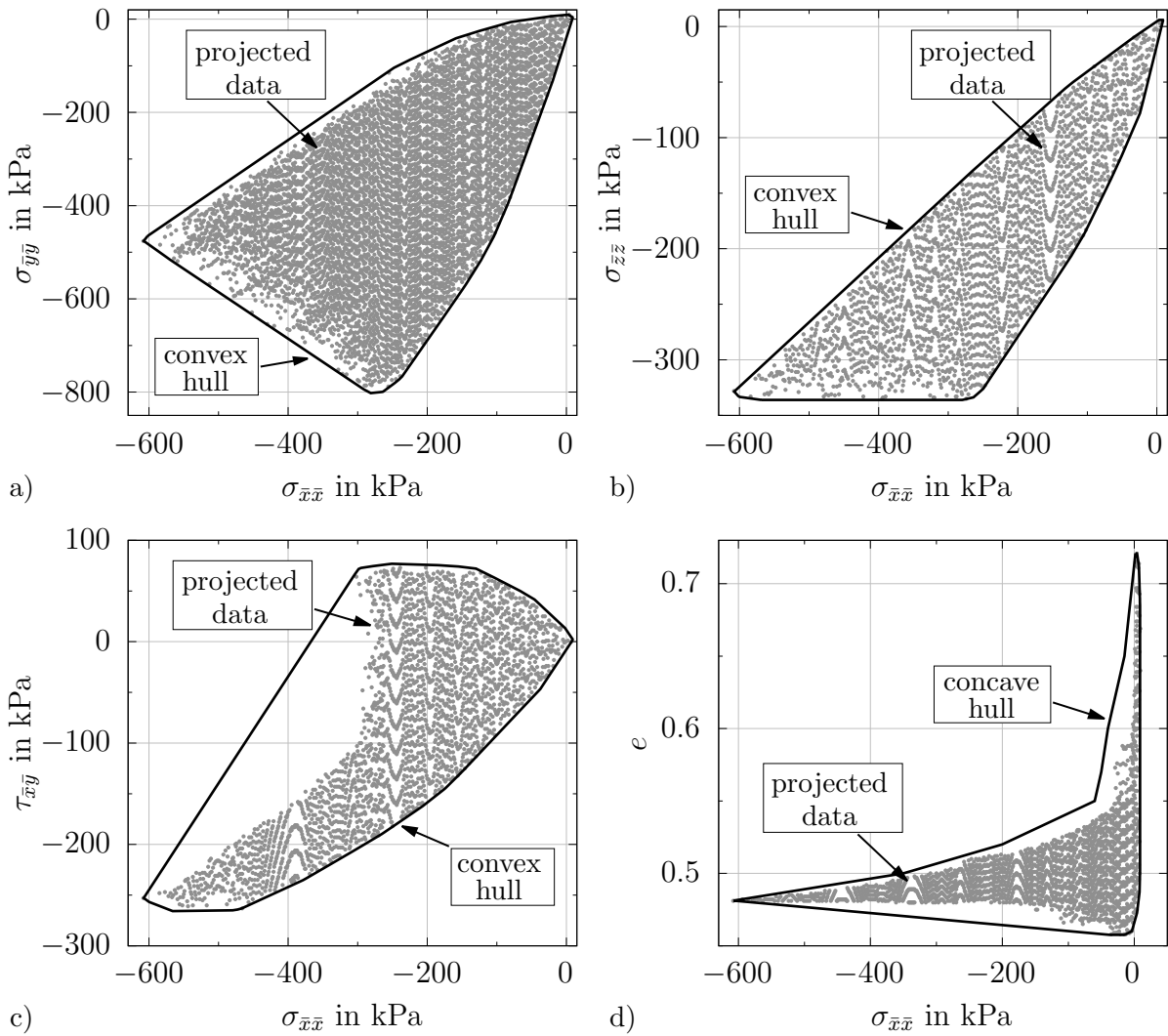


Figure 9.2: Representation of a subset ($\approx 3 - 4\%$) of the analyzed data and 2D projection hulls for (a) $\sigma_{\bar{x}\bar{x}} - \sigma_{\bar{y}\bar{y}}$, (b) $\sigma_{\bar{x}\bar{x}} - \sigma_{\bar{z}\bar{z}}$, (c) $\sigma_{\bar{x}\bar{x}} - \tau_{\bar{x}\bar{y}}$ and (d) $\sigma_{\bar{x}\bar{x}} - e$ planes

sampling methods are uniform or grid sampling, Latin hypercube sampling (McKay et al., 2000), Hammersley sequence sampling (Kalagnanam and Diwekar, 1997) and Monte Carlo sampling (Metropolis and Ulam, 1949). In this study, a modified grid sampling approach with approximately 2.4×10^7 initially generated samples is chosen utilizing quadratic spacing for normal stress-related input parameters and linear spacing for the shear stress and void ratio parameter. Taking into account the constraints defined above in terms of the 2D projection hulls and allowing only for valid combinations in the void ratio versus mean effective stress space via Bauer's law (Bauer, 1996), 71,059 valid samples have been created as training data for the machine learning algorithms. Examples of these samples and the constraint hulls projected on four different planes are depicted in Fig. 9.3. As

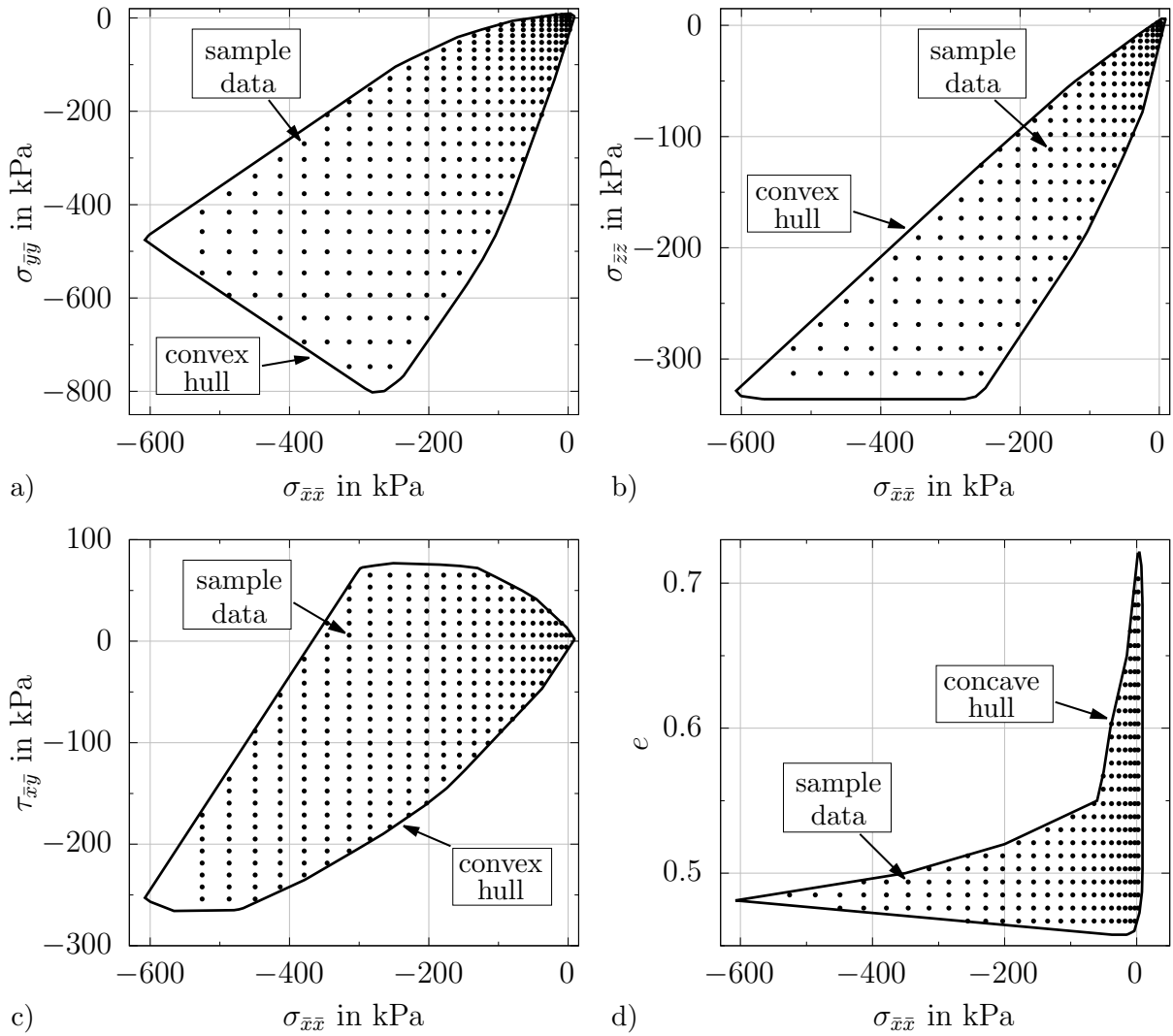


Figure 9.3: Projection hulls and sampled data for (a) $\sigma_{xx} - \sigma_{yy}$, (b) $\sigma_{xx} - \sigma_{zz}$, (c) $\sigma_{xx} - \tau_{xy}$ and (d) $\sigma_{xx} - e$ planes

can be seen from this figure, the quadratic spacing utilized for normal stress-related input variables ensures a larger proportion of samples at smaller stresses.

9.3. Replacement of simple shear tests

Utilizing the samples generated above as training data, different machine learning techniques are evaluated for case representative test data in terms of accuracy of the shear stress versus shear strain curves obtained for the simple shear test and performance with respect to the time required for training and prediction. As the machine learning algorithm has to provide proper estimates for a wide range of input parameter combinations, the challenge is to find an algorithm which is capable to handle five input parameters ($\sigma_{\bar{x}\bar{x}}$, $\sigma_{\bar{y}\bar{y}}$, $\sigma_{\bar{z}\bar{z}}$, $\tau_{\bar{x}\bar{y}}$, e) and large training data sets. The four schemes identified as most applicable for the problem investigated in this study considering the number of input parameters and the size of the training data set are Radial Basis Function (RBF) interpolation, Random Forest (RF) regression, distance weighted K-Nearest Neighbor (KNN) regression and Multi-Layer Perceptron (MLP) regression. The settings of the machine learning algorithms as applied in this study are summarized in Appendix C. As these models are well-established and have been widely used in many scientific studies, detailed explanation are not provided here but can be found elsewhere (Broomhead and Lowe, 1988; Breiman, 2001; Altman, 1992; Hinton, 1990; Hopgood, 2021). Moreover, it should be noted that the machine learning techniques applied in this study stem from the open source python libraries `scipy` (RBF) and `scikit-learn` (RF, KNN and MLP).

To investigate the accuracy of the machine learning algorithms for approximating the simple shear test, different combinations of stress states and void ratios have been selected from the slope model and predictions of the algorithms have been compared with the original response of the hypoplastic model. Typical trends for the evolution of the shear stress with increasing shear strain can be seen in Fig. 9.4. Although only a few selected test samples are depicted here, general trends can be described which hold for the majority of the samples investigated. For intermediate and large stress levels (Fig. 9.4(b) and (c)), all machine learning algorithms are capable to approximate the stress-strain behavior of the soil in a good manner, only showing small deviations for the maximum shear stress and the general trends. For small stress levels, the stress-strain behavior using the different machine learning algorithms shows less good agreement with the benchmark curve obtained using the hypoplastic model. Moreover, it is clear from Fig. 9.4(a) that the RBF model has an almost perfect fit for $\gamma = 0$ and $\gamma \geq 0.15$, whereas for many

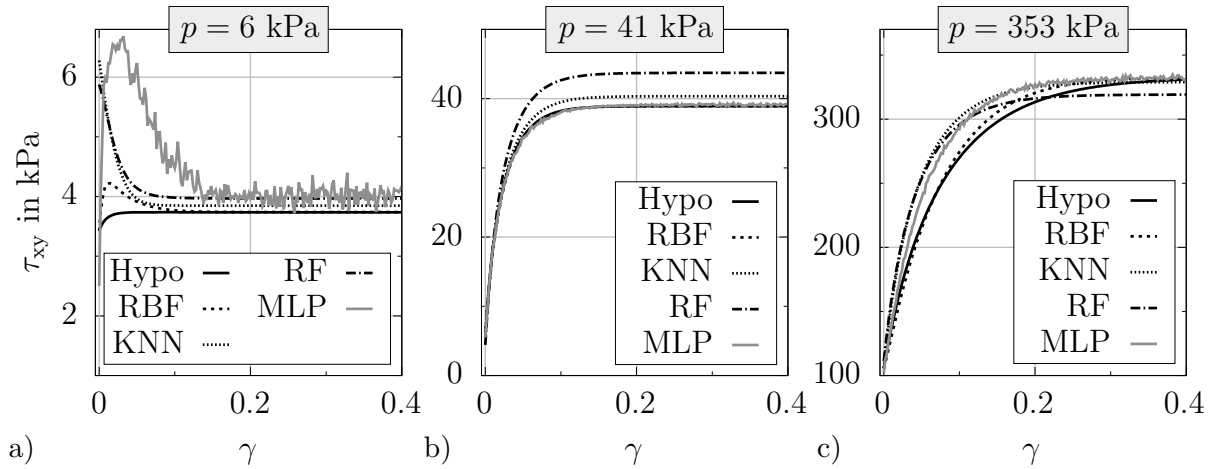


Figure 9.4: Comparison of shear stress evolution in simple shear test derived via Hypoplastic model (benchmark) and trained machine learning algorithms (RBF, RF, KNN and MLP) for test samples at different stress states

samples a peak state followed by softening down to the correct shear stress is observed. The RF and KNN models predict significantly different curve trends for $0 \leq \gamma \leq 0.1$ but yield a tolerable deviation from the benchmark curve for $\gamma > 0.1$. In general, the MLP model does not predict a smooth curve trend but shows scattering of the prediction of about 0.5 kPa which is very dominant for small stress-levels (see also Appendix C). Moreover, a peak and softening behavior is observed for small stress-levels with significant over-estimation of shear stresses for $0 \leq \gamma \leq 0.15$. Considering the relevant factors of safety to be evaluated for the slope stability problem, it can be projected from the curve trends shown in Fig. 9.4(a) that all machine learning algorithms might over-predict the maximum shear stress and, thus, also the maximum factor of safety for small stresses. For the curves depicted in Fig. 9.4 the deviation of the maximum shear stresses from the curve obtained with the hypoplastic model varies between (a) 12.98% - 75.40%, (b) 0.01% - 12.35% and (c) 0.43% - 3.57%. While the largest deviations are seen for $0 \leq \gamma \leq 0.1$, reasonably better agreement is obtained for larger shear strains and can, therefore, also be expected for the prediction of the residual factor of safety. Still, it should be emphasized that, considering the large input parameter space with stresses ranging between 0 kPa and 500 kPa, all four algorithms (RBF, RF, KNN and MLP) are capable to predict shear stresses with a tolerable deviation from the benchmark data.

To quantitatively elaborate the accuracy of the machine learning algorithms, normalized root mean squared errors $\varepsilon_{\text{NRMSE}}$ are calculated comparing the evolution of shear stresses obtained from the hypoplastic model with the predictions given by the four algorithms

under investigation. For 1000 random test samples, predictions with the RF and KNN algorithms led to $\varepsilon_{\text{NRMSE,RF/KNN}} \leq 5\%$, whereas predictions using the MLP and RBF models led to $\varepsilon_{\text{NRMSE,MLP}} \leq 2\%$ and $\varepsilon_{\text{NRMSE,RBF}} \leq 1\%$, respectively. Therefore, the evaluation of $\varepsilon_{\text{NRMSE}}$ is in good agreement with the curve trends shown in Fig. 9.4, indicating that the RBF model best resembles the benchmark simulations using the hypoplastic model. It should be noted that increasing the sample size of the training data can improve the accuracy of machine learning algorithms. However, depending on the type of algorithm, this increase will have an impact on performance, as will be discussed further in the following paragraph.

Training time for all algorithms increases approximately linearly with the size of training samples. However, the time required to train the RBF and KNN models is 2 - 3 orders of magnitude smaller compared to that of the RF and MLP models (Tab. 9.1). Furthermore, trial analyses using the algorithms investigated in this study revealed that the time required to evaluate test samples is independent of the size of the training data set. A potential explanation for the negligible effect of the training data size on the time required for test evaluation is that all models incorporate a parameter that limits the number of training data points used for the evaluation of a specific test data set. In the case of RBF and KNN, a predefined number of neighbors is defined, whereas in the RF approach a predefined number of decision trees representing the forest controls the time required for the evaluation of test samples. In MLP, training data is only used to find appropriate weighting factors and is not used for the evaluation of test data. Note that

Table 9.1: Total time required for training and test evaluation of simple shear test for different machine learning algorithms considering a training data set of $\sim 71,000$ samples

Model	training time [s]	time required [s] for evaluation of N test samples				
		$N = 10$	100	1,000	10,000	100,000
RBF*	< 0.1	~ 0.4	~ 4.7	~ 47.3	~ 495.7	
RF**	~ 310.5	~ 0.2	~ 0.3	~ 0.7	~ 6.7	~ 60.2
KNN [†]	~ 0.2	~ 0.1	~ 0.1	~ 0.2	~ 0.3	~ 2.9
MLP [‡]	~ 14.2	< 0.1	< 0.1	< 0.1	< 0.1	~ 0.4

*Radial Basis Function, **Random Forest, [†]K-Nearest Neighbor

[‡]Multi-Layer Perceptron

for the latter algorithm it is sometimes necessary to halt the training process before no further reductions in error are possible. This is because it is possible to overtrain the perceptron, causing it to become expert at producing the correct output for training data but less skilled at dealing with new data (Hopgood, 2021). However, in terms of the time required for the evaluation of test samples, the four algorithms show significantly different behavior with respect to the size of the test samples. As shown in Tab. 9.1, the time required to evaluate test samples using machine learning algorithms increases with increasing sample size; however, only for the RBF model, the increase in time is linearly proportional to the increase in test sample size. When the efficiency of the algorithms is defined as the fraction of the number of test samples and the time required for evaluation (unit: samples/s), it is observed that the efficiency increases significantly with increasing test sample sizes (except for RBF); for example, the efficiency of the RF model increases from 50.0 to 1661.1 [samples/s] for $N = 10$ and $N = 100,000$ samples, respectively.

The effect of sample size on the performance of the machine learning algorithm should be considered, taking into account the optimization process required to identify the critical slip surface for the slope stability problem. However, since more advanced optimization algorithms require the evaluation of the objective function (FoS) in order to adapt the evolution of the optimization algorithm or the optimal search space, these optimization algorithms cannot fully benefit from the increased efficiency of machine learning algorithms because evaluation is only performed for a limited number of test samples. Simple optimization schemes, on the other hand, such as a brute grid search, which does not require exchanging information about the current local or global most critical slip surface during the optimization process, can fully benefit from the increased efficiency by clearly separating data collection and test evaluation using a machine learning algorithm. Thereby, utilizing the RF, KNN or MLP model, a very fine grid search could still be faster and potentially more accurate compared to an advanced optimization algorithm. In this study, the following strategy is pursued: 1) collect all input data sets, i.e. rotated stress states and void ratios for each point along the slip surface, for every slip surface to be investigated during a brute grid search and 2) perform a single evaluation of the machine learning algorithm with all gathered test samples.

9.4. Assessment of seismic slope stability

This section assesses the accuracy of machine learning algorithms in relation to the results of the strain-dependent slope stability obtained with the hypoplastic model for the

dynamic finite element simulation discussed in Sections 7.2.1 and 7.2.2. Furthermore, the performance of the stability analyses is investigated in terms of the time required for the conventional and adopted approaches, which use element test simulation, and the approximation via the previously discussed algorithms, respectively. Training of the machine learning algorithms is performed in accordance with the sampling strategy discussed in Section 9.2. Based on the suggestions given in Section 9.3, the algorithms were trained at the beginning of the analysis and the test samples generated by a brute grid search optimization were evaluated once per time step. For each time step, about 2,000 slip surfaces each having 15 points along the slip surface ($\sim 30,000$ samples) are investigated. The results are presented in Fig. 9.5 in terms of the maximum factor of safety for the first six seconds of the dynamic loading step.

As can be seen from Fig. 9.5, the general trend of the maximum factor of safety (FoS_{\max}) with respect to the dynamic time is well captured using all algorithms under investigation. All models predict a significant drop of the factor of safety for $2.0\text{ s} \leq t_{\text{dyn}} \leq 3.0\text{ s}$ and a loss of safety, defined as a drop below unity, for $3.0\text{ s} \leq t_{\text{dyn}} \leq 4.0\text{ s}$. To further evaluate the accuracy of the predicted factors of safety, the deviations with respect to the benchmark results obtained using the hypoplastic model are considered. Analysis of the average absolute deviation yields values between $\overline{\Delta FoS_{\max}} = 0.05$ (RBF) and $\overline{\Delta FoS_{\max}} = 0.16$

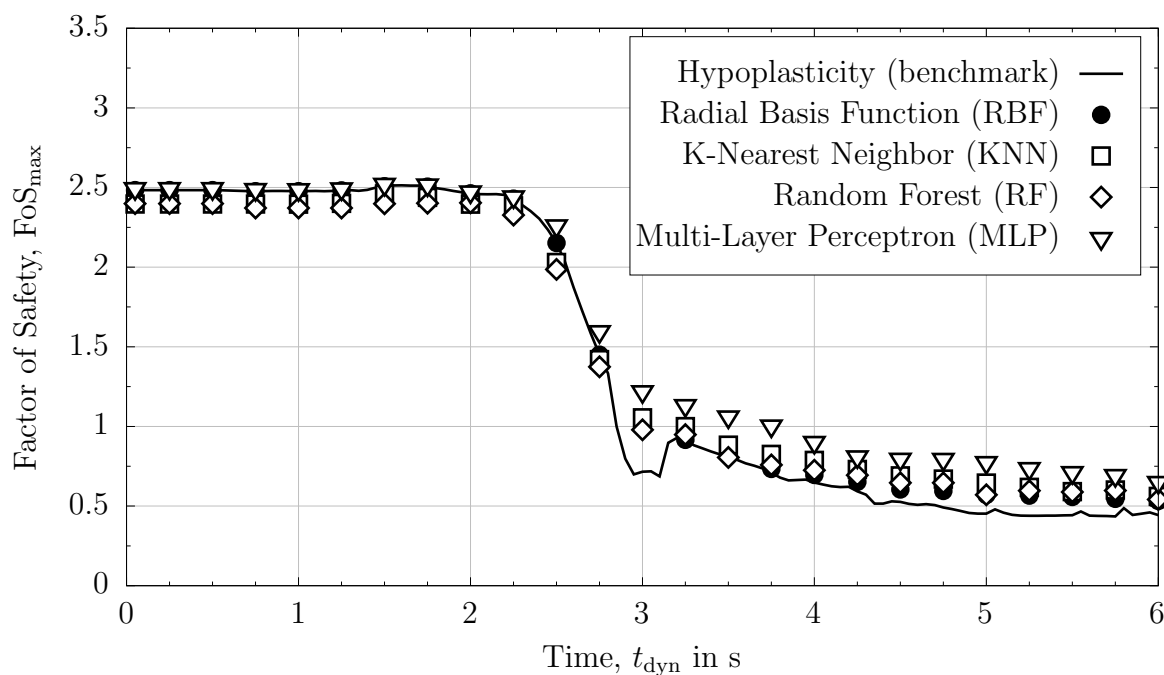


Figure 9.5: Effect of choice of machine learning algorithm on time- and strain-dependent slope stability

(MLP), whereas maximum absolute deviations obtained for $t_{\text{dyn}} = 3.0$ s are larger ranging from $\Delta_{\text{max}}\text{FoS}_{\text{max}} = 0.29$ (RBF) to $\Delta_{\text{max}}\text{FoS}_{\text{max}} = 0.51$ (MLP). Thus, the worst prediction deviates by $\Delta\text{FoS}_{\text{max}} = 0.51$ from the benchmark results. An explanation for larger deviations at $t_{\text{dyn}} \geq 3.0$ s can be given with respect to the stress states and the shape of the critical slip surfaces observed for these time steps. As described in Sections 7.2.1 and 7.2.2, excess pore water pressures are accumulated considerably during the dynamic loading phase as a result of propagating shear waves towards the surface of the slope. Effective stresses and, thereby, the shear resistance close to the ground surface tend to decrease towards zero, increasing the risk for liquefaction and large displacements. Subsequently, shallow slip surfaces become critical due to significant loss of shear strength. Given that all machine learning algorithms demonstrated less good agreement with the hypoplastic model for small stress levels with a tendency to over-predict the maximum shear stress of an individual element test, in exceptional cases greater than 75 % for very small stresses (see Section 9.3), it is interesting to note in Fig. 9.5 that this over-prediction of shear stresses at small stress levels does not affect the prediction of the factor of safety for the strain-dependent slope stability in the same way. The reason for less over-prediction of the FoS_{max} compared to the over-prediction of the shear stresses at certain points along the slip surface is the normalization which considers the shear stresses related to the static equilibrium (Eq. 6.11) which are large compared to the deviations of the shear stresses at the current time step. Still, it should be noted that further improvement of the ML predictions for SDSS can be achieved by using modified sampling approaches, as recently shown by Shakya et al. (2024). When evaluating the strain-dependent slope stability at higher strain levels (e.g. relating to FoS_{res}), it is worth noting that the hypoplastic model and the machine learning algorithms agree even more. This hypothesis is supported by the discussions in Section 9.3 and has also been verified in additional analyses that are beyond the scope of this study.

To conclude the discussions with respect to the applicability of different machine learning algorithms for the concept of strain-dependent slope stability, the performance of the simulations conducted to obtain the factor of safety (Fig. 9.5) is evaluated in terms of the time required to perform a single test, tests within a time step and the full time series (25 time steps). The results are presented in Tab. 9.2 for the hypoplastic model using serial and parallel test simulations as well as for Radial Basis Function (RBF) interpolation, Random Forest (RF) regression, distance weighted K-Nearest Neighbor (KNN) regression and Multi-Layer Perceptron (MLP) regression. As can be seen from this table, the time required to investigate the problem at hand varies strongly with the approach utilized for simulation. Thereby, results of the total time series have been obtained within several

Table 9.2: Comparison of simulations with the hypoplastic model and different machine learning algorithms in terms of the time required to evaluate the time- and strain-dependent slope stability during earthquake loading

	Hypoplasticity		Machine learning algorithm			
	serial	parallel	RBF*	RF**	KNN [†]	MLP [‡]
training	–	–	< 0.1 [s]	5.18 [min]	0.2 [s]	14.16 [s]
single test	1.561 [s]	0.474 [s]	0.0395 [s]	0.00064 [s]	0.00022 [s]	0.00019 [s]
time step	13.17 [h]	4.0 [h]	20.0 [min]	19.34 [s]	6.82 [s]	5.84 [s]
time series	13.72 [d]	4.17 [d]	8.3 [h]	8.06 [min]	2.84 [min]	2.43 [min]
Σ	13.72 [d]	4.17 [d]	8.3 [h]	13.24 [min]	2.84 [min]	2.67 [min]

*Radial Basis Function, **Random Forest, [†]K-Nearest Neighbor

[‡]Multi-Layer Perceptron

days (hypoplastic model), hours (RBF) or minutes (RF, KNN and MLP). Considering that the generation of the training data required 71,000 element test simulations using the hypoplastic model, additional 9.5 hours (0.474 s times the amount of training data samples) could be added to the total estimation time of the machine learning algorithms. However, as long as the parameter set remains unchanged, this effort is only required once. Considering the accuracy of the factors of safety determined using the different machine learning algorithm as well as the time required for evaluation, it is clear that all machine learning algorithms investigated in this study provide very good results. However, the most preferable algorithm might be RBF interpolation if the accuracy of the factor of safety is important or KNN regression if a fast but slightly less accurate evaluation is preferred.

9.5. Influence of optimization technique

The optimization via grid search was chosen up to this point to enable a fair comparison between different simulation approaches in terms of computational costs. However, as the grid search is not a very adequate optimization technique, the critical slip surface

and the corresponding factor of safety (FoS_{\max}) have only been approximated in a rough manner. To check whether a more advanced optimization algorithm enables to identify a more critical slip surface with a smaller factor of safety, additional simulations using the machine learning algorithms RBF, KNN, RF and MLP have been conducted using "Differential Evolution" (DE) (Storn and Price, 1997) as optimization technique. It should be noted here that the usage of DE prohibits evaluation of large data sets of failure surfaces at once as the evolution process during the optimization requires assessment of fitness at each mutation stage to enable mutation and recombination. Thereby, the efficiency of the machine learning algorithms is reduced and the optimization process takes more time (≈ 1 order of magnitude). The increased computational work is attributable to scaling effects of machine learning techniques as well as a higher number of simulations necessary in the DE optimization.

The results are presented in terms of a bar plot (Fig. 9.6) comparing the factor of safety (FoS_{\max}) obtained using the grid search and DE optimization approach for different time steps ($t_{\text{dyn}} = 1.0\text{ s}, 2.0\text{ s}, \dots, 6.0\text{ s}$). Although it is apparent from this figure that the general trends seen for both optimization approaches are very similar, using DE over grid search systematically yields slight improvement for $t_{\text{dyn}} \geq 3.0\text{ s}$. Interestingly, it is seen

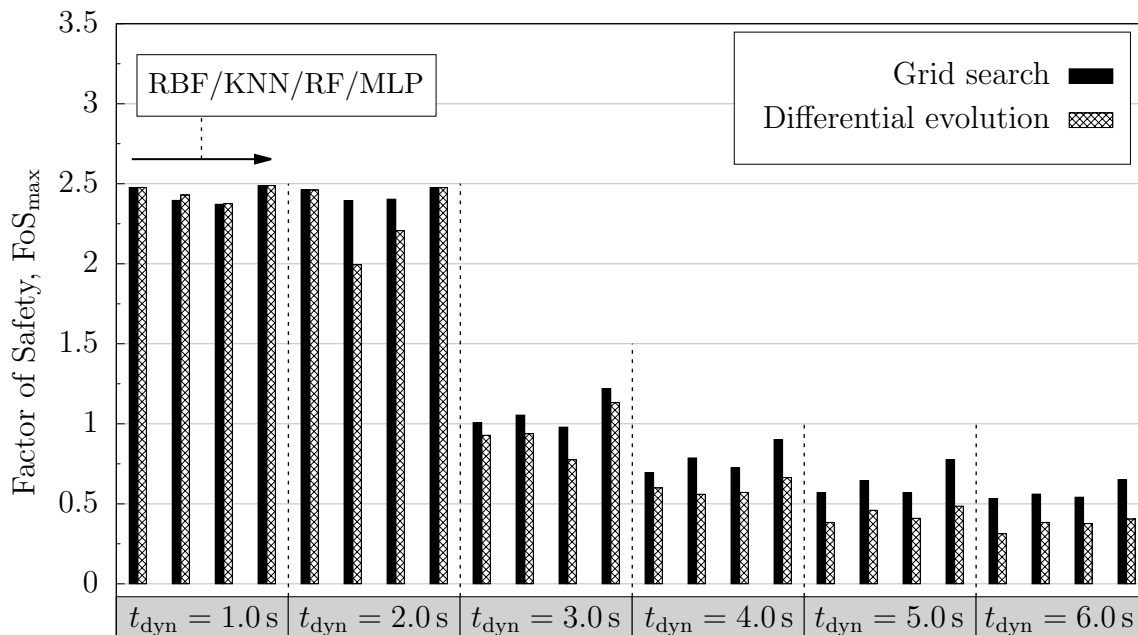


Figure 9.6: Comparison of factor of safety obtained using machine learning algorithms (RBF, KNN, RF, MLP) coupled with grid search and the DE optimization approach at different time steps

for $t_{\text{dyn}} = 1.0$ s, that DE predicts larger FoS for KNN and RF compared to the grid search. A potential explanation for this might be that the initial population within DE was not large enough or not well distributed in the parameter space. However, as this observation is only made in two cases, the general applicability and success using DE is not questioned in this study. In fact, although DE reduces the computational efficiency of the machine learning algorithms by forcing multiple evaluations of small data sets instead of a single evaluation with a large data set (when using grid search), it is recommended to combine the concept of strain-dependent slope stability with advanced optimization techniques to enhance the quality of the FoS prediction.

9.6. Evaluation of failure mechanisms

To investigate if the critical slip surfaces obtained from the analysis of the strain-dependent slope stability using the machine learning algorithms resemble failure mechanisms reasonably, slip surfaces and associated factors of safety obtained from the stability analyses are compared to displacement magnitudes identified in the slope area during the dynamic finite element simulation (Fig. 9.7). For the concept of strain-dependent slope stability and the information transferred from the dynamic finite element simulation to the element test simulations, it should be noted that displacements and shear strains are not directly considered in this approach. Thus, displacements and shear strains may also not necessarily indicate the location of the critical slip surface obtained from the stability analysis. Still, in an indirect way these factors do affect the stability analyses as the current stress state is influenced by the current strain state, the strain history and – if considered in the analysis – the intergranular strain.

Fig. 9.8 shows slip surfaces and associated factors of safety obtained from the strain-dependent slope stability analyses using the KNN algorithm coupled with the grid optimization for $t_{\text{dyn}} = 3.0$ s, 3.5 s and 6.0 s. In general, it is seen from this figure, that for all time steps the most critical slip surfaces associated with the lowest factors of safety resemble a shallow slope failure. In contrast to slip surfaces obtained for time steps at the beginning of the dynamic loading, which enter and exit close to the crest and the toe of the slope, the critical slip surfaces are significantly smaller and mostly enter and exit along the slope surface as soon as the shear waves induced by the dynamic loading reached the slope area. Comparing the spatial distribution and the temporal evolution of the slip surfaces associated with the lowest FoS_{max} values with the displacement patterns obtained from the dynamic finite element simulation, it is apparent that the area of large displace-

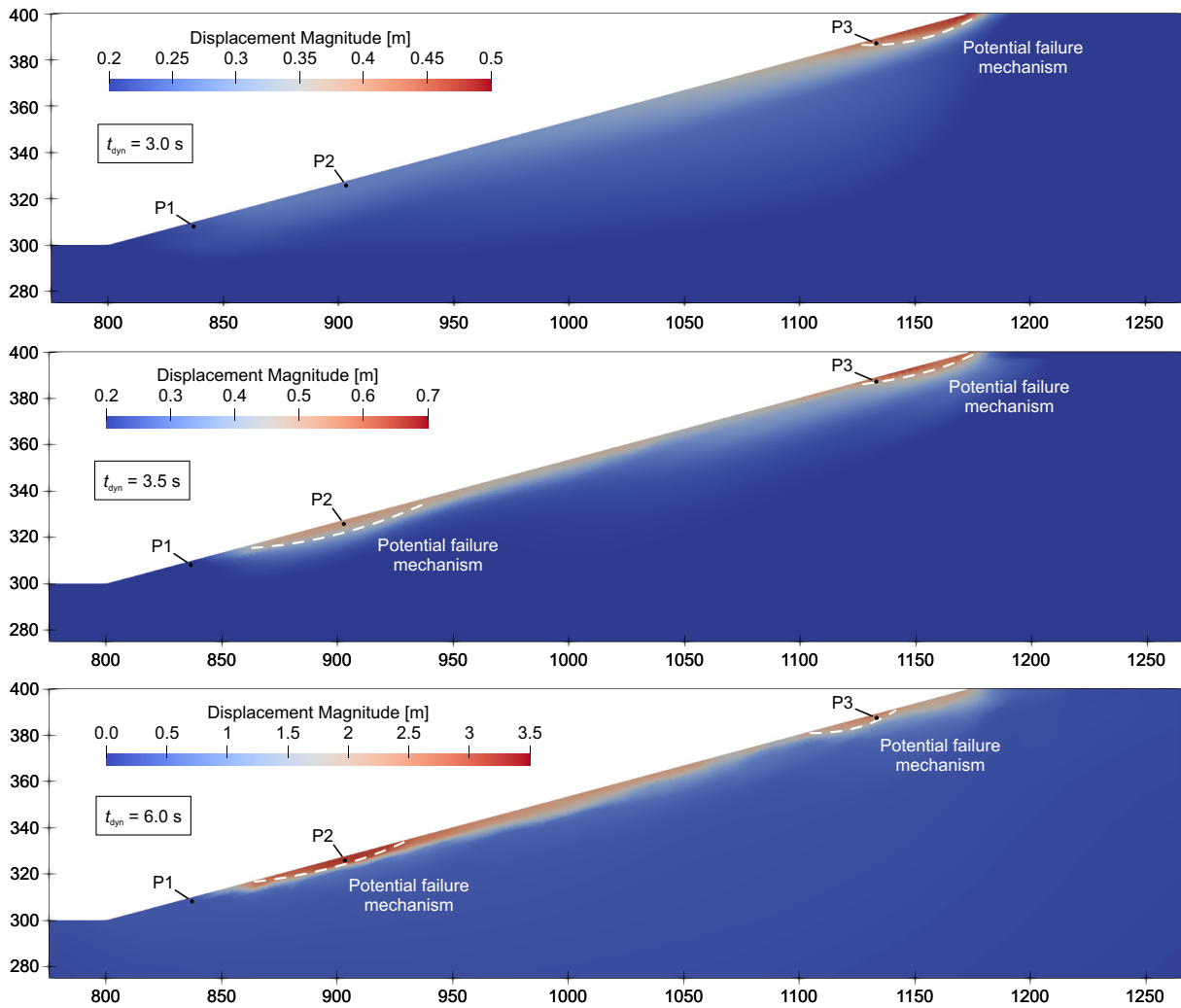


Figure 9.7: Results of the finite element simulation in terms of displacement magnitudes for different time steps during the dynamic loading phase

ments (Fig. 9.7) is well approximated by the location of the few most critical slip surfaces obtained within the stability analysis. This observation holds for $t_{\text{dyn}} = 3.0$ s where the critical area is located close to the crown of the slope as well as for $t_{\text{dyn}} = 3.5$ s and 6.0 s, where a shallow sliding body is observed that almost fully covers the slope surface. Although small factors of safety are also determined via the machine learning algorithms for slip surfaces located close to point P2, the critical slip surface is mostly located close to point P3 (Fig. 9.7). An explanation for this can be given with respect to the development of large excess pore water pressures and significant reduction of effective mean stresses at P3. As the stress level has a decisive impact on the strain-dependent slope stability, it is clear that the critical slip surface will also be located close the area with the highest reduction of effective stresses.

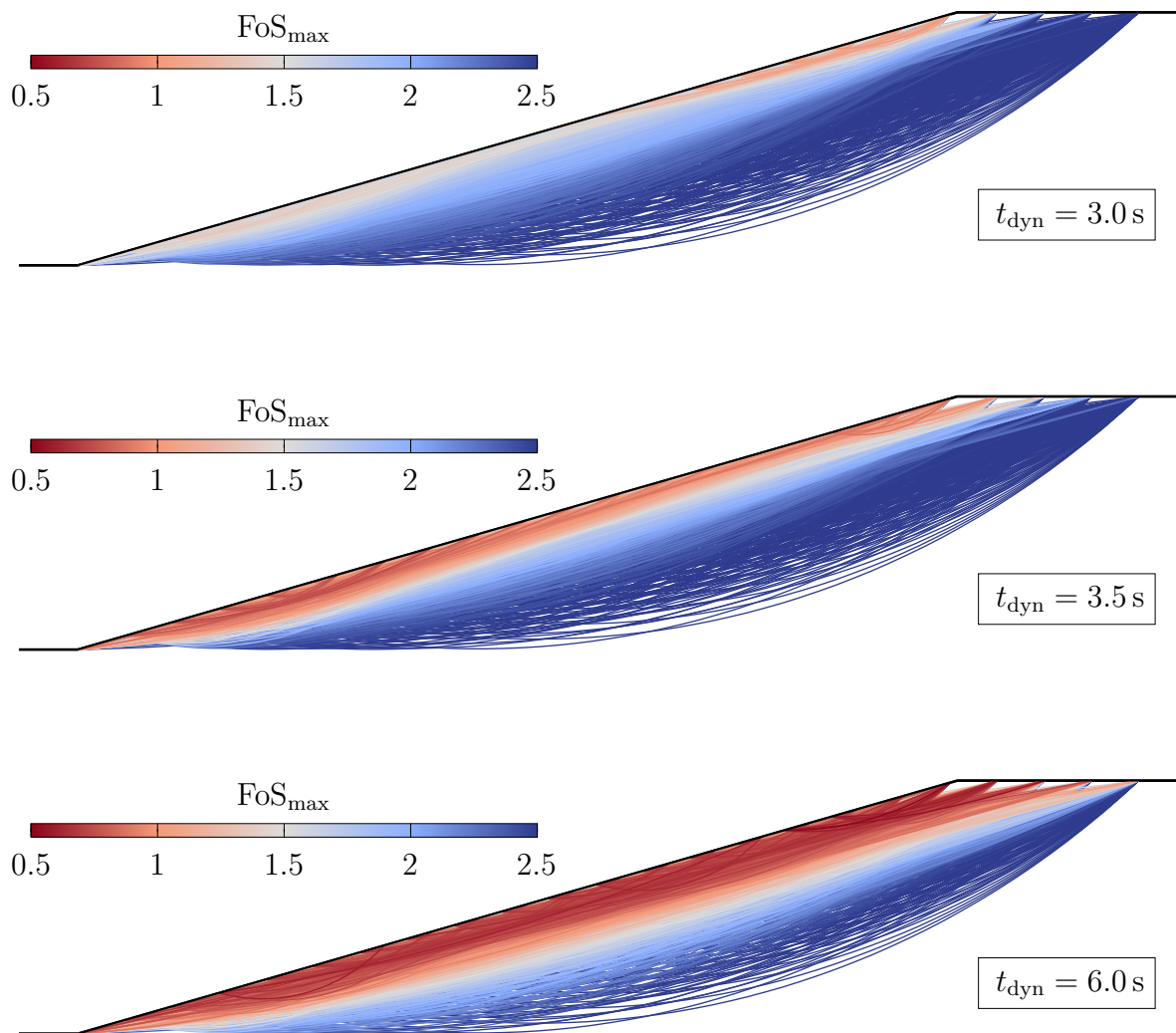


Figure 9.8: Factors of safety associated with different slip surfaces investigated using KNN algorithm for different time steps during the dynamic loading phase

10. Summary, Conclusions and Outlook

10.1. Summary

Stability analyses are used to evaluate the level of safety for slopes, earth dams or other geotechnical structures in terms of a single scalar value – the factor of safety (FoS). Considering slopes subjected to seismic loading, many assumptions are required in common stability approaches, whereby accurate incorporation of effective stresses, excess pore water pressures or accelerations is not ensured among many of them. The current thesis was motivated by the lack of sophisticated and objective approaches for seismic slope stability assessment. While this topic was assessed in preceding works based on simplified stability approaches or with the focus on deformations and liquefaction susceptibility, the present work focuses on the development of seismic slope stability approaches performed parallel or subsequent to dynamic finite element analyses, which can provide accurate spatial and temporal distributions of stresses, excess pore water pressures and accelerations during a seismic event.

The first part of this work focused on the implementation and verification of tools required for the development of approaches to assess the seismic slope stability. A new software package (`geoSlice`) for limit equilibrium analyses based on the concept of the method of slices was developed and verified via comparative analyses with well-established LEM software packages (`GGU-Stability` and `GeoStudio`). Three elastoplastic constitutive models – the Mohr-Coulomb model, the Matsuoka-Nakai model and the General Classic Plasticity model – and a strength reduction scheme were implemented in the finite element software package `numgeo`. Verification was conducted based on simulations of element tests and different boundary value problems, respectively, using benchmark data obtained with two commercial finite element software packages (`Plaxis2D` and `OptumG2`).

The second part of this work was devoted to the development of four approaches for the assessment of seismic slope stability to be applied parallel or subsequent to dynamic finite element analyses (DFEA). The `spatial pseudo-static analysis using LEM` used the

new LEM software package (*geoSlice*), which allows the consideration of spatial distributions of accelerations and accumulated excess pore water pressures in slope stability analyses. In the *cluster-based pseudo-static analysis using FELA*, slope stability analyses are conducted using *OptumG2* with seismic effects approximated in terms of spatial distributions (effective unit weight and shear strength) and clusters (accelerations). Accurate approximations of the failure surface are possible by use of adaptive mesh refinement. The concept of *strain-dependent slope stability (SDSS)* addressed slope stability analyses by determination of the FoS with regard to the response of element test simulations conducted for nodes along a potential slip surface. Changes in density (pyknosity) and confining pressure (barotropy), stress/strain history as well as accumulation of strains are considered by utilizing sophisticated constitutive models and transfer of state variables to the stability analyses. The extension of SDSS for time-dependent problems (e.g. earthquake loading) enables to evaluate FoS time histories. Utilizing the elastoplastic models and the strength reduction scheme implemented in the first part of this work, the *spatial pseudo-static analysis using SRFEA* is concerned with the determination of the FoS in *numgeo*, which was also used for the DFEA. By performing DFEA and SRFEA in the same finite element software package, accurate and automatic transfer of stresses, excess pore water pressures and inertial forces is ensured.

The third part of this work dealt with the application of the seismic slope stability approaches developed in part two of this work for boundary value problems of different scales. To investigate the applicability of the approaches for small and large models, DFEA and subsequent stability analyses were conducted for an opencast slope and two centrifuge model tests. Different effects were studied, for instance the influence of excess pore water pressures on the FoS (LEM, FELA), the orientation of inertial forces (FELA), the consideration of intergranular strain (SDSS), and details regarding the optimization process (LEM, SDSS). Comparison of results obtained from the experiments and the numerical simulations (DFEA) was conducted for both centrifuge model tests.

The last part of this work was concerned with the application of machine learning (ML) approaches within the concept of SDSS. As multiple thousand to a few million element test simulations, for instance direct simple shear (DSS) tests, are required during stability analyses, computational costs related to SDSS may be huge. Replacing these element test simulations by trained ML algorithms, computational costs were significantly reduced. Besides evaluation of accuracy and performance of ML algorithms on the element test level, SDSS with and without ML were compared for the stability assessment of the opencast mine slope subjected to seismic loading.

10.2. Conclusions

In the present work, four approaches based on LEM, FELA, SDSS and SRFEA were developed or extended to enable a more accurate assessment of the seismic slope stability. Stability analyses using all approaches are conducted parallel or subsequent to a DFEA adopted for the determination of realistic stress states and accelerations during earthquake loading. Independent of the boundary value problem under investigation (e.g. opencast mine slopes, centrifuge model tests), the following key aspects are to be noted with regard to the different approaches:

- In contrast to conventional approaches, the approaches developed in this work allow to investigate the evolution of the FoS during the dynamic loading by performing stability analyses at different times of the dynamic loading step. Thereby, slope failure can be evaluated based on the difference between the current and critical FoS, the time span for which the current FoS dropped below the critical FoS and the number of times the current FoS dropped below the critical FoS.
- LEM enables a fast estimation of the FoS during seismic loading. Contrary to conventional LEM software packages, seismic effects are taken into consideration in terms of spatial distributions of accelerations and excess pore water pressures. As inertial forces are considered to be always orientated in driving direction, LEM yields conservative estimates for the FoS. Note that commercial LEM software packages do not allow the import of the aforementioned pre-calculated seismic effects in the stability analyses, highlighting the advantages of the developed program `geoSlice`.
- The FELA approach allows to account for spatial distribution of seismic effects using mapping concepts and a division of the model in clusters. However, two shortcomings of the approach need to be emphasized here as they have counteracting impacts on the FoS. Similar to LEM, inertial forces are orientated in driving direction, while the concept of averaging of accelerations inside clusters leads to a disregard of local peak accelerations, where the former might yield a conservative estimate of the FoS and the latter might result in an overestimation of the FoS. As it is not clear a priori which effect is dominant, both need to be evaluated with regard to the boundary value problem under investigation.
- SDSS is based on the coupling of DFEA and element test simulations, where the latter allow a realistic approximation of the stress–strain behavior in potential slip surfaces by utilizing advanced constitutive models. Compared to existing method-

ologies, such as pseudo-static analyses, SDSS delivers a more comprehensive slope stability assessment during earthquake loading.

- A salient feature of the SDSS is that the same constitutive model can be applied in the dynamic and the stability analysis. This allows to incorporate important aspects of soil behavior in the stability analysis such as the influence of the current stress state, the strain history or the evolution of the soil density. Contrary to conventional approaches for the determination of the slope stability, this approach is not limited to simple elastic, ideal-plastic constitutive models but is applicable to any advanced constitutive model, such as the hypoplastic model used in this work.
- Replacement of the element test simulations required for SDSS by different machine learning algorithms provided good approximations of the actual stress–strain behavior of the soil during shearing while reducing computational costs of the overall stability analyses by 2–3 orders of magnitude.
- The SRFEA approach ensures that dynamic and safety analyses are conducted using the same software package, while the submodel feature in `numgeo` allows to automate stability analyses for multiple time steps during a seismic event. Due to the former, accurate transfer of total and effective stresses is enabled. Inertial forces are orientated in line with the DFEA to ensure static equilibrium in the stability analyses. During a stability analysis, the spatial distributions of inertial forces and excess pore water pressures remain constant. Note that different constitutive models are required for the dynamic and the stability analyses, for instance Hypoplasticity with Intergranular Strain and Matsuoka-Nakai for the former and latter, respectively.

Stability analyses using the approaches developed in the present work were applied to three boundary value problems subjected to seismic loading: a synthetic large opencast mine slope and two real case centrifuge model tests performed in the framework of the VELACS and LEAP projects. These boundary value problems were chosen to demonstrate the applicability of the developed stability approaches, to discuss the advantages and drawbacks as well as implicit assumptions of the approaches and to evaluate the computational costs associated with the approaches. Based on the assessment of the seismic slope stability applying LEM, FELA, SDSS, and SRFEA, the following conclusions can be drawn:

- Investigation of the slope stability of a large opencast mine slope subjected to earthquake loading has demonstrated that slope failure detected based on LEM, FELA, SDSS, and SRFEA is observed considerably earlier than the termination of the

DFEA. This is because the termination of the DFEA is not a precise indicator of the loss of stability. In dynamic analyses, a material failure does not necessarily lead to the termination (non-convergence) of the analysis since the inertial forces prevent the system from becoming kinematic. Analogous to any other analysis involving large deformations, the simulation can run well beyond the point of failure. Therefore, subsequent slope stability analyses are essential for a quantitative assessment of seismic slope stability in terms of FoS.

- Study of a large opencast mine slope and two centrifuge model tests indicated that stability analyses considering inertial forces (LEM, FELA, SRFEA) show an influence of the seismic excitation at an earlier point in time compared to approaches not explicitly accounting for inertial forces (SDSS). This is because shear waves propagate to the slope and have an impact on the slope stability prior to a significant accumulation of excess pore water pressures.
- Contrary to conventional approaches neglecting the influence of accumulated excess pore water pressures Δp^w , it was observed in all three boundary value problems that Δp^w has a decisive impact on the seismic slope stability. Disregard of Δp^w in the stability analyses leads to an overestimation of the FoS and an unsafe design.
- Stability analyses of the VELACS and LEAP centrifuge model tests showed that high frequency seismic excitation results in FoS predictions with high frequency oscillations. In case of dikes or dams with two slope faces (e.g. VELACS centrifuge model) the position of the critical slip surface might change rapidly between both slopes depending on the spatial distribution and the magnitude of the seismic effects.
- Investigation of seismic slope stability of very gentle slopes (e.g. LEAP centrifuge model) using SRFEA revealed that FoS values during a dynamic loading might temporarily exceed the one corresponding to the static situation. This is because for short time spans inertial forces stabilize the slope such that practically no additional shear resistance due to frictional or cohesive tangential forces is required to maintain equilibrium.
- Similar to the consideration of inertial forces in SRFEA, less conservative predictions of the FoS could be obtained with LEM in case inertial forces would be orientated in the same direction as obtained from the DFEA rather than always in driving direction. For cases where the so obtained FoS exceeds the one without consideration of inertial forces, the latter one should be regarded as the critical one.

10.3. Recommendations for further investigations

- Extension of the linear-elastic perfectly-plastic constitutive models implemented in the present work by consideration of material hardening or softening. Note that numerical instabilities and mesh dependency may result from SRFEA with strain softening materials (Galavi and Schweiger, 2010), thus, mesh refinement or regularization approaches such as gradient theories (Zervos et al., 2001; Papanicolopoulos and Zervos, 2010), nonlocal approaches (Eringen, 1981; Bažant and Jirásek, 2003; Galavi and Schweiger, 2010; Summersgill et al., 2017; Staubach et al., 2022b) or others should be used.
- Implementation of large-deformation techniques and application of these techniques for slope stability analyses using SRFEA. Among others, a suitable method is the Particle Finite Element Method (PFEM), that allows modifications of the finite element discretization (e.g. remeshing) during a simulation, while accounting for sophisticated constitutive models. Once implemented, the developed method should be tested and verified using benchmark problems and applications from geotechnical engineering as well as experimental results obtained from laboratory tests.
- In the present work, SDSS was successfully coupled with the Hypoplastic model with/without Intergranular Strain. However, coupling of SDSS with other sophisticated constitutive models for non-cohesive and cohesive soils should be done to investigate the influence of the choice of the constitutive model for the final FoS prediction. Constitutive models for non-cohesive soils could include the ISA Sand model (Fuentes, 2014; Fuentes and Triantafyllidis, 2015) or the Sanisand model (Dafalias and Manzari, 2004), while models for cohesive soils could include the Saniclay model (Taiebat et al., 2010), the AVISA model (Tafili and Triantafyllidis, 2020; Tafili et al., 2023) or the Constitutive Anamnesis Model (Tafili et al., 2022).
- To further extend the research regarding comparison of constitutive models (Wichtmann et al., 2019; Machaček et al., 2021; Triantafyllidis et al., 2022; Wichtmann et al., 2023), parameters of different sophisticated constitutive models should be calibrated for the same set of laboratory tests (e.g. oedometric test, monotonic and cyclic triaxial tests) before being used in DFEA and subsequent stability analyses to assess the influence of the selection of the constitutive model on the seismic slope stability. Note that this comparison would be interesting in combination with all stability approaches discussed in the present work, while coupling with SDSS would be of particular interest.

- In the present study, it has been demonstrated that machine learning (ML) approaches are powerful tools enabling to reduce computational costs associated with the SDSS approach. For the case of an opencast mine slope investigated with SDSS, it was shown that computational costs were significantly reduced, while the accuracy of individual direct simple shear tests at small stress levels showed potential for improvement. Further research should be conducted to obtain more accurate predictions of the stress-strain behavior using ML approaches, for instance by improving sampling methods and fine tuning of ML algorithms.
- Extension of the seismic stability approaches with regard to multiple soil layers. Investigation of case studies and more complex boundary value problems, such as multi-layered slopes or opencast mine slopes with polder structures. Additionally, further centrifuge model tests should be investigated, for instance the LEAP-ASIA-2019 project (Chen et al., 2021; Reyes et al., 2021) or a dam placed on liquefiable soil (Saade et al., 2023), to gain further experience and confidence with the developed stability approaches.
- Besides the determination of slope stability for dynamic problems, such as slopes subjected to earthquake loading or embankments subjected to high frequency vibrations of machine foundations, there are many transient problems that could be investigated. Those applications include rapid water level changes at dikes or reservoirs (e.g. rapid drawdown), infiltration processes as well as flow failures, for instance after a liquefaction event. As the concept of DFEA and subsequent stability analysis can be adapted by replacing the former analysis by a transient one, all approaches developed in the present study can be used to investigate the aforementioned transient problems in terms of the evolution of the FoS with regard to time.

Bibliography

- Abbo, A., Lyamin, A., Sloan, S., Hambleton, J., 2011. A C2 continuous approximation to the Mohr–Coulomb yield surface. *International Journal of Solids and Structures* 48, 3001–3010.
- Abbo, A., Sloan, S., 1995. A smooth hyperbolic approximation to the Mohr-Coulomb yield criterion. *Computers & Structures* 54, 427–441.
- Abbo, A.J., 1997. Finite element algorithms for elastoplasticity and consolidation. University of Newcastle Callaghan.
- Abramson, L.W., Lee, T.S., Sharma, S., Boyce, G.M., 2001. Slope stability and stabilization methods. John Wiley & Sons.
- Almeida, R.C., Feijóo, R.A., Galeao, A.C., Padra, C., Silva, R.S., 2000. Adaptive finite element computational fluid dynamics using an anisotropic error estimator. *Computer Methods in Applied Mechanics and Engineering* 182, 379–400.
- Altman, N.S., 1992. An introduction to kernel and nearest-neighbor nonparametric regression. *The American Statistician* 46, 175–185.
- Ausilio, E., Conte, E., Dente, G., 2000. Seismic stability analysis of reinforced slopes. *Soil Dynamics and Earthquake Engineering* 19, 159–172.
- Baker, R., 1980. Determination of the critical slip surface in slope stability computations. *International Journal for Numerical and Analytical Methods in Geomechanics* 4, 333–359.
- Baker, R., 1981. Tensile strength, tension cracks, and stability of slopes. *Soils and Foundations* 21, 1–17.
- Baker, R., Shukha, R., Operstein, V., Frydman, S., 2006. Stability charts for pseudo-static slope stability analysis. *Soil Dynamics and Earthquake Engineering* 26, 813–823.

- Barrero, A.R., Taiebat, M., Dafalias, Y.F., 2020. Modeling cyclic shearing of sands in the semifluidized state. *International Journal for Numerical and Analytical Methods in Geomechanics* 44, 371–388.
- Bathe, K.J., 2006. *Finite element procedures*. Prentice-Hall, Inc.
- Bauer, E., 1996. Calibration of a comprehensive hypoplastic model for granular materials. *Soils and foundations* 36, 13–26.
- Bažant, Z.P., Jirásek, M., 2003. Nonlocal integral formulations of plasticity and damage: survey of progress, in: *Perspectives in Civil Engineering: Commemorating the 150th Anniversary of the American Society of Civil Engineers*, ASCE. pp. 21–52.
- Beaty, M.H., Byrne, P.M., 2011. Ubsand constitutive model version 904ar. Itasca UDM Web Site 69.
- Benz, T., 2007. Small-strain stiffness of soils and its numerical consequences. volume 5. Univ. Stuttgart, Inst. f. Geotechnik Stuttgart.
- Benz, T., Vermeer, P., Schwab, R., 2009. A small-strain overlay model. *International Journal for Numerical and Analytical Methods in Geomechanics* 33, 25–44.
- Biondi, G., Cascone, E., Maueri, M., 2002. Flow and deformation failure of sandy slopes. *Soil Dynamics and Earthquake Engineering* 22, 1103–1114.
- Bishop, A.W., 1955. The use of the slip circle in the stability analysis of slopes. *Géotechnique* 5, 7–17.
- Bishop, A.W., 1966. The strength of soils as engineering materials. *Géotechnique* 16, 91–130.
- Bishop, A.W., Morgenstern, N., 1960. Stability coefficients for earth slopes. *Géotechnique* 10, 129–153.
- Bolton, M., 1986. The strength and dilatancy of sands. *Géotechnique* 36, 65–78.
- Borja, R.I., 2013. *Plasticity*. volume 2. Springer.
- Bottero, A., Negre, R., Pastor, J., Turgeman, S., 1980. Finite element method and limit analysis theory for soil mechanics problems. *Computer Methods in Applied Mechanics and Engineering* 22, 131–149.

- Boulanger, R., Ziotopoulou, K., 2015. Pm4sand (version 3): A sand plasticity model for earthquake engineering applications. Report No. UCD/CGM-15/01, Center for Geotechnical Modeling, Department of Civil and Environmental Engineering, University of California, Davis, CA.
- Boulanger, R.W., 2019. Nonlinear dynamic analyses of Austrian dam in the 1989 Loma Prieta earthquake. *Journal of Geotechnical and Geoenvironmental Engineering* 145, 05019011–05019011.
- Boulanger, R.W., Ziotopoulou, K., 2018. Pm4silt (version 1): A silt plasticity model for earthquake engineering applications. Report No. UCD/CGM-18/01, Center for Geotechnical Modeling, Department of Civil and Environmental Engineering, University of California, Davis, CA.
- Boulanger, R.W., Ziotopoulou, K., 2019. A constitutive model for clays and plastic silts in plane-strain earthquake engineering applications. *Soil Dynamics and Earthquake Engineering* 127, 105832.
- Bray, J.D., Rathje, E.M., 1998. Earthquake-induced displacements of solid-waste landfills. *Journal of Geotechnical and Geoenvironmental Engineering* 124, 242–253.
- Bray, J.D., Travasarou, T., 2009. Pseudostatic coefficient for use in simplified seismic slope stability evaluation. *Journal of Geotechnical and Geoenvironmental Engineering* 135, 1336–1340.
- Breiman, L., 2001. Random forests. *Machine learning* 45, 5–32.
- Brinkgreve, R., Bakker, H., 1991. Non-linear finite element analysis of safety factors, in: *International conference on computer methods and advances in geomechanics*. 7, pp. 1117–1122.
- Brinkgreve, R., Engin, E., Swolfs, W., 2017. *PLAXIS 2D. Reference manual*. Delft, Netherlands.
- Broomhead, D.S., Lowe, D., 1988. Radial basis functions, multi-variable functional interpolation and adaptive networks. Technical Report. Royal Signals and Radar Establishment Malvern (United Kingdom).
- Buehler, M.M., 2006. *Experimental and Numerical Investigation of Soil-Foundation-Structure Interaction during Monotonic, Alternating and Dynamic Loading*. Ph.D.

- thesis. Veröffentlichung des Instituts für Bodenmechanik und Felsmechanik der Universität Karlsruhe. Heft 166.
- Chen, L., Ghofrani, A., Arduino, P., 2020. Prediction of leap-ucd-2017 centrifuge test results using two advanced plasticity sand models, in: *Model Tests and Numerical Simulations of Liquefaction and Lateral Spreading*. Springer, pp. 423–439.
- Chen, L., Ghofrani, A., Arduino, P., 2021. Remarks on numerical simulation of the leap-asia-2019 centrifuge tests. *Soil Dynamics and Earthquake Engineering* 142, 106541.
- Chen, W.F., 2013. *Limit analysis and soil plasticity*. Elsevier.
- Chen, W.F., Giger, M., Fang, H.Y., 1969. On the limit analysis of stability of slopes. *Soils and Foundations* 9, 23–32.
- Chen, X., Zhang, L., Chen, L., Li, X., Liu, D., 2019. Slope stability analysis based on the coupled eulerian-lagrangian finite element method. *Bulletin of Engineering Geology and the Environment* 78, 4451–4463.
- Cheng, Y.M., Li, L., Chi, S.c., Wei, W., 2007. Particle swarm optimization algorithm for the location of the critical non-circular failure surface in two-dimensional slope stability analysis. *Computers and Geotechnics* 34, 92–103.
- Ching, R., Fredlund, D., 1983. Some difficulties associated with the limit equilibrium method of slices. *Canadian Geotechnical Journal* 20, 661–672.
- Choudhury, D., Nimbalkar, S., 2005. Seismic passive resistance by pseudo-dynamic method. *Géotechnique* 55, 699–702.
- Clausen, J., Andersen, L., Damkilde, L., 2010. On the differences between the drucker-prager criterion and exact implementation of the mohr-coulomb criterion in fem calculations, in: *Proceedings of the 7th European conference on numerical methods in geotechnical engineering*, pp. 101–106.
- Clausen, J., Damkilde, L., Andersen, L., 2006. Efficient return algorithms for associated plasticity with multiple yield planes. *International Journal for Numerical Methods in Engineering* 66, 1036–1059.
- Clerc, M., 2013. *Particle swarm optimization*. John Wiley & Sons.
- Coulomb, C.A., 1776. *Essai sur une application des règles de maximis & minimis à quelques problèmes de statique, relatifs à l'architecture*. De l'Imprimerie Royale.

- Crisfield, M.A., 1981. A fast incremental/iterative solution procedure that handles “snap-through”, in: *Computational methods in nonlinear structural and solid mechanics*. Elsevier, pp. 55–62.
- Dafalias, Y.F., Manzari, M.T., 2004. Simple plasticity sand model accounting for fabric change effects. *Journal of Engineering Mechanics* 130, 622–634.
- Dahmen, I.D., Hinzen, K., Kuntsche, K., 2014. Berücksichtigung von Erdbebeneinwirkungen bei bleibenden Böschungen des Braunkohlentagebaus im Rheinischen Revier. *World of Mining Surface & Underground* 66, 91–100.
- Davis, E., 1968. Theories of plasticity and failures of soil masses. *Soil mechanics, selected topics*, 341–354.
- Dawson, E., Roth, W., Drescher, A., 1999. Slope stability analysis by strength reduction. *Géotechnique* 49, 835–840.
- DIANA FEA BV, 2020. DIANA User’s Manual. Manie, J., <https://dianafea.com/manuals/d102/Diana.html>, Delft, The Netherlands.
- DIN-4084, 2021. Baugrund - Geländebruchberechnungen. Normenausschuss Bauwesen (NABau) im DIN.
- Donald, I., Giam, S., et al., 1988. Application of the nodal displacement method to slope stability analysis, in: *Proceedings of the 5th Australia–New Zealand conference on geomechanics*, Sydney, Australia, p. 460.
- Drucker, D., Prager, W., Greenberg, H., 1952. Extended limit design theorems for continuous media. *Quarterly of Applied Mathematics* 9, 381–389.
- Elia, G., Amorosi, A., Chan, A., Kavvadas, M., 2011. Fully coupled dynamic analysis of an earth dam. *Géotechnique* 61, 549–563.
- Eringen, A.C., 1981. On nonlocal plasticity. *International Journal of Engineering Science* 19, 1461–1474.
- Eyll-Vetter, M., 2015. Significance of geotechnical boundary conditions in planning and designing residual lakes in the rhenish lignite mining area illustrated by the example of the inden opencast mine. *World of Mining* 67, 371–378.
- Farias, M., Naylor, D., 1998. Safety analysis using finite elements. *Computers and Geotechnics* 22, 165–181.

- Fernandez-Merodo, J., Pastor, M., Mira, P., Tonni, L., Herreros, M.I., Gonzalez, E., Tamagnini, R., 2004. Modelling of diffuse failure mechanisms of catastrophic landslides. *Computer Methods in Applied Mechanics and Engineering* 193, 2911–2939.
- Fredlund, D.G., Krahn, J., 1977. Comparison of slope stability methods of analysis. *Canadian Geotechnical Journal* 14, 429–439.
- Fuentes, W., 2014. Contributions in mechanical modelling of fill materials. PhD thesis. Veröffentlichungen des Institutes für Bodenmechanik und Felsmechanik am Karlsruher Institut für Technologie (KIT). Heft 179.
- Fuentes, W., Tafili, M., Triantafyllidis, T., 2018. An ISA-plasticity-based model for viscous and non-viscous clays. *Acta Geotechnica* 13, 367–386.
- Fuentes, W., Triantafyllidis, T., 2015. ISA model: a constitutive model for soils with yield surface in the intergranular strain space. *International Journal for Numerical and Analytical Methods in Geomechanics* 39, 1235–1254.
- Galavi, V., Schweiger, H.F., 2010. Nonlocal multilaminate model for strain softening analysis. *International Journal of Geomechanics* 10, 30–44.
- GEO5 Slope Stability, 2020. Manual, GEO5 Slope Stability. Available at <<https://www.finesoftware.eu/geotechnical-software/slope-stability/>>.
- GeoStudio, 2020. GeoStudio: The modeling software for geo-engineers and earth scientists. Available at <<https://www.geoslope.com/>>.
- GGU-Stability, 2021. Handbuch, GGU-Stability, Version 13, Böschungsbruchberechnungen und Berechnungen von Bodenvernagelungen und Bewehrte-Erde-Wänden nach DIN 4084 und EC 7. Braunschweig.
- Goldscheider, M., Dahmen, D., Karcher, C., 2010. Berücksichtigung von Erdbeben bei Standsicherheitsberechnungen für tiefe Endböschungen unter Wasser. *World of Mining* 62, 252–261.
- Griffiths, D., 1986. Some theoretical observations on conical failure criteria in principal stress space. *International Journal of Solids and Structures* 22, 553–565.
- Griffiths, D., 1990. Failure criteria interpretation based on Mohr-Coulomb friction. *Journal of Geotechnical Engineering* 116, 986–999.

- Griffiths, D., Huang, J., 2009. Observations on the extended Matsuoka–Nakai failure criterion. *International Journal for Numerical and Analytical Methods in Geomechanics* 33, 1889–1905.
- Griffiths, D., Lane, P., 1999. Slope stability analysis by finite elements. *Géotechnique* 49, 387–403.
- Grünthal, G., Bosse, C., Stromeyer, D., 2009. Die neue Generation der probabilistischen seismischen Gefährdungseinschätzung der Bundesrepublik Deutschland. Version 2007 mit Anwendung für die Erdbeben-Lastfälle der DIN 19700:2004-07 "Stauanlagen". Scientific Technical Report STR, 09/07, Deutsches GeoForschungsZentrum GFZ Potsdam.
- Guo, M., Ge, X., Wang, S., 2011. Slope stability analysis under seismic load by vector sum analysis method. *Journal of Rock Mechanics and Geotechnical Engineering* 3, 282–288.
- Gußmann, P., 1986. Die Methode der kinematischen Elemente. Mitteilung 25, Baugrundinstitut Stuttgart.
- Gußmann, P., 1990. Beiträge zur Anwendung der KEM: Erddruck, Grundbruch, Standsicherheit von Böschungen. Mitteilung 32, Baugrundinstitut Stuttgart.
- Gußmann, P., 2000. Effective KEM solutions for the limit load and the slope stability problem. volume 24. John Wiley & Sons, Inc.
- Han, B., Zdravkovic, L., Kontoe, S., Taborda, D.M., 2016. Numerical investigation of the response of the yele rockfill dam during the 2008 wenchuan earthquake. *Soil Dynamics and Earthquake Engineering* 88, 124–142.
- Hazari, S., Sharma, R.P., Ghosh, S., 2020. Swedish circle method for pseudo-dynamic analysis of slope considering circular failure mechanism. *Geotechnical and Geological Engineering* 38, 2573–2589.
- Hilber, H.M., Hughes, T.J., Taylor, R.L., 1977. Improved numerical dissipation for time integration algorithms in structural dynamics. *Earthquake Engineering & Structural Dynamics* 5, 283–292.
- Hinton, G.E., 1990. Connectionist learning procedures, in: *Machine learning*. Elsevier, pp. 555–610.
- Hleibieh, J., Herle, I., 2019a. Numerische Bestimmung der Standsicherheit von Böschungen unter Erdbebeneinwirkung am Beispiel eines Erddamms im Zentrifugenversuch. *geotechnik* 42, 76–87.

- Hleibieh, J., Herle, I., 2019b. The performance of a hypoplastic constitutive model in predictions of centrifuge experiments under earthquake conditions. *Soil Dynamics and Earthquake Engineering* 122, 310–317.
- Hoek, E., Bray, J.D., 1981. *Rock slope engineering*. CRC Press.
- Hopgood, A.A., 2021. *Intelligent Systems for Engineers and Scientists: A Practical Guide to Artificial Intelligence*. CRC press.
- Huang, J., Griffiths, D., 2008. Observations on return mapping algorithms for piecewise linear yield criteria. *International Journal of Geomechanics* 8, 253–265.
- Huang, J., Griffiths, D., 2009. Return mapping algorithms and stress predictors for failure analysis in geomechanics. *Journal of Engineering Mechanics* 135, 276–284.
- Huang, L., Huang, S., Lai, Z., 2020. On an energy-based criterion for defining slope failure considering spatially varying soil properties. *Engineering Geology* 264, 105323.
- Hynes-Griffin, M.E., Franklin, A.G., 1984. Rationalizing the seismic coefficient method. Technical Report. Army Engineer Waterways Experiment Station Vicksburg Ms Geotechnical Lab.
- Itasca Consulting Group, 2020. *FLAC, fast Lagrangian analysis of continua*. Itasca Consulting Group, Minneapolis, Minnesota, USA.
- Jafarian, Y., Lashgari, A., 2017. Seismic sliding analysis of sandy slopes subjected to pore-water pressure buildup. *International Journal of Geomechanics* 17, 04017106.
- Jaky, J., 1944. The coefficient of earth pressure at rest. *Journal of the Society of Hungarian Architects and Engineers*, 355–358.
- Janbu, N., 1954. Application of composite slip surface for stability analysis, in: *Proceedings of European Conference on Stability of Earth Slopes, Sweden, 1954*, pp. 43–49.
- Ji, J., Wang, C.W., Cui, H.Z., Li, X.Y., Song, J., Gao, Y., 2021. A simplified nonlinear coupled newmark displacement model with degrading yield acceleration for seismic slope stability analysis. *International Journal for Numerical and Analytical Methods in Geomechanics* 45, 1303–1322.
- Jiang, H., Wang, X., 2011. A new method to calculate the equivalent Mohr–Coulomb friction angle for cohesive and frictional materials. *International Journal for Numerical and Analytical Methods in Geomechanics* 35, 630–638.

- Jibson, R.W., 2011. Methods for assessing the stability of slopes during earthquakes—a retrospective. *Engineering Geology* 122, 43–50.
- Jurado-Piña, R., Jimenez, R., 2015. A genetic algorithm for slope stability analyses with concave slip surfaces using custom operators. *Engineering Optimization* 47, 453–472.
- Kadlíček, T., Mašín, D., 2020. The strength reduction method in clay hypoplasticity. *Computers and Geotechnics* 126, 103687.
- Kalagnanam, J.R., Diwekar, U.M., 1997. An efficient sampling technique for off-line quality control. *Technometrics* 39, 308–319.
- Karray, M., Hussien, M.N., Delisle, M.C., Ledoux, C., 2018. Framework to assess pseudo-static approach for seismic stability of clayey slopes. *Canadian Geotechnical Journal* 55, 1860–1876.
- Karray, M., Hussien, M.N., Souilem, M., Locat, P., Mompin, R., 2019. Adjustment of spectral pseudo-static approach to account for soil plasticity and zone seismicity. *Canadian Geotechnical Journal* 56, 173–186.
- Kavvas, M., Amorosi, A., 2000. A constitutive model for structured soils. *Géotechnique* 50, 263–273.
- Kishida, T., Boulanger, R.W., Abrahamson, N.A., Driller, M.W., Wehling, T.M., 2009. Seismic response of levees in the Sacramento-San Joaquin Delta. *Earthquake Spectra* 25, 557–582.
- Koiter, W.T., 1953. Stress-strain relations, uniqueness and variational theorems for elastic-plastic materials with a singular yield surface. *Quarterly of Applied Mathematics* 11, 350–354.
- Kolditz, O., Bauer, S., Bilke, L., Böttcher, N., Delfs, J.O., Fischer, T., Görke, U.J., Kalbacher, T., Kosakowski, G., McDermott, C., et al., 2012. OpenGeoSys: an open-source initiative for numerical simulation of thermo-hydro-mechanical/chemical (THM/C) processes in porous media. *Environmental Earth Sciences* 67, 589–599.
- Krabbenhoft, K., 2018. Static and seismic earth pressure coefficients for vertical walls with horizontal backfill. *Soil Dynamics and Earthquake Engineering* 104, 403–407.
- Krabbenhoft, K., 2019. Plastic design of embedded retaining walls. *Proceedings of the Institution of Civil Engineers-Geotechnical Engineering* 172, 131–144.

- Krabbenhoft, K., Lyamin, A., 2015. Strength reduction finite-element limit analysis. *Géotechnique Letters* 5, 250–253.
- Krahn, J., 2003. The 2001 rm hardy lecture: The limits of limit equilibrium analyses. *Canadian Geotechnical Journal* 40, 643–660.
- Krahn, J., Fredlund, D.G., 1977. Evaluation of the University of Saskatchewan slope stability program, R.T.A.C. Academic Press, 1978. Forum, 69-76, Summer (1977).
- Kramer, S., 1996. *Geotechnical earthquake engineering*. 1 ed., Prentice Hall, USA.
- Kramer, S.L., Smith, M.W., 1997. Modified Newmark model for seismic displacements of compliant slopes. *Journal of Geotechnical and Geoenvironmental Engineering* 123, 635–644.
- Kutter, B.L., Manzari, M.T., Zeghal, M., 2020. *Model Tests and Numerical Simulations of Liquefaction and Lateral Spreading: LEAP-UCD-2017*. Springer International Publishing.
- Lagioia, R., Panteghini, A., 2016. On the existence of a unique class of yield and failure criteria comprising Tresca, von Mises, Drucker–Prager, Mohr–Coulomb, Galileo–Rankine, Matsuoka–Nakai and Lade–Duncan. *Proceedings of the royal society A: mathematical, physical and engineering sciences* 472, 20150713.
- Leshchinsky, B., Ambauen, S., 2015. Limit equilibrium and limit analysis: comparison of benchmark slope stability problems. *Journal of Geotechnical and Geoenvironmental Engineering* 141, 04015043.
- Leshchinsky, B., Mason, H., Olsen, M., Gillins, D., 2018. Lateral spreading within a limit equilibrium framework: Newmark sliding blocks with degrading yield accelerations. *Géotechnique* 68, 699–712.
- Leshchinsky, D., San, K.C., 1994. Pseudostatic seismic stability of slopes: Design charts. *Journal of Geotechnical Engineering* 120, 1514–1532.
- Lester, A.M., Sloan, S.W., 2018. A smooth hyperbolic approximation to the Generalised Classical yield function, including a true inner rounding of the Mohr–Coulomb deviatoric section. *Computers and Geotechnics* 104, 331–357.
- Li, C., Su, L., Liao, H., Zhang, C., Xiao, S., 2021. Modeling of rapid evaluation for seismic stability of soil slope by finite element limit analysis. *Computers and Geotechnics* 133, 104074.

- Liao, S.S., Whitman, R.V., 1986. A catalog of liquefaction and non-liquefaction occurrences during earthquakes. Department of Civil Engineering, MIT.
- Lin, J.S., Whitman, R.V., 1983. Decoupling approximation to the evaluation of earthquake-induced plastic slip in earth dams. *Earthquake Engineering & Structural Dynamics* 11, 667–678.
- Liu, S., Shao, L., Li, H., 2015. Slope stability analysis using the limit equilibrium method and two finite element methods. *Computers and Geotechnics* 63, 291–298.
- Liu, S., Su, Z., Li, M., Shao, L., 2020. Slope stability analysis using elastic finite element stress fields. *Engineering Geology* 273, 105673.
- López-Querol, S., Blázquez, R., 2006. Liquefaction and cyclic mobility model for saturated granular media. *International Journal for Numerical and Analytical Methods in Geomechanics* 30, 413–439.
- López-Querol, S., Moreta, P., 2008. Performance of heterogeneous earthfill dams under earthquakes: optimal location of the impervious core. *Natural Hazards and Earth System Sciences* 8, 9–18.
- Loukidis, D., Bandini, P., Salgado, R., 2003. Stability of seismically loaded slopes using limit analysis. *Géotechnique* 53, 463–479.
- Lyamin, A.V., Krabbenhoft, K., Sloan, S.W., 2013. Adaptive limit analysis using deviatoric fields, in: *Proceedings of the VI International Conference on Adaptive Modeling and Simulation*, pp. 448–455.
- Lyamin, A.V., Sloan, S.W., Krabbenhøft, K., Hjiaj, M., 2005. Lower bound limit analysis with adaptive remeshing. *International Journal for Numerical Methods in Engineering* 63, 1961–1974.
- Lysmer, J., 1970. Limit analysis of plane problems in soil mechanics. *Journal of the Soil Mechanics and Foundations Division* 96, 1311–1334.
- Ma, Z., Liao, H., Dang, F., Cheng, Y., 2021. Seismic slope stability and failure process analysis using explicit finite element method. *Bulletin of Engineering Geology and the Environment* 80, 1287–1301.
- Macedo, J., Candia, G., 2020. Performance-based assessment of the seismic pseudo-static coefficient used in slope stability analysis. *Soil Dynamics and Earthquake Engineering* 133, 106109.

- Machaček, J., 2020. Contributions to the numerical modelling of saturated and unsaturated soils. PhD thesis. Veröffentlichungen des Institutes für Bodenmechanik und Felsmechanik am Karlsruher Institut für Technologie (KIT). Heft 187.
- Machaček, J., Staubach, P., Grandas Tavera, C.E., Wichtmann, T., Zachert, H., 2022. On the automatic parameter calibration of a hypoplastic soil model. *Acta Geotechnica* 17, 5253–5273.
- Machaček, J., Staubach, P., Tafili, M., Zachert, H., Wichtmann, T., 2021. Investigation of three sophisticated constitutive soil models: From numerical formulations to element tests and the analysis of vibratory pile driving tests. *Computers and Geotechnics* 138, 104276.
- Machaček, J., Triantafyllidis, T., Staubach, P., 2018. Fully coupled simulation of an open-cast mine subjected to earthquake loading. *Soil Dynamics and Earthquake Engineering* 115, 853–867.
- Mahmoudi, E., Schmüdderich, C., Hölter, R., Zhao, C., Wichtmann, T., König, M., 2020. Stochastic field simulation of slope stability problems: Improvement and reduction of computational effort. *Computer Methods in Applied Mechanics and Engineering* 369, 113167.
- Makdisi, F.I., Seed, H.B., 1978. Simplified procedure for estimating dam and embankment earthquake-induced deformations. *Journal of the Geotechnical Engineering Division* 104, 849–867.
- Mathews, N., Leshchinsky, B.A., Olsen, M.J., Klar, A., 2019. Spatial distribution of yield accelerations and permanent displacements: A diagnostic tool for assessing seismic slope stability. *Soil Dynamics and Earthquake Engineering* 126, 105811.
- Matsui, T., San, K.C., 1992. Finite element slope stability analysis by shear strength reduction technique. *Soils and Foundations* 32, 59–70.
- Matsuoka, H., 1974. Stress-strain relationships of sands based on the mobilized plane. *Soils and Foundations* 14, 47–61.
- Matsuoka, H., Nakai, T., 1974. Stress-deformation and strength characteristics of soil under three different principal stresses, in: *Proceedings of the Japan Society of Civil Engineers*, Japan Society of Civil Engineers. pp. 59–70.

- Matsuoka, H., Sun, D., 1995. Extension of spatially mobilized plane (SMP) to frictional and cohesive materials and its application to cemented sands. *Soils and Foundations* 35, 63–72.
- Mazzoni, S., McKenna, F., Scott, M.H., Fenves, G.L., et al., 2006. Opensees command language manual. Pacific Earthquake Engineering Research (PEER) Center 264, 137–158.
- McKay, M.D., Beckman, R.J., Conover, W.J., 2000. A comparison of three methods for selecting values of input variables in the analysis of output from a computer code. *Technometrics* 42, 55–61.
- Merifield, R., Sloan, S., Yu, H., 1999. Rigorous plasticity solutions for the bearing capacity of two-layered clays. *Géotechnique* 49, 471–490.
- Metropolis, N., Ulam, S., 1949. The Monte Carlo method. *Journal of the American Statistical Association* 44, 335–341.
- Michalowski, R., 1995. Slope stability analysis: a kinematical approach. *Géotechnique* 45, 283–293.
- Michalowski, R.L., 2002. Stability charts for uniform slopes. *Journal of Geotechnical and Geoenvironmental Engineering* 128, 351–355.
- Mittmann, A., Petri, R., Buschhüter, K., 2015. Examination of geotechnical aspects in the approval of residual lakes. *World of Mining* 67, 379–388.
- Montgomery, J., Ziotopoulou, K., 2020. Numerical simulations of selected LEAP centrifuge experiments with PM4Sand in FLAC, in: *Model Tests and Numerical Simulations of Liquefaction and Lateral Spreading*. Springer, pp. 481–497.
- Montoya-Araque, E.A., Suarez-Burgoa, L.O., Medley, E.W., 2020. Application of the tortuous surface method to stochastic analysis of bimslope stability. *Bulletin of Engineering Geology and the Environment* 79, 5329–5340.
- Morgenstern, N., Price, V., 1967. A numerical method for solving the equations of stability of general slip surfaces. *The Computer Journal* 9, 388–393.
- Morgenstern, N.u., Price, V.E., 1965. The analysis of the stability of general slip surfaces. *Géotechnique* 15, 79–93.

- Muraleetharan, K.K., Deshpande, S., Adalier, K., 2004. Dynamic deformations in sand embankments: centrifuge modeling and blind, fully coupled analyses. *Canadian Geotechnical Journal* 41, 48–69.
- Napoli, M.L., Barbero, M., Scavia, C., 2021. Effects of block shape and inclination on the stability of melange bimrocks. *Bulletin of Engineering Geology and the Environment* 80, 7457–7466.
- Nayak, G.C., Zienkiewicz, O.C., 1972. Convenient form of stress invariants for plasticity. *Journal of the Structural Division* 98, 949–954.
- Newmark, N.M., 1959. A method of computation for structural dynamics. *Journal of the Engineering Mechanics Division* 85, 67–94.
- Newmark, N.M., 1965. Effects of earthquakes on dams and embankments. *Géotechnique* 15, 139–160.
- Niemunis, A., 2003. *Extended hypoplastic models for soils*. 1st ed., Politechnika Gdańska, Gdańsk. Habilitation, Monografia 34.
- Niemunis, A., 2008. *Incremental Driver User's manual*. Available from www.pg.gda.pl/~aniem/an-liter.html.
- Niemunis, A., Herle, I., 1997. Hypoplastic model for cohesionless soils with elastic strain range. *Mechanics of Cohesive-frictional Materials: An International Journal on Experiments, Modelling and Computation of Materials and Structures* 2, 279–299.
- Niemunis, A., Prada-Sarmiento, L.F., Grandas-Tavera, C.E., 2011. Praelasticity. *Acta Geotechnica* 6, 67–80.
- Nitzsche, K., Herle, I., 2020. Strain-dependent slope stability. *Acta Geotechnica* 15, 3111–3119.
- Nordal, S., 2008. Can we trust numerical collapse load simulations using non-associated flow rules, in: *Proc. 12th Int. Conf. IACMAG*, pp. 755–762.
- Oberhollenzer, S., Tschuchnigg, F., Schweiger, H.F., 2018. Finite element analyses of slope stability problems using non-associated plasticity. *Journal of Rock Mechanics and Geotechnical Engineering* 10, 1091–1101.
- Onlineyamlttools, 2022. Onlineyamlttools. URL: <https://onlineyamlttools.com/validate-yaml>.

- OptumG2, 2019. Finite Element Program for Geotechnical Analysis, Optum Computational Engineering, www.optumce.com.
- Owen, D., Hinton, E., 1980. Finite elements in plasticity: Theory and practice. Swansea, UK: Pineridge Press Limited.
- Panteghini, A., Lagioia, R., 2014a. A fully convex reformulation of the original Matsuoka–Nakai failure criterion and its implicit numerically efficient integration algorithm. *International Journal for Numerical and Analytical Methods in Geomechanics* 38, 593–614.
- Panteghini, A., Lagioia, R., 2014b. A single numerically efficient equation for approximating the Mohr–Coulomb and the Matsuoka–Nakai failure criteria with rounded edges and apex. *International Journal for Numerical and Analytical Methods in Geomechanics* 38, 349–369.
- Papanicolopoulos, S.A., Zervos, A., 2010. Numerical solution of crack problems in gradient elasticity. *Proceedings of the Institution of Civil Engineers-Engineering and Computational Mechanics* 163, 73–82.
- Pastor, M., Zienkiewicz, O., Chan, A., 1990. Generalized plasticity and the modelling of soil behaviour. *International Journal for Numerical and Analytical Methods in Geomechanics* 14, 151–190.
- Pelecanos, L., Kontoe, S., Zdravković, L., 2015. A case study on the seismic performance of earth dams. *Géotechnique* 65, 923–935.
- Potts, D.M., Zdravković, L., 1999. Finite element analysis in geotechnical engineering: theory. Thomas Telford London.
- Potts, D.M., Zdravković, L., 2012. Accounting for partial material factors in numerical analysis. *Géotechnique* 62, 1053–1065.
- Priebe, H.J., 1995. Die Bemessung von Rüttelstoppeverdichtungen. *Bautechnik* (Berlin, 1984), 183–191.
- Qarmout, M., König, D., Gussmann, P., Thewes, M., Schanz, T., 2019a. Tunnel face stability analysis using Kinematical Element Method. *Tunnelling and Underground Space Technology* 85, 354–367.
- Qarmout, M., Schmüdderich, C., König, D., Gussmann, P., Thewes, M., Wichtmann, T., 2019b. Face stability of a circular tunnel excavated in dry frictional-cohesive soil,

- in: Proceedings of the ETS Tunnelling and Underground Construction Conference & Exhibition 2019, Luxor, Egypt, ETS. pp. 1–10.
- Qin, C.B., Chian, S.C., 2018. Kinematic analysis of seismic slope stability with a discretisation technique and pseudo-dynamic approach: a new perspective. *Géotechnique* 68, 492–503.
- Ramamurthy, T., Rawat, P., 1973. Shear strength of sand under general stress system, in: Proc. 8th ICSMFE, p. 2.
- Rathje, E.M., Antonakos, G., 2011. A unified model for predicting earthquake-induced sliding displacements of rigid and flexible slopes. *Engineering Geology* 122, 51–60.
- Rathje, E.M., Bray, J.D., 2000. Nonlinear coupled seismic sliding analysis of earth structures. *Journal of Geotechnical and Geoenvironmental Engineering* 126, 1002–1014.
- Reyes, A., Yang, M., Barrero, A.R., Taiebat, M., 2021. Numerical modeling of soil liquefaction and lateral spreading using the SANISAND-Sf model in the LEAP experiments. *Soil Dynamics and Earthquake Engineering* 143, 106613.
- RfS, 2013. Richtlinie für die Untersuchung der Standsicherheit von Böschungen der im Tagebau betriebenen Braunkohlenbergwerke (Richtlinie für Standsicherheitsuntersuchungen, RfS). Neufassung mit 1. Ergänzung vom 08.08.2013 - 61.19.2-2-1.
- Riks, E., 1979. An incremental approach to the solution of snapping and buckling problems. *International Journal of Solids and Structures* 15, 529–551.
- Ristinmaa, M., Tryding, J., 1993. Exact integration of constitutive equations in elastoplasticity. *International Journal for Numerical Methods in Engineering* 36, 2525–2544.
- Roscoe, K.H., 1970. The influence of strains in soil mechanics. *Géotechnique* 20, 129–170.
- Saade, C., Li, Z., Escoffier, S., Thorel, L., 2023. Centrifuge and numerical modeling of the behavior of homogeneous embankment on liquefiable soil subjected to dynamic excitation. *Soil Dynamics and Earthquake Engineering* 172, 107999.
- Saltelli, A., Ratto, M., Andres, T., Campolongo, F., Cariboni, J., Gatelli, D., Saisana, M., Tarantola, S., 2008. *Global sensitivity analysis: the primer*. John Wiley & Sons.
- Sarma, S.K., 1973. Stability analysis of embankments and slopes. *Géotechnique* 23, 423–433.

- Schanz, T., Vermeer, P., 1996. Angles of friction and dilatancy of sand. *Géotechnique* 46, 145–151.
- Schmüdderich, C., Gußmann, P., König, D., Schanz, T., 2017a. Vergleichende Untersuchungen zum räumlichen Erdwiderstand mit der Kinematischen-Elemente-Methode. *Bautechnik* 94, 613–623.
- Schmüdderich, C., König, D., Gußmann, P., Schanz, T., 2017b. Zur Berechnung des Erdwiderstands mit der Kinematischen Elemente Methode, in: Wechselwirkung Baugrund - Bauwerk, Tagungsband zum 8. RuhrGeo-Tag 2017, Report Geotechnik, Universität Duisburg-Essen. pp. 147–168.
- Schmüdderich, C., Lavasan, A.A., Tschuchnigg, F., Wichtmann, T., 2020a. Bearing capacity of a strip footing placed next to an existing footing on frictional soil. *Soils and Foundations* 60, 229–238.
- Schmüdderich, C., Lavasan, A.A., Tschuchnigg, F., Wichtmann, T., 2020b. Behavior of nonidentical differently loaded interfering rough footings. *Journal of Geotechnical and Geoenvironmental Engineering* 146, 04020041.
- Schmüdderich, C., Machaček, J., Prada-Sarmiento, L.F., Staubach, P., Wichtmann, T., 2022a. Strain-dependent slope stability for earthquake loading. *Computers and Geotechnics* 152, 105048.
- Schmüdderich, C., Prada-Sarmiento, L.F., Wichtmann, T., 2021. Numerical analyses of the 2D bearing capacity of block-in-matrix soils (bimsoils) under shallow foundations. *Computers and Geotechnics* 136, 104232.
- Schmüdderich, C., Shahrabi, M.M., Taiebat, M., Lavasan, A.A., 2020c. Strategies for numerical simulation of cast-in-place piles under axial loading. *Computers and Geotechnics* 125, 103656.
- Schmüdderich, C., Tschuchnigg, F., Schweiger, H.F., 2022b. Significance of flow rule for the passive earth pressure problem. *Acta Geotechnica* 17, 81–92.
- Schmüdderich, C., Tschuchnigg, F., Wichtmann, T., 2020d. Rigorous lower and upper bounds for the 3D passive earth pressure problem. *Géotechnique Letters* 10, 100–105.
- Schneider-Muntau, B., Medicus, G., Fellin, W., 2018. Strength reduction method in Barodesy. *Computers and Geotechnics* 95, 57–67.

- Schweiger, H., 1994. On the use of drucker-prager failure criteria for earth pressure problems. *Computers and Geotechnics* 16, 223–246.
- Seed, H.B., 1979. Considerations in the earthquake-resistant design of earth and rockfill dams. *Géotechnique* 29, 215–263.
- Seed, H.B., Idriss, I.M., 1971. Simplified procedure for evaluating soil liquefaction potential. *Journal of the Soil Mechanics and Foundations Division* 97, 1249–1273.
- Seed, H.B., Martin, G.R., 1966. The seismic coefficient in earth dam design. *Journal of the Soil Mechanics and Foundations Division* 92, 25–58.
- Shakya, S., Schmüdderich, C., Machaček, J., Prada-Sarmiento, L.F., Wichtmann, T., 2024. Influence of sampling methods on the accuracy of machine learning predictions used for strain-dependent slope stability. *Geosciences* 14, 44.
- Simo, J.C., Hughes, T.J., 2006. *Computational inelasticity*. volume 7. Springer Science & Business Media.
- Simo, J.C., Taylor, R.L., 1985. Consistent tangent operators for rate-independent elastoplasticity. *Computer Methods in Applied Mechanics and Engineering* 48, 101–118.
- Slide2, 2022. *Manual, Slide2 Slope Stability*. Rocscience Inc. Available at <<https://www.rocscience.com/>>.
- Sloan, S., 2005. Geotechnical stability analysis: new methods for an old problem. *Australian Geomechanics* 40, 1–28.
- Sloan, S., 2013. Geotechnical stability analysis. *Géotechnique* 63, 531–571.
- Sloan, S., Booker, J., 1986. Removal of singularities in Tresca and Mohr–Coulomb yield functions. *Communications in Applied Numerical Methods* 2, 173–179.
- Smith, I.M., Griffiths, D.V., Margetts, L., 2013. *Programming the finite element method*. John Wiley & Sons.
- de Souza Neto, E.A., Peric, D., Owen, D.R., 2011. *Computational methods for plasticity: theory and applications*. John Wiley & Sons.
- Spencer, E., 1967. A method of analysis of the stability of embankments assuming parallel inter-slice forces. *Géotechnique* 17, 11–26.

- Spencer, E., 1968. Effect of tension on stability of embankments. *Journal of the Soil Mechanics and Foundations Division* 94, 1159–1173.
- Spencer, E., 1973. Thrust line criterion in embankment stability analysis. *Géotechnique* 23, 85–100.
- Staubach, P., 2022. Contributions to the numerical modelling of pile installation processes and high-cyclic loading of soils. Phd thesis. Schriftenreihe des Lehrstuhls für Bodenmechanik, Grundbau und Umweltgeotechnik der Ruhr Universität Bochum. Heft 73.
- Staubach, P., Machaček, J., Tafli, M., Wichtmann, T., 2022a. A high-cycle accumulation model for clay and its application to monopile foundations. *Acta Geotechnica* 17, 677–698.
- Staubach, P., Machaček, J., Tschirschky, L., Wichtmann, T., 2022b. Enhancement of a high-cycle accumulation model by an adaptive strain amplitude and its application to monopile foundations. *International Journal for Numerical and Analytical Methods in Geomechanics* 46, 315–338.
- Steedman, R., Zeng, X., 1990. The influence of phase on the calculation of pseudo-static earth pressure on a retaining wall. *Géotechnique* 40, 103–112.
- Steward, T., Sivakugan, N., Shukla, S., Das, B., 2011. Taylor's slope stability charts revisited. *International Journal of Geomechanics* 11, 348–352.
- Storn, R., Price, K., 1997. Differential evolution—a simple and efficient heuristic for global optimization over continuous spaces. *Journal of Global Optimization* 11, 341–359.
- Summersgill, F., Kontoe, S., Potts, D., 2017. On the use of nonlocal regularisation in slope stability problems. *Computers and Geotechnics* 82, 187–200.
- Sutherland, H., Mesdary, M., 1969. The influence of the intermediate principal stress on the strength of sand, in: *Proc., 7th Int. Conf. on Soil Mechanics and Foundation Engineering*, Sociedad Mexicana de Mecanica Mexico City. pp. 391–399.
- Tafli, M., Ganal, A., Wichtmann, T., Reul, O., 2023. On the AVISA model for clay—Recommendations for calibration and verification based on the back analysis of a piled raft. *Computers and Geotechnics* 154, 105126.
- Tafli, M., Grandas, C., Triantafyllidis, T., Wichtmann, T., 2022. Constitutive anamnesis model (CAM) for fine-grained soils. *International Journal for Numerical and Analytical Methods in Geomechanics* 46, 2817–2848.

- Tafili, M., Triantafyllidis, T., 2020. AVISA: anisotropic visco-ISA model and its performance at cyclic loading. *Acta Geotechnica* 15, 2395–2413.
- Taiebat, M., Dafalias, Y.F., 2008. SANISAND: Simple anisotropic sand plasticity model. *International Journal for Numerical and Analytical Methods in Geomechanics* 32, 915–948.
- Taiebat, M., Dafalias, Y.F., Peek, R., 2010. A destructuration theory and its application to SANICLAY model. *International Journal for Numerical and Analytical Methods in Geomechanics* 34, 1009–1040.
- Terzaghi, K., 1943. *Theoretical Soil Mechanics*. John Wiley & Sons, Inc, Hoboken, NJ, USA.
- Terzaghi, K., 1950. Mechanism of landslides. *Application of Geology to Engineering Practice*, *Geol. Soc. Am* , 83–123.
- Triantafyllidis, T., Grandas-Tavera, C.E., 2013. Quasi-statischer Ansatz der seismischen Anregung von Böschungen mit nicht-linearer Wellenausbreitung. *Bautechnik* 90, 51–62.
- Triantafyllidis, T., Tafili, M., Macháček, J., 2022. Untersuchungen zur Validierung und Kalibrierung von Technikumsversuchen: Zwischenbericht zur Kalibrierung von Kali 1 - Kali 5 und Rheinbraunton sowie Nachrechnung von Zentrifugenmodell-Versuchen. ITT Ingenieurbüro für Geotechnik, Karlsruhe.
- Tropeano, G., Silvestri, F., Ausilio, E., 2017. An uncoupled procedure for performance assessment of slopes in seismic conditions. *Bulletin of Earthquake Engineering* 15, 3611–3637.
- Tschuchnigg, F., Medicus, G., Schneider-Muntau, B., 2019. Slope stability analysis: Barodesy vs linear elastic–perfectly plastic models, in: *E3S Web of Conferences*, EDP Sciences. p. 16014.
- Tschuchnigg, F., Schweiger, H., Sallinger, M., 2018. Effect of failure criterion on slope stability analysis, in: *Numerical Methods in Geotechnical Engineering IX*. CRC Press, pp. 1055–1062.
- Tschuchnigg, F., Schweiger, H., Sloan, S.W., 2015a. Slope stability analysis by means of finite element limit analysis and finite element strength reduction techniques. part i: Numerical studies considering non-associated plasticity. *Computers and Geotechnics* 70, 169–177.

- Tschuchnigg, F., Schweiger, H., Sloan, S.W., Lyamin, A.V., Raissakis, I., 2015b. Comparison of finite-element limit analysis and strength reduction techniques. *Géotechnique* 65, 249–257.
- Tsiaousi, D., Ugalde, J., Travasarou, T., 2020. Leap-ucd-2017 simulation team fugro, in: *Model Tests and Numerical Simulations of Liquefaction and Lateral Spreading*. Springer, pp. 545–562.
- Tu, Y., Liu, X., Zhong, Z., Li, Y., 2016. New criteria for defining slope failure using the strength reduction method. *Engineering Geology* 212, 63–71.
- Van Langen, H., 1991. Numerical analysis of soil-structure interaction. PhD thesis. Delft University of Technology, The Netherlands.
- Van Langen, H., Vermeer, P., 1990. Automatic step size correction for non-associated plasticity problems. *International Journal for Numerical Methods in Engineering* 29, 579–598.
- Wegener, D., Herle, I., 2012. Zur Steifigkeit bei kleinen Dehnungen im Rahmen der Hypoplastizität. *geotechnik* 35, 229–235.
- Wei, W., Cheng, Y.M., Li, L., 2009. Three-dimensional slope failure analysis by the strength reduction and limit equilibrium methods. *Computers and Geotechnics* 36, 70–80.
- White, D., Teh, K., Leung, C., Chow, Y., 2008. A comparison of the bearing capacity of flat and conical circular foundations on sand. *Géotechnique* 58, 781–792.
- Wichtmann, T., 2005. Explicit accumulation model for non-cohesive soils under cyclic loading. PhD thesis. Schriftenreihe des Instituts für Grundbau und Bodenmechanik der Ruhr Universität Bochum. Heft 38.
- Wichtmann, T., Fuentes, W., Triantafyllidis, T., 2019. Inspection of three sophisticated constitutive models based on monotonic and cyclic tests on fine sand: Hypoplasticity vs. Sanisand vs. ISA. *Soil Dynamics and Earthquake Engineering* 124, 172–183.
- Wichtmann, T., Tafili, M., Staubach, P., Machaček, J., Schmüdderich, C., Lieske, W., 2023. Perspectives, demands and challenges of future research in Soil Mechanics and Soil Dynamics, in: *Herausforderungen in der Geotechnik - 25 Jahre Institut für Geotechnik und Baubetrieb*, Technische Universität Hamburg. pp. 25–85.

- von Wolffersdorff, P.A., 1996. A hypoplastic relation for granular materials with a predefined limit state surface. *Mechanics of Cohesive-frictional Materials* 1, 251–271.
- von Wolffersdorff, P.A., 2019. Informationen und Empfehlungen des Arbeitskreises 1.6 'Numerik in der Geotechnik' Berechnung der Standsicherheit mit der FEM durch Reduzierung der Festigkeitsparameter. *geotechnik* 42, 88–97.
- Wu, Q., Li, D.Q., Liu, Y., Du, W., 2021. Seismic performance of earth dams founded on liquefiable soil layer subjected to near-fault pulse-like ground motions. *Soil Dynamics and Earthquake Engineering* 143, 106623.
- Yang, M., Barrero, A.R., Taiebat, M., 2020. Application of a SANISAND model for numerical simulations of the LEAP 2017 experiments, in: *Model tests and numerical simulations of liquefaction and lateral spreading*. Springer, pp. 595–610.
- Yang, Z., Elgamal, A., Parra, E., 2003. Computational model for cyclic mobility and associated shear deformation. *Journal of Geotechnical and Geoenvironmental Engineering* 129, 1119–1127.
- Youd, T.L., Idriss, I.M., 2001. Liquefaction resistance of soils: summary report from the 1996 NCEER and 1998 NCEER/NSF workshops on evaluation of liquefaction resistance of soils. *Journal of Geotechnical and Geoenvironmental Engineering* 127, 297–313.
- Zace Services Ltd, Software engineering, 2020. ZSOIL.PC 2020 User Manual - Theory. Elmeppress International, Lausanne, Switzerland.
- Zervos, A., Papanastasiou, P., Vardoulakis, I., 2001. A finite element displacement formulation for gradient elastoplasticity. *International Journal for Numerical Methods in Engineering* 50, 1369–1388.
- Zhang, Z.L., Yang, X.L., 2021. Seismic stability analysis of slopes with cracks in unsaturated soils using pseudo-dynamic approach. *Transportation Geotechnics* 29, 100583.
- Zhao, C., Schmüdderich, C., Barciaga, T., Röchter, L., 2019. Response of building to shallow tunnel excavation in different types of soil. *Computers and Geotechnics* 115, 103165.
- Zheng, H., Liu, D., Li, C.G., 2005. Slope stability analysis based on elasto-plastic finite element method. *International Journal for Numerical Methods in Engineering* 64, 1871–1888.

- Zhou, J., Qin, C., 2020. Finite-element upper-bound analysis of seismic slope stability considering pseudo-dynamic approach. *Computers and Geotechnics* 122, 103530.
- Zhu, D., Lee, C., Jiang, H., 2003. Generalised framework of limit equilibrium methods for slope stability analysis. *Géotechnique* 53, 377–395.
- Zhu, D., Lee, C., Qian, Q., Chen, G., 2005. A concise algorithm for computing the factor of safety using the Morgenstern Price method. *Canadian Geotechnical Journal* 42, 272–278.
- Zhu, D., Lee, C., Qian, Q., Zou, Z., Sun, F., 2001. A new procedure for computing the factor of safety using the Morgenstern-Price method. *Canadian Geotechnical Journal* 38, 882–888.
- Zolfaghari, A.R., Heath, A.C., McCombie, P.F., 2005. Simple genetic algorithm search for critical non-circular failure surface in slope stability analysis. *Computers and Geotechnics* 32, 139–152.
- Zou, J.Z., Williams, D.J., Xiong, W.L., 1995. Search for critical slip surfaces based on finite element method. *Canadian Geotechnical Journal* 32, 233–246.

A. geoSlice – Keyword manual

Nodes

Nodes

Nodes:

- [<coordinate 1>, <coordinate 2>]
:

Define coordinates of nodes used to create ground surface, layer boundaries and impenetrable layers.

GwtNodes

GwtNodes:

- [<coordinate 1>, <coordinate 2>]
:

Define coordinates of nodes used to create the ground water table/phreatic level.

Materials and layers

Materials

Materials:

```
- [ $\gamma$ ,  $\gamma_{\text{sat}}$ ,  $\varphi$ ,  $c$ , <label>]
:
```

Define material parameter sets based on the unit weight of the soil above the phreatic level γ , the unit weight of the saturated soil γ_{sat} , the friction angle φ and the cohesion c . Select a material <label> for the output plot.

Layers

Layers:

```
- - <Material number>
- [<Node number i>, <Node number i+1>, <Node number i+2>, ...]
:
```

The definition of each layer consists of two consecutive lines. Layers materials are selected with regard to the corresponding <Material number>. Layer top boundaries are defined in terms of poly-lines of Nodes, where the number of nodes may vary for different layers. The first layer automatically defines the ground surface. Nodes must be selected in a way that layers are defined from left to right or vice versa, spanning over the full horizontal range of the model. Layers are defined from top to bottom, they can overlap with other layers but may not intersect them.

Depth

Depth: d

Define the depth d below the lowest layer y -coordinate to specify the bottom boundary.

Groundwater and pore water pressures

Groundwater

Groundwater:

- [<GwtNode number i>, <GwtNode number i+1>, ...]
 ⋮

Prescribe the ground water table/phreatic level by definition of a poly-line of GwtNodes.

UnitWeightWater

UnitWeightWater: γ_w

Define the unit weight of water γ_w . Although assumed constant for many common applications, a separate input of γ_w was found to be indispensable for the analysis of slope stability problems at elevated gravity levels (e.g. centrifuge model tests).

PWPratio

PWPratio: r_u

Definition of a constant pore water pressure ratio to be considered constant throughout the domain. Note that the **Groundwater** feature is automatically deactivated if $r_u > 0.0$.

DeltaHw

DeltaHw: Δh_w

Define a decrease of the free water level above the ground surface. This decrease may be caused by long waves as a result of seismic ground motion (Goldscheider et al., 2010). Note that the water pressures inside the slope are not influenced by this decrease due to the assumption of a rapid change in the free water level.

Slip surface

EntryExit

EntryExit: [$x_{1,\min}$, $x_{1,\max}$, $x_{2,\min}$, $x_{2,\max}$]

Define two ranges of x -values used for the generation of slip surfaces to be considered in the optimization. The x -values should be assigned in ascending order, though overlap of the ranges (e.g. $x_{1,\max} \geq x_{2,\min}$) is allowed.

hRatio

hRatio: [h_{\min} , h_{\max}]

Define the range of h ratios to be considered in the optimization. Note that the h ratio controls the curvature/radius of the slip surface.

MinWidth

MinWidth: <value>

Define the minimum lateral distance between the entry and exit point.

MinHeight

MinHeight: <value>

Define the minimum absolute height (i.e. sagitta s in Fig. 3.2) of the slip circle. This feature can be used to discard FoS obtained from analyses with very shallow slip surfaces.

NumSlices

NumSlices: N

Define the number of slices N to be used in the slope stability analysis. Note that additional slices may be considered in case the `EnhancedSlices` feature is active.

EnhancedSlices

EnhancedSlices: `<value>`

Activate this feature (`<value> = 1`) to enable a more precise estimation of intersections between the slip surface and layers, phreatic level or other features. Using the `EnhancedSlices` feature, additional slices are added at (very close to) each of these intersections. The `EnhancedSlices` feature is inactive for `<value> = 0`.

DirectionOfFailure

DirectionOfFailure: `<label>`

Define the direction of failure considered in the slope stability analysis. Specify the `<label>` input by choosing `left` or `right`.

Method and optimization

Method

Method: <value>

Define the method of analysis. Select one of the following methods based on the input parameter <value>: Bishop (0), Janbu (1), Spencer (2) and Morgenstern and Price (3).

LambdaSlice

LambdaSlice: <value>

Only relevant in case Bishop or Janbu method have been selected. Define the parameter λ which controls the rotation of the interslice forces. Note that $\lambda = 0$ yields the simplified Bishop and simplified Janbu method.

Tolerance

Tolerance: <value>

Define the allowable error in the iteration process to estimate the FoS for the global equilibrium of forces and/or moments.

Optimization

Optimization: <label>

Define the optimization algorithm used to detect the critical slip surface associated with the smallest FoS. Select between different optimization algorithms by specifying the <label> input: brute grid search (Brute), differential evolution (DE), dual annealing (DA), particle swarm optimization (PSO), simplicial homology global optimization (SHGO).

External loads

Clload

Clload:

- [x , Q , <label>]
⋮

Define concentrated loads acting at the ground surface using the x -coordinate and the magnitude Q . Specify the direction of the load with the <label> option by choosing one of the following inputs: vertical ('V'), horizontal ('H') or perpendicular ('P'). Note that the positive sign convention of the former two relates to the global coordinate system pointing to the right and to the top. Compressive perpendicular loads are defined with a positive value. Specify multiple Clloads by adding further lines. Inclined loads with arbitrary inclination are considered by splitting into horizontal and vertical components.

Dload

Dload:

- [x_1 , x_2 , q_1 , q_2 , <label>]
⋮

Define distributed loads acting at the ground surface using the x_1 and x_2 -coordinates and the respective magnitudes q_1 and q_2 . Specify the direction of the load with the <label> option by choosing one of the following inputs: vertical ('V'), horizontal ('H') or perpendicular ('P'). Note that the positive sign convention of the former two relates to the global coordinate system pointing to the right and to the top. Compressive perpendicular loads are defined with a positive value. Specify multiple Dloads by adding further lines. Inclined distributed loads with arbitrary inclination are considered by splitting into horizontal and vertical components.

Inertial forces and excess pore water pressures

PseudoStatic

PseudoStatic:

- <option>
 - [k_h, k_v] (for <option> = Constant)
 - <label> (for <option> = User)
-

Define seismic coefficients to account for inertial forces in the slope stability analysis. Select <option> = Constant or User to consider constant seismic coefficients throughout the domain or import a spatial distribution of seismic coefficients. In the former case, specify the horizontal and vertical seismic coefficients in the following line. In the latter case, add the path to a *.txt file in the <label> input. Note that the text file should contain table data with columns defined as x, y, k_h, k_v . The data in the text file does not need to be sorted or structured. Note that the x - y coordinates of the data need to be cover to complete size of the model to ensure that interpolation of the data is working properly.

ExcessPWP

ExcessPWP:

- User
 - <label>
-

Define excess pore water pressures Δp^w to be considered in the slope stability analysis. Note that only the input of User data in terms of an import a spatial distribution of excess pore water pressures is enabled. Specify the path to a *.txt file in the <label> input. Note that the text file should contain table data with columns defined as $x, y, \Delta p^w$. The data in the text file does not need to be sorted or structured. Note that the x - y coordinates of the data need to be cover to complete size of the model to ensure that interpolation of the data is working properly.

Composite and non-circular slip surfaces

Bedrock

Bedrock: [<Node number i>, <Node number i+1>, ...]

Define an impenetrable layer that enables to cut the slip surface below this layer, creating a composite slip surface. Specify the location of the impenetrable layer as a poly-line using **Nodes** defined above. Note that the **Bedrock** feature should only be used for in case a weak/strong layer interface is expected to dictate the shape of the critical slip surface.

TopologicalOptimization

TopologicalOptimization: [n_0 , n_{final} , n^s , n^i , χ , $\alpha_{\text{con}} [^\circ]$, $\vartheta_a [^\circ]$, $\vartheta_p [^\circ]$, ε_{tol}]

Perform a post-optimization based on non-circular slip surfaces to investigate if more critical results (i.e. smaller FoS) can be obtained compared to the general optimization using circular slip surfaces. Specify the initial (n_0) and final (n_{final}) number of nodes, the number of variations of each surface (n^s) and internal (n^i) node. The number of nodes is increased if the difference in the critical FoS of two consecutive optimizations of the full slip surface is less than ε_{tol} . Select if the slip surface should be generated based on straight lines ($\chi = 0$) or cubic splines ($\chi = 1$). Specify the maximum concave angle α_{con} and the maximum absolute slopes of the active (ϑ_a) and passive active (ϑ_p) wedge.

TensionCrack

TensionCrack: z_0

Define the maximum tension crack length z_0 . Note that the tension crack length z_{tc} is considered as an additional variable in the optimization process, varying in the range of $0 \leq z_{tc} \leq z_0$. Water pressures in tension cracks are determined based on the global phreatic level.

Structural features

Geogrid

Geogrid:

- [x_1 , x_2 , y , γ , φ , μ , R_{bk}]
 ⋮

Define a geogird to enhance the stability of a slope/dam. Specify the start and end points of a horizontal geogrid (x_1 , x_2 , y), the average unit weight of the soil above the geogrid (γ), the frictional resistance ($\mu \cdot \tan \varphi$) and the ultimate pull-out resistance (R_{bk}).

StoneColumn

StoneColumn:

- [<Material number>, ν_{soil} , φ_{col} , E_{col}/E_{soil} , A_{col}/A]
 ⋮

Consider a soil improvement via stone columns based on modified soil parameters in accordance with Priebe (1995). Specify the <Material number> of the material to be improved, the Poisson's ratio of the soil (ν_{soil}) the friction angle of the column material (φ_{col}), the stiffness ratio between column and soil (E_{col}/E_{soil}) and the areal proportion of the columns (A_{col}/A). Based on the Priebe (1995) approach, modified shear parameters are determined to be used in slope stability analyses.

B. Verification of the General Classic plasticity model

As summarized in Section 2.3.2, the basic idea of the General Classic plasticity model (Lagioia and Panteghini, 2016; Lester and Sloan, 2018) is to use a general formulation of the yield and potential function that enables to switch between many different popular yield functions by selection of three fitting parameters. Verification of the implementation of the General Classic plasticity (GC) model is performed for the GC model with Matsuoka-Nakai yield function (MN^{GC}) by comparison of results from element test simulations with two other implementations of the Matsuoka-Nakai model. The first one is the MN model implemented in this thesis and the second one is the Matsuoka-Nakai no hardening (MNnh) model implemented by Prof. Thomas Benz (see Section 4.4.3 for further details). Note that there are differences in the three Matsuoka-Nakai model implementations with regard to the potential function. To be more specific, the MN^{GC} model uses a MN potential function ($0 \leq \psi \leq \varphi$), the MNnh model uses a Drucker-Prager (DP) potential function ($0 \leq \psi \leq \varphi$), and the MN model uses either a MN potential function (only in combination with an associated flow rule, $\psi = \varphi$) or a DP potential function ($0 \leq \psi \leq \varphi$). To investigate to what extent the three implementations yield similar results, the impact of the potential function on the results of the element test simulations is discussed in the following paragraphs.

In accordance with Section 4.4.3, four element test simulations are conducted for two different materials, a purely frictional ($\varphi = 30^\circ$, $c = 0$ kPa) and a cohesive-frictional ($\varphi = 20^\circ$, $c = 20$ kPa) material. The element tests cover triaxial compression (TXC) and extension (TXE) tests and direct simple shear tests starting from an isotropic (DSS_{iso}) and an anisotropic (DSS_{K_0}) stress state. The elastic material parameters are defined as $E = 30.0$ MPa and $\nu = K_0/(1 + K_0)$ with $K_0 = 1 - \sin \varphi$. The results obtained with Material 1 (purely frictional) and Material 2 (cohesive-frictional) are presented in Fig. B.1 and B.3 and Fig. B.2 and B.4, respectively. Note that the results of the MN (solid black line) and MNnh (circle symbol) model are identical to the ones presented in Section 4.4.3.

In addition, results are presented for the MN model with MN potential surface (red solid line) and the MN^{GC} model with varying dilation angles (square symbol).

It can be seen from the results of the triaxial compression (TXC) tests in the top row of Fig. B.1 and B.2 that MN, MN^{GC} and MNnh yield identical results in terms of the evolution of deviatoric stresses and volumetric strains with increasing axial strains. Note that no differences were to expected for the TXC test as DP and MN surfaces coincide for a Lode angle of $\theta = 30^\circ$. In contrast, it is observed for triaxial extension (TXE) tests presented in the bottom rows of these figures that the volumetric behavior of the MN

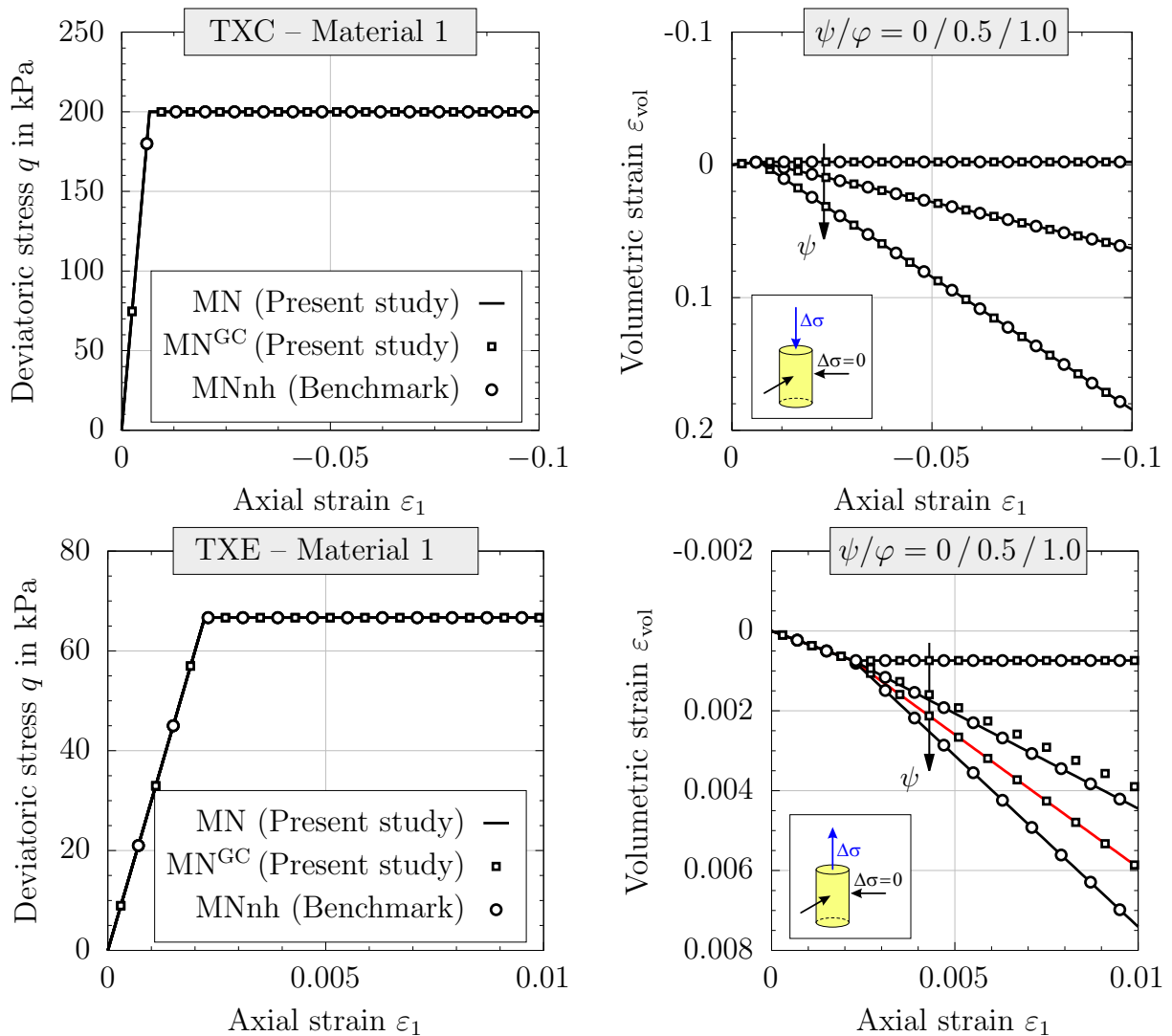


Figure B.1: Deviatoric stresses and volumetric strains during triaxial compression and extension tests on a frictional material ($\varphi = 30^\circ$) simulated using three implementations of the Matsuoka-Nakai (MN) model

model depends on the selection of the potential surface for a Lode angle of $\theta = -30^\circ$. Note that the red line and the square symbols representing the MN model with MN potential surface and the MN^{GC} model are in perfect agreement for $\psi = \varphi$. Although both models have been implemented in this thesis, this good agreement with two different models can be considered a reasonable indicator for valid implementations. Evaluating the influence of the potential function on the volumetric behavior, it is seen that simulations with MN potential function yield smaller volumetric strains compared to those with DP potential function. This can be explained by the direction of the normal vector at $\theta = -30^\circ$ for both the MN and DP surfaces, where the volumetric component of the latter is larger.

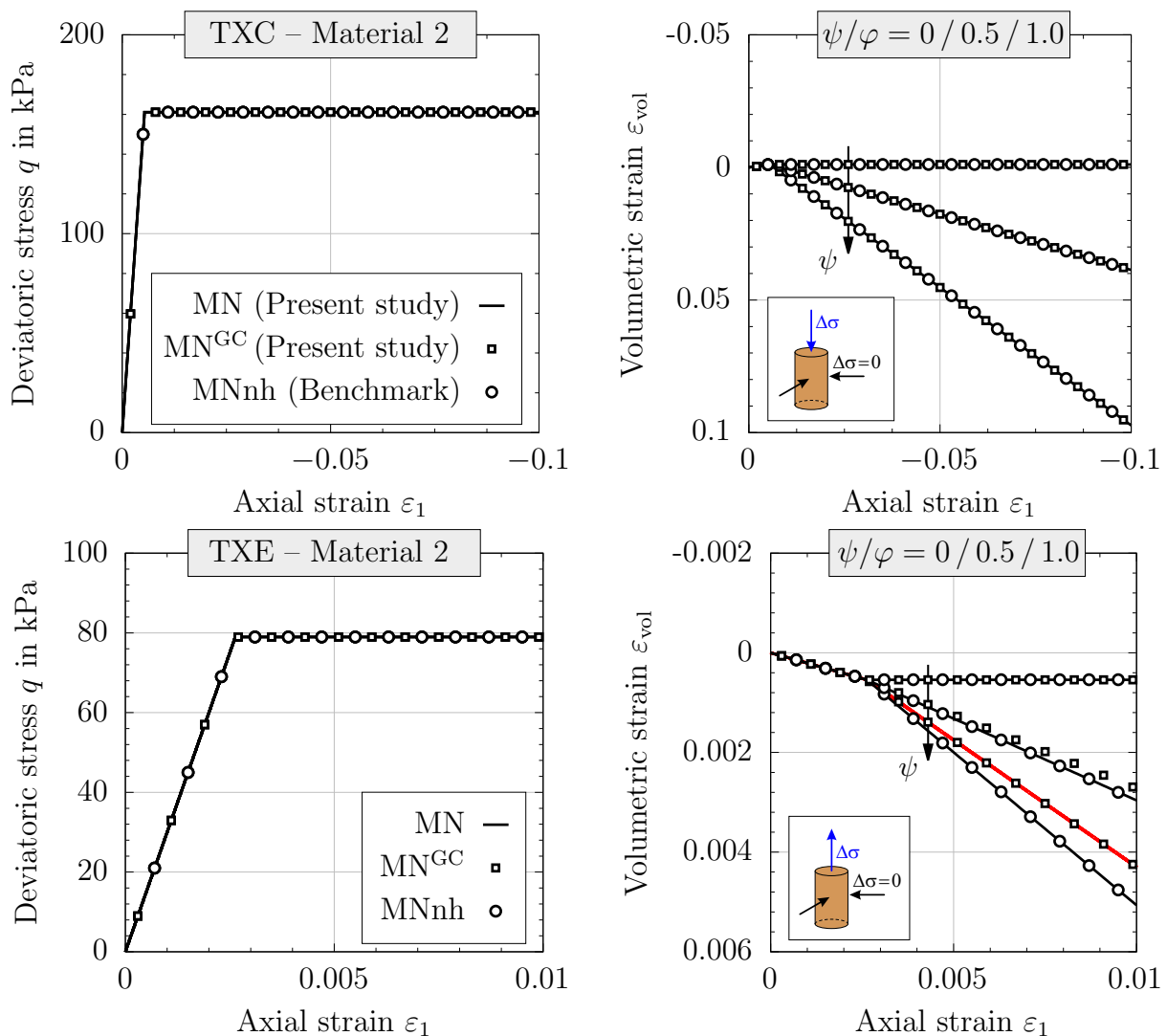


Figure B.2: Deviatoric stresses and volumetric strains during triaxial compression and extension tests on a cohesive-frictional material ($\varphi = 20^\circ$, $c = 20$ kPa) simulated using three implementations of the Matsuoka-Nakai (MN) model

Note that the differences in the volumetric behavior reduce with decreasing dilation angle, where similar volumetric behavior is obtained for $\psi = 0^\circ$.

Analyzing the results of the direct simple shear (DSS) tests with Material 1 and 2 presented in Fig. B.3 and Fig. B.4, respectively, identical results are obtained with the MN model and the MNnh model while good agreement is also seen with the MN^{GC} model. Still, it is observed that the potential function has a minor influence on the evolution of shear stresses and a slightly more pronounced influence on the volumetric behavior. In addition, it is apparent that the differences between simulations with DP and MN po-

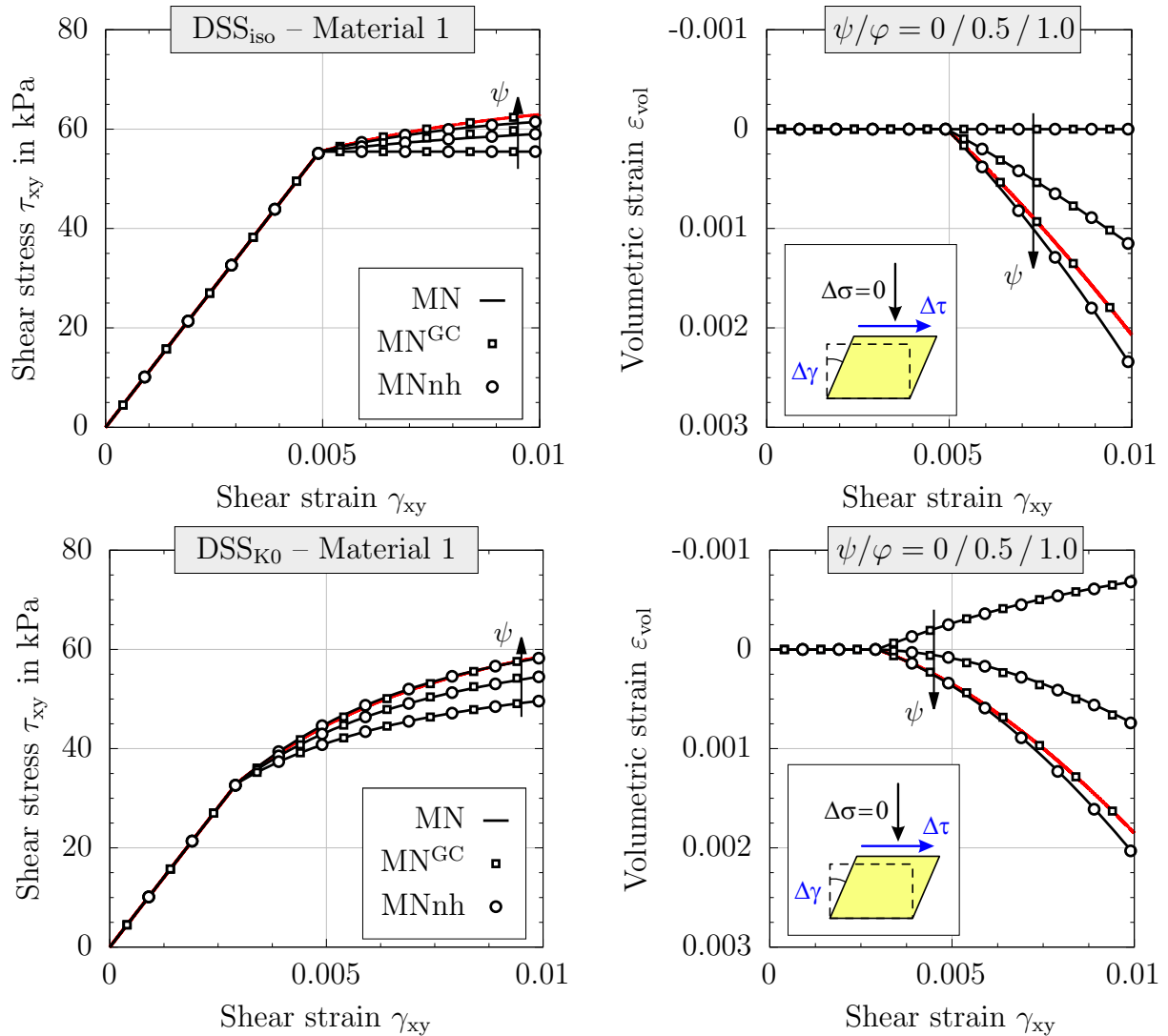


Figure B.3: Shear stresses and volumetric strains during direct simple shear tests starting from an isotropic and K_0 state with a frictional material ($\varphi = 30^\circ$) simulated using three implementations of the Matsuoka-Nakai (MN) model

tential surface are larger for the purely frictional material (Material 1) compared to the cohesive-frictional material (Material 2). Compared to the differences seen for the triaxial extension tests, it is noteworthy that the influence of the potential function is smaller in case of DSS tests. This can be explained by the fact that the differences in the size of the DP and MN surfaces is larger for triaxial extension ($\theta = -30^\circ$) compared to plane strain conditions ($0^\circ \leq \theta \leq 10^\circ$).

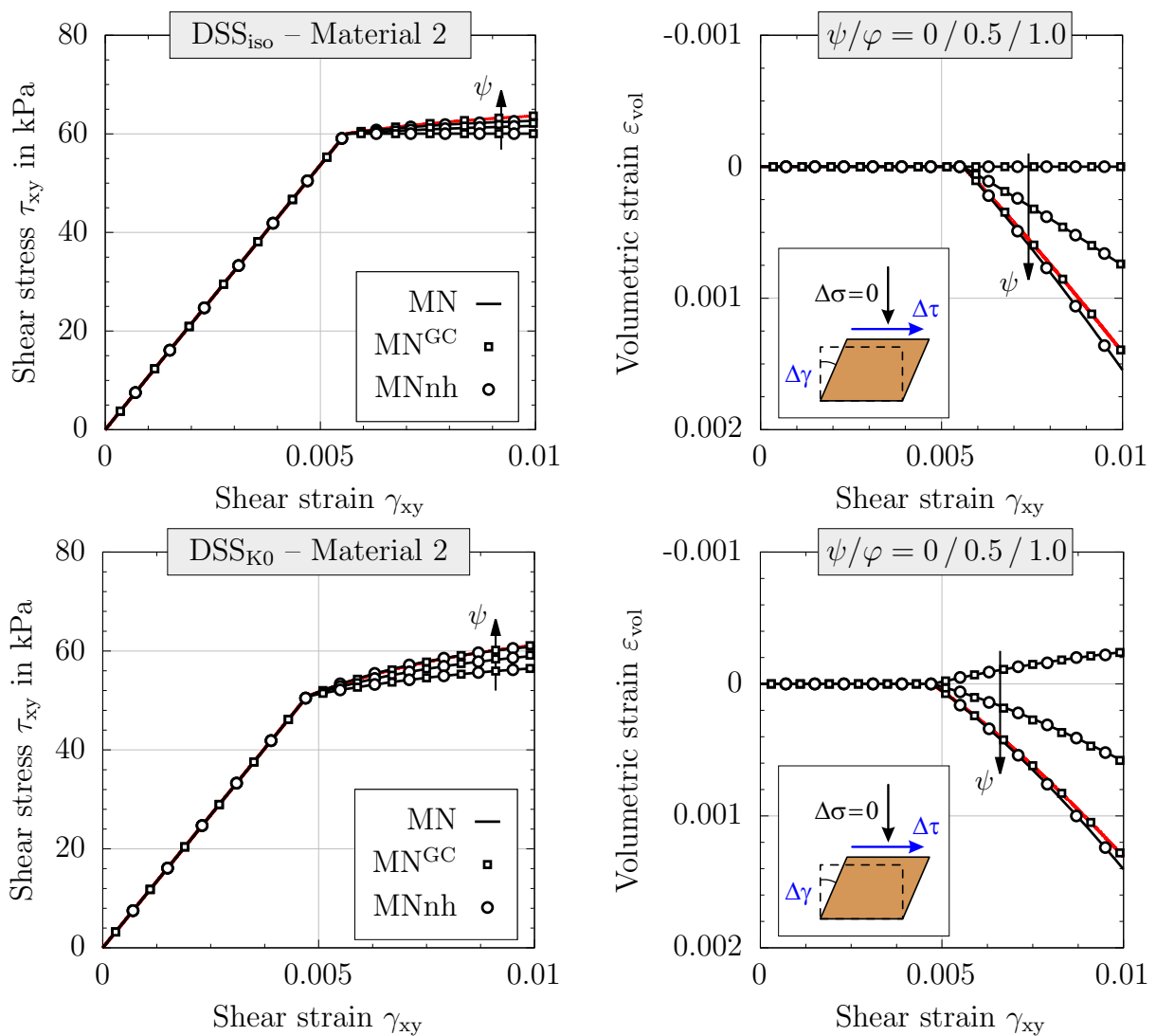


Figure B.4: Shear stresses and volumetric strains during direct simple shear tests starting from an isotropic and K_0 state with a cohesive-frictional material ($\varphi = 20^\circ$, $c = 20$ kPa) simulated using three implementations of the Matsuoka-Nakai (MN) model

C. Settings of machine learning algorithms

Radial Basis Function (RBF) interpolation

Radial Basis Function (RBF) interpolation (`scipy`) allows for the consideration of a limited number of nearest data points (neighbors) to speed-up the evaluation process and avoid large matrix dimensions exceeding memory capacities. The number of neighbors was set to 1,000 to avoid singularities during interpolation due to insufficient nearest data points for all input dimensions. This number ensured to be large enough to avoid singularities and small enough to obtain accurate results. Moreover, the ‘thin plate spline’ kernel ($r^2 \cdot \log(r)$) was used in this study, as trial analyses revealed slightly better agreement with the test data compared to the ‘cubic’ kernel (r^3). Other kernel functions investigated (e.g. ‘multiquadric’, ‘inverse multiquadric’, ‘inverse quadratic’, ‘Gaussian’) resulted in larger deviations from the test data. As trial analyses showed that a small ‘smoothing’ parameter led to good predictions, a value of 0.1 was chosen. Further parameters not mentioned here were chosen equal to default values.

K-Nearest Neighbors (KNN) regression

The K-Nearest Neighbors (KNN) regression (`scikit-learn`) was chosen as it enables a very simple and fast evaluation. In this study, the number of neighbors was selected to 3 based on trial analyses showing decreasing accuracy with test data with increasing number of neighbors. As reported in Section 9.3, weighting of the neighbors was conducted with respect to the inverse distance between the relevant neighbors and the target data point. Moreover, the ‘kd-tree’ algorithm was chosen to compute the nearest neighbors.

Random Forest (RF) regression

The Random Forest (RF) regression (`scikit-learn`) was used as it offers a completely different type of approach due to evaluation of a set of decision trees referred to as estimators. Selection of the settings for the RF approach was primarily based on the objective to keep a balance between accuracy and time while avoiding over-fitting. Therefore, 1,000 trees (estimators) were chosen considering a maximum of three features to be analyzed for finding the best split. Trial analyses showed accurate predictions with decision trees expanding up to the maximum depth. However, the chance for over-fitting was very high. Therefore, a maximum depth of 10 (levels/splits) was chosen. It should be noted that (significant) larger number of estimators or maximum depth could also cause memory errors. The 'squared error' criterion was selected as it provided accurate results in a short period of time.

Multi-layer Perceptron (MLP) regression

The Multi-Layer Perceptron (MLP) regression (`scikit-learn`) was applied considering a default value of one hidden layer with 100 perceptrons, where a variation of the hidden layers did not affect the results strongly. In contrast to that, it was observed that the activation function had a decisive effect on the accuracy. Trial analyses revealed that choosing 'rectified linear unit function', which returns $f(x) = \max(0, x)$, over a 'hyperbolic tangent', a 'logistic sigmoid' or a 'linear' function led to the best results. Moreover, a penalty (regularization term) parameter of $\alpha = 0.0001$ was selected. Trial analyses revealed that α has a decisive impact on the general trend of the shear strain versus shear stress curve. By increasing α , the scattering depicted in Fig. 9.4 was reduced, giving almost smooth curves for $\alpha \approx 0.1$. However, mean squared errors and maximum deviations increased with increasing penalty parameter, while also training time increased significantly. Therefore, it was decided to use a less time consuming and more accurate setting by choosing a small α value at the cost of scattering in the prediction.

**Schriftenreihe des Instituts für Grundbau, Wasserwesen und Verkehrswesen
der Ruhr-Universität Bochum**

Herausgeber: H.L. Jessberger

- 1 (1979) **Hans Ludwig Jessberger**
Grundbau und Bodenmechanik an der Ruhr-Universität Bochum
- 2 (1978) **Joachim Klein**
Nichtlineares Kriechen von künstlich gefrorenem Emschermergel
- 3 (1979) **Heinz-Joachim Gödecke**
Die Dynamische Intensivverdichtung wenig wasserdurchlässiger Böden
- 4 (1979) **Poul V. Lade**
Three Dimensional Stress-Strain Behaviour and Modeling of Soils
- 5 (1979) **Roland Pusch**
Creep of soils
- 6 (1979) **Norbert Diekmann**
Zeitabhängiges, nichtlineares Spannungs-Verformungsverhalten von gefrorenem Schluff unter triaxialer Belastung
- 7 (1979) **Rudolf Dörr**
Zeitabhängiges Setzungsverhalten von Gründungen in Schnee, Firn und Eis der Antarktis am Beispiel der deutschen Georg-von-Neumayer- und Filchner-Station
- 8 (1984) **Ulrich Güttler**
Beurteilung des Steifigkeits- und Nachverdichtungsverhaltens von ungebundenen Mineralstoffen
- 9 (1986) **Peter Jordan**
Einfluss der Belastungsfrequenz und der partiellen Entwässerungsmöglichkeiten auf die Verflüssigung von Feinsand
- 10 (1986) **Eugen Makowski**
Modellierung der künstlichen Bodenvereisung im grundwasserdurchströmten Untergrund mit der Methode der finiten Elemente
- 11 (1986) **Reinhard A. Beine**
Verdichtungswirkung der Fallmasse auf Lastausbreitung in nichtbindigem Boden bei der Dynamischen Intensivverdichtung
- 12 (1986) **Wolfgang Ebel**
Einfluss des Spannungspfades auf das Spannungs-Verformungsverhalten von gefrorenem Schluff im Hinblick auf die Berechnung von Gefrierschächten
- 13 (1987) **Uwe Stoffers**
Berechnungen und Zentrifugen-Modellversuche zur Verformungsabhängigkeit der Ausbaubeanspruchung von Tunnelausbauten in Lockergestein
- 14 (1988) **Gerhard Thiel**
Steifigkeit und Dämpfung von wassergesättigtem Feinsand unter Erdbebenbelastung

- 15 (1991) **Mahmud Thaher**
Tragverhalten von Pfahl-Platten-Gründungen im bindigen Baugrund,
Berechnungsmodelle und Zentrifugen-Modellversuche

Schriftenreihe des Instituts für Grundbau der Ruhr-Universität Bochum

Herausgeber: H.L. Jessberger

- 16 (1992) **Rainer Scherbeck**
Geotechnisches Verhalten mineralischer Deponieabdichtungsschichten
bei ungleichförmiger Verformungswirkung
- 17 (1992) **Martin M. Bizialiele**
Torsional Cyclic Loading Response of a Single Pile in Sand
- 18 (1993) **Michael Kotthaus**
Zum Tragverhalten von horizontal belasteten Pfahlreihen aus langen Pfählen in Sand
- 19 (1993) **Ulrich Mann**
Stofftransport durch mineralische Deponieabdichtungen:
Versuchsmethodik und Berechnungsverfahren
- 20 (1992) **Festschrift anlässlich des 60. Geburtstages von
Prof. Dr.-Ing. H. L. Jessberger**
20 Jahre Grundbau und Bodenmechanik an der Ruhr-Universität Bochum
- 21 (1993) **Stephan Demmert**
Analyse des Emissionsverhaltens einer Kombinationsabdichtung im Rahmen der
Risikobetrachtung von Abfalldeponien
- 22 (1994) **Diethard König**
Beanspruchung von Tunnel- und Schachtausbauten in kohäsionslosem Lockergestein
unter Berücksichtigung der Verformung im Boden
- 23 (1995) **Thomas Neteler**
Bewertungsmodell für die nutzungsbezogene Auswahl von Verfahren zur Altlastensanierung
- 24 (1995) **Ralph Kockel**
Scherfestigkeit von Mischabfall im Hinblick auf die Standsicherheit von Deponien
- 25 (1996) **Jan Laue**
Zur Setzung von Flachfundamenten auf Sand unter wiederholten Lastereignissen
- 26 (1996) **Gunnar Heibroek**
Zur Rissbildung durch Austrocknung in mineralischen Abdichtungsschichten
an der Basis von Deponien
- 27 (1996) **Thomas Siemer**
Zentrifugen-Modellversuche zur dynamischen Wechselwirkung zwischen Bauwerken
und Baugrund infolge stoßartiger Belastung
- 28 (1996) **Viswanadham V. S. Bhamidipati**
Geosynthetic Reinforced Mineral Sealing Layers of Landfills

- 29 (1997) **Frank Trappmann**
Abschätzung von technischem Risiko und Energiebedarf bei Sanierungsmaßnahmen für Altlasten
- 30 (1997) **André Schürmann**
Zum Erddruck auf unverankerte flexible Verbauwände
- 31 (1997) **Jessberger, H. L. (Herausgeber)**
Environment Geotechnics, Report of ISSMGE Technical Committee TC 5 on Environmental Geotechnics

**Schriftenreihe des Instituts für Grundbau und Bodenmechanik der
Ruhr-Universität Bochum**

Herausgeber: Th. Triantafyllidis

- 32 (2000) **Triantafyllidis, Th. (Herausgeber)**
Boden unter fast zyklischer Belastung: Erfahrung und Forschungsergebnisse (Workshop)
- 33 (2002) **Christof Gehle**
Bruch- und Scherverhalten von Gesteinstrennflächen mit dazwischenliegenden Materialbrücken
- 34 (2003) **Andrzej Niemunis**
Extended hypoplastic models for soils
- 35 (2004) **Christiane Hof**
Über das Verpressankertragverhalten unter kalklösendem Kohlensäureangriff
- 36 (2004) **René Schäfer**
Einfluss der Herstellungsmethode auf das Verformungsverhalten von Schlitzwänden in weichen bindigen Böden
- 37 (2005) **Henning Wolf**
Zur Scherfugenbänderung granularer Materialien unter Extensionsbeanspruchung
- 38 (2005) **Torsten Wichtmann**
Explicit accumulation model for non-cohesive soils under cyclic loading
- 39 (2008) **Christoph M. Loreck**
Die Entwicklung des Frischbetondruckes bei der Herstellung von Schlitzwänden
- 40 (2008) **Igor Arsic**
Über die Bettung von Rohrleitungen in Flüssigböden
- 41 (2009) **Anna Arwanitaki**
Über das Kontaktverhalten zwischen einer Zweiphasenschlitzwand und nichtbindigen Böden

**Schriftenreihe des Lehrstuhls für Grundbau, Boden- und Felsmechanik der
Ruhr-Universität Bochum**

Herausgeber: T. Schanz

- 42 (2009) **Yvonne Lins**
Hydro-Mechanical Properties of Partially Saturated Sand
- 43 (2010) **Tom Schanz (Herausgeber)**
Geotechnische Herausforderungen beim Umbau des Emscher-Systems
Beiträge zum RuhrGeo Tag 2010
- 44 (2010) **Jamal Alabdullah**
Testing Unsaturated Soil for Plane Strain Conditions: A New Double-Wall Biaxial Device
- 45 (2011) **Lars Röchter**
Systeme paralleler Scherbänder unter Extension im ebenen Verformungszustand
- 46 (2011) **Yasir Al-Badran**
Volumetric Yielding Behavior of Unsaturated Fine-Grained Soils
- 47 (2011) **Usque ad finem**
Selected research papers
- 48 (2012) **Muhammad Ibrar Khan**
Hydraulic Conductivity of Moderate and Highly Dense Expansive Clays
- 49 (2014) **Long Nguyen-Tuan**
Coupled Thermo-Hydro-Mechanical Analysis: Experimental and Back Analysis
- 50 (2014) **Tom Schanz (Herausgeber)**
Ende des Steinkohlenbergbaus im Ruhrrevier: Realität und Perspektiven für die Geotechnik
Beiträge zum RuhrGeo Tag 2014
- 51 (2014) **Usque ad finem**
Selected research papers
- 52 (2014) **Houman Soleimani Fard**
Study on the Hydro-Mechanical Behavior of Fiber Reinforced Fine Grained Soils,
with Application to the Preservation of Historical Monuments
- 53 (2014) **Wiebke Baile**
Hydro-Mechanical Behaviour of Clays - Significance of Mineralogy
- 54 (2014) **Qasim Abdulkarem Jassim Al-Obaidi**
Hydro-Mechanical Behavior of Collapsible Soils
- 55 (2015) **Veselin Zarev**
Model Identification for the Adaption of Numerical Simulation Models -
Application to Mechanized Shield Tunneling
- 56 (2015) **Meisam Goudarzy**
Micro and Macro Mechanical Assessment of Small and Intermediate Strain
Properties of Granular Material

- 57 (2016) **Oliver Detert**
Analyse einer selbstregulierenden interaktiven Membrangründung für Schüttkörper auf geringtragfähigen Böden
- 58 (2016) **Yang Yang**
Analyses of Heat Transfer and Temperature-induced Behaviour in Geotechnics
- 59 (2016) **Alborz Pourzargar**
Application of suction stress concept to partially saturated compacted soils
- 60 (2017) **Hanna Haase**
Multiscale Analysis of Clay-Polymer Composites for Geoenvironmental Applications
- 61 (2017) **Kavan Khaledi**
Constitutive modeling of rock salt with application to energy storage caverns
- 62 (2017) **Nina Silvia Müthing**
On the consolidation behaviour of fine-grained soils under cyclic loading
- 63 (2017) **Elham Mahmoudi**
Probabilistic analysis of a rock salt cavern with application to energy storage systems
- 64 (2017) **Negar Rahemi**
Evaluation of liquefaction behavior of sandy soils using critical state soil mechanics and instability concept
- 65 (2018) **Chenyang Zhao**
Numerical Modeling of Mechanized Tunnel Excavation: Effects of Sub-systems and Advanced Process Simulation
- 66 (2018) **Tom Schanz (Herausgeber)**
Innovationen im Spezialtiefbau und in der Umweltgeotechnik
Beiträge zum RuhrGeo Tag 2018
- 67 (2019) **Linzhi Lang**
Hydro-Mechanical Behaviour of Bentonite-Based Materials Used for Disposal of Radioactive Wastes
- 68 (2019) **Usama Al-Anbaki**
Hydraulic Interaction of Soil and Nonwoven Geotextiles under Unsaturated Conditions
- 69 (2019) **Abhishek Rawat**
Coupled Hydro-mechanical Behavior of a Compacted Bentonite-Sand Mixture: Experimental and Numerical Investigations

**Schriftenreihe des Lehrstuhls für Bodenmechanik, Grundbau und
Umweltgeotechnik der Ruhr-Universität Bochum**

Herausgeber: T. Wichtmann

- 70 (2019) **Mahmoud Qarmout**
Tunnel face stability using Kinematical Element Method (KEM)
- 71 (2021) **Raoul Hölter**
Optimal Experimental Design in Geotechnical Engineering
- 72 (2022) **Wolfgang Lieske**
Impact of polymer constitution on the hydro-mechanical behaviour of modified bentonite for the application in geotechnical and geoenvironmental engineering
- 73 (2022) **Patrick Staubach**
Contributions to the numerical modelling of pile installation processes and high-cyclic loading of soils
- 74 (2022) **Lingyun Li**
On the hydromechanical behaviour of loess and its effect on slope stability under rainfall infiltration
- 75 (2022) **Debdeep Sarkar**
Influence of particle characteristics on the behaviour of granular materials under static, cyclic and dynamic loading
- 76 (2023) **Torsten Wichtmann (Herausgeber)**
Umbau des Emscher-Systems – Geotechnische Erfahrungen
Beiträge zum RuhrGeo Tag 2023
- 77 (2023) **Abbas Farhat**
Fluidization and erosion of cemented granular materials. Experimental characterization and micromechanical simulation
- 78 (2023) **Andrea Geppetti**
Experimental and numerical investigations on the behaviour of tailing storage facilities under seismic loading
- 79 (2023) **Mohammad Hassan Sanayei**
Micromechanical modelling for the analysis of piping erosion in cemented soils for suction-assisted offshore foundations
- 80 (2024) **Christoph Schmüdderich**
Contributions to the stability assessment of slopes subjected to seismic loading